UNIVERSIDADE FEDERAL DO PARÁ
INSTITUTO DE GEOCIÊNCIAS
PROGRAMA DE PÓS-GRADUAÇÃO EM GEOLOGIA E GEOQUÍMICA

TESE DE DOUTORADO Nº 182

PETROGÊNESE DOS GRANITOS MANDA SAIA E MARAJOARA: CONTRIBUIÇÕES PARA A DEFINIÇÃO DA NATUREZA DO MAGMATISMO PALEOPROTEROZOICO DA PROVÍNCIA CARAJÁS

Tese apresentada por:

RODRIGO FABIANO SILVA SANTOS
Orientador: Prof. Dr. Davis Carvalho de Oliveira (UFPA)

BELÉM – PARÁ
2024

Universidade Federal do Pará
Instituto de Geociências
Programa de Pós-Graduação em Geologia e Geoquímica

PETROGÊNESE DOS GRANITOS MANDA SAIA E MARAJOARA: CONTRIBUIÇÕES PARA A DEFINIÇÃO DA NATUREZA DO MAGMATISMO PALEOPROTEROZOICO DA PROVÍNCIA CARAJÁS

TESE APRESENTADA POR
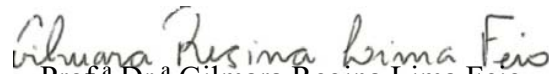
RODRIGO FABIANO SILVA SANTOS

Como requisito parcial à obtenção de Grau de Doutor em Ciências na Área de GEOQUÍMICA E PETROLOGIA, linha de pesquisa EVOLUÇÃO CRUSTAL E METALOGÊNESE.

Data de Aprovação: 13 / 12 / 2024
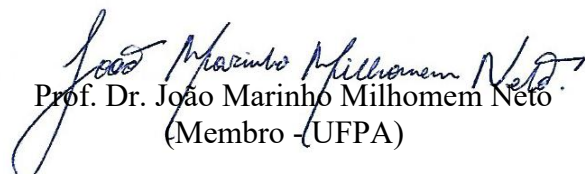
Banca Examinadora:

Prof. Dr. Davis Carvalho de Oliveira
(Orientador – UFPA)

Prof.ª Dr.ª Gilmara Regina Lima Feio
(Membro – UNIFESSPA)

Prof. Dr. Luciano Ribeiro da Silva
(Membro – UFOPA)

Prof. Dr. Valdecir de Assis Janasi
(Membro – USP)

Prof. Dr. João Marinho Milhomem Neto
(Membro – UFPA)

Dedico este trabalho aos meus pais, Eliana e Otávio, à minha amada esposa, Vanessa, e aos professores e amigos que sempre me apoiaram até esse momento.

AGRADECIMENTOS

O autor desta tese expressa seus sinceros agradecimentos a todas as pessoas e entidades que direta ou indiretamente contribuíram para a realização deste trabalho e em particular:

- Ao Programa de Pós-Graduação de Geologia e Geoquímica (PPGG) do Instituto de Geociências da UFPA pelo fornecimento de infraestrutura;

- O presente trabalho foi realizado com apoio da Coordenação de Aperfeiçoamento de Pessoal de Nível Superior - Brasil (CAPES) – Código de Financiamento 001;

- Ao Laboratório de Geologia Isotópica (Pará-Iso) do Instituto de Geociências da UFPA, com destaque para o apoio do Prof. Marco Galarza;

- Ao Laboratório de Microanálises (LM) do Instituto de Geociências da UFPA, em especial à amiga de turma Gisele Marques (técnica administrativa do laboratório) e ao Prof. Cláudio Lamarão (coordenador do laboratório);

- Ao Laboratório de Laminação do Instituto de Geociências da UFPA, com destaque para o apoio da responsável técnica Joelma Lobo;

- Ao orientador Prof. Davis Carvalho de Oliveira, pela oportunidade de realizar minha tese de doutorado, pelos incentivos, principalmente em agosto de 2023 quando fiz o concurso para Santarém, ensinamentos e reflexões tanto dentro quanto fora da geologia nesses mais de 10 anos desde o mestrado; o meu muito obrigado.

- Aos membros do Grupo de Pesquisa Petrologia de Granitoides (GPPG) do Instituto de Geociências da UFPA, pelo suporte técnico-científico e inúmeras discussões; principalmente ao Prof. José de Arimatéia Costa de Almeida na construção do modelo geológico do artigo do Granito Marajoara;

- A secretaria do Programa de Pós-Graduação, Cleida e Joanicy, e Lúcia Imbiriba, da biblioteca do IG, pelo auxílio nas questões administrativas e por toda a atenção.

- A todos os autores dos artigos desta tese;

- A todos os amigos da Sala 3, sem exceções.

"Existem muitas hipóteses em ciência que estão erradas.
Isso é perfeitamente aceitável, elas são a abertura
para achar as que estão certas". *Carl Sagan*

RESUMO

Os granitos Marajoara (GMJ) e Manda Saia (GMS) estão localizados no sudeste do Estado do Pará e representam intrusões circulares com dimensões de *stock* encaixadas em rochas mesoarqueanas do Domínio Rio Maria, na porção centro-sul da Província Carajás. São formados por rochas que afloram sob a forma de extensos lajedos, sobre os quais não foram observados vestígios de deformação no estado sólido (aspecto isotrópico) e frequentemente apresentam enclaves angulosos de suas rochas encaixantes. O GMJ é formado pelas variedades biotita monzogranito equigranular (BMzE) e heterogranular (BMzH), e enclaves porfiríticos (EP) e microgranulares (EM) que são restritos à fácies BMzH. Os conteúdos médios de quartzo e das razões plagioclásio/microclínio variam significativamente, permitindo que estas rochas sejam classificadas como de composição sieno a monzograníticas, e até mesmo granodioríticas no caso dos enclaves microgranulares. São granitos peraluminosos similares aos granitos ferrosos com altas razões K_2O+Na_2O/CaO e $FeOt/(FeOt+MgO)$. São enriquecidos em Rb, Zr, Y, Nb, F e ETR pesados, com as fácies mais evoluídas apresentando baixos conteúdos de Sr e Ba. Nos padrões de ETR, as anomalias negativas de Eu são acentuadas e os ETR pesados mostram um aumento gradual com a diferenciação magmática. Estes granitos incidem no campo dos granitos intraplaca e mostram afinidades geoquímicas com os granitos tipo-A. Suas razões $FeOt/(FeOt+MgO)$ são compatíveis com aqueles dos típicos granitos tipo-A oxidados (BMzH e EP) e reduzidos (BMzE), enquanto o GMS mostra um caráter moderadamente reduzido. Já os EM mostram afinidade com os granitos magnesianos e da série cálcio-alcalina. De acordo com os dados de química mineral de biotita, o GMS e a fácies BMzH do GMJ incidem no campo das rochas da série magnetita, enquanto as rochas da variedade BMzE são semelhantes às rochas da série ilmenita. As análises U–Pb em zircão (SHRIMP) fornecem idade de cristalização de 1884 ± 11 Ma para o GMJ e 1866 ± 10 Ma para o GMS (LA–SF–ICP–MS). Os dados isotópicos de Lu–Hf indicam $\epsilon_{Hf(t)}$ entre -11 e -18 e Hf-T_{DM}^C de 3,2 a 3,6 Ga para o GMJ; e $\epsilon_{Hf(t)}$ entre -13 e -19 e Hf-T_{DM}^C de 3,3 a 3,6 Ga para o GMS. As lacunas composicionais entre as diversas variedades que constituem o GMJ sugerem que seus magmas não são cogenéticos. Modelamento geoquímico sugere que o GMJ e o GMS foram gerados a partir de fusão parcial de rochas tonalíticas, com eventual contribuição metassedimentar, a uma taxa de fusão que varia de 16 a 18% e uma assembleia residual composta por plagioclásio, quartzo, biotita, magnetita e ilmenita. A mistura de magmas félsicos e máficos desempenhou um papel importante na colocação. Os enclaves representam magmatismo básico do manto litosférico enriquecido que foi injetado na câmara magmática durante o processo de subducção,

interagindo em graus variados com o magma formador do granito Marajoara. Essa hipótese pode ser reforçada pela ocorrência de um dique composto de diabásio-granito porfirítico de 1,88 Ga na região de Rio Maria. O modelo proposto sugere que o magma granítico inicialmente formou uma câmara magmática, seguida por injeções repetidas de magma máfico, resultando em convecção em pequena escala. Subsequentemente, grandes volumes de magma máfico quente entraram na câmara, levando a processos de mistura. Enclaves microgranulares e porfiríticos foram formados devido à mistura de magmas em áreas onde havia contrastes de temperatura entre magmas félsicos e máficos. Os resultados apresentados neste trabalho destacam a importância da crosta arqueana para a origem dos granitos paleoproterozoicos, cuja colocação em níveis crustais rasos ocorreu através de um sistema alimentador de diques como consequência de tectônica extensional.

Palavras-chave: Granito tipo-A; enclaves; paleoproterozoico; Província Carajás; Cráton Amazônico.

ABSTRACT

The Marajoara (MJG) and Manda Saia (MSG) granites are located in southeastern Pará State, Brazil, and represent circular intrusions with stock dimensions embedded in Mesoarchean rocks of the Rio Maria Domain, in the central-southern portion of the Carajás Province. These rocks outcrop as extensive pavements, exhibiting no solid-state deformation features (isotropic aspect) and frequently containing angular enclaves of the surrounding host rocks. The MJG comprises equigranular biotite monzogranite (eBMzG) and heterogranular (hBMzG) varieties, as well as porphyritic (pME) and microgranular enclaves (ME) restricted to the hBMzG facies. Quartz content and plagioclase/microcline ratios vary significantly, allowing these rocks to be classified from syenogranitic to monzogranitic, and even granodioritic in the case of microgranular enclaves. They are peraluminous granites, similar to ferroan granites with high K_2O+Na_2O/CaO and $FeOt/(FeOt+MgO)$ ratios, enriched in Rb, Zr, Y, Nb, F, and heavy REEs, with more evolved facies displaying low Sr and Ba contents. In REE patterns, negative Eu anomalies are prominent, and heavy REEs show a gradual increase with magmatic differentiation. These granites fall within the intraplate granite field and exhibit geochemical affinities with A-type granites. Their $FeOt/(FeOt+MgO)$ ratios align with typical oxidized (hBMzG and pME) and reduced (eBMzG) A-type granites, while the MSG displays a moderately reduced character. The ME, however, show affinity with magnesian and calc-alkaline series granites. According to biotite mineral chemistry, MSG and the hBMzG facies of MJG fall within the magnetite series field, while eBMzG rocks are similar to ilmenite series rocks. SHRIMP zircon U–Pb analyses provide crystallization ages of 1884 ± 11 Ma for MJG and 1866 ± 10 Ma for MSG (LA–SF–ICP–MS). Lu–Hf isotopic data indicate $\varepsilon_{Hf(t)}$ between -11 and -18 and Hf-T_{DM}^C from 3.2 to 3.6 Ga for MJG; and $\varepsilon_{Hf(t)}$ between -13 and -19 and Hf-T_{DM}^C from 3.3 to 3.6 Ga for MSG. The compositional gaps among the various MJG varieties suggest that their magmas are not cogenetic. Geochemical modeling suggests that MJG and MSG were generated by partial melting of tonalitic rocks, with occasional metasedimentary contributions, at a melting rate ranging from 16 to 18%, with a residual assemblage of plagioclase, quartz, biotite, magnetite, and ilmenite. Felsic and mafic magma mixing played an important role in the emplacement. The enclaves represent enriched lithospheric mantle-derived magmatism injected into the magma chamber during the subduction process, interacting to varying degrees with the magma forming the Marajoara granite. This hypothesis may be reinforced by the occurrence of a 1.88 Ga diabase-porphyritic granite composite dyke in the Rio Maria region. The proposed model suggests that the granitic magma initially formed a

magma chamber, followed by repeated mafic magma injections, resulting in small-scale convection. Subsequently, large volumes of hot mafic magma entered the chamber, leading to mixing processes. Microgranular and porphyritic enclaves were formed due to magma mixing in areas where there were temperature contrasts between felsic and mafic magmas. The results presented in this study highlight the importance of the Archean crust in the origin of Paleoproterozoic granites, which were emplaced in shallow crustal levels through a dyke feeder system as a result of extensional tectonics.

LISTA DE ILUSTRAÇÕES

CAPÍTULO 3

LISTA DE TABELAS

SUMÁRIO

CAPÍTULO 1 INTRODUÇÃO

1.1 APRESENTAÇÃO

A petrogênese de granitos tem sido tema de intenso debate desde a década de 1970, quando as primeiras classificações alfabéticas (I, S, M e A) surgiram (Chappell & White 1974, Loiselle & Wones 1979). A controvérsia girou em torno das interações complexas entre diferentes processos magmáticos e as múltiplas fontes potenciais de magma (Frost & Frost, 2011), onde a fusão parcial de rochas crustais destaca-se como um mecanismo primário para a geração de magmas graníticos (Collins *et al*. 1982, Anderson 1983, Whalen *et al*. 1987, Stevens & Clemens 1993, Johannes & Holtz 1996, Clemens & Watkins 2001). Além disso, a petrogênese dos granitos também é influenciada pela cristalização fracionada e por processos de sistema aberto, como mistura de magmas e contaminação crustal. Com relação aos granitos tipo-A, eles foram inicialmente caracterizados por Loiselle & Wones (1979) como aqueles gerados ao longo de zonas de *rift* e dentro de blocos continentais estáveis, sendo moderadamente alcalinos, com alta razão FeO/FeO+MgO, baixa fugacidade de oxigênio (fO_2) e baixo teor de H_2O. No entanto, estudos experimentais demonstraram a diversidade dos magmas tipo-A em termos de conteúdos de H_2O e estado de oxidação (Dall'Agnol *et al*. 1999b). De acordo com essas características, o modelo envolvendo a fusão de resíduos granulíticos na crosta profunda, dos quais foram previamente extraídos *melts* félsicos altamente hidratados, demonstrou a inadequação de fontes empobrecidas na geração de granitos tipo-A típicos (Creaser *et al*. 1991).

Maciços anorogênicos de afinidade tipo-A e idade paleoproterozoica foram amplamente descritos na Província Carajás, localizada no sudeste do Cráton Amazônico. Tais plútons foram individualizados em três diferentes suítes de acordo com sua mineralogia, assinatura geoquímica, estado de oxidação de seus magmas e presença de prospectos de estanho, wolfrâmio e molibdênio associados a eles (Dall'Agnol *et al*. 2005). Os granitos da Suíte Jamon são oxidados e classificados como a série da magnetita, com veios de quartzo portadores de wolframita. Aqueles da Suíte Velho Guilherme são reduzidos e semelhantes aos da série da ilmenita de Ishihara (1977), sendo a cassiterita uma fase comum no granito e nos veios de quartzo. Os plútons da Suíte Serra dos Carajás são moderadamente reduzidos. As fases oxidadas a reduzida diminuem os teores de magnetita e titanita, e os valores de suscetibilidade magnética aumentam a razão FeOt/(FeOt+MgO) em rocha total e mineral. Mesmo com a compreensão crescente sobre a granitogênese paleoproterozoica da Província Carajás, ainda é necessário

aprimorar o entendimento sobre a composição de suas rochas-fonte e os processos que controlaram a distinta natureza de seus magmas e o papel dos tipos oxidado e reduzido durante a formação e colocação dos plútons.

Associado aos plútons do tipo-A, nota-se a presença de enclaves microgranulares máficos (EMM) amplamente distribuídos, e sua associação com diques máficos fornecem evidências do papel dos magmas máficos na formação e evolução de magmas graníticos (Barbarin 2005, Cheng *et al.* 2012, Yu *et al.* 2018). Neste sentido, alguns pesquisadores argumentam que a presença desses enclaves no interior dos plútons exibindo bordas de resfriamento e xenocristais serve como evidência indicativa da interação física entre magmas máficos e félsicos contemporâneos (Barbarin 2005, Siuda & Bagiński 2019). Essas rochas frequentemente exibem texturas distintas que também sugerem processos de mistura de magmas, tais como: textura rapakivi, quartzo ocelar, zonas de inclusão em fenocristais, zoneamento composicional complexo em plagioclásio (*cf.* Hibbard 1991). Além disso, análises geoquímicas podem rastrear a mistura de magmas; por exemplo, a dominância de composições intermediárias, resultantes da interação de magmas básicos e ácidos, e tendências lineares em diagramas do tipo Harker (Reubi & Blundy 2009, Ruprecht *et al.* 2012, Kumar *et al.* 2017).

O Granito Marajoara da Província Carajás, apresenta ambiguidades quanto à tipologia, pois é formado por magmas tanto reduzidos (série ilmenita) quanto oxidados (série magnetita). Além disso, o plúton exibe muitas estruturas incomuns relacionadas à interação física entre magmas félsicos contemporâneos. Tais aspectos distinguem o plúton Marajoara de qualquer outro *stock* granítico da Província Carajás, que em sua maioria não apresentam contrastes composicionais acentuados entre suas fácies, bem como na natureza de seus magmas formadores. Portanto, buscando-se contribuir para um maior entendimento sobre a diversidade composicional desta granitogênese, esta tese trata busca determinar a natureza dos magmas geradores do Granito Manda Saia e das diferentes fácies do Granito Marajoara e de seus enclaves (microgranulares e porfiríticos), bem como determinar o papel dos diques félsicos e máficos durante a evolução destes plútons. Os resultados obtidos nesta pesquisa permitiram propor mecanismos e processos que contribuam para um modelo geral que discuta a origem (incluindo a rocha-fonte) e evolução dos granitos paleoproterozoicos de afinidade rapakivi (Tipo-A) da Provincia Carajás. Também serão apresentados novos dados geocronológicos U–Pb SHRIMP em zircão para determinar de forma mais precisa as idades de cristalização dos plútons estudados, assim como a suas assinaturas isotópicas a partir de dados de Hf e Nd.

Esta tese foi elaborada de acordo com o modelo de integração de artigos. Desta forma, o corpo central apresenta dois artigos científicos: o primeiro, que corresponde ao capítulo 2, já foi publicado; e o segundo, que corresponde ao capítulo 3, foi submetido ao periódico internacional Precambrian Research. Os capítulos com os artigos são antecedidos por um capítulo de caráter introdutório (capítulo 1), que aborda a apresentação da pesquisa, contexto geológico e tectônico regional, as principais características do magmatismo anorogênico da Província Carajás, assim como a apresentação do problema, os objetivos da tese e materiais e métodos utilizados. O capítulo final (capítulo 4) sumariza, de forma integrada, as discussões e as conclusões alcançadas nos dois artigos e no desenvolvimento da tese de modo geral. Os artigos serão apresentados de acordo com a seguinte ordem:

Capítulo 2 – *Artigo 1:* **Geochemistry, zircon U-Pb geochronology and Lu–Hf isotopes of the Manda Saia granite: Petrological affinity and magma source of evolved A-type granites from the Carajás province, southeastern Amazonian craton, Brazil.**

Publicado na revista *Lithos*, este artigo apresenta os resultados obtidos para o Granito Manda Saia, recentemente mapeado em semidetalhe a sudeste de Xinguara, na Província Carajás. O estudo integra dados de petrografia, geoquímica, suscetibilidade magnética, química mineral de biotita, geocronologia U–Pb e Lu-Hf LA–ICP–MS em zircão e isótopos de Nd. As informações apresentadas permitiram caracterizar e definir a natureza do magmatismo do plúton granítico supracitado, além de definir sua idade de cristalização e estabelecer

comparações com suítes afins da Província Carajás e de outros crátons.

Capítulo 3 – *Artigo 2:* **Petrogenesis and emplacement of the Paleoproterozoic A-type Marajoara pluton and its microgranular enclaves in the Carajás province, southeastern Amazonian craton: Constraints from geochemistry, zircon geochronology, Nd–Hf isotopes, hidden evidence of coexistence between contrasting magmas and new insights from a composite dike.**

Submetido a revista *Precambrian Research*, esse artigo apresenta o aprimoramento de dados geocronológicos (U–Pb SHRIMP e Lu–Hf LA–ICP–MS em zircão), além de química mineral de biotita e modelamento geoquímico para o granito Marajoara. Destaca, ainda, a importância dos processos de mistura de magma entre líquidos félsicos e máficos na dinâmica da câmara magmática geradora do plúton Marajoara e enclaves microgranulares. Assim como no granito Manda Saia, os estudos possibilitaram determinar a idade do plúton, estabelecer comparações com suítes anorogênicas e outros granitos tipo-A da Província Carajás e de outros crátons.

1.2 LOCALIZAÇÃO E ACESSO ÀS REGIÕES DE ESTUDO

As áreas de estudo estão localizadas na Folha Araguaia (SB–22) no sudeste do Estado do Pará. O Granito Marajoara (GMJ) está inserido na interface das folhas SB–22–Z–C–V e SB–22–Z–C–VI e localiza-se na área da Vila Marajoara, ao norte do município de Redenção (Fig. 1). O acesso à área é feito por via terrestre partindo de Belém até a cidade de Marabá, e a partir desta, segue-se pela BR–155 em direção à Vila Marajoara, município de Pau D'Arco. O Granito Manda Saia (GMS), que se encontra na folha SB–22–Z–C–III, está localizado a sudeste da cidade de Xinguara, mais precisamente entre a localidade de Placa de São Francisco e a Fazenda Manda Saia.
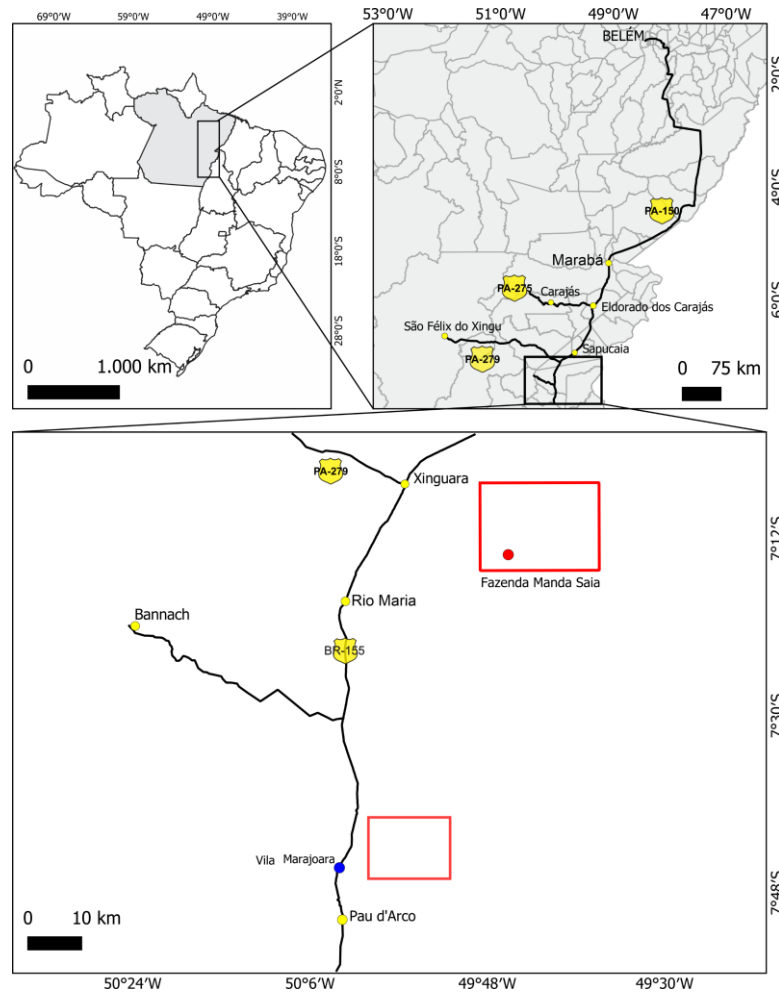
Figura 1 - Mapa de localização dos granitos estudados

1.3 APRESENTAÇÃO DO PROBLEMA E JUSTIFICATIVA DA TESE

O GMJ foi inicialmente estudado por Rocha Júnior (2004) e Azevedo (2013), cujos principais aspectos geológicos e petrográficos foram abordados em seus Trabalhos de Conclusão de Curso. Santos *et al*. (2018) aprofundaram a discussão sobre os principais aspectos evolutivos do GMJ e definiram sua idade de cristalização. Os autores mostraram ainda que o GMJ possui assinatura geoquímica de granitos tipo-A, e que este seria ainda formado por magmas de natureza claramente distinta, o que definiria seu caráter ambíguo. Além disso, possui afinidades composicionais tanto com granitos oxidados da Suíte Jamon quanto com aqueles reduzidos da Suíte Velho Guilherme (granitos da série magnetita/oxidados e granitos da série ilmenita/reduzidos, respectivamente). Favacho (2013) realizou um estudo petrográfico e de suscetibilidade magnética nas rochas do Granito Manda Saia (GMS) e concluiu que ele apesenta maior afinidade petrográfica com a Suíte Serra dos Carajás. Porém, esse trabalho foi produzido com um número reduzido de amostras e conclui que pesquisas mais aprofundadas

utilizando ferramentas como geoquímica e geocronologia devem ser elaboradas. Recentemente, Santos (2020) desenvolveu uma dissertação de mestrado sobre o GMS abordando seus principais aspectos petrográficos e geoquímicos.

A petrogênese das suítes de granitos tipo-A do Paleoproterozoico da Província Carajás foi abordada por Dall'Agnol *et al*. (2005). Estes autores concluíram que os granitos da Suíte Jamon foram gerados em condições de fugacidade de oxigênio (fO_2) relativamente altas (fO_2 – tampão NNO + 0.5), temperatura de cristalização entre 900 e 870 ℃, pressão de colocação de $3,2 \pm 0,7$ kbar e tendo uma provável fonte quartzo-feldspática. Por outro lado, os plútons que constituem a Suíte Velho Guilherme foram formados sob condições reduzidas (fO_2 – abaixo do tampão FMQ), temperatura de cristalização de ~850 ℃, pressão de colocação de $1,0 \pm 0,5$ kbar, sendo a fonte de seus magmas ligada a granitoides com contribuição sedimentar. Para os plútons da Suíte Serra dos Carajás atribui-se condições de fO_2 relativamente reduzida (entre a Suíte Jamon e a Velho Guilherme), temperatura de cristalização abaixo de 870 ℃ e uma fonte quartzo-feldspática de composição intermediária àquelas das demais suítes, ou ainda, podendo ser similar à fonte da Suíte Velho Guilherme, porém mais máfica, ou resultado de maior grau de fusão parcial. Dentro desse contexto, e levando-se em consideração o contraste composicional existente entre as variedades petrográficas que formam o GMJ e o GMS, torna-se necessário determinar os parâmetros de cristalização (temperatura, pressão de colocação, fO_2 e conteúdo de H_2O) de seus magmas a fim de esclarecer a natureza da(s) sua(s) fonte(s), as condições de colocação e os mecanismos envolvidos na construção dos plútons.

Os dados U–Pb SHRIMP obtidos para a fácies BMzH do GMJ apontam para uma idade de cristalização de $1885 \pm 5,9$ Ma, que é concordante com aquela obtida para os demais granitos paleoproterozoicos da Província Carajás (Santos *et al*. 2018). No entanto, esta idade foi obtida em apenas 5 cristais de zircão cujo número de grãos seria inadequado para a submissão de um manuscrito em periódicos internacionais. Dessa forma tornou-se indispensável a obtenção de dados geocronológicos complementares para a variedade datada. Levando-se em consideração a ausência ou escassez de evidências de participação de magmas mantélicos na construção dos granitos tipo-A de Carajás, e o fato de que, em particular, a evolução do GMJ envolveu processos de mistura entre magmas contrastantes, onde magmas provenientes do manto litosférico poderiam ser modificados por processos de *mixing* com magmas crustais (Santos *et al*. 2018), torna-se evidente a necessidade de investigar a contribuição desses processos para a formação do GMJ. Desta forma, a obtenção de dados isotópicos (Nd–Hf) tornaram-se indispensáveis para a definição da petrogênese doa granitos estudados e do papel de líquido(s)

cálcico-alcalino(s)/magnesiano(s) na construção da câmara magmática que representa o plúton, além de contribuir para o avanço do conhecimento sobre os processos magmáticos que deram origem aos granitos anorogênicos da Província Carajás. Por sua vez, o GMS era desprovido de datação geocronológica, e essa escassez de informações sobre esse plúton não permitiu que fossem realizados estudos comparativos entre ele e os demais granitos anorogênicos da Província Carajás. O amplo contraste existente no conhecimento dos magmas que geraram o GMS e aqueles que formaram os demais corpos anorogênicos que ocorrem na região de Rio Maria era evidente e precisava ser minimizado.

1.4 OBJETIVOS

Com base no exposto acima, este trabalho visou contribuir para a definição mais precisa da natureza e dos processos de formação dos plútons Marajoara e Manda Saia, assim como aperfeiçoar a caracterização isotópica desses dois plútons. Para propor um modelo que integre a origem, evolução e construção desses granitos, contribuindo dessa forma para o avanço do conhecimento sobre o contexto evolutivo dos granitos paleoproterozoicos da Província Carajás, deverão ser atingidos os seguintes objetivos específicos:

I. Reavaliar os dados existentes (geoquímicos e petrográficos) e realizar a caracterização mineralógica (óxidos de Fe–Ti) das diferentes fácies com intuito de estimar seus parâmetros de cristalização (T, P, fO$_2$);

II. Definir a(s) fonte(s) e os processos magmáticos envolvidos na evolução do GMJ e GMS (fusão parcial, cristalização fracionada, mistura de magma, cristalização fracionada com assimilação, injeção de líquidos graníticos independentes);

III. Refinar os dados geocronológicos existentes sobre o GMJ e definir com mais rigor sua idade de cristalização/colocação e determinar a idade de cristalização do GMS;

IV. Definir as assinaturas isotópicas de Hf em zircão para determinar as fontes de seus magmas;

V. Definir de forma precisa a fonte de seus magmas;

VI. Sugerir o enquadramento dos granitos supracitados como pertencentes a uma das suítes paleoproterozoicas da Província Carajás.

1.5 MATERIAIS E MÉTODOS

1.5.1 Pesquisa bibliográfica

Compreende o levantamento bibliográfico alusivo à geologia da Província Carajás e de outros crátons arqueanos, tendo prioridade os artigos e livros sobre tópicos pertinentes à geologia e evolução crustal de granitos anorogênicos, geologia estrutural, petrografia, geoquímica, geocronologia e geoquímica isotópica de associações graníticas correlativas aos granitos Marajoara e Manda Saia, além de estudos de química mineral e petrologia experimental aplicados à gênese de rochas plutônicas graníticas.

1.5.2 Mapeamento geológico

Foi realizado um mapeamento geológico do GMJ na escala de 1:71.000. As amostras (Fig. 3) foram coletadas durante os trabalhos de Rocha Júnior (2004) e Santos *et al.* (2018). Foram descritos 23 afloramentos dos quais 19 foram coletadas amostras para petrografia, geoquímica e 1 amostra para geocronologia (Fig. 3). No GMS foi realizado um mapeamento na escala 1:181.000 no trabalho de Santos (2020), sendo que foram descritos 22 afloramentos dos quais 13 amostras foram coletadas para análises petrográficas e geoquímicas e 1 para datação geocronológica (Fig. 4). Houve uma concentração de afloramentos em algumas porções devido à falta de estradas vicinais e à densa vegetação que encobre os corpos graníticos. A diferença nas escalas de mapeamento é resultante dos diferentes tamanhos dos plútons.

O foco dessas descrições de afloramentos foi nos aspectos litológicos e estruturais, com ênfase nas relações de contato dos corpos granitoides com suas rochas encaixantes e, internamente, entre suas diferentes fácies, acompanhado de coleta sistemática de amostras para estudos petrográficos. Para a localização dos pontos descritos e amostrados, foi utilizado um GPS (*Global Positioning System*) com precisão de aproximadamente 3 m. Também foram utilizados modelos digitais de elevação SRTM (*Shuttle Radar Topography Mission*) com resolução de 15 m, imagens de satélite (Landsat TM, Google Earth) e imagens de aerogamaespectrometria (canal do K), devidamente processadas em ambiente SIG.

1.5.3 Petrografia

As lâminas polidas e delgadas foram preparadas na Oficina de Laminação do Instituto de Geociências da UFPA. Foram realizadas 33 análises modais em amostras representativas das diferentes fácies do GMJ, enquanto no GMS foram 10 análises de Santos (2020) as quais foram

posteriormente plotadas nos diagramas Q–A–P e Q–(A+P)-M seguindo a classificação conforme estabelecido pela IUGS (Le Maitre *et al.* 2002). As composições modais foram obtidas com cerca de 1.800 pontos por amostra, distribuídos numa malha de 0,4 mm de espaçamento no contador automático de pontos *Hardledge* da fabricante Endeeper.
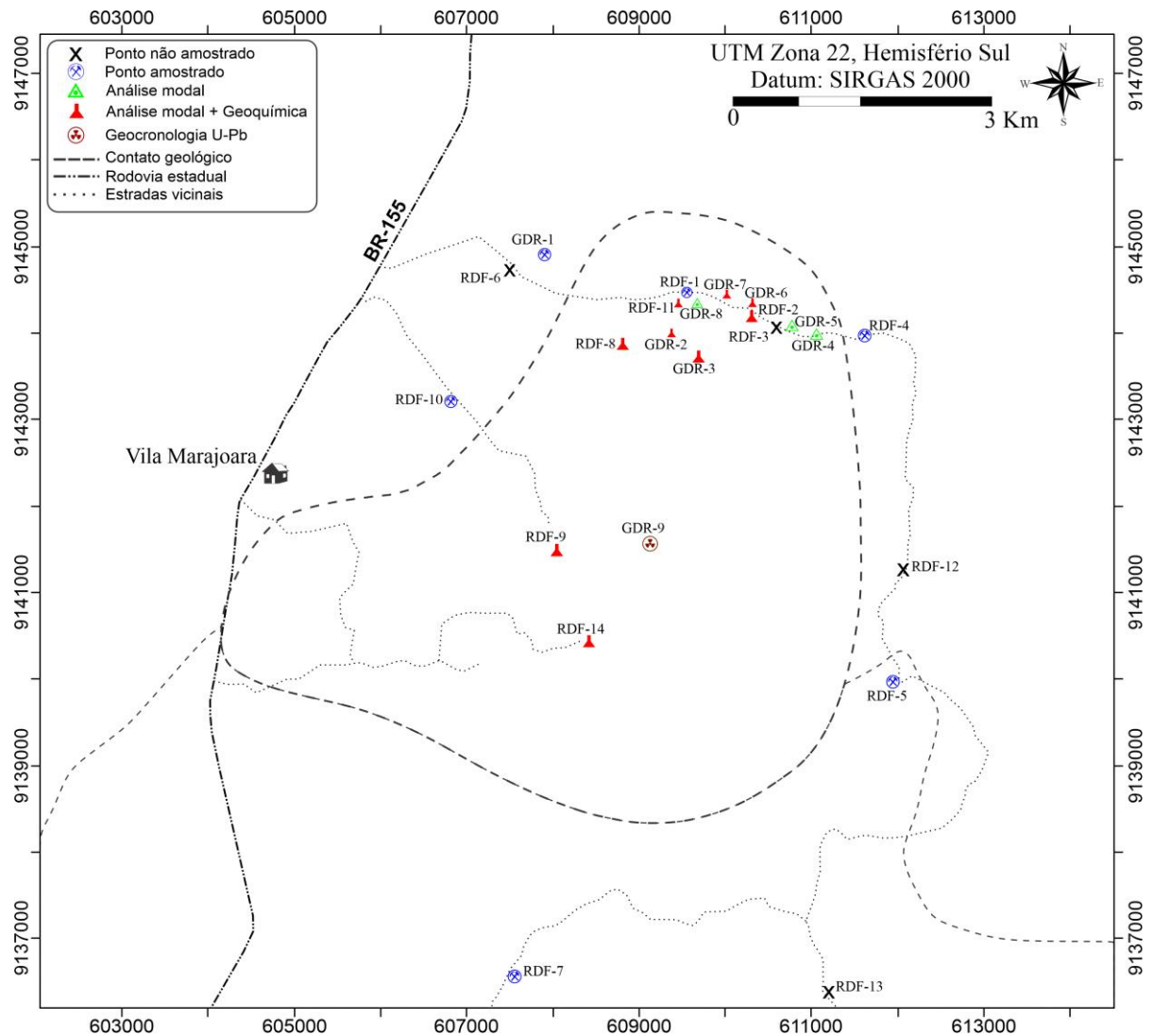
Figura 2 - Mapa de amostragem do Granito Marajoara.
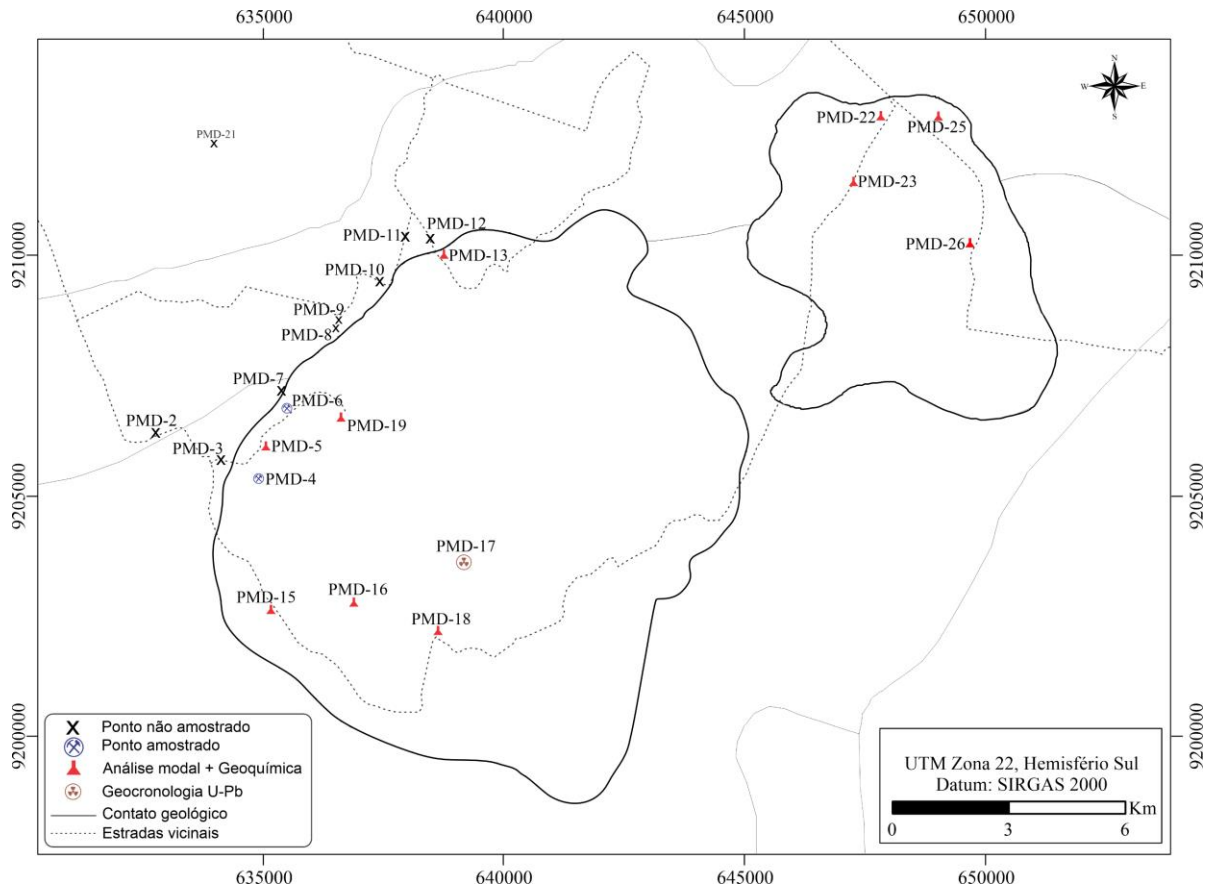
Figura 3 - Mapa de amostragem do Granito Manda Saia.

1.5.4 Química mineral

Para o estudo de química mineral do GMJ, foram selecionadas amostras representativas de cada variedade petrográfica. As amostras foram analisadas no Laboratório de Microssonda Eletrônica do Instituto de Geociências da Universidade de Brasília (microssonda JEOL JXA – 8230), em seções pré-selecionadas de biotita, com pontos analisados, sempre que possível, nos núcleos e nas bordas, a fim de obter uma caracterização mais precisa de sua composição. As condições analíticas foram 15 kV para a tensão de aceleração da coluna, 10 nA para a corrente do feixe e um tempo de análise de 10s. Os cristais usados para as análises foram LIFH para V, Fe, Ni e Ba; PETJ para K, Ca, Cl, P e Sr; LIF para Ti, Mn e Cr; TAP para Na, Si, Al e Mg; e LDE1 para F. Os padrões usados para calibração do instrumento foram microclina (Si, Al e K), albita (Na), andradita (Fe e Ca), pirofanita (Ti e Mn), vanadinita (Cl e V), forsterita (Mg) e topázio (F).

Os dados de química mineral de biotita do GMS foram obtidos no Laboratório de Microanálises–LABMEV na UFPA usando uma microssonda eletrônica JEOL JXA–8230 equipada com cinco espectrômetros dispersivos de comprimento de onda (WDSs). Cinco

lâminas polidas de amostras representativas do Granito Manda Saia foram inicialmente revestidas com carbono para eliminar a carga eletrostática na superfície da amostra e, em seguida, analisadas. As análises WDS foram realizadas da seguinte forma: tensão de aceleração da coluna de 15 kV, corrente de 20 nA, tempos de análise de 20 s para elementos maiores e 40 s para elementos menores e traços, e diâmetro do feixe de 1 µm para todas as biotitas. A precisão analítica foi de ±1% e ±10% para elementos maiores e menores, respectivamente. Os cristais usados para as análises WDS de todos os minerais foram: fluoreto de lítio (LiFH) para V, Mn, Fe, Ni e Ba; pentaeritritol (PETJ) para K, Ca, Ti e Sr; ftalato ácido de tálio (TAP) para Na, Si, Al e Mg; e elemento de dispersão em camadas (LDE1) para F. Os padrões utilizados foram: andradita (Si e Ca), albita (Na), hematita (Fe), microclina (Al e K), olivina (Mg), pirofanita (Ti e Mn), topázio (F) e vanadinita (V e Cl).

A fugacidade de oxigênio (fO$_2$) é avaliada com base nos teores de Al, Fe e Mg de anfibólios e biotitas. No caso de o GMJ não ter anfibólio e no GMS ter sido descrito apenas um único cristal de anfibólio que apresenta sinais de alteração, a fugacidade foi determinada de acordo com os resultados das biotitas. O parâmetro de cristalização pressão (P) é calculado através de equações do geobarômetro Al-em-hornblenda (Anderson & Smith 1995), entretanto, o GMJ não apresenta em sua mineralogia a hornblenda. Portanto, a pressão de cristalização e colocação do GMJ será estimada a partir dos outros dados disponíveis: geológicos, estruturais, petrográficos, além da correlação com os demais plútons anorogênicos da Província Carajás.

A magnetita tem sido utilizada para determinar o estado de oxidação de magmas silicáticos, assim como titanita, além de representarem parâmetros úteis para a história petrogenética e metalogenética destes magmas, uma vez que suas composições são sistematicamente sensíveis a variações nas condições de sua formação (Dupuis & Beaudoin 2011, Nadoll *et al.* 2014).

1.5.5 Geoquímica de rocha total

Um total de 19 amostras representativas do GMJ e 11 do GMS, previamente selecionadas nos estudos petrográficos, foram escolhidas para análise geoquímica de rocha total. As amostras selecionadas foram trituradas, pulverizadas, homogeneizadas e quarteadas no Oficina de Preparação de Amostras (OPA) do Instituto de Geociências da UFPA. As amostras do GMS foram analisadas no laboratório da empresa de procedimentos analíticos ALS Geochemistry Laboratories (Minas Gerais, Brasil), enquanto as rochas do GMJ ficaram a cargo da ACME *Analytical Laboratories* Ltda. (Vancouver, Canadá). Em ambos os laboratórios os

elementos maiores e menores (SiO_2, TiO_2, Al_2O_3, Fe_2O_3t, MnO, MgO, CaO, Na_2O e P_2O_5) analisados por ICP-AES (*Inductively Coupled Plasma – Atomic Emission Spectrometry*), enquanto os elementos traços (Ba, Rb, Sr, Zr, Nb, Y, Hf, Ta e Th), incluindo os elementos terras raras (La, Ce, Pr, Nd, Sm, Eu, Gd, Tb, Dy, Ho, Er, Tm, Yb e Lu), foram analisados por ICP–MS (*Inductively Coupled Plasma - Mass Spectrometry*). Os dados obtidos permitiram realizar a caracterização geoquímica, com base nos procedimentos indicados em Ragland (1989) e Rollinson & Pease (2021), e diagramas elaborados com auxílio do programa GCDkit.

1.5.6 Modelamento geoquímico

O modelamento geoquímico foi feito pretendendo avaliar possíveis linhas evolutivas baseando-se nos principais processos magmáticos tais como AFC, fusão parcial, cristalização fracionada e mistura utilizando principalmente programas específicos tais como o PETROMODELER (Ersoy 2013), GENESIS (Teixeira 2005) e bem como planilhas do Microsoft Office Excel geradas pelos autores desta tese. Detalhes de como foram realizados esses cálculos, como equações e coeficientes de partição, são apresentados e discutidos nos capítulos 2 e 3.

1.5.7 Datações U–Pb e Pb–Pb

Foram realizadas análises geocronológicas em uma amostra (GDR-9FB) representativa da fácies biotita monzogranito heterogranular do GMJ pelo método U-Pb em zircão (*in situ*) pelo sistema SHRIMP IIe (*Sensitive High Resolution Ion Microprobe*), no Laboratório de Geologia de Alta Resolução do Instituto de Geociências da Universidade de São Paulo (GeoLabIGc-USP). Uma amostra (PMD-17) do GMS foi analisada pelo método U–Pb em zircão por LA–SF–ICP–MS (*Laser Ablation Sector Field Ion Coupled Plasma Mass Spectrometry*), no Laboratório de Geologia Isotópica da Universidade Federal de Ouro Preto (UFOP).

Em torno de 10 a 20 kg de cada amostra representativa foram trituradas, moídas e peneiradas nas frações 250, 175, 125 e 75 µm, realizadas na Oficina de Preparação de Amostras (OPA) e no Laboratório de Preparação Mineral (LPM), ambos na UFPA. Os cristais de zircão foram separados por meio de líquido pesado (bromofórmio) e separador magnético isodinâmico do tipo *Frantz*. Entre 80 e 100 cristais de zircão de cada amostra foram selecionados com o auxílio de lupa binocular e, em seguida, montados em um disco de epóxi em conjunto com os padrões analíticos, polidos até a metade de sua espessura a fim de expor o interior dos cristais,

e revestida com uma película de carbono. Antes das datações com o método U–Pb *in situ*, foram examinadas estruturas internas, sobrecrescimentos, fraturas, inclusões e defeitos físicos dos cristais, utilizando imagens de elétrons retroespalhados (BSE – *Backscattered Electron Images*) e catodoluminescência (CL – *Cathodoluminescence*), obtidas pela microssonda eletrônica modelo JEOL JXA–8230, do Laboratório de Microanálises da UFPA, operando sob condições de voltagem de aceleração de 15 kV e corrente do feixe de 20 µA, com distância de trabalho de 11 mm.

As análises realizadas pelo sistema SHRIMP IIe seguem os procedimentos analíticos segundo Stern (1998) e Sato *et al*. (2014). O padrão utilizado foi o zircão TEMORA–2 (416,78 ± 0,33 Ma; Black *et al*. 2003) como padrão de razão isotópica. O tamanho do ponto do feixe de íons primários foi de 30 µm. Os cálculos de idade e a apresentação dos resultados isotópicos no diagrama de concórdia foram executados utilizando o software Isoplot/EX 3.0 desenvolvido por Ludwig (2003). A abordagem para estabelecer as estatísticas mais robustas e determinar a idade U-Pb ideal segue as diretrizes fornecidas por Spencer *et al*. (2016). Dado que todas as amostras excedem 1,5 Ga em idade, o cálculo da idade foi baseado na média ponderada das razões $^{207}Pb/^{206}Pb$, e a adequação do MSWD (*Mean Square Weighted Deviation*) foi avaliada tanto para dispersão excessiva quanto insuficiente.

Para o sistema LA–SF–ICP–MS, foi utilizado o equipamento ICP-MS *sector field* da Thermo–Finnigan Element 2 acoplado a um sistema de laser ultravioleta CETAC LSX–213 G2+ (λ = 213 nm) Nd:YAG, através do método definido por Frei & Gerdes (2009). Hélio foi usado como gás de arraste para aumentar a eficiência de transporte do material ablacionado. Cada ponto analítico tinha 20 µm de diâmetro. As abundâncias absolutas e as razões U–Th–Pb foram determinadas em relação aos padrões primários de zircão GJ–1 (608,5 ± 1,5 Ma; Jackson *et al*. 2004) e ao zircão secundário BB (560 ± 0,4 Ma; Santos *et al*. 2017). Todas as correções e a redução dos dados brutos foram processadas utilizando uma planilha Excel offline (adaptada de Chemale Júnior *et al*. 2012) para calcular os valores corrigidos das razões isotópicas ($^{206}Pb/^{238}U$, $^{232}Th/^{238}U$, $^{207}Pb/^{206}Pb$) e incertezas (nível de 1σ em %). Os cálculos de idade e a apresentação dos resultados isotópicos no diagrama de concórdia foram realizados com o programa Isoplot/EX 3.0 de Ludwig (2003). A estratégia para definir as estatísticas mais robustas e determinar a "melhor" idade U-Pb é a recomendada por Spencer *et al*. (2016). Como todas as amostras são mais antigas que 1,5 Ga, a idade foi calculada usando a média ponderada das razões $^{207}Pb/^{206}Pb$, e a aceitabilidade do MSWD foi avaliada tanto para dispersão excessiva quanto insuficiente.

As análises isotópicas usando o método de evaporação de Pb em monocristais de zircão foram realizadas no Laboratório de Geologia Isotópica (Pará-Iso) do Instituto de Geociências da UFPA, seguindo a metodologia desenvolvida por Kober (1987). As análises foram realizadas em um espectrômetro de massa de ionização térmica FINNIGAN MAT 262. Os resultados são apresentados com um desvio de 2σ e corrigidos para fracionamento de massa e Pb comum ou contaminação, usando o modelo de evolução de Pb em dois estágios proposto por Stacey & Kramers (1975), com a razão $^{204}Pb/^{206}Pb$ adotada por Macambira *et al*. (1994).

1.5.8 Geoquímica isotópica de Lu–Hf em zircão

As análises *in situ* de isótopos de Hf em zircão foram realizadas no Laboratório de Geologia Isotópica (Pará-Iso) do Instituto de Geociências da UFPA por um LA–MC–ICP–MS (*Laser Ablation Multi-Collector Ion Coupled Plasma Mass Spectrometer*) de alta resolução, modelo Neptune, marca Thermo Finnigan, equipado com uma sonda laser Nd:YAG 213nm, modelo LSX–213 G2 da marca CETAC seguindo os procedimentos estabelecidos por Milhomem Neto *et al*. (2017). Como material de referência para a razão $^{176}Hf/^{177}Hf$, foi utilizado o zircão Mud Tank (731 ± 1 Ma, Horstwood *et al.* 2016).

Os isótopos de Lu, Hf e Yb foram medidos com base nas razões isotópicas $^{173}Yb/^{171}Yb$, $^{179}Hf/^{177}Hf$, $^{175}Lu/^{177}Hf$ e $^{176}Hf/^{177}Hf$ para corrigir as interferências isobáricas dos isótopos Lu e Yb na massa 176. Portanto, as interferências isobáricas de ^{176}Lu e ^{176}Yb foram ajustadas utilizando uma equação com um fator de fracionamento de massa (β) para Lu e Yb e a intensidade dos sinais observados nos isótopos livres de interferência ^{175}Lu e ^{173}Yb, normalizados a partir de suas abundâncias isotópicas aceitas: $^{176}Lu/^{175}Lu = 0,026549$ (Chu *et al.* 2002) e $^{176}Yb/^{173}Yb = 0,786956$ (Thirlwall & Anczkiewicz 2004). O fator β (Hf, Yb e Lu) foi calculado para cada medida realizada, pois seu valor é influenciado pela razão medida entre os isótopos de interesse. Para corrigir o fracionamento isotópico causado pelo equipamento durante as análises, de acordo com a lei exponencial (Russel *et al*. 1978), as razões isotópicas de Yb foram normalizadas, assumindo um valor de 1,12466 para $^{173}Yb/^{171}Yb$ (Thirlwall & Anczkiewicz 2004). Por outro lado, as razões isotópicas de Hf foram normalizadas utilizando um valor de 0,7325 para a razão $^{179}Hf/^{177}Hf$ (Patchett & Tatsumoto 1980). Para realizar esses cálculos de correção e obter os valores corrigidos das razões $^{176}Hf/^{177}Hf$ e $^{176}Lu/^{177}Hf$ para cada ponto analisado, os dados brutos foram processados em uma macro do Microsoft Excel, com aproximadamente 40 valores sendo selecionados de um total de 60 dados integrados de 1,049 s/ponto (Milhomem Neto *et al.* 2017).

1.5.9 Geoquímica isotópica de Sm–Nd em rocha total

As análises foram realizadas em 10 amostras representativas do Granito Marajoara no Laboratório de Geocronologia da Universidade de Brasília (UnB), utilizando um espectrômetro de massa Finnigan MAT 262 dotado de sete coletores tipo copo Faraday móveis e uma multiplicadora de elétrons central. Gioia & Pimentel (2000) descrevem o protocolo analítico adotado no Laboratório de Geocronologia da UnB. A extração de Sm e Nd seguiu a técnica de troca catiônica, usando uma coluna de teflon contendo resina L-N spec (HDEHP–*diethylhexyl phosphoric acid supported on* PTFE *powder*). O Sm e Nd separados foram depositados em filamento de rênio e analisados em modo estático no espectrômetro. A precisão das razões Sm/Nd e $^{143}Nd/^{144}Nd$ é superior a ± 0.5% 344 (2σ) e ± 0.005% (2σ), respectivamente, baseado em repetições de análises de padrões internacionais de rocha (BHVO-1 e BCR-1). As razões isotópicas foram normalizadas para $^{146}Nd/^{144}Nd = 0,7219$ (fracionamento de massa corrigido no modo exponencial) e a constante de desintegração utilizada para os cálculos foi de $6,54 \times 10^{-12}$ ano^{-1}. Os valores de Nd-T_{DM} foram calculados usando o modelo de DePaolo (1981) e a macro Isoplot 4.15 (Ludwig 2009).

2 CONTEXTO GEOLÓGICO DA PROVÍNCIA CARAJÁS

A Província Carajás (PC), situada na porção sudeste do Cráton Amazônico (CA), é um dos seus principais terrenos arqueanos. A PC está inserida no domínio Arqueano da Província Amazônia Central (Tassinari & Macambira 2004) ou, segundo o modelo de Santos (2003), representa uma província arqueana independente (Fig. 4a). Vários modelos de compartimentação tectônica foram propostos para a PC (Souza *et al*. 1996, Althoff *et al*. 2000, Dall'Agnol *et al*. 2013). Vasquez & Rosa-Costa (2008), baseados na proposta de Santos (2003), sugeriram denominar a porção sul da província como Domínio Rio Maria (DRM) e a sua porção central e norte como Domínio Carajás (DC). Dall'Agnol *et al*. (2013) mantiveram o DRM e subdividiram o DC em Domínio Sapucaia (DS), Domínio Canaã dos Carajás (DCC) e Bacia Carajás (BC). Esses três domínios teriam evoluído de maneira distinta do Domínio Rio Maria (Fig. 4b). Costa *et al*. (2020) não seguiram esse modelo e interpretação, pois acreditam que estruturas do tipo *dome and keel* controlaram a evolução do Domínio Rio Maria e da porção sul do antigo Domínio Carajás. Oliveira *et al*. (2023) adotam, de forma geral, a proposta de Dall'Agnol *et al*. (2013), mas seguem as denominações de Terreno Sapucaia e Terreno Canaã dos Carajás.

Os domínios supracitados são intrudidos por um grande volume de corpos graníticos do tipo-A do Paleoproterozoico (1,88 Ga) e diques relacionados (Dall'Agnol *et al*. 2006, Dall'Agnol & Oliveira 2007, Silva *et al*. 2016, Teixeira *et al*. 2017), sendo delimitados por grandes descontinuidades regionais com orientação E-W. Essas regiões apresentam diferenças em sua evolução geológica, identificadas a partir das distintas associações litológicas que serão detalhadas a seguir.
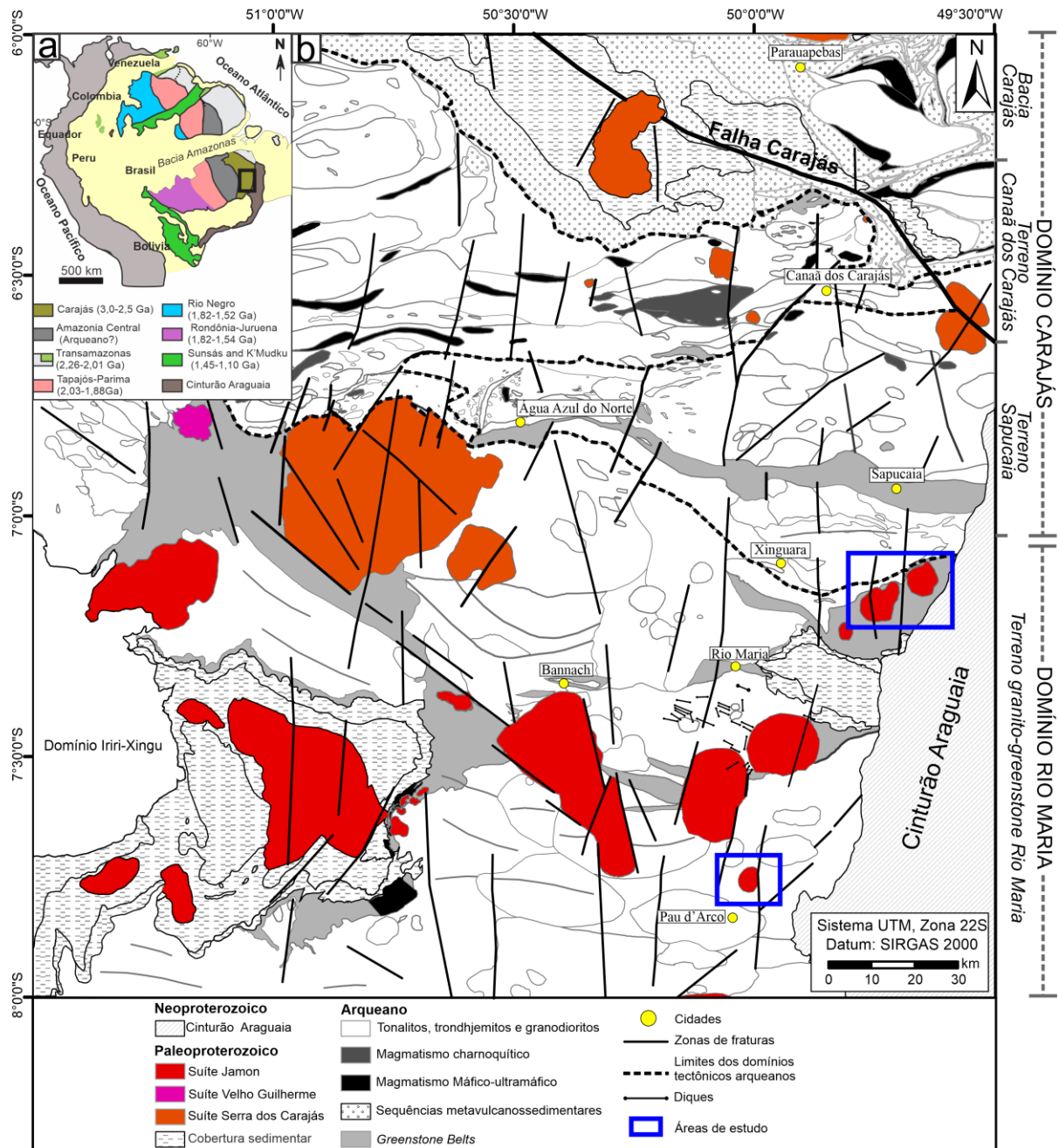
Figura 4 - (a) Cráton amazônico dividido em províncias geocronológicas (Santos 2003) mostrando a Província Carajás e a área da Fig. 1b; (b) Mapa geológico da Província Carajás mostrando granitos paleoproterozoicos (modificado de Oliveira *et al*., 2023), a localização das áreas de estudo e os limites estimados dos terrenos tectônicos arqueanos da Província Carajás de acordo com Dall'Agnol *et al*. (2013).

2.1 DOMÍNIO RIO MARIA

O Domínio Rio Maria está situado na porção sul da Província Carajás e é representado por associações mesoarqueanas, compostas principalmente por sequências de *greenstone belts*, rochas máfica-ultramáficas, associações de trondhjemitos e tonalitos (TTG), rochas sanukitoides, granodioritos e granitos potássicos (Silva 2022). Os *greenstones belts* são representados pelos grupos Andorinhas e Gradaús-Tucumã (3,0 a 2,9 Ga; Macambira &

Lancelot 1991, Souza *et al.* 1996, Lafon *et al.* 2000, Souza *et al.* 2001, Rolando & Macambira 2003, Santos-Silva *et al.* 2021). No complexo máfico-ultramáfico estão os complexos Guará-Pará e Serra Azul (Pimentel & Machado 1994, Santos-Silva *et al.* 2021). Os granitoides são: (1) suítes TTGs (2,98-2,92 Ga) representadas por Tonalito Arco Verde e Trondhjemito Mogno, Tonalito Carapanã e Tonalito Mariazinha (Gastal 1987, Pimentel & Machado 1994, Guimarães *et al.* 2010, Almeida *et al.* 2011, Silva-Silva *et al.* 2020); (2) Suítes sanukitoides e granitoides com alto Mg (2,87 Ga; Oliveira *et al.* 2009, Gabriel & Oliveira 2014); (3) Leucogranitos potássicos – Granito Mata Surrão e Xinguara, e cálcico-alcalinos - Suíte Guarantã (2,87-2,86 Ga; Leite *et al.* 2004, Almeida *et al.* 2010, 2013). As coberturas sedimentares paleoproterozoicas são representadas pelas sequências dos grupos Rio Fresco e Gemaque (Santos & Pena Filho 2000) formadas durante o Sideriano, sucedidas pela sedimentação orosiriana dos conglomerados da Formação Gorotire (Barbosa *et al.* 1966, Vasquez & Rosa-Costa 2008, Santos-Silva *et al.* 2021).

2.2 MAGMATISMO ANOROGÊNICO DA PROVÍNCIA CARAJÁS

Os granitos anorogênicos da Província Carajás englobam um conjunto de corpos intrusivos que intrudem as rochas arqueanas nos diversos domínios da PC. Esses granitos apresentam idades de cristalização ente 1,86 e 1,89 Ga, que se formaram em ambiente extensional e são contemporâneos a diques de diabásio e dacitos/granitos pórfiros de direções WNW–ESE a NNW–SSE (Dall'Agnol *et al.* 2005, Oliveira *et al.* 2010, Silva *et al.* 2016, Teixeira *et al.* 2019). São reunidos nas suítes Jamon, Serra dos Carajás e Velho Guilherme, as quais são individualizadas segundo suas características petrográficas, geoquímicas e estado de oxidação dos seus magmas. Além das suítes supracitadas, vale ressaltar a ocorrências dos granitos Gogó da Onça, Gradaús, Rio Branco, São João e Seringa, que, até o momento, não foram inseridos em nenhuma dessas suítes.

Os plútons tipo-A da Província Carajás foram colocados em profundidades crustais rasas (~1–3 kbar), e frequentemente ocorrem xenólitos angulares das rochas encaixantes, sobretudo nas bordas dos granitos, sugerindo alto contraste de viscosidade entre seus magmas e as rochas encaixantes arqueanas (Dall'Agnol *et al.* 2005). Diques máficos e félsicos cortam as unidades arqueanas e, localmente, os granitos (Gastal 1987, Rivalenti *et al.* 1998, Silva Júnior *et al.* 1999, Ferreira 2009, Silva *et al.* 2016). Levando em consideração a geoquímica, são granitos meta a peraluminosos e exibem altas razões Na_2O/K_2O e $FeOt/(FeOt+MgO)$ e são, assim sendo, ferrosos, de acordo com a classificação de Frost *et al.* (2001). Têm elevados

conteúdos de HFSE (*High Field Strength Elements*) e assinatura do tipo-A oxidados e reduzidos (Dall'Agnol & Oliveira 2007).

2.2.1 Suíte Jamon

A Suíte Jamon ocorre no Domínio Rio Maria e nela estão inseridos os granitos Jamon (Dall'Agnol *et al.* 1999a), Musa (Gastal 1987), Redenção (Oliveira *et al.* 2002), Bannach (Almeida *et al.* 2006), Marajoara (Santos *et al.* 2018) e Manda Saia (Santos *et al.* 2023). Esses granitos são caracterizados por composições essencialmente monzograníticas e, subordinadamente, sienograníticas, geralmente com megacristais de feldspato alcalino manteados por plagioclásio configurando a textura rapakivi, e seus principais minerais acessórios sendo allanita, apatita, ilmenita, magnetita, titanita, zircão e fluorita nas fácies mais evoluídas (Oliveira *et al.* 2002, Almeida *et al.* 2006). A presença de titanita e magnetita associadas é um forte indício de que essas rochas foram geradas em condições oxidantes e de fugacidade de oxigênio (fO$_2$) relativamente elevada (Dall'Agnol *et al.* 1999a, Almeida *et al.* 2007). A maior parte dos plútons dessa suíte apresenta zoneamento concêntrico, onde os granitos menos evoluídos ocupam as zonas externas e os mais evoluídos a região central de cada corpo granítico. Nos granitos Bannach, Jamon e Redenção as principais fácies são relacionadas por cristalização fracionada (Dall'Agnol *et al.* 1999a). Contudo, na porção central dos granitos Bannach e Redenção ocorrem *stocks* de leucogranitos provavelmente derivados de um magma independente (Almeida *et al.* 2006, Oliveira *et al.* 2009, Mesquita *et al.* 2018).

2.2.2 Suíte Serra dos Carajás

Os granitos tipo-A de ~1,88 Ga que ocorrem na Bacia Carajás são inseridos na Suíte Serra dos Carajás (Dall'Agnol *et al.* 2005) a qual é constituída pelos granitos Serra dos Carajás, Cigano e Pojuca (Barros *et al.* 1995, Javier Rios *et al.* 1995, Dall'Agnol *et al.* 2005). Esses granitos são marcados por uma homogeneidade composicional essencialmente monzogranítica e, subordinamente, sienogranítica, e com mineralogia acessória: zircão, apatita, magnetita, ilmenita, allanita e titanita rara ou ausente. Localmente podem ocorrer granitos hidrotermalizados onde a ocorrência de topázio e fluorita são comuns, e a turmalina por vezes pode estar presente (Barros *et al.* 1995, Javier Rios *et al.* 1995). Pode ocorrer a presença de magnetita, porém sem ilmenita associada. Essas rochas foram formadas em condições de baixa fO$_2$ e sua assinatura geoquímica é própria de granitos tipo-A moderadamente reduzidos (Dall'Agnol & Oliveira 2007).

2.2.3 Suíte Velho Guilherme

A Suíte Velho Guilherme, ocorre principalmente na região do Xingu, e engloba os granitos ricos em estanho Velho Guilherme, Antônio Vicente, Benedita, Bom Jardim, Mocambo e Serra da Queimada. São normalmente sienogranitos, monzogranitos e, subordinadamente, álcali-feldspato granitos com características subalcalinas e alcalinas. As fácies mais evoluídas apresentam alteração hidrotermal pós-magmática intensa. Há ocorrência de mineralizações de cassiterita, fluorita, molibdenita, topázio e wolframita, sendo comuns nesses corpos, geralmente acompanhando as rochas mais evoluídas e intensamente hidrotermalizadas assim como corpos de greinsens associados (Lamarão *et al.* 2012, Teixeira *et al.* 2002). São mineralogicamente ricos em fluorita e com rara presença de titanita e magnetita (fases menos evoluídas), e são mais pobres em máficos do que as rochas das outras suítes, com conteúdo modal de mineral opaco menor que 0,1%. Isto implica baixos valores de SM, implicando em um caráter mais reduzido (Dall'Agnol & Oliveira 2007).

2.2.4 Demais granitos anorogênicos da Província Carajás

Além das três suítes supracitadas, pode-se destacar os granitos Seringa (Paiva Júnior. *et al.* 2011), Rio Branco (Santos *et al.* 2013), São João (Lima *et al.* 2014), Gradaús (Abrantes Júnior & Lamarão 2011, Carvalho 2017, Nery 2019, Nery *et al.* 2023) e Gogó da Onça (Teixeira *et al.* 2017, 2018, 2019) que não foram, até o momento, inseridos a nenhuma das suítes intrusivas. Os trabalhos realizados nesses granitos, sugerem maiores semelhanças com os granitos da Suíte Serra dos Carajás. Entretanto, apresentam divergências, e, portanto, não foram inseridos nessas suítes paleoproterozoicas de maneira definitiva.

O Granito Seringa é constituído por sienogranitos e monzogranitos, com mineralogia acessória que incluem zircão, magnetita, ilmenita, apatita e allanita. A magnetita atinge proporções maiores que 1% nos monzogranitos e até 0,5% nas rochas mais evoluídas, sendo mais frequente que a ilmenita, com conteúdo modais de opacos variando de 2,6% a 0,3% e valores moderados de SM, similares aos da Suíte Serra dos Carajás (Paiva Júnior *et al.* 2011). O Granito São João é composto por monzogranitos e sienogranitos, que seccionam unidades TTGs pertencentes ao Domínio Rio Maria. Apresenta mineralogia acessória que incluem zircão, apatita, allanita, magnetita e ilmenita, com conteúdo modal de opacos inferior a 1% e valores moderados de SM (Lima *et al.* 2014). A ausência de titanita magmática e a associação de magnetita e ilmenita conferem a esse granito valores moderados de SM e, portanto, caráter

moderadamente reduzido (Dall'Agnol & Oliveira 2007, Lima *et al.* 2014). O Granito Gradaús é intrusivo em metassedimentos do Grupo Rio Fresco que recobrem unidades arqueanas pertencentes ao Domínio Rio Maria, possui cerca de 800 Km^2, e é composto por rochas monzograníticas a sienograníticas, apresentando textura granular hipidiomórfica a porfirítica, com mineralogia acessória constituída por apatita, allanita, zircão, ilmenita, magnetita, fluorita. É um plúton moderadamente reduzido e com valores de SM moderada a baixa (Carvalho 2017). O Granito Gogó da Onça é composto por granodiorito, monzogranitos e sienogranitos de textura granular hipidiomórfica a localmente granofírica, com mineralogia acessória composta por apatita, allanita, zircão, ilmenita e magnetita, com conteúdo modal de opacos inferior a 1% e valores moderados de SM (Teixeira *et al.* 2017). O Granito Rio Branco é composto essencialmente por sienogranitos, com mineralogia acessória que incluem zircão, allanita, fluorita, hematita e magnetita (rara). As fases minerais secundárias estão relacionadas aos processos de alteração pós-magmática e são representadas por albita, topázio, fluorita, muscovita, siderofilita e óxidos e/ou hidróxidos de ferro e valores de SM baixos (Santos *et al.* 2013).

Datações geocronológicas realizadas em zircão por diversos métodos como U–Pb e Pb–Pb, indicam idades de cristalização de ~1,88 Ga para esses granitos (Machado *et al.* 1991, Dall'Agnol *et al.* 1999a, 2005, Teixeira *et al.* 2017, 2018). Dados isotópicos de Nd, foram adquiridos e definem idades T_{DM} do Arqueano (~3,35 Ga a 2,60 Ga; Dall'Agnol *et al.* 2005, Rämö *et al.* 2002, Teixeira *et al.* 2018, 2019) e valores de ε_{Nd} bastante negativos (–12 a –8). Os valores de ε_{Nd} das suítes Jamon (–10,5 a –8,1) e Serra dos Carajás (–9,7 a –7,9) são similares e maiores que aqueles da Suíte Velho Guilherme (–12,1 a –12,2). Além destes, dados isotópicos de Lu–Hf obtidos por Teixeira *et al*. (2019) revelam idades T_{DM} ~ 3,12 Ga a 3,58 Ga e valores de ε_{Hf} extremamente negativos que variam entre –9,8 e –17,3. Tais dados associados podem ser interpretados como indicativo de fontes crustais arqueanas para petrogênese desses magmas. Uma síntese dos principais dados geocronológicos e isotópicos obtidos até então, são mostrados nos capítulos 2 e 3.

CAPÍTULO 2 GEOCHEMISTRY, ZIRCON U-Pb GEOCHRONOLOGY AND Lu‑Hf ISOTOPES OF THE MANDA SAIA GRANITE: PETROLOGICAL AFFINITY AND MAGMA SOURCE OF EVOLVED A-TYPE GRANITES FROM THE CARAJÁS PROVINCE, SOUTHEASTERN AMAZONIAN CRATON, BRAZIL

Artigo publicado em: Lithos

Doi: https://doi.org/10.1016/j.lithos.2023.107412

Geochemistry, zircon U-Pb geochronology and Lu-Hf isotopes of the Manda Saia granite: Petrological affinity and magma source of evolved A-type granites from the Carajás province, southeastern Amazonian craton, Brazil

Rodrigo Fabiano Silva Santos [a,b,*], Davis Carvalho de Oliveira [a,b], Bhrenno Marangoanha [a,b], Marco Antonio Galarza [a,c], Marcelo Reis Santos [a,b]

[a] Post-Graduate Program in Geology and Geochemistry (PPGG), Institute of Geosciences (IG), Federal University of Pará (UFPA), Post Office 8608, 66075-110 Belém, Pará, Brazil
[b] Group of Research on Granitoid Petrology, IG, UFPA, Brazil
[c] Isotopic Geology Laboratory, IG, UFPA, Belém, PA, Brazil

ABSTRACT

The Manda Saia granite occurs in the Carajás province, southeastern Amazonian craton, and it is represented by two semicircular intrusive stocks in the Mesoarchean granitoid and greenstone belt sequence of the Rio Maria domain. The stocks are composed of hololeucocratic, red-colored monzo- and syenogranite rocks. Biotite is the main ferromagnesian mineral, and amphibole is rare and was formed later. The rocks are ferroan, calc-alkalic, peraluminous and present a restricted and high SiO_2 range (74.80 and 77.70%), high $FeOt/FeOt+MgO$ (0.89–0.98) ratios and enrichment in rare earth elements (REEs, 111–497 ppm), with moderate negative Eu anomalies (0.04–0.63). The plutons are classified as ferroan A-type granites and were formed under moderately reduced to moderately oxidized conditions, similar to those those in the Serra dos Carajás suite. They also show affinities with the more evolved members from both the reduced Velho Guilherme suite and oxidized Jamon suite from the Carajás province. The Manda Saia granite has a zircon U-Pb crystallization age of 1866 ± 10 Ma and is derived from partial melting of the Mesoarchean crust of tonalitic composition, as indicated by strongly negative ε_{Hf} values (-12 to -18). The emplacement of these plutons is related to extensional tectonics with magma transport at shallow crustal levels.

1. Introduction

Since the introduction of the terms type I- and S- granites by Chappell and White (1974), granitic rocks have been commonly classified according to the nature of their protolith, with crustal melting as the main mechanism for the generation of granites (Arndt, 2013). In this sense, Loiselle and Wones (1979) created the term A-type, which was intended to classify granites with high levels of $Na_2O + K_2O$; high field strength elements (HFSEs) (Zr, Nb and REE); high $FeOt/(FeOt+MgO)$ ratios; low concentrations of Ba, Sr and Eu; low oxygen fugacity (fO_2); reduced H_2O contents; and that are related to anorogenic environments, whose chemical compositions are different from those of types -I and -S. Whalen et al. (1987) added typical characteristics of A-type granites, including high SiO_2, Ga, Y, Ce and Zn contents; high Ga/Al ratio, and low Al_2O_3 and CaO contents. Thus, the "alphabetical classification" was created to refer more adequately to the chemical composition and its contribution to the understanding of the petrogenetic evolution of granitoids compared to its relationship with specific petrological mechanisms involved in the genesis of magmatic rocks (e.g., partial melting). However, the distinction among the different types is not always simple. This is particularly true in the case of highly fractionated type-A and type-I granites ($SiO_2 > 72\%$), where the geological context under study must be considered in the definition.

In several cratons around the world, anorogenic magmatism has occurred since the Neoarchean, especially in the Paleoproterozoic and Mesoproterozoic, as evidenced by the formation of the anorthosite–mangerite–charnockite–granite rapakivi (AMCG) and rapakivi granites (Rämö and Haapala, 1995). This formation probably occurred due to the lithospheric crust being relatively thinner in that period and being affected by mantle plumes, in addition to the existence of

---

ABSTRACT

The Manda Saia granite occurs in the Carajás province, southeastern Amazonian craton, and it is represented by two semicircular intrusive stocks in the Mesoarchean granitoid and greenstone belt sequence of the Rio Maria domain. The stocks are composed of hololeucocratic, red-colored monzo- and syenogranite rocks. Biotite is the main ferromagnesian mineral, and amphibole is rare and was formed later. The rocks are ferroan, calk-alkalic, peraluminous and present a restricted and high SiO_2 range (74.80 and 77.70%), high FeOt/FeOt+MgO (0.89–0.98) ratios and enrichment in rare earth elements (REEs, 111–497 ppm), with moderate negative Eu anomalies (0.04–0.63). The plutons are classified as ferroan A-type granites and were formed under moderately reduced to moderately oxidized conditions, similar to those in the Serra dos Carajás suite. They also show affinities with the more evolved members from both the reduced Velho Guilherme suite and oxidized Jamon suite from the Carajás province. The Manda Saia granite has a zircon U–Pb crystallization age of 1866 ± 10 Ma and is derived from partial melting of the Mesoarchean crust of tonalitic composition, as indicated by strongly negative ε_{Hf} values (–12 to –18). The emplacement of these plutons is related to extensional tectonics with magma transport at shallow crustal levels.

Keywords: Granite, Paleoproterozoic, A-Type, Ilmenite series, Carajás

1 INTRODUCTION

Since the introduction of the terms type I- and S- granites by Chappell and White (1974), granitic rocks have been commonly classified according to the nature of their protolith, with crustal melting as the main mechanism for the generation of granites (Arndt, 2013). In this sense, Loiselle and Wones (1979) created the term A-type, which was intended to classify granites with high levels of $Na_2O + K_2O$; high field strength elements (HFSEs) (Zr, Nb and REE); high FeOt/(FeOt+MgO) ratios; low concentrations of Ba, Sr and Eu; low oxygen fugacity (fO_2); reduced H_2O contents; and that are related to anorogenic environments, whose chemical compositions are different from those of types -I and -S. Whalen et al. (1987) added typical characteristics of A-type granites, including high SiO_2, Ga, Y, Ce and Zn contents; high Ga/Al ratio, and low Al_2O_3 and CaO contents. Thus, the "alphabetical classification" was created to refer more adequately to the chemical composition and its contribution to the understanding of the petrogenetic evolution of granitoids compared to its relationship with specific petrological mechanisms involved in the genesis of magmatic rocks (e.g., partial

melting). However, the distinction among the different types is not always simple. This is particularly true in the case of highly fractionated A-type and I-type granites ($SiO_2 > 72\%$), where the geological context under study must be considered in the definition.

In several cratons around the world, anorogenic magmatism has occurred since the Neoarchean, especially in the Paleoproterozoic and Mesoproterozoic, as evidenced by the formation of the anorthosite–mangerite–charnockite–granite rapakivi (AMCG) and rapakivi granites (Rämö and Haapala, 1995). This formation probably occurred due to the lithospheric crust being relatively thinner in that period and being affected by mantle plumes, in addition to the existence of significant supercontinents.

Many anorogenic granitic massifs of Paleoproterozoic age, with A-type affinity and dimensions ranging from stocks to batholiths, have been described in the Carajás province, which is situated in the southeastern part of the Amazonian craton. The importance given to these granites is due, among other factors, to the existence of mineral deposits of cassiterite and, locally, wolframite associated with them. Many A-type plutons from the Carajás province, which intrudes into the Archean basement rocks, were grouped by Dall'Agnol et al. (2005) in the Jamon, Serra dos Carajás and Velho Guilherme suites according to their mineralogy, geochemistry, oxidation state of their magmas and magnetic susceptibility. The granites of the Jamon suite are oxidized and classified as the magnetite series, and the granites of the Velho Guilherme suite are reduced and akin to those of the ilmenite series (Ishihara, 1977). The granites in the Serra dos Carajás suite can be ambiguous, as they are more like the reduced granites, but they may contain moderate magnetite contents. The oxidized to the reduced phases decrease the modal contents of opaque minerals and magnetite and magnetic susceptibility values and increase the FeOt/(FeOt+MgO) ratio in whole rock, amphibole, and biotite. Titanite is typically associated with magnetite in oxidized granites, and magnetite is generally absent in reduced granites.

The Manda Saia granite, which is the object of this work, belongs to the the Jamon suite, but it has not been geologically mapped in detail, and petrographic and geochemical information and geochronological data are lacking. Thus, its age of crystallization and petrological affinities are still undetermined. The results obtained in this research aim to contribute to a more precise definition of the nature, source and formation processes of the Manda Saia granite, as well as to define its isotopic characterization from Hf–Pb isotopes in zircon. The understanding of the origin and evolution of the Manda Saia granite will contribute

to the advancement of knowledge about the evolutionary context of the Paleoproterozoic granites in the Carajás province.

2 GEOLOGICAL SETTING

The Carajás province is located on the southeastern margin of the Amazonian Craton and represents an Archean core limited by Proterozoic belts. According to Tassinari and Macambira (2004), the Carajás province is part of the Central Amazon province, while Santos (2003) consider it an independent Archean province (Fig. 1a). There is agreement that the Carajás province corresponds to an older Archean segment of the Amazonian craton that was not affected by the Transamazonian cycle (2.26–1.95 Ga; Vasquez et al., 2008). During the evolution of the Amazonian craton, there was extensive post-tectonic and anorogenic magmatism that produced hundreds of stocks and batholiths, mainly in the Paleoproterozoic (~1880 Ma; Dall'Agnol et al., 1999a, Santos et al., 2018; Teixeira et al., 2018). The Carajás province is composed of a variety of granitoids and greenstone sequences and is covered in the north by the 2.76 Ga volcano-sedimentary basin, where important Au, Cu, Fe and Mn mineral deposits are located. The Carajás province initially divided by Santos (2003) into the Rio Maria and Carajás has been divided by Dall'Agnol et al. (2013) into the Canaã dos Carajás domain (3.0–2.70 Ga) and the Carajás basin, Mesoarchean Rio Maria domain (2.98–2.86 Ga) and Mesoarchean to Neoarchean Sapucaia domain (2.95–2.73 Ga). At the end of the Archean, these domains were stabilized, remaining stable until ca. 1880 Ma, when A-type granites formed and were emplaced (Dall'Agnol et al., 2005).
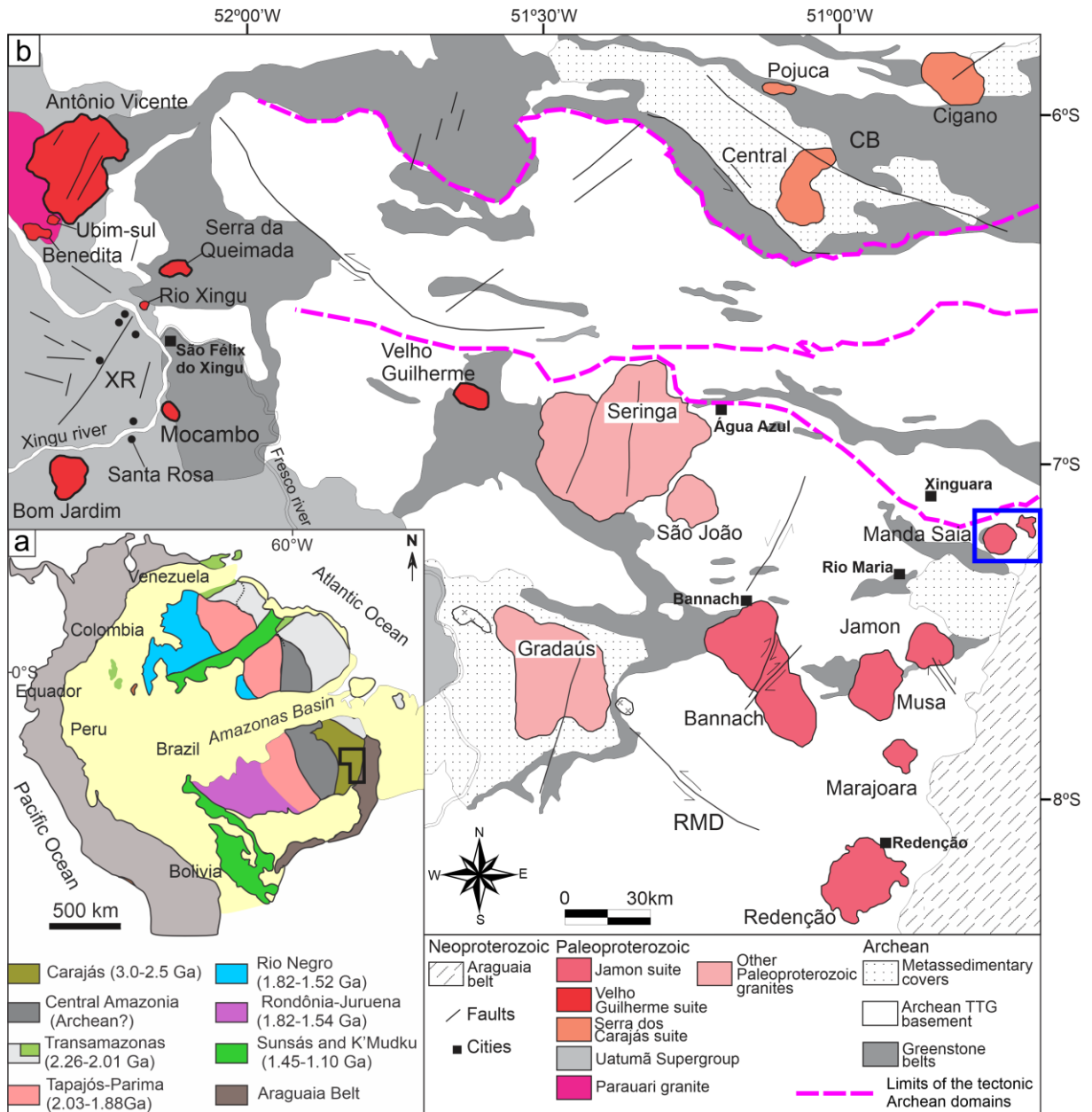
Figure 1 - (a) Amazonian craton divided into geochronological provinces (Santos et al., 2004), and the location of the Manda Saia granite; (b) geologic map of the Carajás province, showing the Paleoproterozoic granites (Dall'Agnol et al., 2005 modified).

2.1 ANOROGENIC GRANITES FROM THE CARAJÁS PROVINCE

The Carajás province A-type granitoids crystallized during the Orosirian (1880 to 1857 Ma; Santos et al., 2018; Teixeira et al., 2018) in an extensional tectonic environment, where granitic magmatism coexisted with dike swarms (Silva et al., 2016; Teixeira et al., 2019). These granites are disseminated throughout the Carajás province and are classified into three suites (Fig. 1): Jamon, Velho Guilherme and Serra dos Carajás. A summary of the ages of the Carajás province Paleoproterozoic granites is shown in Fig. 2.

In the Rio Maria domain, the oxidized A-type granites intruded into the Jamon suite (Dall'Agnol et al., 1999a), which is composed of the Jamon, Bannach, Manda Saia, Marajoara, Musa, and Redenção granites (Fig. 1b). They are composed of monzogranites and syenogranites, and in the most mafic facies, biotite, amphibole and subordinate clinopyroxene are present. Allanite, apatite, ilmenite, titanite, and zircon are accessory minerals. Rapakivi texture and microgranular enclaves are commonly visible in the Redenção and Marajoara plutons (Oliveira et al., 2009; Santos et al., 2018). In the Carajás basin of the northern Carajás province, moderately reduced granites constitute the Serra dos Carajás suite, consisting of the Serra dos Carajás, Pojuca and Cigano plutons (Dall'Agnol et al., 2005). The suite is composed of hornblende–biotite monzogranites and syenogranites. Accessory minerals are the same as those in the Jamon suite but with less magnetite and titanite and more abundant fluorite. The reduced granites in the Xingu region are intrusive in diverse Archean rocks belongs to the Velho Guilherme suite, which is composed of the Velho Guilherme, Antônio Vicente, Benedita, Bom Jardim, Mocambo and Rio Xingu granites (Lamarão et al., 2012; Teixeira et al., 2002). They are reduced syenogranite biotite, monzogranite and subordinate alkali-feldspar granite. Late to postmagmatic hydrothermal alterations strongly affect the more evolved leucogranitic facies.

2.2 GEOLOGICAL AND STRUCTURAL ASPECTS OF THE MANDA SAIA GRANITE

The Manda Saia granite occurs at the northeast end of the Rio Maria domain, where it is intrusive in the Mesoarchean basement. In the northern portion, it cuts the rocks of the Rio Maria granodiorite, and in its eastern and western portions and along its entire southern border, it is intrusive in the metabasalts of the Babaçu group greenstone belt (Fig. 3a). Its contacts occur along extensive shear zones and/or normal faults, while its intrusive character is shown by its truncating the regional ENE–WSW foliation of the basement rocks. The Manda Saia granite occurs in the form of two semicircular plutons that have an aerogamaespectrometric signature (Th/K ratio) that is distinct from that of the country rocks (Fig. 3b). They have stock dimensions (between 60 and 95 km^2) that are visible in a digital elevation model (SRTM – Shuttle Radar Topography Mission) as small saw shapes aligned NE–SW and NW–SE that can reach up to 450 m in altitude (Fig. 3c).
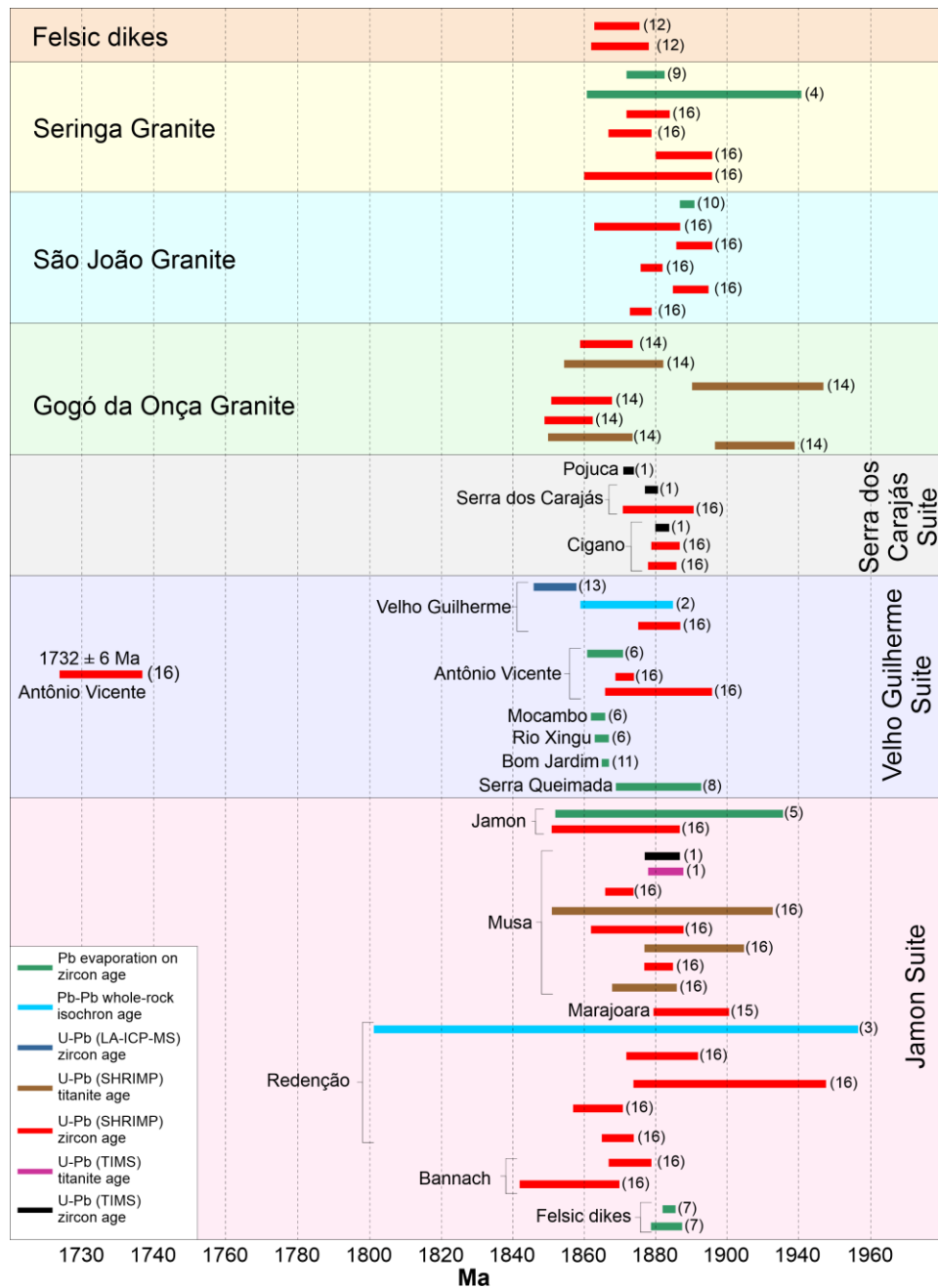
Figure 2 - Age histogram of the Paleoproterozoic granites of the Carajás province (modified from Teixeira et al. 2018). Data source: (1) Machado et al. (1991); (2) Rodrigues et al. (1992); (3) Barbosa et al. (1995); (4) Avelar (1996); (5) Dall'Agnol et al. (1999a); (6) Teixeira et al. (2002); (7) Dall'Agnol et al. (2005); (8) Pinho et al. (2006); (9) Paiva Jr. (2009); (10) Lima (2011); (11) Lamarão et al. (2012); (12) Silva et al. (2016); (13) Antônio et al. (2017); (14) Teixeira et al. (2017); (15) Santos et al. (2018); (16) Teixeira et al. (2018).

These alignments are coincident with the regional lineament patterns that affect both granitic bodies and their country rocks in the Carajás province; these patterns are the response to the extension that generated normal NE–SW and NW–SE faults (Oliveira et al., 2008). However, such relief features manifest as circular structures inside these bodies (Fig. 3a), similar to the features defined as ring faults in other massifs of the Rio Maria domain (Oliveira et al., 2008, 2010, Santos et al., 2018).

The Manda Saia granite outcrops in the form of extensive slabs (Fig. 4a), formed by rocks with a grayish pink color and isotropic character (Fig. 4b). In the marginal portions of the bodies, pegmatoid pockets containing centimeter-sized crystals of quartz, feldspars, and biotite mark the final stages of pluton crystallization (Fig. 4c). The occurrences of angular xenoliths of mafic rock that are more common at the edges of the plutons (Fig. 4d) and the absence of signs of deformation in the solid state in the rocks suggest the existence of a high-contrast viscosity between the intrusions and their country rocks.

3 METHODS

3.1 PETROGRAPHY

Optical microscopy was performed using transmitted light. The polished sections were prepared at the thin section laboratory at Federal University of Pará (UFPA). Ten modal analyses were performed on representative samples of the Manda Saia granite. The modal compositions were obtained with approximately 1,800 points per sample, which were distributed in a mesh with a spacing of 0.4 mm in the automatic point counter Hardledge Endeeper, and the rocks were classified according to the IUGS (International Union of Geological Sciences).

3.2 WHOLE-ROCK GEOCHEMISTRY

Whole-rock geochemical analysis was obtained from 11 representative samples of Manda Saia granite. Approximately 6 kg of samples for whole-rock chemical analysis were grounded at the Federal University of Para (UFPA) by using both primary and secondary jaw crushers until the particles were between 0.3 and 0.1 mm in size. This material was powdered in an agate swing mill to reach a particle size of <10 μm. Eleven analyses were obtained at the ALS Geochemistry Laboratories, Minas Gerais, Brazil, and these analyses were made by inductively coupled plasma atomic emission spectroscopy (ICP–AES) for major elements and inductively coupled plasma mass spectrometry (ICP–MS) for trace elements (including rare earth elements). GCDkit 6.1 software (Janousek et al., 2006) was used to generate the geochemical diagrams.
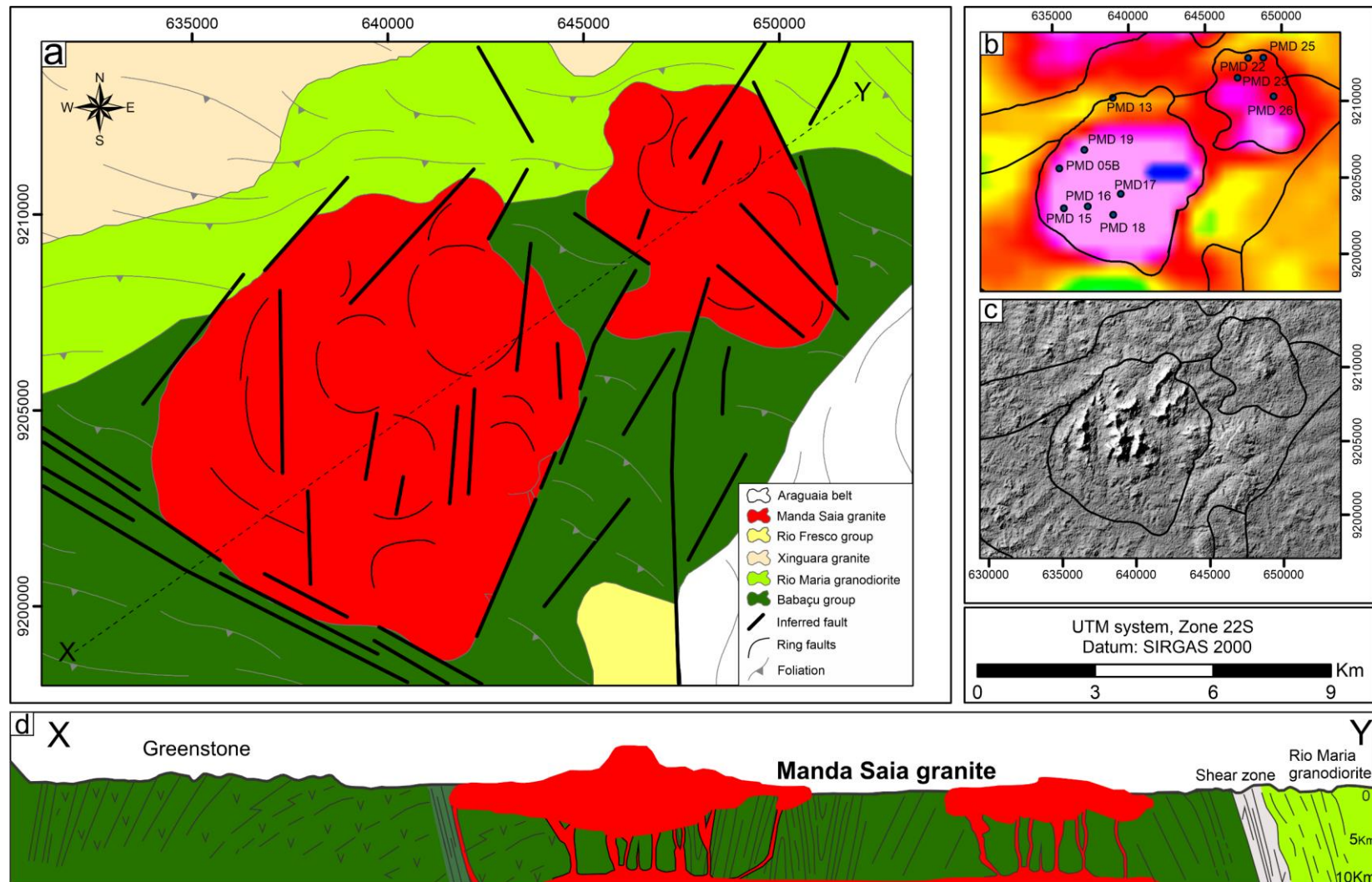
Figure 3 - (a) Geological map of the Manda Saia granite; (b) and (c) aerogeophysical image of the Th/K ratio and digital elevation model (SRTM), respectively, showing the contrast between the Manda Saia granite and Archean country rocks; (d) 10 km-deep horizontal cross-section idealized for the occurrence area of the Manda Saia granite, exposing the form of the emplacement of the bodies in relation to their host rocks and their inferred depth (see line X-Y on the map for the location).
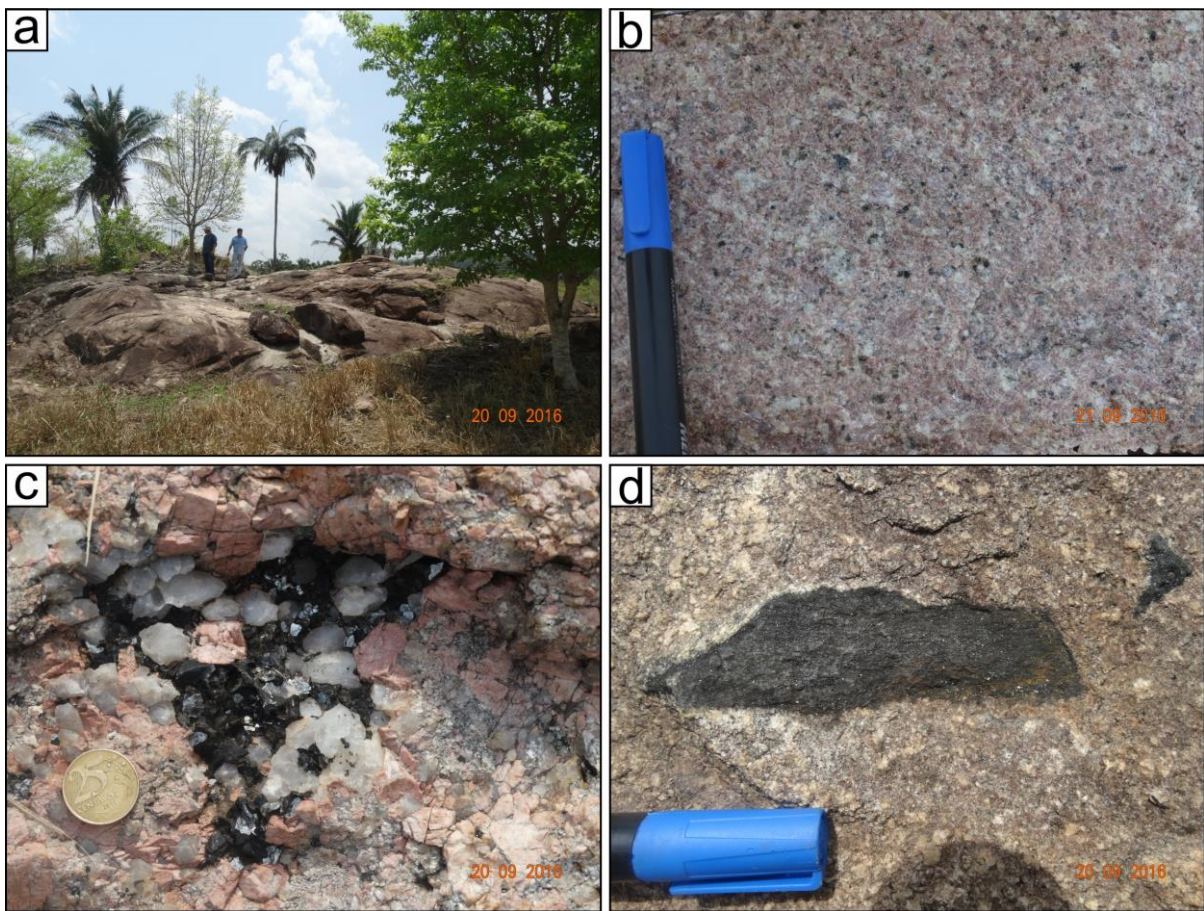
Figure 4 - Mesoscopic aspects of the Manda Saia granite. (a) Outcrop formed by metric slabs; (b) medium equigranular phaneritic texture; (c) pegmatoid pockets composed of centimeter-sized crystals of quartz, feldspars, and biotite; (d) angular mafic xenolith that is common along the Manda Saia granite edges.

3.3 U–Pb ZIRCON GEOCHRONOLOGY

Zircon grains from sample PMD-17 were separated at the Isotopic Geology Laboratory, Federal University of Pará (Pará-Iso/UFPA). Approximately 10 kg of rock was crushed, ground, and sieved in fractions of 250, 175, 125 and 75 μm and then processed using an isodynamic magnetic separator and bromoform, followed by handpicking under a binocular microscope.

To execute the laser ablation sector field of LA–SF–ICP–MS, zircon grains were assembled in epoxy resin and polished to show the crystal centers. The internal structure of the zircons was checked using cathodoluminescence (CL) and backscattered electron (BSE) imaging to select potential target sites for U–Pb analyses. CL and BSE images were produced using a JEOL JXA-8230 scanning electron microprobe (SEM) working at 15 kV, 20 mA and a working distance of 11 mm at the Microanalysis Laboratory, Federal University of Pará (UFPA).

The analyses were performed on an LA–SF–ICP–MS at the Isotopic Geochemistry Laboratory of the Federal University of Ouro Preto (UFOP), Brazil, with a Thermo-Scientific Element 2 Sector Field (SF) ICP–MS coupled to a CETAC LSX-213 G2+ (λ =213 nm) Nd:YAG laser according to the methods of Frei and Gerdes (2009). Helium was used as a carrier gas to increase the transport efficiency of the ablated material. Each analytical spot was 20 µm in diameter. The absolute abundances and U–Th–Pb ratios were determined relative to primary zircon standards GJ-1 (608.5 ± 1.5 Ma; Jackson et al., 2004), and secondary zircon BB (560 ± 0.4 Ma; Santos et al., 2017). All corrections and raw data reduction are processed using an offline Excel spreadsheet (adapted from Chemale Jr. et al., 2012) in order to calculate the corrected values of the isotopic ratios ($^{206}Pb/^{238}U$, $^{232}Th/^{238}U$, $^{207}Pb/^{206}Pb$) and uncertainties (1s level in %). Age calculations and the presentation of isotopic results in the Concordia diagram are performed with the Isoplot/EX 3.0 program of Ludwig (2003). The strategy to define the most robust statistics and to determine the "best" U-Pb age is that recommended by Spencer et al. (2016). As all the samples are older than 1.5 Ga, the age was calculated using the weighted mean of the $^{207}Pb/^{206}Pb$ ratios, and the acceptability of the mean square weighted deviation (MSWD) has been evaluated for over- and under-dispersion.

3.4 Lu–Hf ISOTOPE DATA

LA–MC–ICP–MS in situ zircon Lu–Hf analyses were carried out using a high-resolution multicollector Neptune Thermo Finnigan mass spectrometer coupled with a Nd:YAG LSX-213 G2 CETAC laser microprobe at the Isotope Geology laboratory (Pará-Iso), Federal University of Pará, Brazil, following the routine implemented by Milhomem et al. (2017). The analytical parameters for operating the ICP–MS were 16.0 L/min of argon (Ar) gas cooler flow; 0.7 to 0.8 L/min of auxiliary argon gas; 1.2 to 1.3 L/min of argon carrier gas, 1200 W of power, -2000 of extraction, low resolution static analysis mode, and eight Faraday collectors. The spot diameter of the laser was 50 µm, and during the analysis, the flow of helium gas (He), which was responsible for transporting the ablated material to the ICP–MS, varied from 450-500 mL/min, with a frequency of 10 Hz and a total ablation time of approximately 60 seconds. Using 50% power provided an energy density of 4-5 J/cm^2 and allowed us to obtain a signal on the order of 1 to 3 volts for ^{178}Hf. The Mud Tank zircon (732±1 Ma; Black and Gulson, 1978) was used as a reference material for the $^{176}Hf/^{177}Hf$ ratio, so the analytical sequence involved three analyses of the sample interspersed with one of the reference zircon.

To correct the isobaric interferences of isotopes Lu and Yb with a mass of 176, the isotopes of Lu, Hf and Yb were measured concomitantly based on isotopic ratios ^{173}Yb/^{171}Yb, ^{179}Hf/^{177}Hf, ^{175}Lu/^{177}Hf and ^{176}Hf/^{177}Hf. Thus, the isobaric interferences of ^{176}Lu and ^{176}Yb were corrected using an equation involving a mass fractionation factor (β) for Lu and Yb and the intensity of the signals observed in the interference-free isotopes ^{175}Lu and ^{173}Yb, which were normalized from their abundances of accepted isotopes ^{176}Lu/^{175}Lu=0.026549 (Chu et al., 2002) and ^{176}Yb/^{173}Yb=0.786956 (Thirlwall and Anczkiewicz 2004). The factor β (Hf, Yb and Lu) was calculated for each measurement since its value depends directly on the ratio measured between the isotopes of interest. On the other hand, to correct for the isotopic fractionation caused by the equipment during the analyses, according to the exponential law (Russel et al., 1978), the Yb isotopic ratios were normalized to ^{173}Yb/^{171}Yb, assuming a value of 1.12466 (Thirlwall and Anczkiewicz 2004), and the isotopic ratios of Hf were normalized using a value of 0.7325 for the ^{179}Hf/^{177}Hf ratio (Patchett and Tatsumoto 1980). To carry out these correction calculations and obtain the corrected values of the ^{176}Hf/^{177}Hf and ^{176}Lu/^{177}Hf ratios for each analyzed point, the raw data were processed with a Microsoft Excel macro, with approximately 45 (after a 2σ outlier test) values being selected from a total of 50 integrated data points of 1.049 s/point (Milhomem Neto et al., 2017).

3.5 MAGNETIC SUSCEPTIBILITY

Magnetic susceptibility measurements were performed on 11 hand samples at the Laboratory of Magnetic Petrology of the Institute of Geosciences of the Federal University of Pará using an MS-30 susceptibility meter, manufactured by ZH INSTRUMENTS, which allows measurements of materials with magnetic susceptibility varying up to 1×10^{-7} SI. The magnetic susceptibility of the rock was determined through comparative measurements of inductance. The procedure consisted of first obtaining the inductances of the coil that are in direct contact with the air (without the sample) and, later, those that are in contact with the sample; this process yields the representative magnetic susceptibility of each sample calculated via the ratio between the measurements of air inductance and the measurements performed on the sample.

3.6 MINERAL CHEMISTRY

Mineral chemical data were acquired using a JEOL JXA-8230 electron microprobe equipped with five wavelength dispersive spectrometers (WDSs). Five polished thin sections of representative samples from the Manda Saia granite were first carbon coated to eliminate

electrostatic charge-up on the sample surface and then analyzed. WDS analyses were as follows: column accelerating voltage of 15 kV, current of 20 nA, analysis times of 20 s for major elements and 40 s for minor and trace elements, and beam diameters 1 μm for all biotites. The analytical precision was ±1% and ±10% for major and minor elements, respectively. The matrix effects were corrected by the ZAF methods. The crystals used for the WDS analyses of all minerals were lithium fluoride (LiFH) for V, Mn, Fe, Ni and Ba; pentaerythritol (PETJ) for K, Ca, Ti and Sr; thallium acid phthalate (TAP) for Na, Si, Al and Mg; and layered dispersion element (LDE1) for F. Standards were andradite (Si and Ca), microcline (Al and K), hematite (Fe), olivine (Mg), albite (Na), pyrophanite (Ti and Mn), vanadinite (V and Cl) and topaz (F).

4 RESULTS

4.1 MODAL COMPOSITION AND PETROGRAPHIC CLASSIFICATION

The data obtained from the modal analysis (Tab. 1) of the Manda Saia granite show that the average contents of quartz and plagioclase/microcline ratios vary significantly, allowing these rocks, when plotted on the QAP diagram, to be classified with a composition that varies from monzo- to syenogranite (Fig. 5), according to the classification established by the IUGS (Le Maitre et al., 2002). Due to the reduced mafic mineral amount (M<5%), they can be classified as hololeucocratic (Fig. 5). Biotite (rarely amphibole) is the ferromagnesian mineral present in these rocks, and the primary accessory minerals are titanite, opaque minerals, allanite, apatite, and zircon. Chlorite, epidote, sericite–muscovite, clay minerals and fluorite represent the secondary phases.

Table 1 - Modal compositions of the Manda Saia granite.

Sample	PMD 13	PMD 15	PMD 25	PMD 26	PMD 05B	PMD 16	PMD 17	PMD 18	PMD 19	PMD 22
Variety	Syenogranite				Monzogranite					
Minerals (vol%)										
Quartz	29.05	35.40	28.65	35.70	33.65	36.35	33.05	37.90	43.10	35.60
Alkali feldspar	24.15	16.85	15.10	16.30	25.25	31.45	28.95	22.15	28.85	29.10
Plagioclase	44.50	45.55	52.95	45.30	38.60	27.95	35.00	35.20	25.80	34.20
Biotite	1.75	1.15	0.75	1.20	1.65	3.95	2.35	1.15	1.50	0.90
Muscovite	0.30	0.95	1.95	0.40	0.15	0.05	0.05	2.65	–	0.10
Epidote	–	–	0.30	0.50	0.05	–	0.35	0.35	0.05	–
Zircon	0.05	–	–	–	0.05	0.15	–	–	–	–
Allanite	0.05	–	0.05	0.10	0.10	–	0.15	0.15	0.10	–
Titanite	–	–	–	–	–	0.05	–	–	–	–
Fluorite	0.10	0.10	0.20	0.35	0.35	–	–	0.40	0.40	0.05
Opaque minerals	0.05	–	0.05	–	0.10	0.05	0.05	–	0.20	0.05
Apatite	–	–	–	–	–	–	0.05	0.05	–	–
Pl/Mc	0.54	0.37	0.29	0.36	0.65	1.13	0.83	0.63	1.12	0.85
A + P	68.65	62.40	68.05	61.60	63.85	59.40	63.95	57.35	54.65	63.30
Color index (M')	1.85	1.15	1.10	1.80	1.85	4.15	2.85	1.65	1.65	0.90

Abbreviations: A+P (alkali-feldspar + plagioclase), Pl/Mc (plagioclase/microcline).
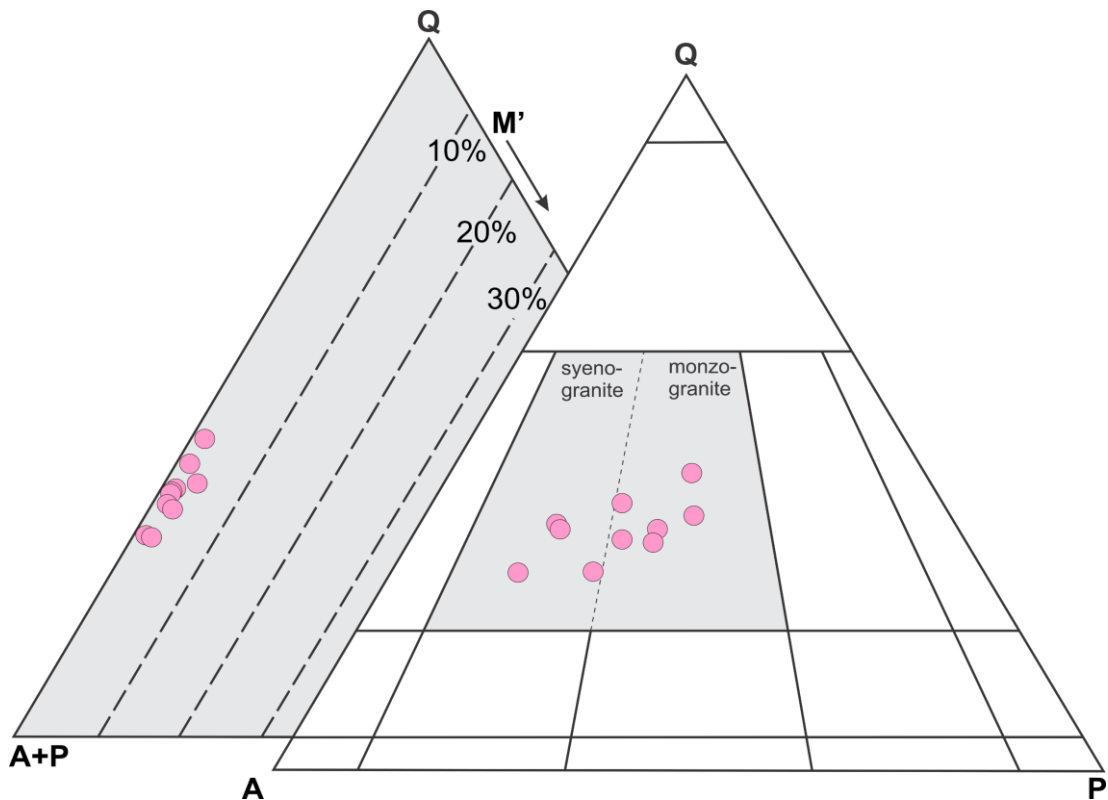
Figure 5 - Q-A-P and Q-(A+P)-M plots for the Manda Saia granite.

4.2 TEXTURAL ASPECTS

The Manda Saia granite rocks have a medium to coarse heterogranular texture (Fig. 6a) with porphyritic variations (Fig. 6b). Among the felsic minerals, there is greater development of microcline (Fig. 6b), reaching dimensions up to 35 mm and with partly corroded or rounded rims (Fig. 6a). Inclusions of fine quartz crystals are frequent in the feldspar rims of the porphyritic rocks, while granophyric intergrowth involves the entire microcline crystal. The fine feldspar crystals (0.2 to 1.2 mm) occur as interstitial grains, which are included in the more developed crystals or compose the matrix. The larger alkali-feldspar crystals are partially replaced by chessboard albite, and the contacts among them commonly show swapped rims of intergranular albite (Fig. 6c).

Plagioclase crystals reach dimensions up to 7 mm, where normal zoning is more evident and the albitic rims are fine and regular. Their compositions, in general, range from sodium oligoclase (An_{12-20}) in most crystals to albite (An_{7-10}) at the rims (Fig. 6d). Relationships that can be interpreted as synneusis (Vance, 1965 - Fig. 6e) are also observed. Quartz occurs as two textural varieties. Qz1 is the most developed type, reaching dimensions of up to 3.5 mm (Fig. 6a). Their habits vary from subhedral to anhedral, and they commonly form aggregates and have straight to moderately undulating extinction. Qz2 usually occurs as inclusions in the rims

of feldspar crystals, marking their growth phases, or as interstitial grains. Eventually, the larger microcline crystals assume a poikilitic aspect in their rims (Fig. 6b). Myrmequitic and granophyric intergrowths are also frequent (Fig. 6a). In the former type, tiny quartz crystals are associated with albite in vermicular forms and droplets when they are in contact with the microcline. The granophyric texture, in turn, represents the intergrowth of quartz and alkali-feldspar and is similar to the micrographic texture and to the coarser graphic intergrowths common in pegmatite.

Biotite is the most important mafic mineral, reaching 1.6% in the Manda Saia granite. Its crystals are of lamellar habit with strong pleochroism ranging from dark green to pale yellow (Fig. 6f). Accessory minerals represented by zircon, epidote, titanite and opaque minerals reach 1% and are associated with biotite aggregates. Amphibole is restricted to occurring as an interstitial phase (PMD-15 sample). Its pleochroism varies from dark green to olive green (Fig. 6g). Fluorite is fine-grained and occurs as inclusions in quartz and oligoclase or is associated with mafic aggregates (Fig. 6h). The transformation from opaque to goethite is observed locally (Fig. 6h).

4.3 MAJOR AND TRACE ELEMENTS

The Manda Saia granite presents SiO_2 contents ranging from 74.8 to 77.7% (Tab. 2), where a negative correlation is observed with the compatible element contents ($TiO_2+Fe_2O_3t+MgO+CaO$), which decrease with the increase in the silica contents (Fig. 7a). An inverse behavior is observed for K_2O+Na_2O/CaO values (9.0-30.6; Fig. 7b), as well as for the Rb/Sr ratio (3.5–36.3) and Nb contents (36.3–77.4 ppm) that increase in the direction of the more SiO_2-enriched rocks (Fig. 7c and d). Notably, the PMD-15 sample has anomalous values for both the Rb/Sr ratio (586.1) and Nb content (136 ppm). Other trace elements, such as Zr (215–93 ppm) and Ba (686–2 ppm), have contents that decrease with increasing SiO_2 (Fig. 7e and f).
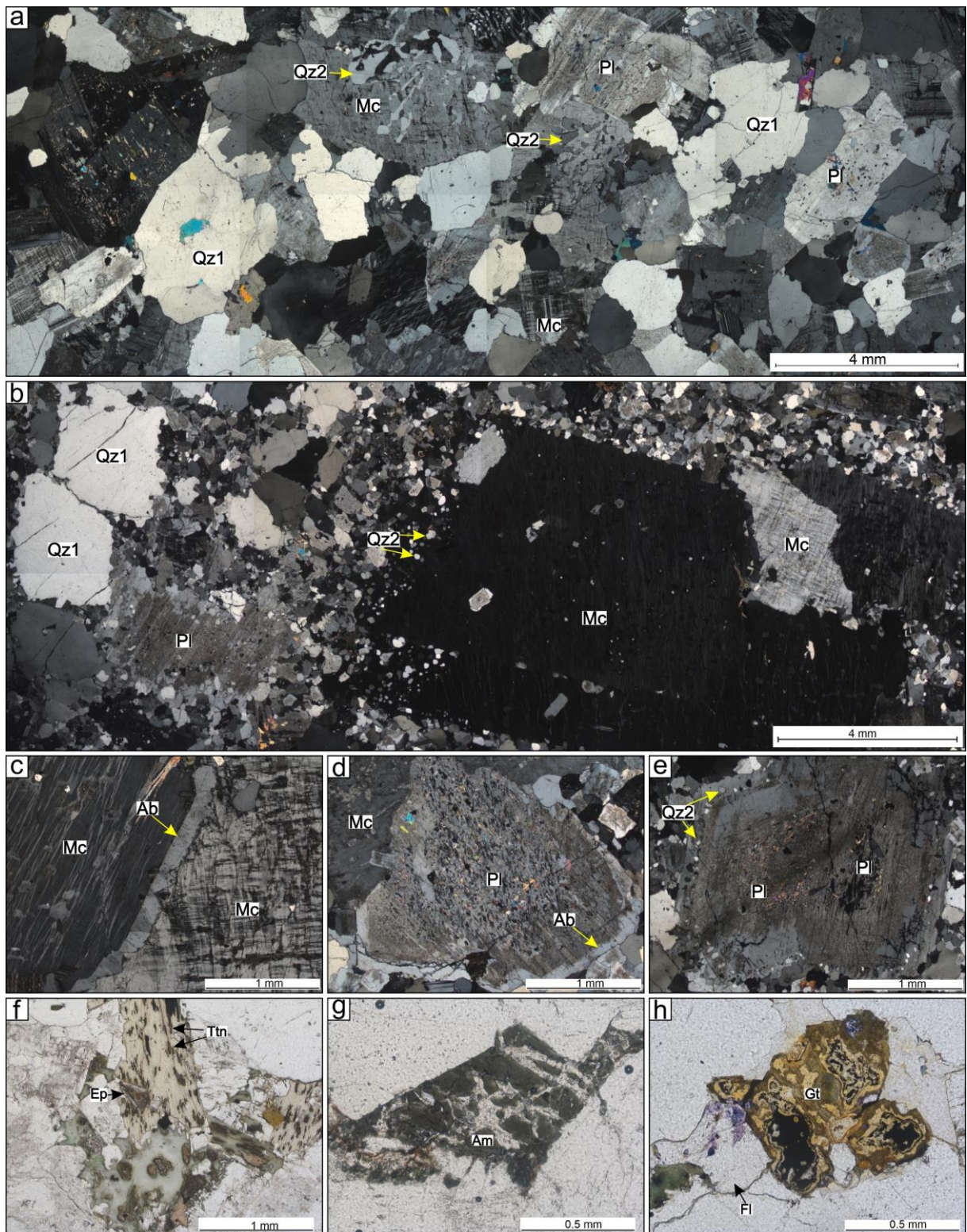
Figure 6 - Representative photomicrographs of the Manda Saia granite: (a) undeformed, quartz–feldspathic and granophyric medium equigranular texture; (b) coarse porphyritic heterogranular texture; (c) intergranular albite texture known as swapped rims; (d) albitic rims on plagioclase; (e) synneusis texture or epitaxial growth in plagioclase; (f) titanite in the biotite cleavage planes; (g) strongly fractured interstitial amphibole; (h) goethite formed by the alteration of magnetite in contact with fluorite. Abbreviations: Ab (albite); Am (amphibole); Ep (epidote); Fl (fluorite); Gt (goethite); Mc (microcline); Pl (plagioclase); Qz (quartz); Ttn (titanite).

4.4 RARE EARTH ELEMENTS

The samples of the Manda Saia granite (Fig. 8a) show rare earth element (REE) patterns analogous to those of other Paleoproterozoic plutons from the Carajás province (Fig. 8). They have enrichments in light (La/Sm_N = 3.63–10.08) and heavy (Gd/Yb_N = 0.38–0.99) REEs with low La/Yb_N (1.88–17.63) and moderate negative Eu anomalies (Eu/Eu^* = 0.31–0.62). However, their REE patterns are different from those plutons of the Jamon suite by less fractionated heavy REE patterns, which also differ from the Velho Guilherme suite by their less pronounced negative Eu anomalies (Fig. 8b). The PMD-15 sample has anomalous characteristics in relation to the other samples of the Manda Saia granite. It presents accentuated negative Eu anomalies (Eu/Eu^* = 0.04) and greater enrichment in heavy REEs (Gd/Yb_N = 0.11), similar to those observed in evolved granites, as well as those of the Velho Guilherme suite (Fig. 8a). On the other hand, it is suggested that the Manda Saia granite had more affinities with the ETR patterns of the plutons from the Serra dos Carajás suite, despite presenting lower enrichment in light REEs (Fig. 8b). In the multielement diagram, the amplitudes of the negative Ba, Sr, P and Ti anomalies of the Manda Saia granite samples are closer to those of the Jamon and Serra dos Carajás suites (Fig. 8c-d). Their patterns of enrichment in Th and U are similar to those of the Velho Guilherme suite (Fig. 8d), as well as the intensity of the negative anomalies of the PMD-15 sample.

4.5 CLASSIFICATION, TYPOLOGY, AND TECTONIC AFFINITY

The Manda Saia granite is characterized by high contents of SiO_2 (>74%), moderate contents of HFSEs, ΣETR (110.97–496.73 ppm) and $Na_2O + K_2O$ (7.90–8.56%), as well as high $FeOt/(FeOt+MgO)$ ratios (0,89–0.98) and low concentrations of CaO (0.28–0.93%), Al_2O_3 (11.85–13.50%) and Sr (1.80–98.50 ppm). In diagram A–B (Debon and Le Fort, 1983), the rocks of the Manda Saia granite are essentially peraluminous (Fig. 9a) with ASI (Alumina saturation index) > 1 (Tab. 2). The investigated samples show alkaline affinity according to the alkalinity ratio (A.R.) of Wright (1969), that ranging from 3.92 to 4.57 (Tab. 2). In the MALI (modified alkali-lime index) diagram, which considers the behavior of feldspars in relation to the history of differentiation and the source of ferroan granitic magmas, the rocks of the Manda Saia granite plot in the field of calcium-alkaline granites (Fig. 9b).

Table 2 - Geochemical compositions of the Manda Saia granite.

Sample	PMD	PMD	PMD	PMD	PMD	PMD	PMD	PMD	PMD	PMD	PMD
	23	19	15	17	13	16	25	22	18	26	5
Major elements (wt%)											
SiO_2	74.80	75.50	75.70	75.90	76.00	76.40	76.50	76.60	77.20	77.30	77.70
TiO_2	0.13	0.20	0.01	0.15	0.15	0.17	0.08	0.15	0.08	0.08	0.08
Al_2O_3	13.35	12.50	13.50	12.75	11.85	13.10	12.90	12.65	12.60	12.55	12.05
Fe_2O_3*	1.32	1.53	0.59	1.34	1.43	1.36	1.04	1.45	0.90	1.10	0.63
MnO	0.03	0.05	0.17	0.03	0.04	0.03	0.03	0.06	0.01	0.03	0.02
MgO	0.14	0.12	0.01	0.10	0.11	0.13	0.06	0.13	0.07	0.06	0.05
CaO	0.90	0.89	0.28	0.85	0.71	0.93	0.61	0.89	0.87	0.81	0.73
Na_2O	3.50	3.09	4.52	3.31	3.10	3.64	3.73	3.51	3.58	3.60	3.17
K_2O	5.02	5.07	4.04	5.10	4.80	4.76	4.63	4.53	4.76	4.54	5.02
P_2O_5	0.03	0.03	0.01	0.02	0.01	0.04	0.02	0.03	0.01	0.01	0.01
LOI	0.66	0.58	0.50	0.86	0.68	0.55	0.78	0.69	1.00	0.72	0.72
Total	99.88	99.56	99.33	100.41	98.88	101.11	100.38	100.69	101.08	100.80	100.18
Trace elements (ppm)											
Ba	627.00	686.00	2.00	378.00	183.00	543.00	218.00	311.00	29.70	168.50	174.00
Rb	354.00	339.00	1055.00	376.00	359.00	430.00	501.00	392.00	443.00	497.00	399.00
Sr	98.50	95.90	1.80	56.50	31.60	82.10	39.90	64.50	12.20	33.60	34.30
Zr	175.00	215.00	107.00	175.00	187.00	174.00	115.00	203.00	190.00	134.00	93.00
Nb	49.30	36.30	136.00	36.40	49.20	43.50	54.80	60.80	49.40	77.40	48.60
Y	61.10	37.00	63.90	40.10	59.10	35.70	68.50	68.40	196.00	106.50	44.70
Ga	25.40	24.50	38.40	25.50	23.30	26.60	29.80	27.10	29.10	29.50	23.70
Sc	3.00	3.00	6.00	3.00	4.00	5.00	4.00	5.00	3.00	7.00	2.00
Th	46.50	56.70	19.70	50.70	76.70	44.20	42.30	53.30	86.70	46.30	33.00
U	17.75	11.40	9.88	11.40	24.10	15.00	13.85	17.40	26.00	22.10	11.10
V	15.00	12.00	10.00	10.00	10.00	10.00	11.00	14.00	12.00	12.00	9.00
La	72.90	122.00	31.70	109.50	133.50	90.60	40.70	83.80	92.00	47.40	20.60
Ce	135.50	217.00	63.30	195.50	236.00	162.50	83.80	155.50	114.50	102.50	40.60
Pr	13.65	19.95	7.82	17.25	21.30	15.20	9.07	15.25	19.35	11.25	4.58
Nd	45.60	62.70	23.00	53.00	62.20	49.80	31.10	50.90	69.90	39.90	15.80
Sm	7.64	8.68	3.45	7.17	8.34	6.92	5.35	8.19	12.80	7.39	3.57
Eu	1.52	1.30	0.04	1.08	0.92	1.17	0.67	1.20	1.78	0.71	0.63
Gd	6.92	5.74	2.35	5.80	7.10	5.56	4.39	7.30	15.00	6.59	3.86
Tb	1.11	0.92	0.43	0.88	1.17	0.90	0.70	1.28	2.60	1.10	0.72
Dy	7.71	5.37	3.39	5.69	7.89	5.41	4.71	8.27	17.15	7.11	5.15
Ho	1.80	1.12	0.83	1.28	1.78	1.17	1.12	1.92	4.26	1.92	1.24
Er	6.50	3.65	4.42	4.14	6.16	3.96	4.80	6.93	15.40	8.04	4.72
Tm	1.20	0.63	1.37	0.72	1.05	0.74	0.98	1.24	2.89	1.50	0.87
Yb	9.11	4.67	16.80	5.26	8.03	5.81	9.27	9.33	23.90	12.20	7.39
Lu	1.64	0.75	3.40	0.88	1.29	0.98	1.85	1.68	4.21	2.43	1.24
FeOt/FeOt+MgO	0.89	0.92	0.98	0.92	0.92	0.90	0.94	0.91	0.92	0.94	0.92
Mg#	17.36	13.45	3.25	12.88	13.22	15.92	10.26	15.08	13.35	9.75	13.59
K_2O+Na_2O/CaO	9.47	9.17	30.57	9.89	11.13	9.03	13.70	9.03	9.59	10.05	11.22
ASI	1.04	1.03	1.10	1.02	1.02	1.02	1.05	1.03	1.00	1.02	1.01
AR	2.93	2.71	4.28	2.90	2.95	3.16	3.47	3.15	3.27	3.34	2.97
Rb/Sr	3.59	3.53	586.11	6.65	11.36	5.24	12.56	6.08	36.31	14.79	11.63
ΣREE	312.80	454.48	162.30	408.15	496.73	350.72	198.51	352.79	395.74	250.04	110.97
(La/Yb)N	5.40	17.63	1.27	14.05	11.22	10.53	2.96	6.06	2.60	2.62	1.88
Eu/Eu*	0.63	0.53	0.04	0.50	0.36	0.56	0.41	0.47	0.39	0.31	0.52

AR:alakalinity ratio Al_2O_3 + CaO + total alkalis / Al_2O_3 + CaO - total alkalis % weight (Wright, 1969); ASI = Alumina saturation index (Frost et al., 2001); Fe_2O_3* = total iron recalculated as Fe_2O_3. LOI = loss on ignition. Eu/Eu* = Eu_N/[(Sm_N / Gd_N)/2]. La_N, Yb_N, Eu_N, Sm_N and Gd_N normalized to C1 chondrite (McDonough and Sun, 1995).
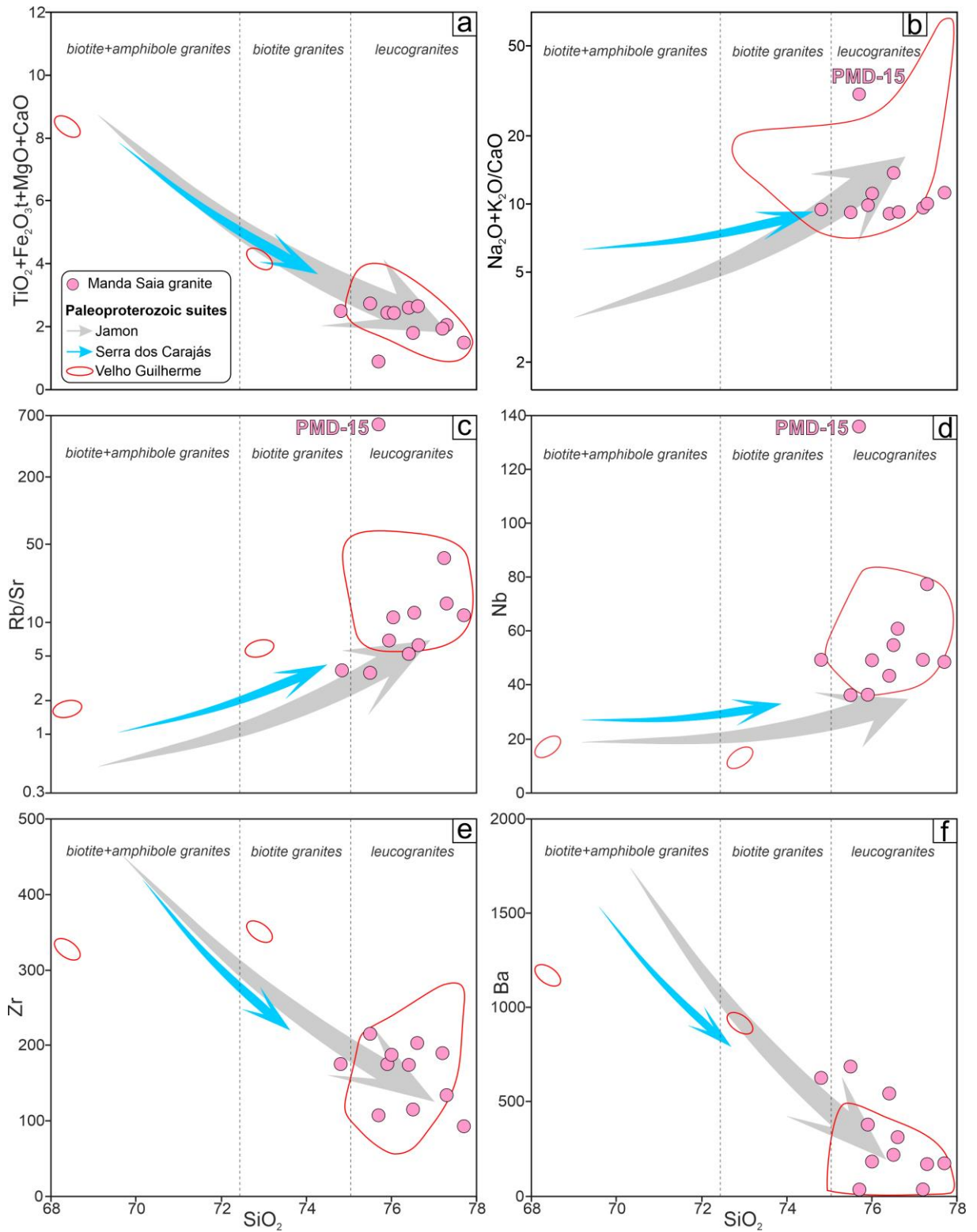
Figure 7 - Harker diagrams (in wt%) for the samples of the Manda Saia granite compared to the other Paleoproterozoic plutons from the Jamon, Serra dos Carajás and Velho Guilherme suites from the Carajás province.
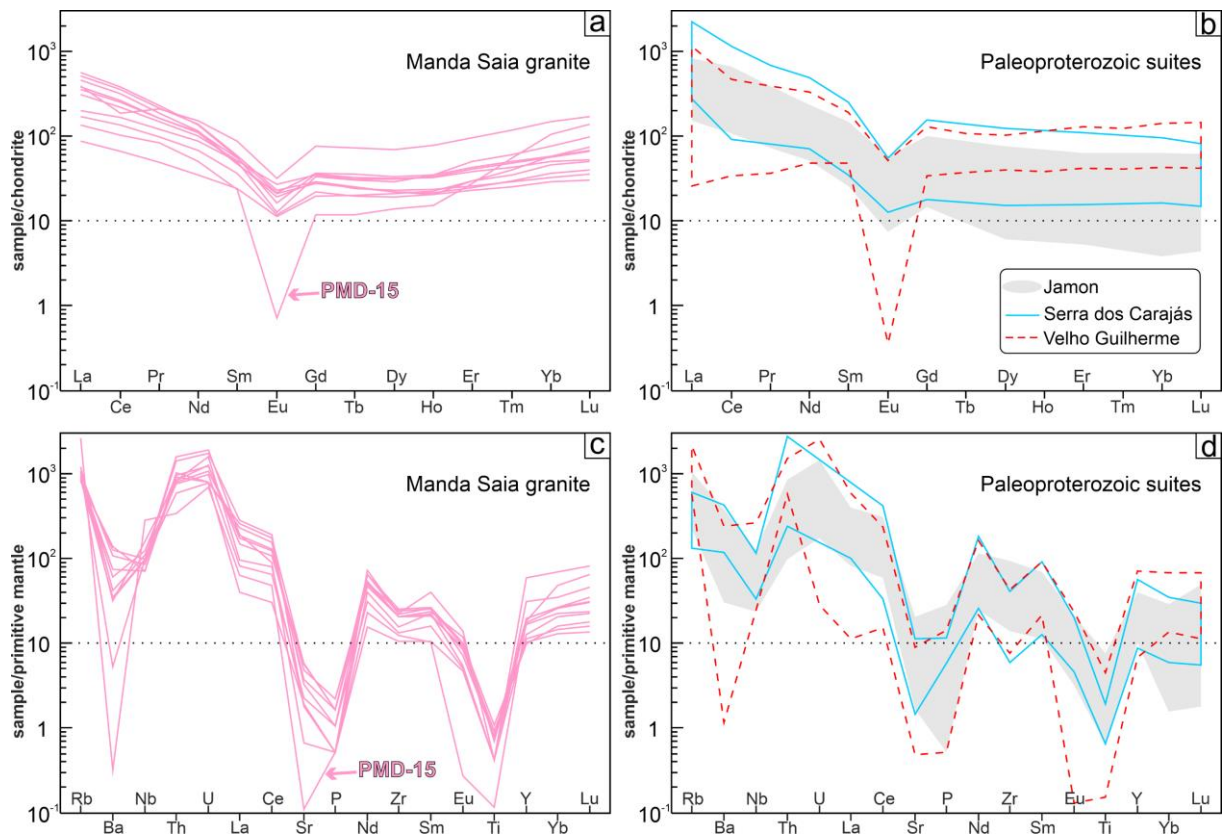
Figure 8 - (a and b) REE and (c and d) multielement patterns of the Manda Saia granite, with values normalized to C1 chondrites and pyrolite (McDonough and Sun, 1995), respectively.

In the classification proposed by Frost et al. (2001), which uses the Fe* index (FeOt/FeOt+MgO) to distinguish ferroan granites from those of magnesian affinity, the Manda Saia granite rocks are classified as ferroan granites (Fe*>0.9 – Fig. 9c). Their geochemical features are compatible with those of A-type granites according to the major- and trace element-based discrimination diagrams of Whalen et al. (1987) and Dall'Agnol and Oliveira (2007) (Fig. 9d and 9e, respectively). Using the parameters of Pearce et al. (1984), in the Nb–Y diagram, the Manda Saia granite is correlated to intraplate granites (Fig. 9f).
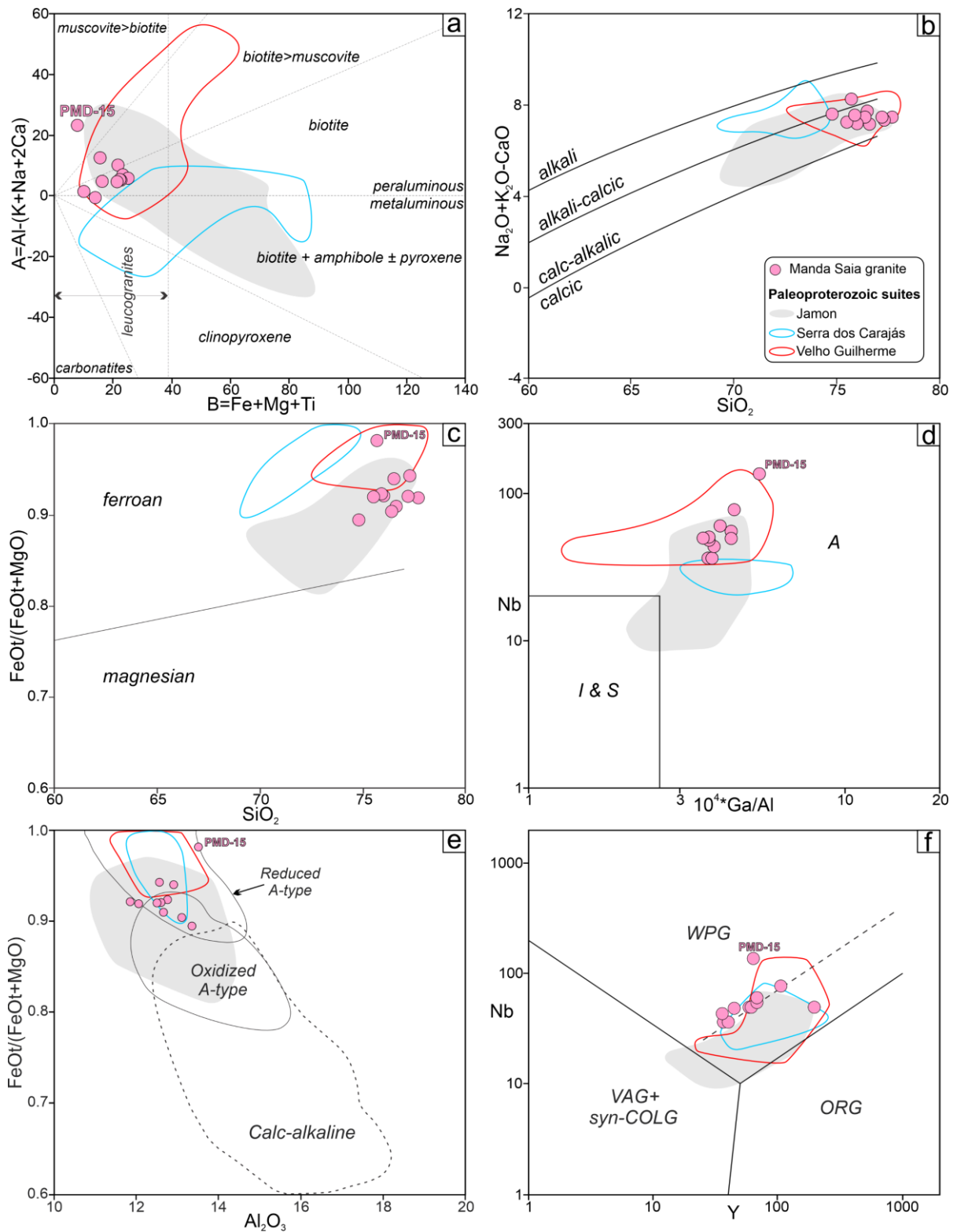
Figure 9 - Geochemical classification and typology of the Manda Saia granite: (a) A-B diagram from Debon and Le Fort (1988); (b) Na_2O+K_2O-CaO (MALI) vs. SiO_2 diagram (Frost et al., 2001); (c) SiO_2 vs. FeOt/FeOt+MgO diagram (Frost et al., 2001); (d) $10^4*Ga/Al$ vs. Nb diagram (Whalen et al., 1987); (e) Al_2O_3 vs. $CaO/(FeOt+MgO+TiO_2)$ diagram (Dall'Agnol and Oliveira, 2007) and (f) Y vs. Nb diagram (Pearce et al., 1984).

4.6 U–Pb ZIRCON DATING

Approximately 28 crystals were analyzed, of which 8 provided results for calculating ages (Tab. 3). The cathodoluminescence images of the Manda Saia granite crystals (Fig. 10) show crystals with few fractures, rare irregular inclusions, concentric oscillatory zoning, euhedral to subhedral crystals without inherited nuclei, pyramidal terminations that can sometimes be subrounded, and sizes varying from approximately 100 to 150 μm in length and 60 to 160 μm in width. All ages were calculated assuming a degree of concordance of 100 ± 7%. The U–Pb diagram shows an upper intercept age of 1866 ± 10 Ma (2σ, MSWD = 0.18, n = 20), with a $^{207}Pb/^{206}Pb$ weighted average age of 1866 ± 10 Ma (2σ, MSWD = 0.18, n=20), and a Concordia age of 1866 ± 12 Ma (2σ, MSWD = 1.8, n=9), the obtained mean age is interpreted as of crystallization of the Manda Saia granite. This age is concomitant with the crystallization ages of Paleoproterozoic A-type granites from the Carajás province (Fig. 11a).

Table 3 - Zircon U–Pb isotope data obtained by LA–SF–ICP–MS for the Manda Saia granite (PMD-17).

PMD-17					Isotopics Ratios [c]							Ages (Ma)						
Spot ID	f_{206} [a]	U	Th	Th/U [b]	$^{207}Pb/^{235}U$	1σ	$^{206}Pb/^{238}U$	1σ	Rho [d]	$^{207}Pb/^{206}Pb$ [e]	1σ	$^{206}Pb/^{238}U$ 1σ		$^{207}Pb/^{235}U$ 1σ		$^{207}Pb/^{206}Pb$ 1σ		Conc. [f]
	(%)	ppm	ppm			(%)		(%)			(%)		abs		abs		abs	(%)
1.2 *	0.00	91	204	2.24	5.2543	1.9	0.3358	1.6	0.84	0.1135	1.0	1866	26	1861	16	1856	19	100.3
1.3	0.00	33	57	1.74	5.5106	2.0	0.3490	1.6	0.81	0.1145	1.2	1930	27	1902	18	1872	22	101.4
1.7 *	0.00	146	318	2.18	5.2710	1.9	0.3367	1.6	0.85	0.1135	1.0	1871	27	1864	17	1857	19	100.4
2.1 *	0.51	95	181	1.91	5.1474	2.3	0.3285	1.7	0.71	0.1136	1.6	1831	27	1844	20	1859	30	99.3
2.2	1.00	150	150	1.00	5.5228	2.8	0.3503	1.8	0.62	0.1143	2.2	1936	29	1904	25	1870	40	101.7
2.3	0.00	63	164	2.61	4.9838	2.1	0.3141	1.7	0.79	0.1151	1.3	1761	26	1817	18	1881	24	96.9
2.4 *	0.26	47	148	3.13	5.2414	2.0	0.3366	1.6	0.81	0.1129	1.2	1870	27	1859	17	1847	21	100.6
3.1 *	0.00	283	654	2.31	5.3573	1.9	0.3401	1.6	0.83	0.1143	1.1	1887	26	1878	17	1868	20	100.5
3.2 *	0.00	44	123	2.82	5.2509	2.0	0.3356	1.7	0.82	0.1135	1.2	1866	27	1861	17	1856	21	100.2
3.3	0.23	139	294	2.11	5.7096	2.2	0.3607	1.7	0.78	0.1148	1.4	1986	29	1933	19	1877	25	102.7
3.4	0.11	109	167	1.53	5.0896	2.0	0.3218	1.6	0.79	0.1147	1.2	1799	25	1834	17	1875	22	98.0
4.1	0.00	99	206	2.07	5.1152	2.1	0.3235	1.7	0.79	0.1147	1.3	1807	26	1839	18	1875	24	98.3
4.2	0.00	81	160	1.98	4.4464	2.1	0.2849	1.7	0.79	0.1132	1.3	1616	24	1721	18	1851	23	93.9
4.3	0.00	52	95	1.81	5.0452	2.0	0.3188	1.6	0.80	0.1148	1.2	1784	25	1827	17	1876	22	97.6
4.5	0.38	170	396	2.33	4.9549	2.2	0.3139	1.7	0.74	0.1145	1.5	1760	25	1812	19	1872	27	97.1
5.2 *	0.00	64	170	2.68	5.3514	2.1	0.3402	1.7	0.81	0.1141	1.2	1887	27	1877	18	1866	22	100.5
6.1	0.20	92	227	2.47	5.5482	2.1	0.3524	1.7	0.81	0.1142	1.2	1946	28	1908	18	1867	22	102.0
7.1 *	0.00	175	258	1.48	5.3470	2.0	0.3393	1.6	0.83	0.1143	1.1	1883	26	1876	17	1869	20	100.4
8.1 *	0.32	45	117	2.62	5.4740	2.1	0.3486	1.7	0.80	0.1139	1.3	1928	28	1897	18	1862	23	101.7
9.1	0.00	57	100	1.74	5.5835	2.1	0.3537	1.6	0.79	0.1145	1.3	1952	27	1914	18	1872	23	102.0
4.4	*0.91*	*160*	*219*	*1.37*	*5.0300*	*2.4*	*0.2661*	*1.7*	*0.72*	*0.1371*	*1.7*	*1521*	*23*	*1824*	*20*	*2191*	*29*	*83.4*
1.1	*0.07*	*707*	*1380*	*1.95*	*4.7831*	*1.9*	*0.3192*	*1.6*	*0.85*	*0.1087*	*1.0*	*1786*	*25*	*1782*	*16*	*1777*	*18*	*100.2*
3.3	*0.00*	*116*	*175*	*1.52*	*4.7961*	*1.9*	*0.3209*	*1.6*	*0.84*	*0.1084*	*1.0*	*1794*	*25*	*1784*	*16*	*1773*	*19*	*100.5*
5.1	*1.26*	*907*	*953*	*1.05*	*2.2800*	*3.4*	*0.1209*	*2.6*	*0.77*	*0.1368*	*2.2*	*736*	*18*	*1206*	*24*	*2187*	*37*	*61.0*
5.3	*0.38*	*221*	*608*	*2.75*	*5.0477*	*2.1*	*0.2979*	*1.6*	*0.76*	*0.1229*	*1.4*	*1681*	*24*	*1827*	*18*	*1998*	*25*	*92.0*
6.2	*0.70*	*1147*	*1123*	*0.98*	*1.4295*	*2.7*	*0.0914*	*2.2*	*0.81*	*0.1134*	*1.6*	*564*	*12*	*901*	*16*	*1854*	*29*	*62.6*
7.2	*0.57*	*401*	*458*	*1.14*	*2.1122*	*2.5*	*0.1441*	*1.8*	*0.74*	*0.1063*	*1.7*	*868*	*15*	*1153*	*17*	*1737*	*30*	*75.3*
8.1	*0.00*	*645*	*596*	*0.92*	*1.8173*	*1.9*	*0.1395*	*1.6*	*0.81*	*0.0945*	*1.1*	*842*	*12*	*1052*	*13*	*1517*	*21*	*80.1*

[*] Concordant zircon. *Italics = zircon excluded from age calculation.*

[a] Fraction of the non-radiogenic ^{206}Pb in the analyzed zircon spot, where $f_{206} = [^{206}Pb/^{204}Pb]c / [^{206}Pb/^{204}Pb]s$ (c = common; s = sample).

[b] Th/U ratios and amount of Pb, Th and U (in ppm) are calculated relative to GJ-1 reference zircon.

[c] Corrected for background and within-run Pb/U fractionation and normalized to reference zircon GJ-1 (ID-TIMS values/measured value); $^{207}Pb/^{235}U = (^{207}Pb/^{206}Pb) * (^{238}U/^{206}Pb) * 137.88$.

[d] Rho is the error correlation defined as the quotient of the propagated errors of the $^{206}Pb/^{238}U$ and the $^{207}/^{235}U$ ratio.

[e] Corrected for mass-bias by normalising to GJ-1 reference zircon and common Pb using the model Pb composition of Stacey and Kramers (1975).

[f] Degree of concordance = ($^{206}Pb/^{238}U$ age / $^{207}Pb/^{235}U$ age) * 100, according to Horstwood et al. (2016).
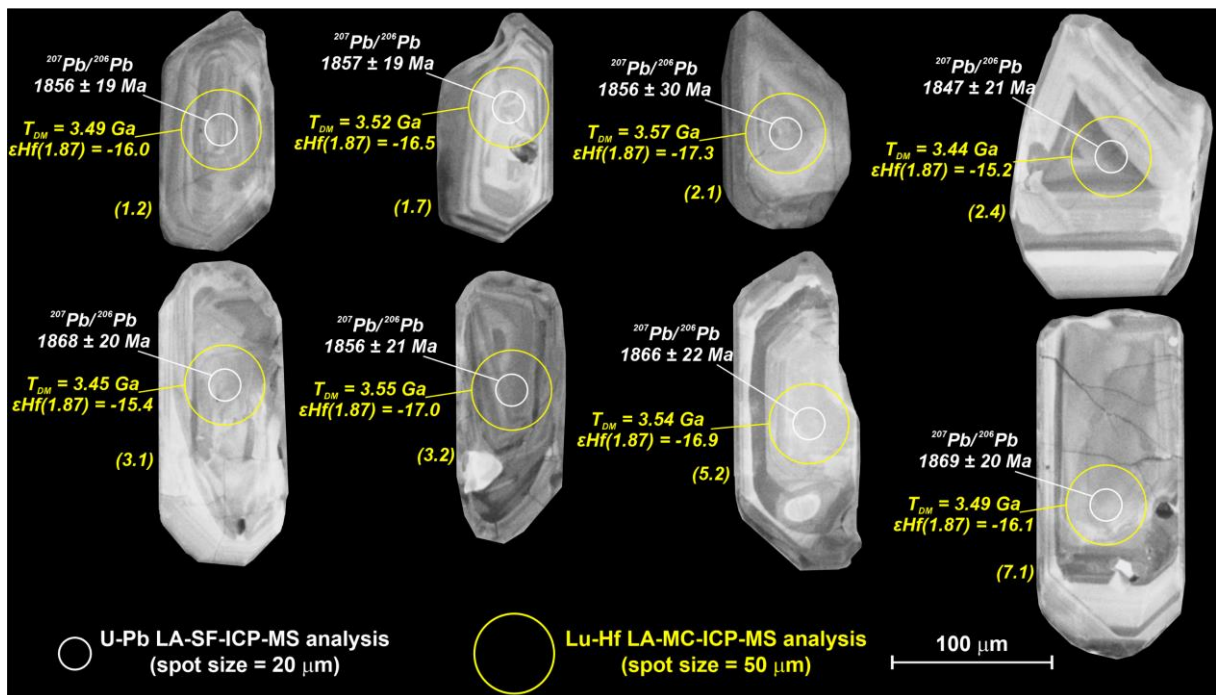
Figure 10 - Cathodoluminescence images of representative zircon grains from the Manda Saia granite, with their respective in situ U–Pb (^{207}Pb/^{206}Pb ages; white values) and Lu–Hf (ε_{Hf} and Hf-T$_{DM}{}^C$; yellow values) data. The numbers in parentheses correspond to the analyzed spots. (For interpretation of the references to color in this figure legend, the reader is referred to the web version of this article).
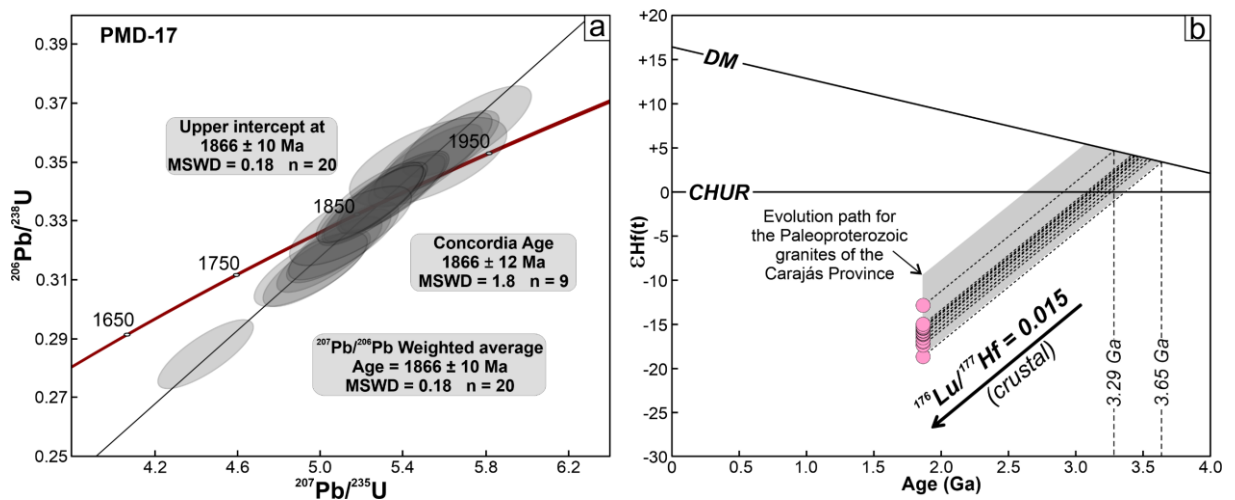
Figure 11 - Isotopic data for the Manda Saia granite: (a) Concordia diagram showing U–Pb analyses for zircon crystals; (b) evolution diagrams of the isotopic composition of $\varepsilon_{Hf}(t)$ vs. age (Ga). Values for the CHUR (uniform chondritic reservoir) are according to Bouvier et al. (2008) and those for DM (depleted mantle) are according to Andersen et al. (2009).

4.7 Lu–Hf ZIRCON ISOTOPES

The crystals with subconcordant to concordant U–Pb ages that produced the concordance curve (Fig. 11a) of the Manda Saia granite were analyzed by LA–MC–ICP–MS, and their data are shown in Table 4. The Hf isotopic analyses exhibit values of the ^{176}Hf/^{177}Hf ratio that initially vary between 0.281190 and 0.281317; all of them have strongly negative

values of $\varepsilon_{Hf}(t)$ from -12.89 to -18.68 and Hf-T_{DM}^{C} from the Paleoarchean (3.2–3.6 Ga), suggesting the incorporation of Archean crustal sources in their formation, with a long crustal residence time for the Manda Saia granite.

Table 4 - Lu–Hf isotopic data on zircon by LA–MC–ICP–MS. *Calculated from the ratio $^{176}Lu/^{177}Hf = 0.015$, mean value for the continental crust (Griffin et al., 2002).

Spot ID	$^{176}Hf/^{177}Hf$	2SE	$^{176}Lu/^{177}Hf$	2SE	$^{176}Yb/^{177}Hf$	2SE	$\varepsilon_{Hf}(0)$	$t_{(U-Pb)}$ (Ma)	$^{176}Hf/^{177}Hf_{(Zr,t)}$	$\varepsilon_{Hf}(t)$	T_{DM}^{C} (Ga)*
1.2	0.281315	0.000031	0.004842	0.000144	0.211717	0.003296	-52.0	1866	0.281143	-16.0	3.49
1.3	0.281234	0.000106	0.002046	0.000143	0.094739	0.005723	-54.9	1866	0.281161	-15.4	3.45
1.7	0.281197	0.000097	0.001941	0.000045	0.079596	0.002938	-56.1	1866	0.281129	-16.5	3.52
2.1	0.281317	0.000044	0.005949	0.000744	0.351993	0.031614	-51.9	1866	0.281106	-17.3	3.57
2.2	0.281222	0.000038	0.002025	0.000151	0.112524	0.006031	-55.3	1866	0.281150	-15.8	3.47
2.4	0.281249	0.000051	0.002380	0.000421	0.095655	0.007767	-54.3	1866	0.281165	-15.2	3.44
3.1	0.281315	0.000035	0.004347	0.000095	0.217129	0.003999	-52.0	1866	0.281160	-15.4	3.45
3.2	0.281224	0.000048	0.003034	0.000124	0.130344	0.004794	-55.2	1866	0.281116	-17.0	3.55
3.4	0.281255	0.000067	0.005237	0.000214	0.286923	0.009924	-54.1	1866	0.281069	-18.6	3.65
4.1	0.281190	0.000054	0.000880	0.000046	0.046860	0.003052	-56.4	1866	0.281159	-15.4	3.45
4.3	0.281259	0.000045	0.003404	0.000179	0.130759	0.006985	-53.9	1866	0.281139	-16.2	3.50
4.5	0.281282	0.000091	0.003712	0.000172	0.142918	0.005898	-53.1	1866	0.281151	-15.7	3.47
5.2	0.281243	0.000047	0.003552	0.000355	0.162590	0.010324	-54.5	1866	0.281117	-16.9	3.54
6.1	0.281297	0.000037	0.004125	0.000793	0.233357	0.029992	-52.6	1866	0.281150	-15.7	3.47
7.1	0.281202	0.000042	0.001715	0.000148	0.080653	0.006236	-56.0	1866	0.281141	-16.1	3.49
8.1	0.281267	0.000044	0.000993	0.000108	0.047739	0.002128	-53.7	1866	0.281232	-12.8	3.29
9.1	0.281214	0.000044	0.001183	0.000039	0.063385	0.002331	-55.6	1866	0.281172	-15.0	3.42

5 DISCUSSION

5.1 PETROLOGICAL AFFINITIES

The Manda Saia granite shows geochemical, mineralogical and textural affinities with the more evolved varieties that constitute the Paleoproterozoic granites from the Carajás province. All the studied granitic samples have high SiO_2 (>74 wt%) contents and very high FeO*/MgO (8.5–53.1), (K_2O+Na_2O)/CaO (9.0–30.6) and Rb/Sr ratios as well as very low Mg# (3.25–17.4). In addition, the plutons are composed of monzo- to syenogranitic rocks with low mafic mineral (> 5%) and allanite contents, a scarcity of magmatic titanite and the occurrence of later interstitial amphibole (common in reduced magmas). The presence of chlorite, fluorite and pegmatite pockets indicates the concentration of volatiles during the formation of Manda Saia granite rocks, which influenced the crystallization of amphibole in granitic magmas (Dall'Agnol et al., 1999b). In magmas that are rich in fluorine and REEs, Ca amphiboles (i.e., hastingsite) can crystallize as late phases close to the solidus (Siegel et al., 2017). Considering such aspects, the studied plutons show affinities with the granites of the Velho Guilherme and Serra dos Carajás suites. Regarding the granites of the Jamon suite, the Manda Saia granite differs mainly from their less evolved facies, which are marked by the frequent presence of early amphibole associated with calcic plagioclase aggregates and high ferromagnesian mineral contents (5–20%), where magmatic titanite is a common phase and is coupled with magnetite, ilmenite, and allanite (Oliveira et al., 2009). The Manda Saia granite contains a tiny amount of

magnetite that resembles the biotite-bearing leucogranite related to the final stages of the construction of the plutons of the Jamon suite.

To reinforce the petrological affinities attributed to the Manda Saia granite, magnetic susceptibility data were obtained and compared with those of other plutons from the Carajás province. The magnetic susceptibility values (see supplementary data table A) are related to the modal content of magnetite, indicating that the Manda Saia granite is close to the reduced granites, with a magnetic susceptibility interval between log -4.2 and -2.2 $\times 10^{-3}$ SI (Fig. 12). The limits of their magnetic susceptibility values are almost completely coincident with those of the moderately to strongly reduced granites of the Serra dos Carajás and Velho Guilherme suites. On the other hand, such values differ widely from those of the oxidized granites of the Jamon suite.

	Paleoproterozoic suites			Manda Saia granite
	Jamon	Serra dos Carajás	Velho Guilherme	
MS interval $(x10^{-3})$	1.3-1.7	0.05-0.32	0.63-4	0.017-3.9
Opaques (vol%)	2	0.1	0.7	0.05-0.2
Primary magnetite	Abundant	Variable	Common in amphibole-bearing facies	Sparce
Ilmenite	Common in monzogranites	Common to all facies	Common to all facies	Variable
Hematite/Martite	Common	Common	Common	Absent
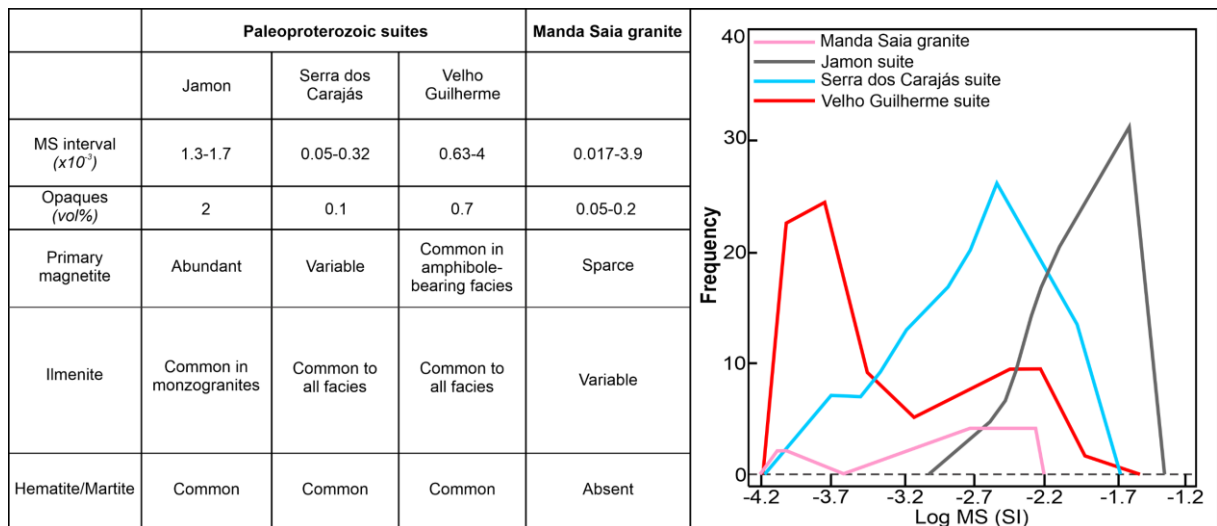
Figure 12 - Comparative magnetic susceptibility data obtained for the Manda Saia granite and Paleoproterozoic suites from the Carajás province (comparison data are obtained from Santos et al. (2013).

The Fe* index was used by Dall'Agnol and Oliveira (2007) to distinguish A-type granites with an oxidized nature from those with a reduced nature. In the diagram of Al_2O_3 vs. Fe* (Fig. 9e), the behavior of the analyzed samples allows us to distinguish them as weakly oxidized to moderately reduced. The PMD-15 sample, in turn, has the highest value for the Fe* index (~1.0), similar to what is found in heavily reduced granites.

The biotite from Manda Saia pluton has iron rich compositions (see supplementary data table B), whose crystals from PMD-15 sample approaching final member Annite (Fig. 13a), and they are considered as neoformed phases (Fig. 13b). According to Nachit et al. (2005) neoformation of biotite is resulting from circulation of late- to post-magmatic fluids from older rocks nearby. In the ternary Fe^{2+}- Fe^{3+}- Mg diagram (Wones and Eugster, 1965), all primary

biotite analyses plot below the NNO (nickel-nickel oxide) buffer and lie on the ilmenite series, consistent with the QFM (quartz–fayalite–magnetite) buffer (Fig. 13c). However, in that pluton, magnetite and ilmenite are scarce and are therefore different from the magnetite and ilmenite series of Ishihara (1977). In addition, biotite has an Fe/(Fe + Mg) ratio (0.60 to 0.75) that is different from both magnetite- and ilmenite-series granites from the United States, as well as those reduced from Fennoscandia and Laurentia (Fig. 13d). The composition of the biotite is comparable to that of the Serra dos Carajás suite, as well as the more evolved facies of the oxidized Jamon suite and the less evolved facies of the reduced Velho Guilherme suite. The $Al^{IV} + Al^{VI}$ Fe/(Fe+Mg) diagram indicates that the Manda Saia granite crystallized under moderate fO_2 conditions (~NNO+0.5).

The largest petrogenic affinity of the Manda Saia granite with the moderately oxidized granites of the Serra dos Carajás suite is also observed from their REEs and multielement distribution patterns. It is more enriched in heavy REEs compared to the pattern presented by the Jamon Suite granites (Fig. 8b). Except for the PMD-15 sample, the Manda Saia granite is distinguished from the Velho Guilherme suite by the contrast in magnitudes of the negative Eu, Sr, P and Ti anomalies, which are strongly accentuated in reduced granites (Fig. 8a).

5.2 ORIGIN OF THE MANDA SAIA GRANITE-FORMING MAGMA

A-type granites can provide important information about the extensional magmatic processes within the lithosphere and their contribution to the growth of the upper continental crust. Some petrogenetic models have been proposed for the generation of such granites: i) crustal anatexia caused by mafic underplating (Rämö & Happala 1995); ii) fractionation of alkaline basalts derived from the mantle (Turner et al., 1992); iii) low degree of partial melting of an anhydrous granulitic residue from the lower crust, enriched in F and/or Cl, from which a granitic melt was previously extracted (King et al., 1997); iv) melting of calcium-alkaline rocks under low pressure at shallow crustal levels (Patiño Douce, 1997); v) hybridization between anatectic granite and mafic magmas derived from the mantle (Mingram et al., 2000); and vi) partial melting of tonalites and granodiorites (Creaser et al., 1991). For the Paleoproterozoic ferroan calc-alkaline granites from the Carajás province, Dall'Agnol et al. (2005) proposed Archean sources where a quartz–dioritic source was assumed for the oxidized granites (magnetite series) of the Jamon suite, while for the magma forming the reduced granites (ilmenite series) from the Velho Guilherme suite, a more enriched source is suggested, including components of sedimentary rocks. The plutons of the Serra dos Carajás suite either

had a somewhat more mafic source than the Velho Guilherme suite or were derived via a higher degree of melting.
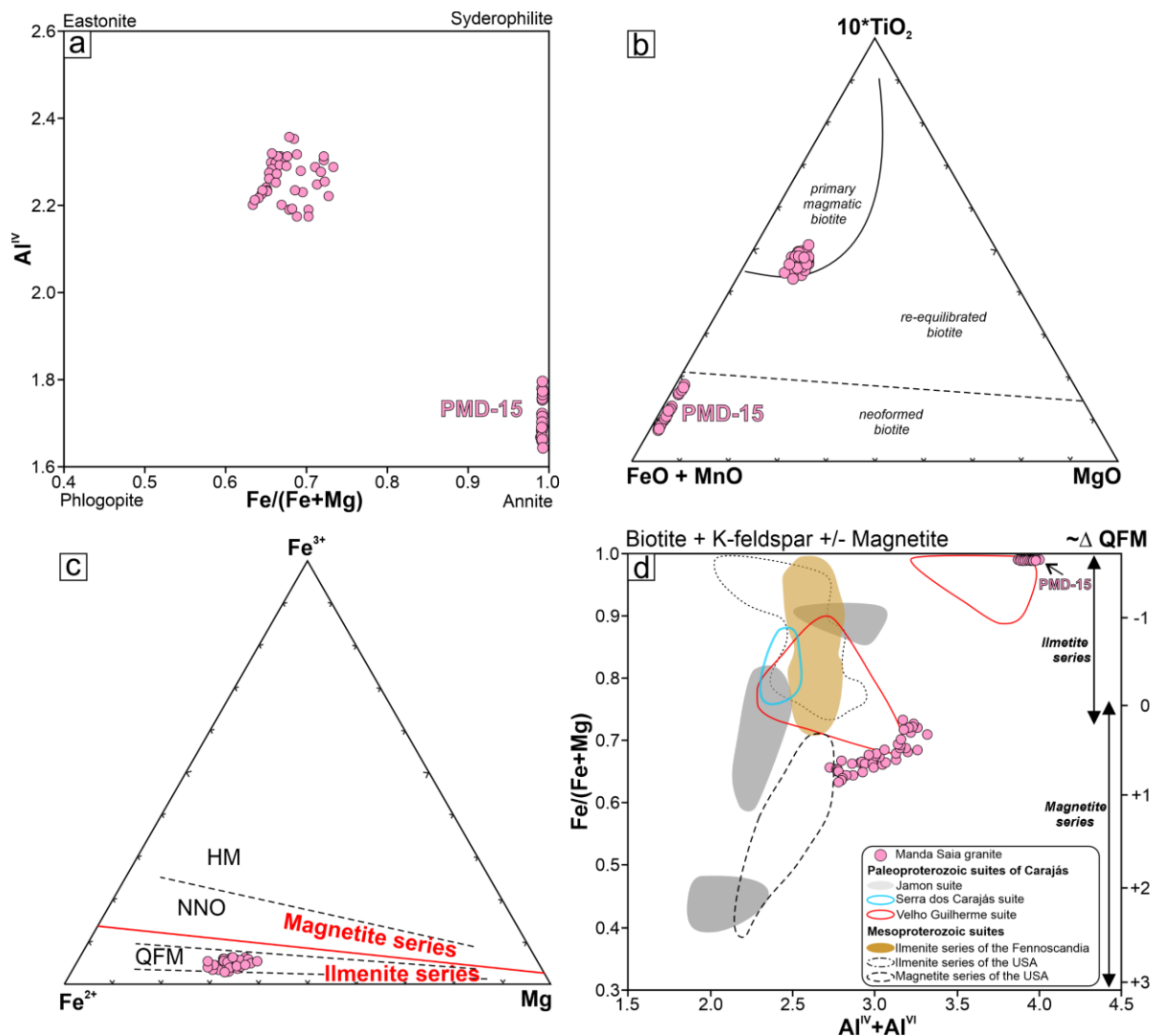
Figure 13 - Petrological affinity of the Manda Saia granite: (a) Al^{IV} vs. $Fe/(Fe + Mg)$ diagram (Rieder, 1998); (b) ternary diagram $10*TiO_2 - FeO + MnO - MgO$ in wt % (Nachit et al., 2005); (c) ternary $Fe^{2+}-Fe^{3+}-Mg$ diagram along with the fO_2 buffers of Wones and Eugster (1965); the three oxygen fugacity buffers include quartz–fayalite–magnetite (QFM), nickel–nickel oxide (NNO), and hematite–magnetite (HM); (d) $Fe/(Fe + Mg)$ vs. $Al^{IV} + Al^{VI}$ diagram, showing the biotite composition of Manda Saia granite and that of A-type granites of the Carajás suites (Dall'Agnol et al., 2005); A-type Mesoproterozoic granites from the United States according to Anderson and Bender (1989): dashed fields are the magnetite-series granites based on the Bowmans Wash, Davis Dam, Fort Huachuca, Gold Butte, Holy Moses, Newberry and Parker Dam plutons; dotted fields are the ilmenite-series granites based on the Pikes Peak (Barker et al., 1975) and Sherman (Frost et al., 1999) batholiths; the golden yellow field is the ilmenite series based on the Obbnäs and Bodom plutons from Fennoscandia (Kosunen, 2004). (For interpretation of the references to color in this figure legend, the reader is referred to the web version of this article).

Numerous mass-balance calculations have been performed to find the nature of the Manda Saia granite source and the processes that the magma underwent until its eventual crystallization (Tables 5-7), utilizing the software GENESIS 4.0 which adapts the relative

proportions of residual minerals from the source to create the composition of the expected melt. The quality of the calculated data is trustful if the sum of the squared residuals ($\sum R^2$) ≤ 1.2 and permit us to continue to trace element modeling using Excel sheets created by the authors based on the equilibrium partial melting equation (Wilson, 1989, Equation (1)):

$$\frac{CL}{C0} = \frac{1}{F + D - FD}$$

where *CL* (liquid) and *C*0 (solid) are the trace element concentrations, F is the weight fraction of melt formed and D is the bulk distribution coefficient for the residual solids at the moment when melt is removed from the system. The mineral/liquid partition coefficients (Kd) used in the modeling were obtained from the online database https://earthref.org/KDD/, and they are presented in the Supplementary Data (Table C).

Table 5 - Modeling major and trace element compositions and residual mineral assemblages for generation of the Manda Saia granite protolith by partial melting of Arco Verde tonalite.

	F-62/92-26 (C$_0$)[a]	Residue (Cs)	Composition of minerals					Calculated	PMD-19
	Tonalite[b]	Bulk	Pl[f]	Qz	Bt[c]	Mag[d]	Ilm[d]	Magma (CL')	Biotite syenogranite (CL)[b]
			62.02%	28.91%	6.69%	2.09%	0.28%		
Major elements (weight %)									
SiO$_2$	70.47	69.16	60.67	100.00	39.11	0.00	0.00	76.44	76.42
TiO$_2$	0.32	0.33	0.00	0.00	2.57	0.00	50.00	0.22	0.20
Al$_2$O$_3$	15.61	16.20	24.34	0.00	16.41	0.00	0.00	12.69	12.65
FeO*	3.24	3.61	0.14	0.00	19.25	100.00	50.00	1.42	1.40
MnO	0.04	0.08	0.10	0.00	0.22	0.00	0.00	0.02	0.05
MgO	0.80	0.79	0.00	0.00	11.80	0.00	0.00	0.25	0.12
CaO	3.25	4.20	6.77	0.00	0.00	0.00	0.00	0.53	0.90
Na$_2$O	4.87	4.88	7.88	0.00	0.00	0.00	0.00	3.43	3.13
K$_2$O	1.40	0.75	0.00	0.00	10.62	0.00	0.00	5.00	5.13
Trace elements (ppm)									
Ba	234.0							530.9	686.0
Rb	75.8							304.0	339.0
Sr	255.0							102.0	95.9
Y	9.1							32.7	37.0
Zr	239.0			$\sum R^2 = 0.263$				328.7	215.0
Nb	14.0			Melt fraction				28.7	36.3
La	62.0			F = 18%				128.9	122.0
Ce	109.1							225.9	217.0
Nd	34.6							60.4	62.7
Sm	5.1							8.7	8.7
Eu	0.9							1.4	1.3
Gd	3.8							5.8	5.7
Yb	0.7							3.6	4.7
Lu	0.1							0.6	0.7

$\sum R^2$ = sum of the squared residuals. All iron is reported as FeO. [a] Althoff (1996), [b] Original oxide values recast to 100%. [c] Leite (2001), [d] Martin (1987), Bt – biotite, Ilm – ilmenite, Mag – magnetite, Pl – plagioclase, Qz – quartz.

An examinations of geochemical modelling approaches has shown that Mesoarchean Arco Verde (F-62/92-26) and Caracol (AABG–34) tonalite gneisses have compositions appropriated for the generation of the Manda Saia granite (PMD–19) with a partial melting rate of 18% (Fig. 14a,b), leaving a residual assembly consisting of plagioclase (62%), quartz (22–

28%), biotite (6–14%), magnetite (1–2%) and ilmenite (0.3%). In addition, considering the PMD-15 sample present affinity to the reduced magmas akin to the Velho Guilherme suite and strongly peraluminous character, geochemical calculation was performed to tracing its source.

Table 6 - Modeling major and trace element compositions and residual mineral assemblages for generation of the Manda Saia granite protolith by partial melting of Caracol tonalite.

	AABG-34 (C$_0$)[a]	Residue (Cs)	Composition of minerals					Calculated	PMD-19
	Tonalite[b]	Bulk	Pf	Qz	Bt[c]	Mag[d]	Ilm[d]	Magma (CL')	Biotite syenogranite (CL)[b]
			61.60%	22.43%	14.43%	1.32%	0.22%		
Major elements (weight %)									
SiO$_2$	68.82	67.22	63.79	100.00	38.10	0.00	0.00	76.37	76.42
TiO$_2$	0.42	0.53	0.00	0.00	2.90	0.00	50.00	0.15	0.20
Al$_2$O$_3$	15.89	16.78	23.15	0.00	17.46	0.00	0.00	12.50	12.65
FeO*	3.94	4.56	0.00	0.00	21.69	100.00	50.00	1.35	1.40
MnO	0.06	0.05	0.00	0.00	0.36	0.00	0.00	0.06	0.05
MgO	1.07	1.29	0.00	0.00	8.96	0.00	0.00	0.11	0.12
CaO	3.10	3.35	5.43	0.00	0.00	0.00	0.00	1.09	0.90
Na$_2$O	4.41	4.62	7.49	0.00	0.00	0.00	0.00	3.19	3.13
K$_2$O	2.30	1.60	0.14	0.00	10.50	0.00	0.00	5.20	5.13
Trace elements (ppm)									
Ba	402.0							596.9	686.0
Rb	127.3							322.8	339.0
Sr	259.2							103.4	95.9
Y	21.0							35.5	37.0
Zr	148.7			$\Sigma R^2 = 0.076$				224.8	215.0
Nb	11.3			Melta fraction				15.6	36.3
La	27.0			F = 18%				105.9	122.0
Ce	62.9							208.9	217.0
Nd	26.6							64.0	62.7
Sm	4.9							9.1	8.7
Eu	1.0							1.3	1.3
Gd	4.6							6.6	5.7
Yb	1.6							4.7	4.7
Lu	0.2							0.8	0.7

$\Sigma R2$ = sum of the squared residuals. All iron is reported as FeO. [a] Ronaib (2013), [b] Original oxide values recast to 100%. [c] Leite (2001), [d] Martin (1987), Bt – biotite, Ilm – ilmenite, Mag – magnetite, Pl – plagioclase, Qz – quartz.

Table 7 - Modeling major and trace element compositions and residual mineral assemblages for generation of the Manda Saia granite protolith by partial melting of 80% Arco Verde tonalite and 20% metasedimentary.

	AM-04[a]	MCS-43B[b]	Modeled source	Residue (Cs)	Composition of minerals						Calculated	PMD-15
	Tonalite	Metasedimentary	80% tonalite + 20% metasedimentary[c]	Bulk	Pl[d]	Qz	Bt[d]	Amp[d]	Mag[e]	Ilm[e]	Magma (CL')	Biotite syenogranite (CL)[c]
					49.08%	31.36%	14.12%	4.10%	0.79%	0.55%		
Major elements (weight %)												
SiO$_2$	66.22	74.88	69.61	68.46	60.60	100.00	39.00	45.17	0.00	0.00	76.68	76.65
TiO$_2$	0.47	0.44	0.47	0.51	0.00	0.00	1.59	0.27	0.00	50.00	0.04	0.01
Al$_2$O$_3$	15.11	11.90	14.82	14.90	24.72	0.00	17.00	8.96	0.00	0.00	13.76	13.67
FeO*	4.45	3.38	4.34	4.91	0.13	0.00	20.20	22.76	100.00	50.00	0.57	0.54
MnO	0.07	0.07	0.07	0.06	0.00	0.00	0.26	0.67	0.00	0.00	0.16	0.17
MgO	1.50	0.13	1.51	1.97	0.00	0.00	11.48	8.05	0.00	0.00	-0.18	0.01
CaO	3.90	1.61	3.52	3.86	6.86	0.00	0.00	12.00	0.00	0.00	0.33	0.28
Na$_2$O	3.60	2.94	3.55	3.73	7.49	0.00	0.00	1.20	0.00	0.00	4.29	4.58
K$_2$O	2.26	1.23	2.10	1.59	0.16	0.00	10.40	0.94	0.00	0.00	4.26	4.09
Trace elements (ppm)												
K	18760.3	10210.2	17050.3								44867.0	33536.0
Rb	136.7	337.9	176.9								656.1	1055.0
Y	60.3	3.5	48.9								57.9	63.9
Zr	167.2	17.7	137.3								186.9	107.0
Hf	4.7	2.7	4.3								17.0	15.5
Th	9.5	5.2	8.6			$\Sigma R^2 = 0.186$					20.1	19.7
U	3.6	0.8	3.0			Melt fraction					11.7	9.9
La	34.2	26.1	32.6			F = 14%					26.8	31.7
Ce	52.1	30.4	47.8								59.5	63.3
Nd	29.5	11.7	25.9								22.4	23.0
Sm	5.9	2.0	5.1								4.0	3.5
Eu	1.1	0.6	1.0								0.2	0.0
Er	4.9	0.9	4.1								4.0	4.4
Yb	4.9	1.1	4.1								17.0	16.8
Lu	0.7	0.2	0.6								3.3	3.4

ΣR^2 = sum of the squared residuals. All iron is reported as FeO. [a] Almeida (2010), [b] Sousa (2020) [c] Original oxide values recast to 100% [d] Leite (2001), [e] Martin (1987), Amp – Amphibole, Bt – biotite, Ilm – ilmenite, Mag – magnetite, Pl – plagioclase, Qz – quartz.

The results shown that reduced magmas are generated by partial melting of a source composite by Mesoarchean Arco Verde tonalite (AM-04) with contribution of metasedimentary rocks from Greenstone Belt Sapucaia (MCS-43B) leaving amphibole (4.1%) as residual mineral (Fig. 14c). These results are in accordance with the Lu–Hf isotopic data with strongly negative ε$_{Hf}$ values (-12 to -18) and T$_{DM}$ from 3.2 Ga to 3.6 Ga, suggesting that the Manda Saia Granite parent magmas were derived from Meso- to Paleoarchean TTG crust (Fig. 11b).
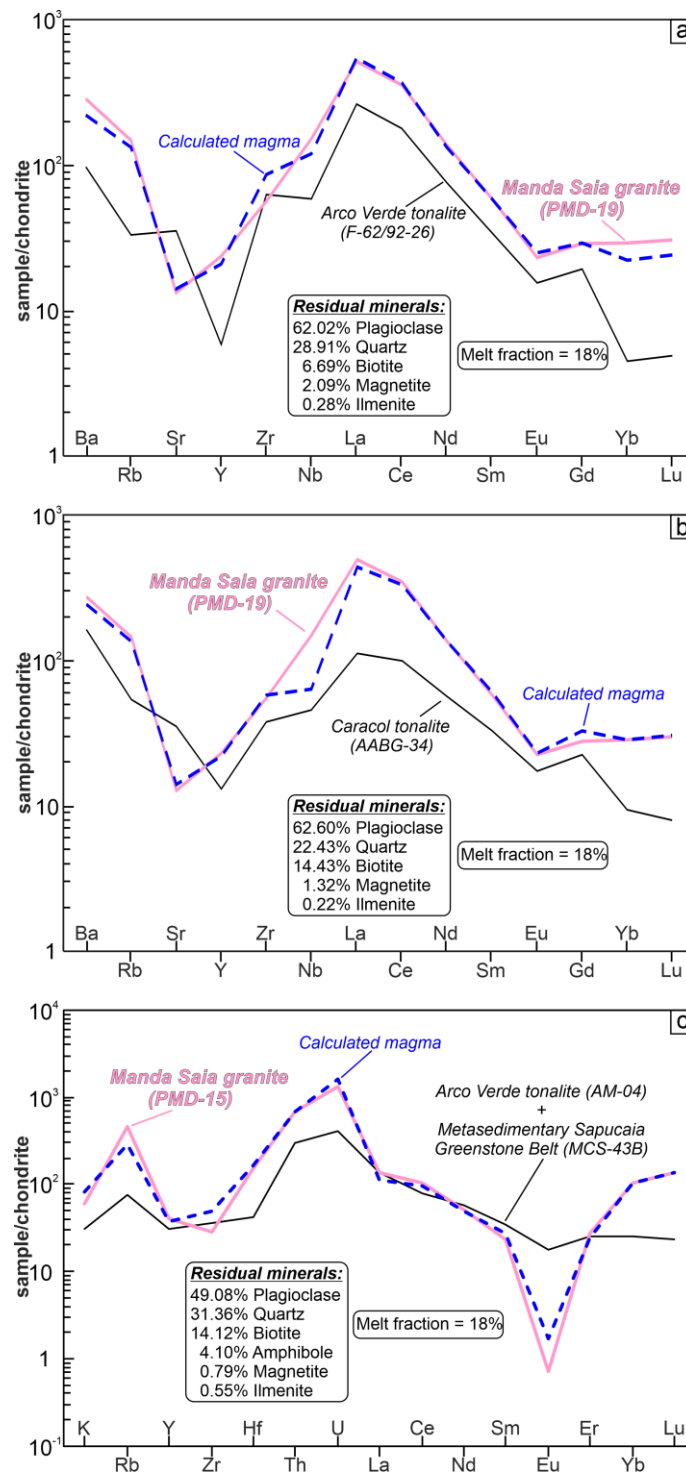
Figure 14 - Trace element models for generation of the Manda Saia granite from a tonalitic protolith generated by partial melting: (a) Arco Verde tonalite; (b) Caracol tonalite and (c) partial melt of 80% Arco Verde tonalite and 20% metasedimentary rock. Chondrite (C1) normalization values are from McDonough and Sun (1995).

5.3 CONSIDERATIONS ABOUT THE ASCENSION AND EMPLACEMENT OF THE MANDA SAIA GRANITE

The Manda Saia granite is intrusive in Mesoarchean granitoids and metabasalts of the greenstone belt sequence (Fig. 3), whose regional dominant foliation is truncated at the contact

with the stock. Their difference in ~1.0 Ga ages, as well as the frequent presence of angular xenoliths (host rocks) in the inner portions of the pluton and the lack of orientation of both sets of enclaves and granite varieties indicate that the Manda Saia granite magma was emplaced at shallow crustal levels (epizone) in the absence of regional strain. This high-viscosity contrast also assumes that the magma had a low crystal/liquid ratio at the time of emplacement.

The Manda Saia granite is composed of circular or oval-shaped plutons with well-defined outer limits on geological maps. The occasional contacts delimited by extensive straight lineaments, with some angular recesses, are coincident with the regional lineament systems (NW–SE, N–S and NE–SW) and suggest that the control in the emplacement was exerted by discontinuities prior to the intrusion (Fig. 3d). The occurrence of ring structures outlined by densely porphyritic rocks suggests that the main preexisting fracturing network was active until the end of massif construction, providing conduits for more evolved magma batches. In this way, the geological features suggest that brittle deformation played an important role during the emplacement of the magmas that built the Manda Saia granite and dike swarm associated with Paleoproterozoic magmatism.

The controversy related to the transport of felsic magmas started when some authors restricted the performance of diapirism, which was until then considered the main ascent mechanism, due to some limiting physical parameters (Olivera et al., 2010). Diapirism requires anomalously hot crust to be considered an efficient magma transport process. It becomes an even more impracticable mechanism in shallow crust since the ductile structures observed in the host rocks around the pluton are not recognized as generated by the passage of a diapir in experimental models (Mahon et al., 1988).

The contact relationships of the Manda Saia granite with its country rocks are analogous to those described for the other plutons from Paleoproterozoic A-type granite suites. By reconciling the tabular geometry (lacoliths) inferred from the batholiths of the Jamon suite (Oliveira et al., 2008), the rheological behavior of its country rocks and the reduced or negligible influence of regional strain during the emplacement of the Manda Saia granite, it is suggested that the transport of the magma occurred through dikes (Fig. 3d). Deep faults served as a channel for magma ascent, and tectonic discontinuities would represent zones of weakness that favored emplacement at shallow crustal levels (~1.0 ± 0.5 kbar). The arrangement of these plutons along a belt that follows the general trend defined by swarms of felsic and mafic dikes,

from WNW–ESE to NNW–SSE, and that coexist with A-type plutons, indicates that they were emplaced in an extensional tectonic setting following the trend of NNE–SSW to ENE–WSW.

Temperatures needed for the extraction of melts originating during vapor-absent partial melting of granodiorite and tonalite are high (900-950 °C; Creaser et al., 1991). The heat required to reach these high temperatures can be generated by the intrusion and crystallization of mantle-derived melts into the crust, by high geothermal gradients characteristic of continental crust in extension, or by a combination of these factors. In this scenario, the magma forming the A-type granites from the Carajás province initiated crystallization at a temperature of ~870 °C and high pressure (> 6 kbar), which gradually decreased to a temperature of ~700 °C and a pressure of 3.2 ± 0.7 kbar in the final crystallization/emplacement stages (Dall'Agnol et al., 2005). According to thermometry Equation provided after Watson and Harrison (1983), zircon crystallization temperature of the Manda Saia intrusions was calculated from 815 to 744 °C.

The extensional tectonics suggested for the emplacement of the Manda Saia granite, as well as for the other A-type granites in the Carajás province, can be interpreted to be a result of the fragmentation of a Paleoproterozoic supercontinent at ~2.0 Ga associated with underplating of mantle magmas (Rämö et al., 2002).

6 CONCLUSIONS

The Manda Saia granite has a geochemical signature of evolved ferroan peraluminous A-type granites related to an intraplate setting. Their FeOt/(FeOt+MgO) ratios for both whole rocks and biotite and their REE patterns are analogous to those found for the moderately oxidized granites of the Serra dos Carajás suite. The limits of magnetic susceptibility, as well as the scarcity of magmatic titanite and magnetite, denounce the moderately oxidized character of the Manda Saia granite that resembles the biotite-bearing leucogranite of ambiguous affinity that is related to the final construction stages of the Jamon suite oxidized plutons (magnetite series) and the less evolved reduced pluton (ilmenite series) rocks from the Velho Guilherme suite. In addition, biotite has an Fe/(Fe + Mg) ratio (0.89 to 0.91) that is different from both magnetite- and ilmenite-series granites elsewhere in the world.

Geochemical modeling suggests that the Manda Saia granite was generated from partial melting of quartz–feldspar rocks with similar compositions to the Arco Verde or Caracol tonalites of the Rio Maria domain. A melting rate of 18% and a residual assemblage composed

of plagioclase, quartz, biotite, magnetite, and ilmenite are required to produce shallow granitic plutons.

The U–Pb analyses of zircons provided an age of crystallization of 1866 ± 10 Ma, which is coincident with those of the other Paleoproterozoic granites of the Carajás province. Lu–Hf isotopic data indicate strongly negative ε_{Hf} values ranging from -12 to -18 and Hf-T_{DM}^{C} ages from 3.2 Ga to 3.6 Ga, indicating that the Manda Saia granite parent magmas were derived from Meso- to Paleoarchean TTG crust that represents a deeper and older crust in relation to those exposed in the Carajás province (3.0 to 3.2 Ga). The results presented in this paper attest to the importance of the Archean crust for the origin of Paleoproterozoic granites, whose emplacement at shallow crustal levels was given through a dike feeding system as a consequence of related extensional tectonics.

ACKNOWLEDGMENTS

REFERENCES

Almeida, J.A.C., 2010. Geologia, geoquímica, geocronologia e petrogênese das suítes TTG e dos leucogranitos arqueanos do Terreno Granito-Greenstone de Rio Maria, Sudeste do Cráton Amazônico. Programa de Pós-Graduação em Geologia e Geoquímica, Instituto de Geociências, Universidade Federal do Pará, Belém, 208p. Dr. Thesis (in Portuguese).

Althoff, F.J., 1996. Étude pétrologique et structurale des granitoïdes de Marajoara (Pará, Brésil): leur rôle dans l'évolution archéenne du craton Amazonien (2.7– 3.2 Ga). Université Henri Poincaré, Nancy I, France. 296p. Dr. Thesis. (in French).

Andersen, T., Andersson, U.B., Graham, S., Aberg, G., Simonsen, S.L., 2009. Granitic magmatism by melting of juvenile continental crust: new constraints on the source of Paleoproterozoic granitoids in Fennoscandia from Hf isotopes in zircon. J. Geol. Soc. 166, 233-247.

Anderson, J.L., Bender, E.E., 1989. Nature and origin of Proterozoic A-type granitic magmatism in the southwestern United States of America. Lithos 23, 19– 52.

Antonio, P.Y.J., D'Agrella-Filho, M.S., Trindade, R.I.F., Nédélec, A., Oliveira, D.C., Silva, F.F., Roverato, M., Lana, C., 2017. Turmoil before the boring billion: Paleomagnetism of the 1880–1860 Ma Uatumã event in the Amazonian craton. Gondwana Res. 49, 106–129.

Arndt, N.T., 2013. The formation and evolution of the continental crust: Geochemical Perspectives, 2(3):405–533.

Avelar, V.G., 1996. Geocronologia Pb-Pb por evaporação em monocristal de zircão, do magmatismo da região de Tucumã, SE do Estado do Pará, Amazônia oriental. Federal University of Pará. Dissertation. Graduated Program on Geology and Geochemistry. Institute of Geosciences, pp. 199 (in Portuguese).

Barbosa, A.A., Lafon, J.M., Neves, A.P., Vale, A.G., 1995. Geocronologia Rb–Sr e Pb–Pb do Granito Redenção, SE do Pará: implicações para a evolução do magmatismo proterozóico da região de Redenção. Boletim do Museu Paraense Emílio Goeldi. Cien. Terra 7, 147– 164 (in Portuguese).

Barker, F., Wones, D.R., Sharp, W.N., Desborough, G.A., 1975. The Pikes Peak batholith, Colorado Front Range, and a model for the origin of the gabbro–anorthosite–syenite– potassic granite suite. Precambrian Research 2, 97– 160.

Black, L.P., Gulson, B.L., 1978. The age of the Mud Tank carbonatite, strangways range, northernTerritory. BMR Journal of Australian Geology and Geophysics 3, 227-232.

Bouvier, A., Vervoort, J. D., & Patchett, P. J., 2008. The Lu–Hf and Sm–Nd isotopic composition of CHUR: constraints from unequilibrated chondrites and implications for the bulk composition of terrestrial planets. Earth and Planetary Science Letters, 273(1-2), 48-57.

Chappell, B.W., White, A.J.R., 1974. Two contrasting granite types. Pacific Geology, 8:173-174.

Chappell, B.W., Bryant, C.J., Wyborn, D., 2012. Peraluminous I-type granites. Lithos, 153:142–153.

Chemale Jr. F., Kawashita K., Dussin I.V., Ávila J.N., Justino D., Bertotti A., 2012. U-Pb zircon in situ dating with LA-MC-ICP-MS using a mixed detector configuration. Anais da Academia Brasileira de Ciências, 84(2):275-295.

Chu, N.C., Taylor, R.N., Chavagnac, V., Nesbitt, R.W., Boella, R.M., Milton, J.A., German, C.R., Bayon, G., Burton, K., 2002. Hf isotope ratio analysis using multicollector inductively coupled plasma mass spectrometry: an evaluation of isobaric interference corrections. J. Anal. Atomic Spectrom. 17, 1567-1574.

Creaser, R.A., Price, R.C., Wormald, R.J., 1991. A-type granites revisited: assessment of a residual-source model. Geology, 19(2):163–166.

Dall'Agnol, R., Rämö, O.T., Magalhães, M.S., Macambira, M.J.B., 1999a. Petrology of the anorogenic, oxidised Jamon and Musa granites, Amazonian Craton: implications for the genesis of Proterozoic A-type granites. Lithos 46, 431–462.

Dall'Agnol, R., Scaillet, B., Pichavant, M., 1999b. An experimental study of a lower Proterozoic A-type granite from the eastern Amazonian craton, Brazil. J. Petrol. 40, 1673–1698.

Dall'Agnol, R., Teixeira, N.P., Rämö, O.T., Moura, C.A.V., Macambira, M.J.B., Oliveira, D.C., 2005. Petrogenesis of the Paleoproterozoic, rapakivi, A-type granties of the Archean Carajás Metallogenic Province, Brazil. Lithos, 80(1-4), 102-129.

Dall'Agnol R., Oliveira, D.C., 2007. Oxidized, magnetite-series, rapakivi-type granites of Carajás, Brazil: Implications for classification and petrogenesis of A-type granites. Lithos, 93(3-4):215–233.

Dall'Agnol, R., Oliveira, D.C., Guimarães, F.V., Gabriel, E.O., Feio, G.R.L., Lamarão, C.N., Althoff, F.J., Santos, P.A., Teixeira, M.F.B., Silva, A.C., Rodrigues, D.S., Santos, M.J.P., Silva, C.R.P., Santos, R.D., Santos, P.J.L., 2013. Geologia do Subdomínio de Transição do Domínio Carajás – Implicações para a evolução arqueana da Província Carajás - Pará. SBG, Simpósio de Geologia da Amazônia. vol. 13 CD-ROM, Anais, Belém. (in Portuguese).

Debon F., Le Fort P., 1983. A chemical–mineralogical classification of common plutonic rocks and associations. Transactions of the Royal Society of Edinburgh, Earth Sciences, 73(3):135–149.

Frei, D., Gerdes, A., 2009. Accurate and precise in-situ zircon U-Pb age dating with high spatial resolution and high sample throughput by automated LA-SF-ICP-MS. Chemical Geology, 261(3–4): 261–270.

Frost, C.D., Frost, B.R., Chamberlain, K.R., Edwards, B., 1999. Petrogenesis of the 1.43 Ga Sherman batholith, SE Wyoming, USA: a reduced, rapakivi-type anorogenic granite. Journal of Petrology 40, 1771–1802.

Frost, B.R., Barnes C., Collins W., Arculus, R., Ellis D., Frost, C., 2001. A chemical classification for granitic rocks. Journal of Petrology, 42(11):2033–2048.

Griffin, W.L., Wang, X., Jackson, S.E., Pearson, N.J., O'Reilly, S.Y., 2002. Zircon geochemistry and magma mixing, SE China: in-situ analysis of Hf isotopes, Tonglu and Pingtan igneous complexes. Lithos 61, 237-269.

Ishihara, S., 1977. The magnetite-series and ilmenite-series granitic rocks. Mining Geology, 27(145), 293–305.

Jackson, S.E., Pearson, N.J., Griffin, W.L., Belousova, E.A., 2004. The application of laser ablation-inductively coupled plasma-mass spectrometry to in situ U-Pb zircon geochronology. Chemical Geology, 211: 47–69.

Janoušek, V., Farrow, C.M., Erban, V., 2006. Interpretation of whole-rock geochemical data in igneous geochemistry: introducing Geochemical Data Toolkit (GCDkit). Journal of Petrology, 47(6), 1255-1259.

King, P.L., White, A.J.R., Chappell, B.W., Allen, C.M., 1997. Characterization and origin of aluminous A-type granites from the Lachlan Fold Belt, southeastern Australia. Journal of Petrology, 38(3):371-391.

Kosunen, P.J., 2004. Petrogenesis of mid-Proterozoic A-type granite: Case Studies from Fennoscandia (Finland) and Laurentia (New Mexico). Department of Geology, University of Helsinki, Finland, Dr. Thesis.

Lamarão, C.N., Pinho, S.C.C., Paiva Júnior, A.L., Galarza-Toro, M.A., 2012. Mineralogy and geochemistry of the Paleoproterozoic, tin mineralized Bom Jardim Granite of the Velho Guilherme Suite, eastern Amazonian Craton. Journal of South American Earth Sciences 38, 159–173.

Leite, A.A.S., 2001. Geoquímica, petrogênese e evolução estrutural dos granitoides arqueanos da região de Xinguara, SE do Cráton Amazônico. Belém, Universidade Federal do Pará, Centro de Geociências, Brazil, Dr. Thesis. (in Portuguese).

Le Maitre, R.W., Streckeisen, A., Zanettin, B., Le Bas, M.J., Bonin, B., Bateman, P., Bellieni, G., Dudek, A., Efremova, J., Keller, J., Lameyre, J., Sabine, P.A., Schmidt, R., Sørensen, H., Woolley, A.R., 2002. Igneous rocks. A classification and glossary of terms. In: Recommendations of the International Union of Geological Sciences Subcommission on the Systematics of Igneous Rocks. Cambridge University Press, Cambridge, p. 252.

Lima, P.H.A., 2011. Geologia, petrografia e geocronologia do Granito São João, Província Carajás, SSE do Pará. Trabalho de Conclusão de Curso – Federal University of Pará, Belém, pp. 1–47 (in Portuguese).

Loiselle, M.C., Wones, D.R., 1979. Characteristics and origin of anorogenic granites. Abstracts with programs-Geological Society of America 11, 468.

Ludwig, K.R., 2003. User's Manual for Isoplot/Ex Version 3.00 e A Geochronology Toolkit for Microsoft Excel, vol. 4. Berkeley Geochronological Center, Special Publication, 70 p.

Machado, N., Lindenmayer, Z., Krogh, T.E., Lindenmayer, D., 1991. U-Pb geochronology of Archean magmatism and basement reactivation in the Carajás area, Amazon Shield, Brazil. Precambrian Res. 49, 329–354.

Milhomem Neto, J.M.., Lafon, J.M., Galarza, M.A., 2017. Lu-Hf em zircão por LA-MC-ICP-MS no laboratório Pará-Iso (UFPA): metodologia e primeiro exemplo de aplicação na porção sudeste do Escudo das Guianas, estado do Amapá. In: Lima A.M & Gorayeb P. (eds.) Contribuições à geologia da Amazônia, 10, p. 195-208. (in Portuguese).

Mingram, B., Trumbull, R.B., Littman, S., Gerstenberger, H., 2000. A petrogenetic study of anorogenic felsic magmatism in the Cretaceous Paresis ring complex, Namibia: evidence for mixing of crust and mantle-derived components. Lithos 54, 1 –22.

McDonough, W.F., Sun, S.S., 1995. The composition of the Earth. Chem. Geol. 120 (3-4), 223-253.

Mahon, K.I., Harrison, T.M., Drew, D.A., 1988. Ascent of a granitoid diapir in a temperature varying medium. Journal of Geophysics, 93(B2):1174-1188.

Martin, H., 1987. Petrogenesis of Archaean trondhjemites, tonalites and granodiorites from eastern Finland: major and trace element geochemistry. J. Petrol. 28, 921-953.

Nachit, H., Ibhi, A., Abia, E.H., Ohoud, M.B., 2005. Discrimination between primary magmatic biotites, reequilibrated biotites and neoformed biotites. Comptes Rendusl'Academie Science. France 337, 1415–1420.

Oliveira, D.C., Dall'Agnol, R., Silva, J.B.C., Almeida, J.A.C., 2008. Gravimetric, radiometric, and magnetic susceptibility study of the Paleoproterozoic Redenção and Bannach plutons: implications for architecture and zoning of A-type granites. Journal of South American Earth Sciences, 25(1):100–115.

Oliveira, D.C., Dall'Agnol, R., Barros, C.E.M., Oliveira, M.A., 2009. Geology, geochemistry and magmatic evolution of the Paleoproterozoic, anorogenic oxidized A-type Redenção granite of the Jamon Suite, eastern Amazon Craton, Brazil. The Canadian Mineralogist 47 (6), 1441–1468.

Oliveira, D.C., Sérgio, P.N., Ricardo, I.F.T., Roberto, D.A., Gorki, M., Paulo, B.C., 2010. Magnetic anisotropy of the Redenção granite, eastern Amazonian craton (Brazil): implications for the emplacement of A-type. Tectonophysics, 493(1-2):27-41.

Paiva Jr., A.L., 2009. Geologia, petrografia, geocronologia e geoquímica do Granito anorogênico Seringa, Província Mineral de Carajás, SSE do Pará. Federal University of Pará. Dissertation. Graduated Program on Geology and Geochemistry. Institute of Geosciences, pp. 158, (in Portuguese).

Patchett, P.J., Tatsumoto, M., 1980. A routine high-precision method for Lu-Hf isotope geochemistry and chronology. Contributions to Mineralogy and Petrology, 75:263-267.

Patiño Douce, A.E., 1997. Generation of metaluminous A-type granites by low-pressure melting of calc-alkaline granitoids. Geology, 25(8):743–746.

Pearce, J.A., Harris, N.B.W., Tindle, A.G., 1984. Trace element discrimination diagrams for the tectonic interpretation of granitic rocks. Journal of Petrology, 25(4):956-983.

Pinho, S., Fernandes, C., Teixeira, N., Paiva Jr., A., Cruz, V., Lamarão, C., Moura, C., 2006. O magmatismo paleoproterozoico da região de São Félix do Xingu, Província Estanífera do sul do Pará: petrografia e Geocronologia. Rev. Bras. Geociências 36, 724–732.

Rämö, O.T., Haapala, I., 1995. One hundred years of rapakivi granite. Mineralogy and Petrology 52, 129–185.

Rämö, O.T., Dall'Agnol, R., Macambira, M.J.B., Leite, A.A.S., Oliveira, D.C., 2002. 1.88 Ga oxidized A-type granites of the Rio Maria region, eastern Amazonian craton, Brazil: Positively anorogenic!. Journal of Geology, 110(5):603-610.

Rieder, M., 1998. Nomenclature of the micas. Clay Clay Miner. 63, 267–279.

Rodrigues, E.S., Lafon, J.M., Scheller, T., 1992. Geocronologia Pb-Pb da Província Mineral de Carajás: primeiros resultados. In: SBG, Congresso Brasileiro de Geologia, 37, São Paulo, Brazil. vol. 2. Boletim de resumos expandidos, pp. 183–184.

Ronaib, C., Oliveira, D.C., 2013. Geologia, petrografia e geoquímica das associações TTG e leucogranodioritos do extremo norte do Domínio Rio Maria. Boletim do Museu Paraense Emílio Goeldi - Ciências Naturais 8 (3), 383–415.

Russell, W.A., Papanastassiou, D.A., Tombrello, T.A., 1978. Ca isotope fractionation on the earth and other solar system materials. Geochim. Cosmochim. Acta, 42:1075-1090.

Santos, J.O.S., 2003. Geotectonics of the Guyana and Central Brazil Schields. In: Bizzi, L.A., Schobbenhaus, C., Vidotti, R.M., Gonçalves, J.H. (Eds.), Geology, Tectonics and Mineral Resources of Brazil. Companhia de Pesquisa de Recursos Minerais, Brasília, pp. 169–226 ISBN 85–230–0790-3.

Santos, P.A., Feio, G.R.L., Dall'Agnol, R., Costi, H.T., Lamarão, C.N., Galarza, M.T., 2013. Petrography, magnetic susceptibility and geochemistry of the Rio Branco granite, Carajás province, southeast of Pará, Brazil. Braz. J. Genet. 43, 2–15.

Santos, M.M., Lana, C., Scholz, R., Buick, I., Schmitz, M.D., Kamo, S.L., Wiedenbeck, M., 2017. A new appraisal of Sri Lankan BB zircon as a reference material for LA-ICP-MS U-Pb geochronology and Lu-Hf isotope tracing. Geostandards and Geoanalytical Research, 41(3), 335-358.

Santos, R.F.S, Oliveira, D.C., Silva, F.F., 2018. Geocronologia U-Pb, classificação e aspectos evolutivos do Granito Marajoara, Província Carajás. Geologia USP. Série Científica, 18(4):89-124. (in Portuguese).

Siegel, K., Williams-Jones, A.E., Van Hinsberg, V.J., 2017. The amphiboles of the REE-rich A-type peralkaline Strange Lake pluton –fingerprints of magma Evolution. Lithos 288–289 (2017) 156–174.

Silva, F.S., Oliveira, D.C., Antonio, P.Y., D'Agrella-Filho, M., Lamarão, C.N., 2016. Bimodal magmatism of the Tucumã area, Carajás Province: U-Pb geochronology, classification and processes. Journal of South American Earth Sciences 72, 95–114.

Spencer, C.J., Kirkland, C.L., Taylor, R.J.M., 2016. Strategies towards statistically robust interpretations of in situ U-Pb zircon geochronology. Geoscience Frontiers 7, 581e589.

Sousa, S.D., 2020. O Greenstone Belt Sapucaia: implicações para a evolução crustal mesoarqueana da Província Carajás, Instituto de Geociências, University of São Paulo, São Paulo. Dr. Thesis (in Portuguese).

Tassinari, C.C.G., Macambira, M.J.B., 2004. A evolução tectônica do Cráton Amazônico. In: Matesso-Neto, V., Bartorelli, A., Carneiro, C.D.R., Britto-Neves, B.B. (Eds.), Geologia do Continente Sul-Americano. São Paulo, SP, Brazil, pp. 471–485 (in Portuguese).

Teixeira, N.P., Bettencourt, J.S., Moura, C.A.V., Dall'Agnol, R., Macambira, E.M.B., 2002. Archean crustal sources for Paleoproterozoic tin-mineralized granites in the Carajás Province, SSE Pará, Brazil: Pb–Pb geochronology and Nd isotope geochemistry. Precambrian Research 119, 257–275.

Teixeira, M.F.B., Dall'Agnol, R., Santos, J.O.S., Sousa, L.A.M., Lafon, J.-M., 2017. Geochemistry, geochronology and Nd isotopes of the Gogó da Onça Granite: a new Paleoproterozoic A-type granite of Carajás Province, Brazil. J. S. Am. Earth Sci. 80, 47–65.

Teixeira, M.F.B., Dall'Agnol, R., Santos, J.O.S., Oliveira, D.C., Lamarão, C.N., McNaughton, N.J., 2018. Crystallization ages of Paleoproterozoic A-type Granite Suites and Related Granites of Carajás Province, Amazon Craton: constraints from U-Pb geochronology of zircon and titanite. Journal of South American Earth Sciences 88, 312–331.

Teixeira, M.F.B., Dall'Agnol, R., Santos, J.O.S., Kemp, A., Evans, N., 2019. Petrogenesis of the paleoproterozoic (orosirian) A-type granites of Carajas province, Amazon craton, Brazil: combined in situ HfO isotopes of zircon. Lithos 323–333, 1–22.

Thirlwall, M.F., Anczkiewicz, R., 2004. Multidynamic isotope ratio analysis using MC–ICP–MS and the causes of secular drift in Hf, Nd and Pb isotope ratios. International Journal of Mass Spectrometry, 235:59-81.

Turner, S.P., Foden, J.D., Morrison, R.S., 1992. Derivation of some A-type magmas by fractionation of basaltic magma; an example from the Padthaway Ridge, South Australia. Lithos 28, 151– 179.

Vance, J.A., 1965. Zoning in igneous plagioclase: patchy zoning. The Journal of Geology, 73(4):636-651.

Vasquez, M.L., Macambira, M.J.B., Armstrong, R.A., 2008. Zircon geochronology of granitoids from the western Bacajá domain, southeastern Amazonian craton, Brazil: Neoarchean to Orosirian evolution. Precambrian Research 161, 279–302.

Watson, E. B., & Harrison, T. M. (1983). Zircon saturation revisited: temperature and composition effects in a variety of crustal magma types. *earth and planetary science letters*, *64*(2), 295-304.

Whalen, J.B., Currie, K.L., Chappell, B.W., 1987. A-types granites: geochemical characteristics, discrimination and petrogenesis. Contributions of Mineralogy and Petrology, 95(4):407–419.

Wilson, M., 1989. Igneous Petrogenesis e A Global Tectonic Approach. Springer, Dordrecht.

Wones, D.R., Eugster, H.P., 1965. Stability of biotite: experiment, theory and application. Am. Mineral. 50, 1228–1272.

Wright, J.B., 1969. A simple alkalinity ratio and its application to questions of non-orogenic granite genesis. *Geological Magazine*, *106*(4), 370-384.

CAPÍTULO 3 PETROGENESIS AND EMPLACEMENT OF THE PALEOPROTEROZOIC A-TYPE MARAJOARA PLUTON AND ITS MICROGRANULAR ENCLAVES IN THE CARAJÁS PROVINCE, SOUTHEASTERN AMAZONIAN CRATON: CONSTRAINTS FROM GEOCHEMISTRY, ZIRCON GEOCHRONOLOGY, Nd–Hf ISOTOPES, HIDDEN EVIDENCE OF COEXISTENCE BETWEEN CONTRASTING MAGMAS AND NEW INSIGHTS FROM A COMPOSITE DIKE

Autores:

Rodrigo Fabiano Silva Santos

Davis Carvalho de Oliveira

José de Arimatéia Costa de Almeida

Roberto Dall'Agnol

Bhrenno Marangoanha

Marco Antonio Galarza Toro

Cláudio Nery Lamarão

Fernando Fernandes da Silva

PRECAM-D-24-00442 - Confirming your submission to Precambrian

em@editorialmanager.com
para mim

This is an automated message.

Petrogenesis and emplacement of the Paleoproterozoic A-type Marajoara pluton and its microgranular enclaves in the evidence of coexistence between contrasting magmas and new insights from a composite dike

Dear Santos Fabiano Silva Santos,

We have received the above referenced manuscript you submitted to Precambrian Research. It has been assigned the

To track the status of your manuscript, please log in as an author at https://www.editorialmanager.com/precam/, and na

Thank you for submitting your work to this journal.

Petrogenesis and emplacement of the Paleoproterozoic A-type Marajoara pluton and its microgranular enclaves in the Carajás province, southeastern Amazonian craton: Constraints from geochemistry, zircon geochronology, Nd–Hf isotopes, hidden evidence of coexistence between contrasting magmas and new insights from a composite dike

Rodrigo Fabiano Silva Santos [a, b,*], Davis Carvalho de Oliveira [a, b], José de Arimatéia Costa de Almeida [a, b], Roberto Dall'Agnol [b, d], Bhrenno Marangoanha [a, b], Marco Antonio Galarza Toro [b, c], Cláudio Nery Lamarão [a, b], Fernando Fernandes da Silva [a, f]

a Grupo de Pesquisa Petrologia de Granitoides (GPPG), Instituto de Geociências (IG), Universidade Federal do Pará (UFPA), Rua Augusto Corrêa, 01, CEP 66075-110, Belém, Pará, Brazil

b Programa de Pós-graduação em Geologia e Geoquímica (PPGG), IG-UFPA, Belém, Pará, Brazil

c Laboratório de Geologia Isotópica (Pará-Iso), IG-UFPA, Belém, Pará, Brazil

d Laboratório de Microanálises, IG-UFPA, Belém, Pará, Brazil

e Instituto Tecnológico Vale (ITV), Rua Boaventura da Silva, 955, Belém 66055-090, PA, Brazil

f Universidade Federal do Sul e Sudeste do Pará (UNIFESSPA), Instituto de Geociências e Engenharias (IGE), Marabá, Pará, Brazil

* Corresponding author

E-mail addresses: rfssantos@ufpa.br (R.F.S. Santos), davis@ufpa.br (D.C. Oliveira), ari@ufpa.br (J.A.C Almeida), roberto.dallagnol@itv.org (R. Dall'Agnol), bhrenno@ufpa.br (B. Marangoanha), antogt@ufpa.br (M.A. Galarza), lamarao@ufpa.br (C.N. Lamarão), ffernandes@unifesspa.edu.br (F.F. Silva)

ABSTRACT

The Marajoara granite is a stock that intruded into Mesoarchean granitoids in the Rio Maria domain. It is composed of equigranular (eBMzG) and heterogranular (hBMzG) monzogranites. A rapakivi texture and the occurrence of microgranular enclaves (ME) and porphyritic ME (pME) are restricted to the hBMzG facies. The magnetic susceptibility values and the presence of magnetite indicate that the hBMzG facies is akin to granites from the magnetite series, whereas the eBMzG variety shows affinity with the granites of ilmenite series. These granites are peraluminous and similar to ferron granites. The hBMzG and pME show affinities with oxidized and the eBMzG with reduced A-type granites in the Jamon and Velho Guilherme suites, respectively. The ME have affinities with magnesian granites and the calc-alkaline series. U–Pb zircon analyses (SHRIMP) yield a crystallization age of 1884 ± 11 Ma for the hBMzG. Lu–Hf and Sm–Nd isotope data indicate that the Marajoara pluton-forming magma originated from a Meso- to Paleoarchean crustal source ($\varepsilon_{Hf}(t)$ values of -11 to -18 and ε_{Nd} (t) values of -9 to -11; Hf-T_{DM}^C model ages of 3.21 to 3.62 Ga and Nd-T_{DM}^C ages of 2.91 to 3.62 Ga). The varieties that constitute the Marajoara pluton are not cogenetic and the original magmas and

were generated from partial melting of tonalitic rocks, with metasedimentary contribution in the case of eBMzG. Felsic–mafic magma mixing played an important role in the crystallization history of the pluton. The enclaves represent a basic magma from the lithospheric mantle that was injected into the magma chamber during underplating, where it interacted with the Marajoara pluton. This hypothesis is reinforced by the occurrence of a 1.88 Ga porphyry granite–diabase composite dike in the Rio Maria area. Microgranular and porphyritic enclaves formed due to the mixing of the felsic and mafic magmas. The results presented in this work highlight the importance of the Archean crust for the origin of Paleoproterozoic granites, whose emplacement at shallow crustal levels occurred through a dike feeder system resulting from extensional tectonics.

Keywords: A-type granite, Magma mixing, Paleoproterozoic, Carajás, Composite dike, Isotopic data

1 INTRODUCTION

The petrogenesis of granites has been the subject of heated debate since the 1970s, when the first alphabetical classifications (e.g., I, S, M, and A) emerged (Chappell and White, 1974; Loiselle & Wones, 1979). The controversy has revolved around the complex interactions between different magmatic processes and multiple potential magma sources (Frost & Frost, 2011; Dall'Agnol et al. 2012 and references therein). The partial melting of crustal rocks stands out as a primary mechanism for generating granitic magmas (Collins et al., 1982; Anderson, 1983; Whalen et al., 1987; Stevens and Clemens, 1993; Johannes and Holtz, 1996; Clemens and Watkins, 2001). Additionally, granite petrogenesis is also influenced by fractional crystallization and/or open-system processes such as magma mixing and crustal contamination. A-type granites were initially characterized by Loiselle & Wones (1979) as those generated along rift zones within stable continental blocks and are moderately alkaline, and reduced with high FeO/FeO+MgO ratio, and low H_2O contents. However, experimental studies have demonstrated the diversity of A-type magmas in terms of H_2O content and redox state (Dall'Agnol et al., 1999b). It was demonstrated that the model involving the melting of granulitic residues in the deep crust, from which highly hydrated felsic melts were previously extracted, was inadequate to explain the origin of typical A-type granites (Creaser et al., 1991).

Anorogenic massifs of A-type affinity and Paleoproterozoic age have been described in the Carajás province, which is situated in the southeastern part of the Amazonian craton. These granites are arranged into three different suites according to their mineralogy, geochemistry, oxidation state of their magmas and associated ore deposits (Dall'Agnol et al., 2005). The plutons of the Jamon suite are oxidized, have associated wolframite deposits are classified as

magnetite-series granites (Ishihara, 1977). Those of the Velho Guilherme suite are reduced, have associated cassiterite deposits and are akin to the ilmenite series granites,. The plutons of the Serra dos Carajás suite are moderately reduced. From the oxidized to reduced granites, the contents of magnetite and titanite, and the magnetic susceptibility values decrease, and the FeOt/(FeOt+MgO) ratios in whole-rock and mineral samples increase. Even with our increasing understanding of Paleoproterozoic granite genesis within the Carajás province, insights into the composition of the source rocks, the processes that controlled the distinct nature of the magmas, and the roles of oxidized and reduced types during the formation and emplacement of the plutons are still needed.

Within these A-type plutons, the presence of widespread mafic microgranular enclaves (ME) and their association with mafic dikes provide evidence of the role of mafic magmas in the formation and evolution of A-type granitoid magmas (Barbarin, 2005; Cheng et al., 2012; Yu et al., 2018). The presence of enclaves with chilled margins and xenocrysts within the granites serves as evidence of physical interaction between coeval mafic and felsic magmas (Barbarin, 2005; Siuda and Bagiński, 2019). These rocks often display distinctive textures such as rapakivi textures, ocellar quartz, inclusion zones in phenocrysts, compositional zoning in plagioclase, and biotite blades, suggesting the occurrence of magma mingling processes (Hibbard, 1991). Furthermore, geochemical analyses can reveal evidence of magma mixing, such as the prevalence of intermediate compositions resulting from the interaction of basic and acidic magmas and linear trends in Harker-type diagrams (Reubi and Blundy 2009, Ruprecht et al., 2012; Kumar et al., 2017).

The typology of the Paleoproterozoic A-type Marajoara granite in the Carajás province is ambiguous, as it is composed of both reduced (ilmenite–series) and oxidized (magnetite–series) magmas. In addition, the pluton displays many unusual structures related to physical interactions between felsic and mafic coeval magmas. This paper concerns the characteristics and origins of the different facies that form the granites of the Marajoara pluton, the associated ME, and undisturbed composite felsic and mafic dikes. The results obtained in this research, including its zircon crystallization age (U–Pb SHRIMP) and isotopic signature using Hf and Nd data, allows the definition of a general model of the evolution and origin (including source rock) of the Marajoara granite and associated enclaves. Comparisons between these granites and other Proterozoic granites were made to provide a better understanding of the geochemical signatures and protoliths of rapakivi-affinity granites and A-type granites in general.

2 GEOLOGICAL BACKGROUND

The Carajás province is defined as the main Archean nucleus of the Amazonian craton (Almeida et al., 1981) and it is surrounded by Proterozoic belts. Tassinari and Macambira (2004) classify it as part of the Central Amazon province, whereas Santos et al. (2003) argue a status of an independent Archean province (Fig. 1a). The consensus is that the Carajás province represents an older Archean segment of the Amazonian craton unaffected by the Transamazonian cycle (2.26–1.95 Ga; Vasquez et al., 2008). The Carajás province (Fig. 1b). It has been subdivided into two tectonic domains (Santos, 2003; Vasquez and Rosa-Costa, 2008): (i) the Mesoarchean Rio Maria domain to the south represents a well-preserved granite–greenstone terrane (3.0–2.86 Ga; Macambira and Lancelot, 1996; Althoff et al., 2000; Souza et al., 2001; Oliveira et al., 2011; Almeida et al., 2011, 2013; Silva et al., 2023), and (ii) the Meso- to Neoarchean Carajás domain to the north is characterized by a more complex evolution (3.0–2.73 Ga; Machado et al.,1991; Pidgeon et al., 2000; Feio et al., 2013; Tavares et al., 2018; Marangoanha et al., 2019; Silva et al., 2023). These domains are essentially defined by different granitoids and greenstone belts sequences and are separated by approximately E–W–trending shear zones. The northern region is overlain by a metamorphosed volcano–sedimentary basin dating back to approximately 2.76 Ga, which hosts significant mineral deposits of Au, Cu, Fe, and Mn.

Throughout the Amazonian craton's evolution, extensive posttectonic and anorogenic magmatism occurred, resulting in numerous stocks and batholiths, predominantly of Paleoproterozoic to Mesoproterozoic age (Dall'Agnol et al., 2005; Bettencourt et al., 2016; Santos et al., 2018; Teixeira et al., 2018). In the Carajás province, its domains underwent stabilization by the end of the Archean, which was sustained until approximately 1.88 Ga, coinciding with the formation and emplacement of A-type granites (Dall'Agnol et al., 2005; Oliveira et al., 2009; Santos et al. 2023).

2.1 A-TYPE GRANITES IN THE CARAJÁS PROVINCE

The A-type granitoids of the Carajás province crystallized during the Orosirian period (1880 to 1857 Ma; Santos et al., 2018; Teixeira et al., 2018) within an extensional tectonic setting, and the formation of granitic magmas coincided with the formation of dike swarms (Dall'Agnol et al., 2005; Silva et al., 2016; Teixeira et al., 2018; Antonio et al., 2021). These granites are distributed across the province and can be categorized into three suites (see Fig. 1):

Jamon, Velho Guilherme and Serra dos Carajás. In the Rio Maria domain, the oxidized A-type granites are classified within the Jamon suite (Dall'Agnol et al., 1999b) and consist of the Jamon, Bannach, Manda Saia, Marajoara, Musa and Redenção granites (Fig. 1b). These granites comprise monzo- and syenogranites with biotite, with biotite and amphibole, along with scarce clinopyroxene in the more mafic facies. Primary accessory minerals include allanite, apatite, ilmenite, titanite, and zircon. Rapakivi textures and microgranular enclaves are frequently observed in the Redenção, Bannach, and Marajoara plutons (Almeida et al., 2006; Oliveira et al., 2009; Santos et al., 2018).
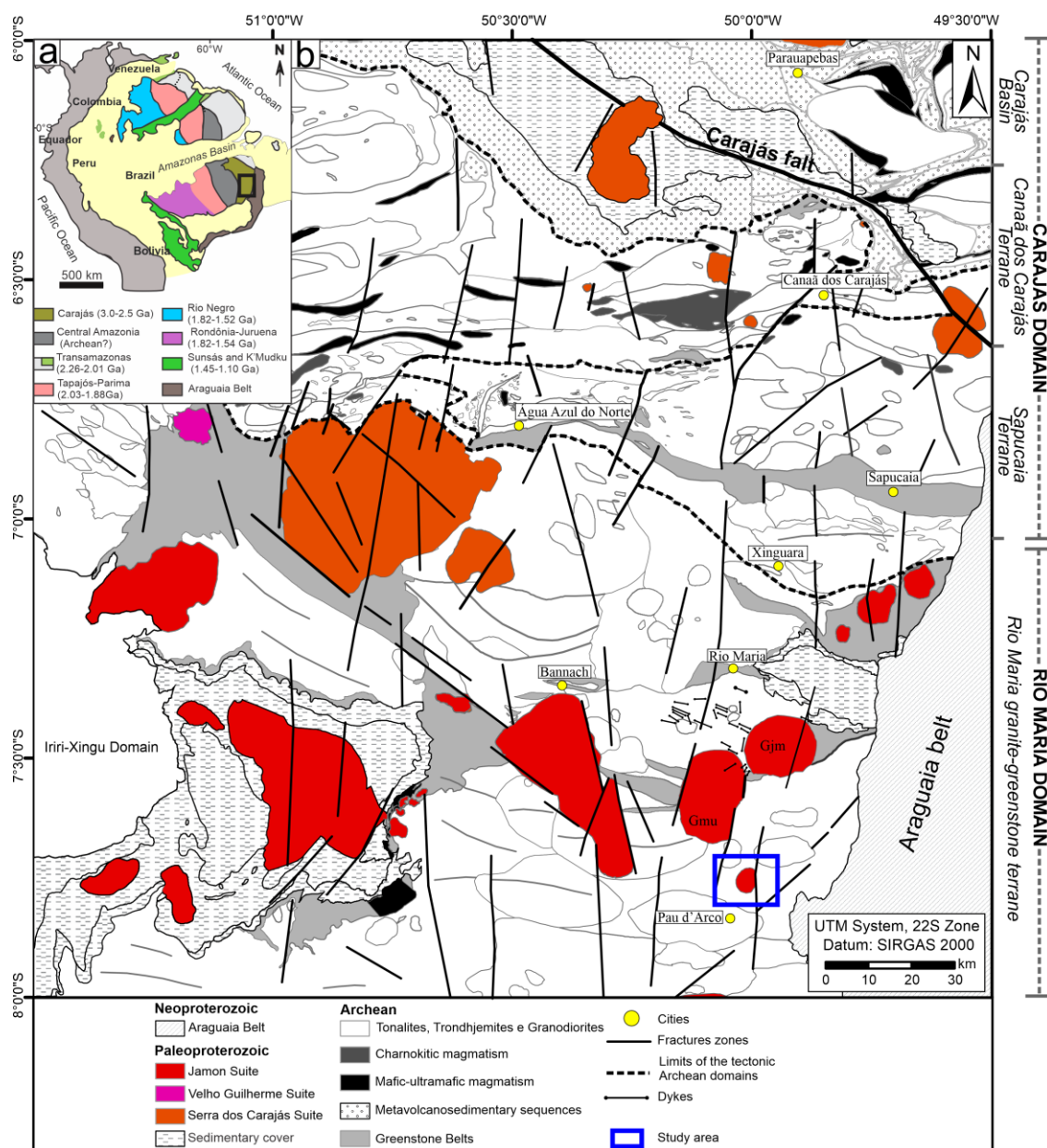
Figure 1 - (a) Amazonian craton divided into geochronological provinces (Santos et al., 2003) showing the Carajás province and the area of Fig. 1b; (b) Geologic map of the Carajás province showing Paleoproterozoic granites (modified from Oliveira et al., 2023), the location of the study area, and the estimated limits of the tectonic Archean terranes of the Carajás province according Dall'Agnol et al. (2013).

In the Carajás Basin, which is located in the northern region of the Carajás province, moderately reduced granites form the Serra dos Carajás suite, which includes the Serra dos Carajás, Pojuca and Cigano plutons (Javier Rios et al., 1995; Dall'Agnol et al., 1999b, 2005). These granites are characterized by hornblende–biotite monzogranites and syenogranites. The accessory minerals are similar to those in the Jamon suite, albeit with less magnetite and titanite and a greater abundance of fluorite. The reduced granites found in the Xingu region, intruding various Archean rocks, belongs to the Velho Guilherme suite and include the Velho Guilherme, Antônio Vicente, Benedita, Bom Jardim, Mocambo and Rio Xingu granites (Teixeira, 1999; Teixeira et al., 2002; Lamarão et al., 2012). These rocks are characterized as reduced biotite syenogranites, monzogranites, and subordinate alkali feldspar granites. Late to postmagmatic hydrothermal alterations significantly affected the more evolved leucogranitic facies.

Geochronological dating carried out on zircon via various methods, such as U–Pb and Pb–Pb dating, yields a crystallization age of ~1.88 Ga for the A-type granites in the Carajás province (Machado et al., 1991; Dall'Agnol et al, 1999b, 2005; Teixeira et al. 2017, 2018). Nd isotope data defined Archean T_{DM} ages (~3.35 Ga to 2.60 Ga; Rämö et al., 2002, Dall'Agnol et al., 2005; Teixeira et al., 2018, 2019) and highly negative ε_{Nd} values (-12 to -8) for those granites. The ε_{Nd} values of the Jamon (-10.5 to -8.1) and Serra dos Carajás (-9.7 to -7.9) suites are similar and higher than those of the Velho Guilherme suite (-12.1 to -12.2). Additionally, Lu–Hf isotope data obtained by Teixeira et al. (2019) reveal T_{DM} ages of ~3.12 Ga to 3.58 Ga and extremely negative ε_{Hf} values ranging from -9.8 to -17.3. Combining these isotopic data allows interpretation of an Archean crustal source for the petrogenesis of these magmas. A summary of the main geochronological and isotopic data obtained thus far is shown in Table 1. Note that the data of the Marajoara granite obtained in this paper are also included in the table.

3 METHODS

3.1 PETROGRAPHY

Transmitted light optical microscopy was utilized for analysis. Thirty-three modal analyses were conducted on representative samples of the Marajoara granite. The modal compositions were obtained with approximately 1,800 points per sample, distributed in a mesh with a spacing of 0.4 mm in an automatic point counter Hardledge Endeeper. The rocks were classified according to the recommendations of the Subcommission on Igneous Rock Systematics of the International Union of Geological Sciences (IUGS) (Le Maitre et al., 2002).

3.2 WHOLE-ROCK GEOCHEMISTRY

Approximately 5 kg samples for whole-rock chemical analysis were ground using both primary and secondary jaw crushers until the particles reached sizes between 0.3 and 0.1 mm. This material was powdered in an agate swing mill to achieve a particle size of <10 μm. Nineteen analyses were conducted at ACME Analytical Laboratories Ltd. (Vancouver, Canada) via inductively coupled plasma atomic emission spectroscopy (ICP–AES) for major elements and inductively coupled plasma mass spectrometry (ICP–MS) for trace elements, including rare earth elements. GCDkit 6.1 software (Janousek et al., 2006) was employed to generate the geochemical diagrams.

Table 1 - Geochronological data of the Paleoproterozoic granites and dikes of the Carajás province.

Suites	Pluton	Age (Ma)	Material	Method	Sm-Nd		Lu-Hf	
					T_{DM} (Ga)	ε_{Nd} (T)	T_{DM} (Ga)	ε_{Hf} (T)
Jamon	Jamon	1885 ± 32 [3]	Zircon	Pb evaporation	3.02	-9.7 [3]		
	Jamon	1870 ± 18 [10]	Zircon	U-Pb SHRIMP	2.87	-9.5 [3]		
	Musa	1882 ± 4 [10]	Zircon	U-Pb SHRIMP	2.82	-9.4 [3]	3.40	-14.4 [11]
	Redenção	1870 ± 68 [6]	Zircon	Pb evaporation	2.78	-8.8 [4]	3.40	-14.5 [4]
	Redenção	1883 ± 9 [10]	Zircon	U-Pb SHRIMP	2.81	-10.5 [4]	3.35	-13.6 [11]
	Redenção	1865 ± 6 [10]	Zircon	U-Pb SHRIMP				
	Bannach	1875 ± 6 [10]	Zircon	U-Pb SHRIMP	2.84	-9.6 [4]	3.38	-14.2 [11]
	Bannach	1857 ± 14 [10]	Zircon	U-Pb SHRIMP				
	Manda Saia	1866 ± 10 [13]	Zircon	U-Pb LA-ICP-MS	2.71	-8.4 [4]	3.65	-18.6 [13]
Serra dos Carajás	Cigano	1884 ± 4 [10]	Zircon	U-Pb SHRIMP	2.67	-9.5 [6]	3.43	-14.9 [11]
	Pojuca	1874 ± 2 [1]	Zircon	U-Pb TIMS	3.35	-9.7 [6]		
	Serra dos Carajás	1880 ± 2 [1]	Zircon	U-Pb TIMS	2.61	-7.9 [6]	3.40	-14.4 [11]
	Serra dos Carajás	1882 ± 10 [10]	Zircon	U-Pb SHRIMP	2.73	-9.2 [6]	3.44	-15.0 [11]
Velho Guilherme	Antônio Vicente	1882 ± 15 [10]	Zircon	U-Pb SHRIMP	3.25	-12.1 [5]	3.40	-14.2 [11]
	Serra da Quiemada	1882 ± 12 [7]	Zircon	Pb evaporation				
	Mocambo	1862 ± 32 [5]	Zircon	Pb evaporation	2.98	-7.9 [5]		
	Bom Jardim	1867 ± 1 [12]	Zircon	Pb evaporation				
	Velho Guilherme	1873 ± 13 [2]	Whole-rock	Pb-Pb isochron			3.34	-14.2 [11]
	Velho Guilherme	1882 ± 6 [10]	Zircon	U-Pb SHRIMP			3.36	-13.7 [11]
Other granites and dikes	Seringa	1889 ± 8 [10]	Zircon	U-Pb SHRIMP	2.86	-10.7 [11]	3.47	-15.5 [11]
	São João	1877 ± 3 [10]	Zircon	U-Pb SHRIMP	2.91	-10.8 [11]	3.53	-16.7 [11]
	Gogó da Onça	1866 ± 10 [9]	Zircon	U-Pb SHRIMP	2.80	-9.07 [9]	3.52	-16.5 [11]
	Gradaús	1882 ± 9 [8]	Zircon	Pb evaporation				
	Felsic dike	1881 ± 3 [14]	Zircon	U-Pb SHRIMP				
	Intermediate dike	1874 ± 110 [15]	Whole-rock	Rb-Sr				
	Mafic dike	1802 ± 22 [16]	Mafic agregate	K-Ar				

Data sources: (1) Machado et al. (1991); (2) Rodrigues et al. (1992); (3) Dall'Agnol et al. (1999b); (4) Rämö et al. (2002); (5) Teixeira et al. (2002); (6) Dall'Agnol et al. (2005); (7) Pinho et al. (2006); (8) Abrantes Jr. (2011); (9) Teixeira et al. (2017); (10) Teixeira et al. (2018); (11) Teixeira et al. (2019); (12) Lamarão et al. (2012); (13) Santos et al. (2023); (14) Silva et al. (2016); (15) Rivalenti et al. (1998); (16) Silva Jr. et al. (1999).

3.3 ZIRCON GEOCHRONOLOGY

3.3.1 U–Pb SHRIMP

Zircon grains from sample GDR-9FB were isolated at the Isotopic Geology Laboratory, Federal University of Pará (Pará-Iso/UFPA), Brazil. Approximately 7 kg of rock was crushed, pulverized, sieved to obtain fractions of 75, 125, 175 and 250 μm, treated with bromoform and an isodynamic magnetic separator, and then handpicked under a binocular microscope. To carry out zircon analysis on a sensitive high-resolution ion microprobe (SHRIMP), the crystals were embedded in epoxy resin and polished to expose their crystal cores. The internal structure of the zircons was examined via cathodoluminescence (CL) and backscattered electron (BSE) imaging to identify suitable target sites for U–Pb analyses. CL and BSE images were generated via a JEOL JXA-8230 scanning electron microprobe (SEM) operating at 15 kV, 20 mA, and 11 mm working distance.

The analyses were performed using a SHRIMP IIe system installed at the High-Resolution Geology Laboratory, University of São Paulo, Brazil (GeoLab/USP). The instrumental performance and analytical procedures of the SHRIMP system were documented by Stern (1998) and Sato et al. (2014). The standard used was TEMORA-2 zircon (416.78 ± 0.33 Ma; Black et al., 2003) as the isotope ratio standard. The primary ion beam spot size was 30 μm. The age calculations and presentation of the isotopic results on the concordia diagram were performed with the Isoplot/EX 3.0 software developed by Ludwig (2003). The approach used to establish the most robust statistics and determine the optimal U–Pb age adhered to the guidelines provided by Spencer et al. (2016). Given that all samples exceed 1.5 Ga in age, the calculation of age was based on the weighted mean of the $^{207}Pb/^{206}Pb$ ratios, and the suitability of the mean square weighted deviation (MSWD) was assessed for both over- and underdispersion.

3.3.2 Pb–Pb evaporation

Isotopic analyses of zircon monocrystals via the Pb evaporation method were conducted at the Isotopic Laboratory (Pará-Iso) of the Geosciences Institute of the Federal University of Pará, following the methodology developed by Kober (1987). The analyses were performed on a FINNIGAN MAT 262 thermal ionization mass spectrometer. The results are presented with a 2σ deviation and corrected for mass fractionation and common Pb or contamination on the

basis of the double-stage Pb evolution model proposed by Stacey and Kramers (1975), with the $^{204}Pb/^{206}Pb$ ratio adopted by Macambira et al. (1994).

3.4 Lu–Hf ISOTOPE DATA

LA–MC–ICP–MS in situ zircon Lu–Hf analyses were conducted using a high-resolution multicollector Neptune Thermo Finnigan mass spectrometer equipped with a Nd:YAG LSX–213 G2 CETAC laser microprobe at the Isotope Geology Laboratory (Pará-Iso/UFPA), following the procedures established by Milhomem et al. (2017). As a reference material for the $^{176}Hf/^{177}Hf$ ratio, the Mud Tank zircon (731±1 Ma Horstwood et al., 2016) was utilized.

The isotopes of Lu, Hf, and Yb were measured on the basis of the isotopic ratios of $^{173}Yb/^{171}Yb$, $^{179}Hf/^{177}Hf$, $^{175}Lu/^{177}Hf$, and $^{176}Hf/^{177}Hf$, respectively, to correct for isobaric interferences of isotopes of Lu and Yb with mass 176. Therefore, the isobaric interferences of ^{176}Lu and ^{176}Yb were adjusted via an equation with a mass fractionation factor (β) for Lu and Yb and the intensity of the signals observed in the interference-free isotopes ^{175}Lu and ^{173}Yb, normalized to the accepted abundances of their isotopes ($^{176}Lu/^{175}Lu=0.026549$, Chu et al., 2002; and $^{176}Yb/^{173}Yb=0.786956$, Thirlwall and Anczkiewicz, 2004). The factor β (Hf, Yb and Lu) was calculated for each measurement performed, as its value is influenced by the ratio measured between the isotopes of interest. To correct the isotopic fractionation caused by the equipment during the analyses, according to the exponential law (Russel et al., 1978), the Yb isotope ratios were normalized, assuming a value of 1.12466 for $^{173}Yb/^{171}Yb$ (Thirlwall and Anczkiewicz, 2004). Similarly, the isotopic ratios of Hf were normalized using a $^{179}Hf/^{177}Hf$ ratio value of 0.7325 (Patchett and Tatsumoto, 1980). To perform these correction calculations and obtain the corrected values of the $^{176}Hf/^{177}Hf$ and $^{176}Lu/^{177}Hf$ ratios for each analyzed point, the raw data were processed in a Microsoft Excel macro, with approximately 40 values selected from a total of 60 integrated data points of 1.049 s/point (Milhomem Neto et al., 2017).

3.5 Sm–Nd ISOTOPE DATA

The Sm–Nd analyses were conducted on 10 representative samples of the Marajoara granite and enclaves at the Geochronology Laboratory of the University of Brasília (UnB), Brazil, using a Finnigan MAT 262 mass spectrometer equipped with seven movable Faraday cup collectors and a central electron multiplier. The analytical procedures were in accordance with those of Gioia & Pimentel (2000). The extraction of Sm and Nd followed the cation

exchange technique and used a Teflon column containing L-N spec resin. The separated Sm and Nd were deposited on a Re filament and analyzed in static mode on the spectrometer. The precision of the Sm/Nd and $^{143}Nd/^{144}Nd$ ratios was better than $\pm$ 0.5% (2σ) and $\pm$ 0.005% (2σ), respectively, on the basis of repeated analyses of international rock standards (BHVO-1 and BCR-1). The isotopic ratios were normalized to $^{146}Nd/^{144}Nd$ = 0.7219, and the decay constant used for the calculations was 6.54×10^{-12} year^{-1}. The Nd-T_{DM} values were calculated using the DePaolo (1981) model.

3.6 MAGNETIC SUSCEPTIBILITY

Magnetic susceptibility (MS) measurements were obtained for 27 hand samples at the Magnetic Petrology Laboratory of the Federal University of Pará using an SM-30 susceptibility meter developed by ZH INSTRUMENTS, enabling measurements with a magnetic susceptibility sensitivity of 1×10^{-7} SI. The statistical treatment of the data was performed with the Minitab 16 program, which was used to generate probability diagrams and frequency histograms.

3.7 MINERAL CHEMISTRY

Mineral chemical data were obtained using a JEOL JXA-8230 electron microprobe equipped with five wavelength dispersive spectrometers (WDSs), and the complementary mineral composition of opaque minerals was analyzed using a LEO 1430 scanning electron microscope (SEM) equipped with an energy dispersive spectrometer (EDS) at the Microanalysis Laboratory of the Federal University of Pará (UFPA). To eliminate electrostatic charge on the sample surface, the polished thin sections of samples from the Marajoara granite were first carbon-coated and then analyzed. The analyses were performed on preselected crystals of biotite and Fe–Ti oxides (magnetite and ilmenite). The analytical operating conditions for the EDS analyses were 20 kV for the column acceleration voltage, and those of the WDS analyses included a column accelerating voltage of 15 kV, a current of 20 nA, analysis times of 20 s for major elements and 40 s for minor and trace elements, and a beam diameter of 1 μm for all minerals. The analytical precision was ±1% and ± 10% for major and minor elements, respectively. The crystals used for the WDS analyses of all minerals were pentaerythritol (PETJ) for K, Ca, Ti and Sr; lithium fluoride (LiFH) for V, Mn, Fe, Ni and Ba; thallium acid phthalate (TAP) for Na, Si, Al and Mg; and layered dispersion element (LDE1) for F. The standards were albite (Na), andradite (Si and Ca), hematite (Fe), microcline (Al and K), olivine

(Mg), pyrophanite (Ti and Mn), topaz (F), and vanadinite (V and Cl).

4 RESULTS

4.1 GENERAL ASPECTS

4.1.1 Geological features within the Marajoara pluton

The Marajoara granite occurs as a subcircular stock with an outcrop area of approximately 42 km^2 intruding Mesoarchean granitoids of the Rio Maria domain and crosscutting the ENE–WSW regional foliation found in the Arco Verde tonalite (2.97 Ga) and in the Guarantã suite leucogranites (2.87 Ga). The borders of the stock are dominated by flat relief, whereas the central portion is made up of hills and mountains that reach up to 600 m in elevation. This relief forms a set of oriented crests in two main directions (NE–SW and NW–SE) that are easily observed (Fig. 2a) in a digital elevation model (SRTM – Shuttle Radar Topography Mission) and in aerogammaspectrometric images (Fig. 2b). The relief features in this area also include ring structures, which delimit the facies inside the pluton (Fig. 2c). The stock is composed of hololeucocratic rocks with monzogranitic composition. Two petrographic facies are present: equigranular biotite monzogranite (eBMzG – Fig. 3a) and heterogranular biotite monzogranite (hBMzG – Fig. 3b). The eBMzG is slightly more enriched in mafic minerals, generally has a medium equigranular texture, whereas the hBMzG facies has a medium to coarse inequigranular texture with coarse feldspar crystals.

Porphyritic ME are common and present subcircular shapes with dimensions ranging from a few centimeters (Fig. 3c) to 3 m in length (Fig. 3d). They are always associated with the hBMzG facies (Fig. 3b) and exhibit features of magma mingling processes, in which coarse feldspar crystals and, more rarely, quartz, belonging to the host granite, are found inside the enclaves. These enclaves have porphyritic textures with quartz, microcline and plagioclase phenocrysts, and they are immersed in a finer-grained matrix and exhibit compositions ranging from granodioritic to monzogranitic. When devoid of phenocrysts, these enclaves present a microgranular appearance, are more enriched in mafic minerals and are more angular (Fig. 3e). Xenoliths of the surrounding rocks occur both in the granite and in the porphyry enclaves (Fig. 3b) in the contact zone. The xenoliths are strongly deformed, angular, and dark gray in color and are essentially composed of plagioclase, quartz and mafic minerals. The eBMzG variety occupies the periphery of the pluton, where the relief is flatter, whereas the hBMzG facies forms the framework of the mountains and hills in the central portion of the stock (Fig. 3f).
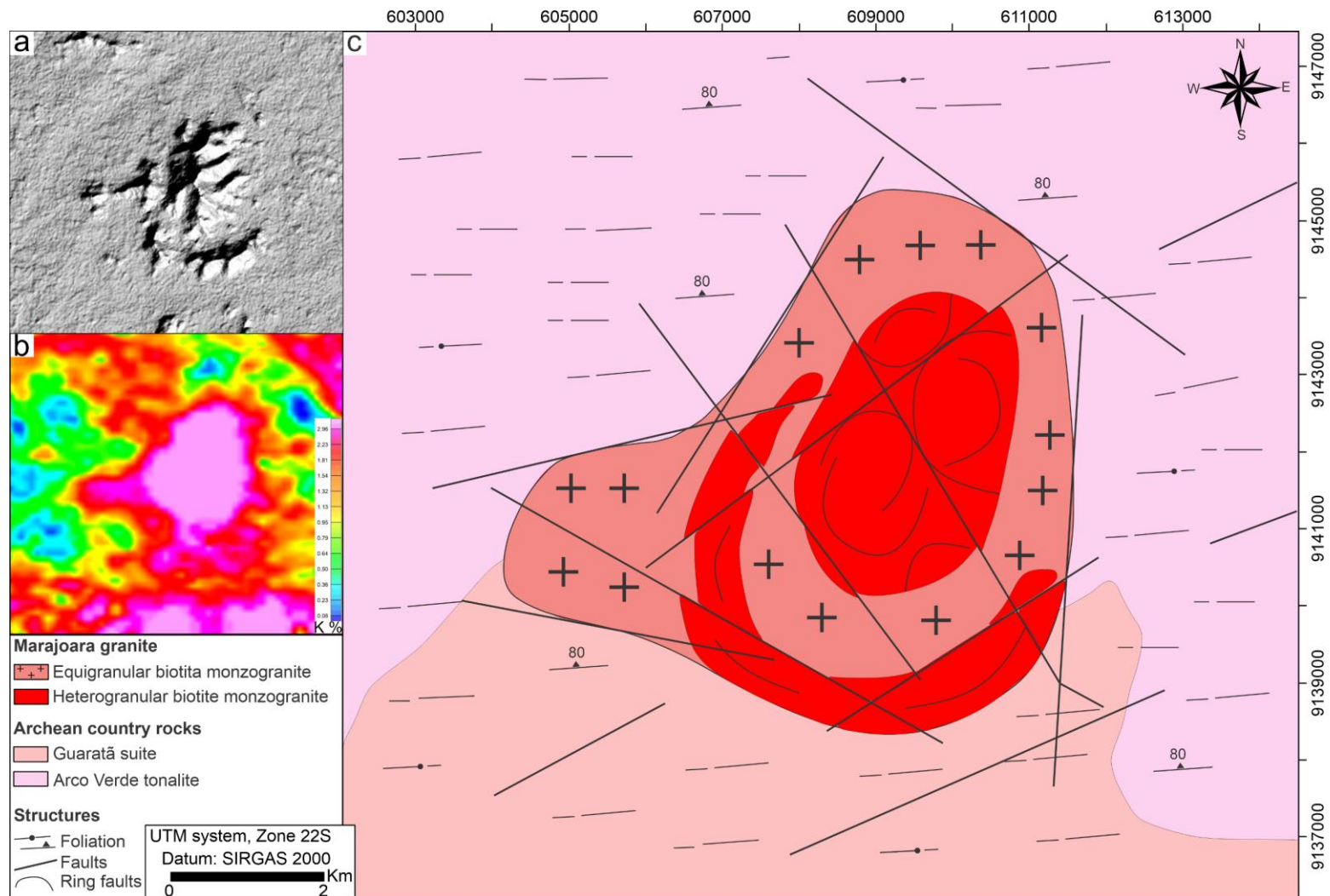
Figure 2 - Geological characteristics of the Marajoara granite: (a) and (b) Digital elevation model (SRTM) and aerogammaspectrometric image (K channel), respectively, showing contrast between the Marajoara granite and the Archean country rocks; (c) Geological map of the Marajoara pluton showing the spatial distribution of petrographic facies.
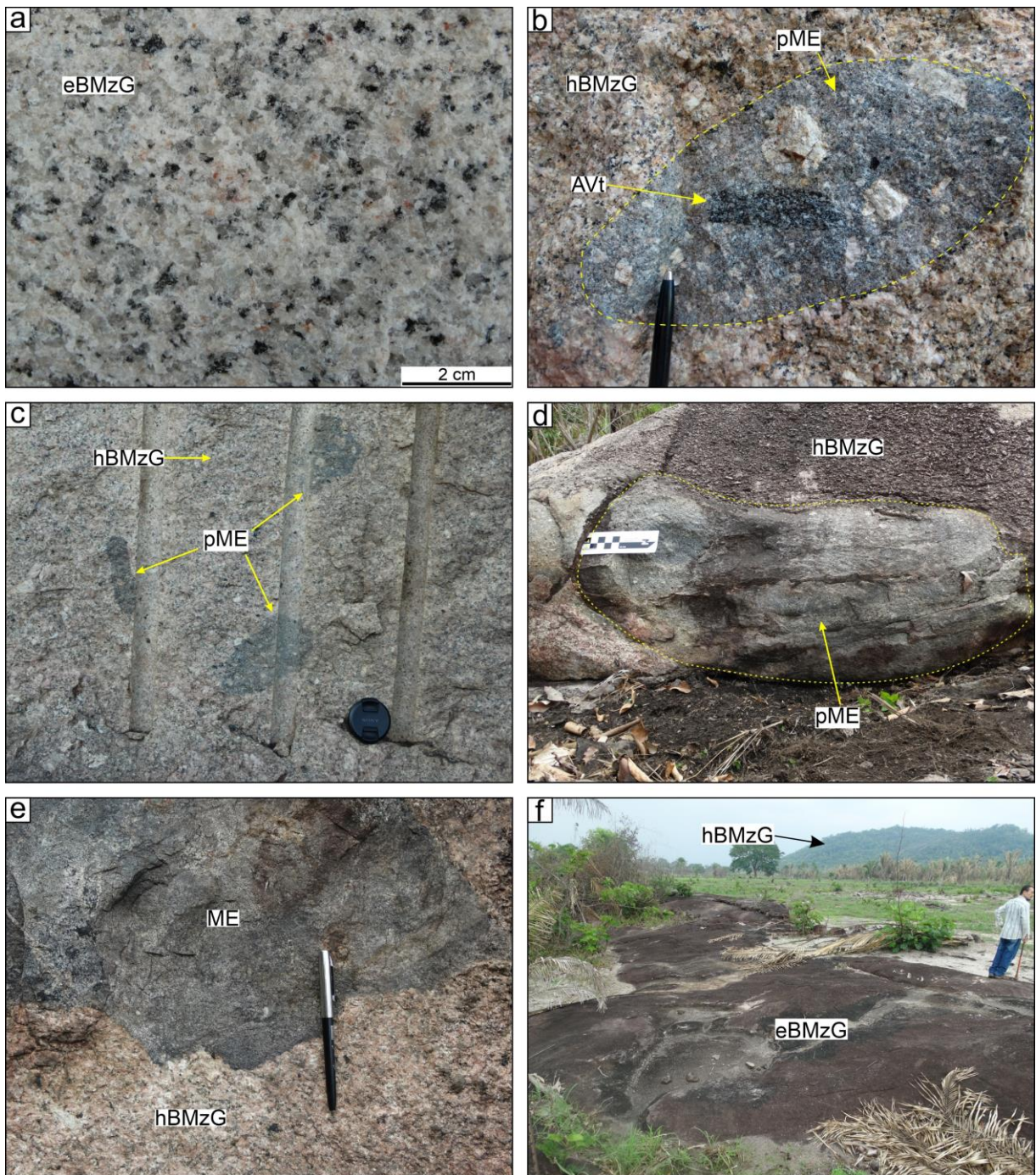
Figure 3 - Mesoscopic aspects of the Marajoara granite: (a) Equigranular phaneritic texture in eBMzG; (b) Porphyritic microgranular enclave occurring as a rounded enclave within the hBMzG facies, showing dropped alkali feldspar crystals and an angular xenolith from the Mesoarchean basement; (c) centimetric porphyritic microgranular enclaves occurring in a globular form in the hBMzG facies; (d) metric pME with a subcircular shape; (e) approximately straight contacts between the microgranular enclave and the hBMzG facies; (f) geomorphological contrast between granite varieties. Key: hBMzG (heterogranular biotite monzogranite), eBMzG (equigranular biotite monzogranite), ME (microgranular enclave), pME (porphyritic microgranular enclave), AVt (Arco Verde tonalite).

4.1.2 Composite dikes

The Mesoarchean units of the Rio Maria domain are cut by a swarm of dikes oriented in the WNW–ESE direction with variable compositions from mafic to intermediate to felsic (Silva Jr. et al., 1999; Silva et al., 2016; W. Teixeira et al., 2018; Antonio et al., 2021; Fig. 1) associated and with ages similar to the Jamon suite. The available geochemical data indicate that the three associations must not have evolved from the same parental magma through fractional crystallization or other magmatic processes. The felsic dikes have been correlated with Paleoproterozoic A-type rapakivi granite suites (Dall'Agnol et al., 1999a). Numerous occurrences of mafic and felsic dikes contemporaneous with granitic magmatism have been described, especially in southeastern Finland (Rämö and Haapala, 1995), including composite dikes (Rämö, 1991). An example of a silicic–basic composite dike, with field features indicating interaction processes between magmas of contrasting composition, was also described in the Rio Maria region in these associations (Dall'Agnol et al., 2006). Mapped for up to 0.3 km along strike, this composite dike features narrow (0.5–1 m) mafic borders on opposite sides of a thicker (3–4 m) central granite porphyry dikelet and appears to be symmetrical across its width (Fig. 4a). The internal boundaries between the granite porphyry and mafic dikelets are generally planar and parallel (Fig. 4b); however, within the granite phase, a few rounded mafic enclaves up to 30 cm across are found locally (Fig. 4c). Evidence of mingling with the felsic magma is provided through the presence of xenocrysts (Fig. 4d), indicating that the magmas presented a low viscosity contrast and that they coexisted in a partial liquid state.
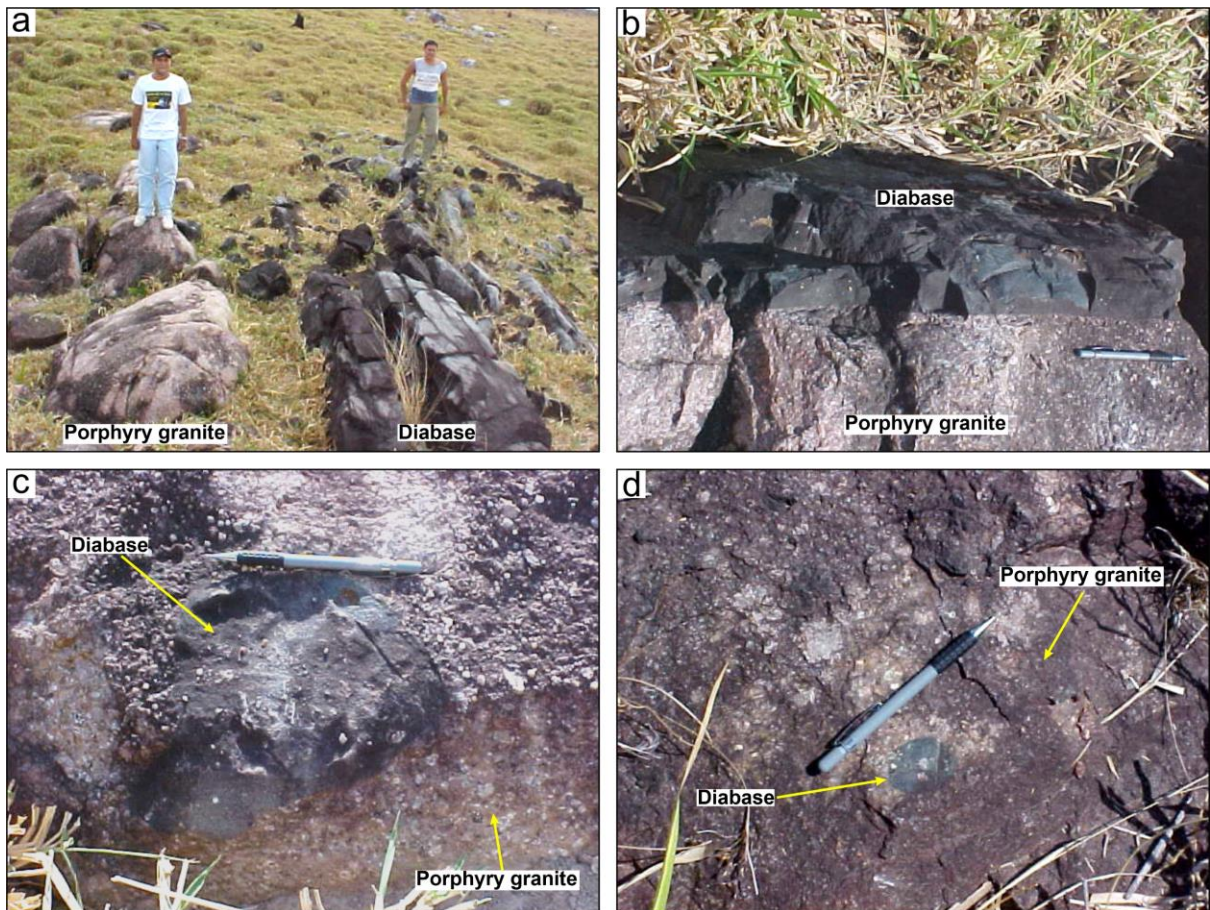
Figure 4 - Field relationships of the composite dike: (a) composite dike intersecting the Mesoarchean Rio Maria granodiorite; (b) porphyry granite dike, showing straight and regular contact with diabase; (c) and (d) diabase enclaves in the porphyry granite, showing clear evidence of mingling with felsic magma through the presence of dropped crystals derived from the porphyry granite.

4.2 PETROGRAPHY AND MODAL COMPOSITION OF THE MARAJOARA PLUTON

Petrographically, the Marajoara granite is hololeucocratic (M<10%) and has a monzogranitic composition, with local medium equigranular, medium to coarse heterogranular and porphyritic rocks (Table 2 and Fig. 5). Titanite, opaque minerals, allanite, apatite and zircon occur as the primary accessory minerals, whereas chlorite, epidote, sericite-muscovite, clay minerals and fluorite are secondary phases. The pME and ME are limited in volume but are important for understanding the evolution of the Marajoara granite. The pME have a transitional composition between granodiorite and monzogranite and M' between 6.1 and 7.4%, whereas the ME are essentially granodioritic and have ~20% mafic minerals (Table 2; Fig. 4).

Table 2 - Representative modal compositions of the rocks of the Marajoara pluton.

Facies	hBMzG				eBMzG			Porphyritic MEs				MEs	
Sample	GDR 9F-B	RDF 8	RDF 9A	RDF 14A/B	GDR 8B	RDF 2	RDF 11	GDR 9DB	GDR 9F-A	RDF 9B3	RDF 14B	RDF 9B1	RDF 9B2
Minerals (vol%)													
Quartz	46	38.1	30.8	34	30.2	33.6	32.9	35.7	43.3	29.5	39.7	26.8	25
Microcline	25.2	32.3	31.5	29.7	38.5	28.3	27.6	21.7	16.1	19.9	16.3	10.9	10.1
Plagioclase	26.6	22.9	31.7	28.7	26.5	31.6	31.4	34.2	33.2	41.4	35.8	46.4	47.3
Biotite	1.3	1.6	2.9	3.1	3.1	3.9	5.4	5.5	5.4	5.2	5.8	18	19.5
Opaque minerals	0.1	0.9	1	0.7	−	0.3	−	1	0.5	0.7	0.7	1.5	1.3
Titanite	−	0.6	0.3	0.3	0.2	0.3	0.2	−	−	−	−	0.1	0.1
Allanite	−	0.2	0.2	0.5	0.2	0.3	0.1	−	−	0.2	0.2	−	0.1
Secondary minerals	0.4	3.3	1.2	2.6	0.9	1.5	2.1	1.5	0.9	3.1	1.3	0.9	0.4
Pl/Mc	1.1	0.7	1	1	0.7	1.1	1.1	1.6	2.1	2.8	2.2	4.1	4.7
Color index (M')	1.7	3.3	4.3	4.7	3.5	4.8	5.7	7.4	6.8	6.1	6.7	19.8	21.1

Abbreviations: Pl/Mc (plagioclase/microcline ratio); hBMzG - heterogranular biotite monzogranite; eBMzG - equigranular biotite monzogranite; MEs - microgranular enclaves.
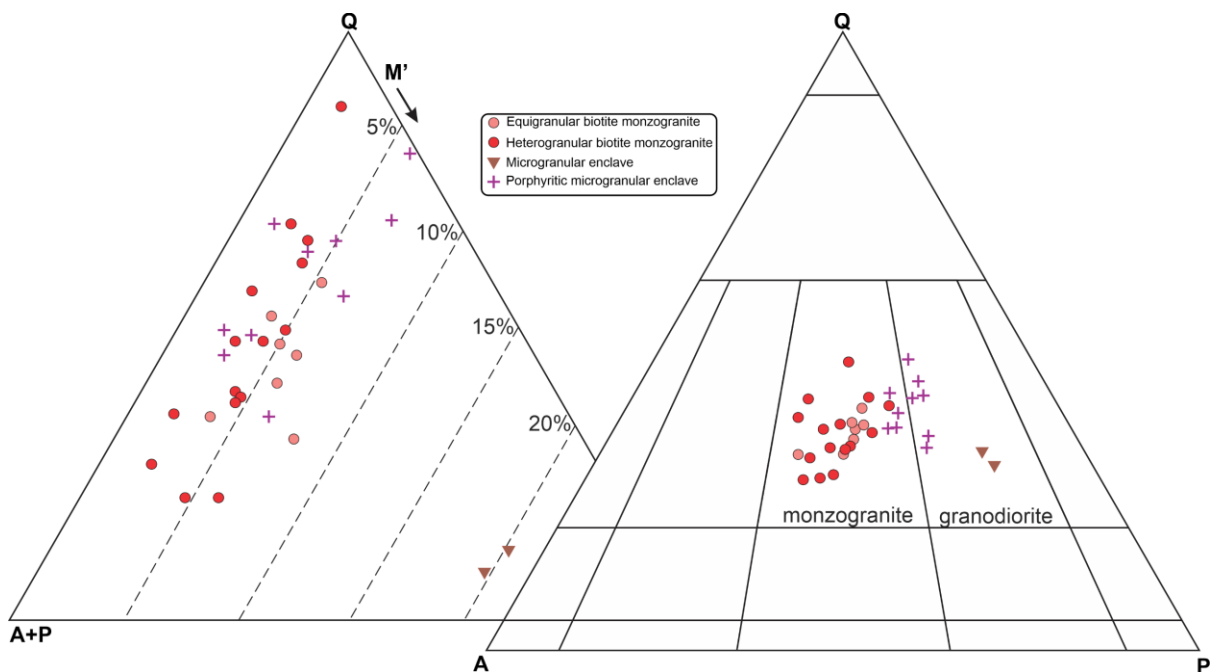
Figure 5 - Q-A-P and Q-(A+P)-M plots for the Marajoara granite (Le Maitre et al., 2002).

The eBMzG facies displays a hypidiomorphic granular texture with sub- and automorphic crystals of feldspars and quartz. The perthitic microcline is locally altered, resulting in the formation of chessboard albite (Fig. 6a, cf. Smith, 1974). Biotite occurs as lamellae ranging in size from 0.3 to 1.5 mm, is brownish in color, and occasionally forms mafic aggregates with inclusions of opaque minerals, apatite, allanite and zircon, which exhibit pleochroic halos (Fig. 6b). The biotite lamellae edges sometimes appear corroded and transformed into muscovite, particularly when in contact with quartz, indicating a reaction of the initially formed biotite with the remaining liquid or hydrothermal fluids (Fig. 6c). Ilmenite appears only as individual ilmenite (I Ilm), in the form of subautomorphic to xenomorphic (Fig.

6d) very fine crystals, which are included in feldspars or are present along the cleavage planes of biotite and chlorite.

The hBMzG facies presents a medium to coarse heterogranular hypidiomorphic texture. Locally, there are alkali feldspar crystals mantled by plagioclase in rapakivi-like texture (Fig. 6e). At microcline/microcline contacts, swapped rims of intergranular albite (Fig. 6f) are common (Smith, 1974). Plagioclase crystals exhibit patchy zoning (Vance, 1965), with irregular sodic zones infiltrating the resorbed calcic cores of the crystals (Fig. 6g). Biotite, the main ferromagnesian phase, occurs in small modal percentages and , generally display the same features described in the eBMzG facies, however, biotite underwent intense alteration into chlorite. In addition to biotite/chlorite, the mafic aggregates consist of opaque minerals (magnetite and ilmenite), and, in smaller proportions, allanite, primary titanite, zircon, and epidote. Two distinct generations of magnetite were identified, one from magmatic crystallization and the other from the alteration of ferromagnesian minerals in the postmagmatic stage. The primary magnetite occurs as subhedral crystals (Fig. 6h), is disseminated and included in feldspars, and sometimes presents apatite inclusions. In contrast, secondary or late magnetite is restricted and occurs as very fine-grained anhedral crystals, which are distributed along the cleavage planes of biotite and chlorite.

The granitic enclaves are associated with the hBMzG facies. They exhibit a porphyritic texture (pME) or, a fine-grained equigranular texture (ME). The pME displays microcline, plagioclase, and subordinately quartz phenocrysts immersed in a fine- to very fine-grained matrix, which constitutes approximately 70% of the rock (Fig. 6i). Compared to the ME, in addition to textural aspects it differs significantly also in modal compositional particularly in total mafic and biotite content and Pl/Mc ratio. The plagioclase crystals exhibit irregular contours and corroded rims, often displaying relationships (Fig. 6j) that can be interpreted as features of synneusis (Vance, 1965) or epitaxy (Dowty, 1980). Coarse quartz crystals frequently exhibit signs of corrosion. In more advanced stages of imbalance, these crystals show roughly rounded sections, reinforcing the hypothesis that they could represent xenocrysts derived from the granitic magma and partially dissolved (Fig. 6k). Magnetite, the dominant opaque mineral, appears relatively well preserved (Fig. 6l), with only incipient martitization.

4.3 GEOCHEMISTRY

4.3.1 Major and trace elements

On the basis of geochemical data, a description of the main compositional characteristics, classification and typification of the studied rocks is presented. The data obtained in this study are also compared with the main granites of the Jamon, Serra dos Carajás and Velho Guilherme suites in the Carajás province. The SiO_2 contents range from 74.80 to 77.70 wt% (Table 3). With increasing SiO_2 content, there are clear decreases in the sum of the compatible elements (TiO_2 + Fe_2O_3t + MgO + CaO) (Fig. 7a) and increases in the Na_2O + K_2O/CaO ratio (0.89–1.64; Fig. 7b) in the most evolved rocks. In the variation diagrams for trace elements, there is similar behavior: the Sr/Ba ratio and the Y and Nb contents increase slightly in the direction of the most silica-enriched rocks, although the microgranular enclaves have slightly higher Sr/Ba ratios (Fig. 7c and d). The contents of Zr (215–93 ppm) tend to decrease with increasing SiO_2 content (Fig. 7f).

4.3.2 Rare earth elements

The facies that constitute the Marajoara granite exhibit enrichment in heavy REEs (HREEs) and light REEs (LREEs), characterized by low La/Yb$_N$ ratios (Fig. 8a). The eBMzG facies displays a more fractionated pattern with pronounced negative Eu anomalies, which are of lower magnitude in the hBMzG facies (Fig. 8b). In contrast, the enclaves do not show enrichment in HREEs (horizontal pattern), and slight fractionation of these elements is observed in the ME (Fig. 8c). Unlike the granitic rocks, these enclaves also exhibit the least fractionated pattern of negative Eu anomalies, ranging from moderate in pME to discrete in ME.
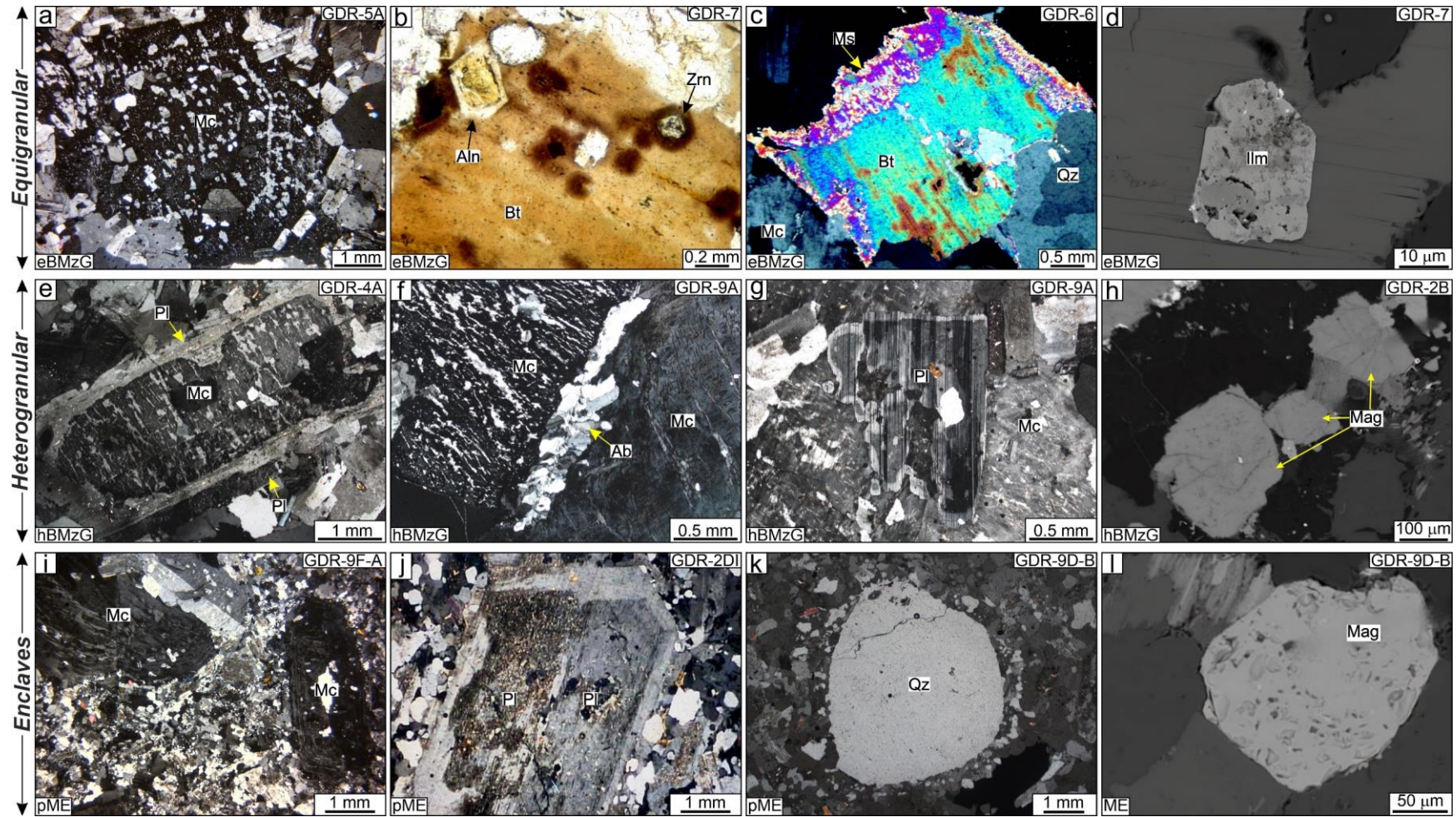
Figure 6 - Photomicrographs of the Marajoara granite: (a) albite chessboard in microcline; (b) biotite with inclusions of allanite and zircon, showing pleochroic halos; (c) biotite bordered by muscovite; (d) subautomorphic individual ilmenite; (e) rapakivi texture; (f) swapped rims of intergranular albite; (g) plagioclase with patchy zoning where the resorbed zones are filled with albite-rich plagioclase; (h) primary subhedral crystal of magnetite; (i) porphyritic texture of pME; (j) plagioclases with synneusis features; (k) quartz xenocryst likely derived from coeval granitic magma; (l) subhedral magnetite with incipient martitization. Abbreviations: Ab (albite); Aln (allanite); Bt (biotite); Chl (chlorite); Ep (epidote); Mc (microcline); Ms (muscovite); Op (opaque mineral); Pl (plagioclase); Qz (quartz); Zrn (zircon).

Table 3 - Geochemical compositions of the Marajoara granite.

Facies	ME			pME						hBMzG					eBMzG				
Sample	RDF	RDF	RDF	GDR	RDF	GDR	RDF	RDF	RDF	GDR	GDR	GDR	RDF	RDF	GDR	GDR	RDF	GDR	RDF
	9B2	9BL2	9B1	9B	14BL	2D	14B	9BL3	9BL1	9A	3	2A	8	9A	7	6	11	5A	2
Major elements (wt%)																			
SiO$_2$	62.88	65.41	68.24	70.92	72.05	72.27	72.33	72.51	72.96	72.97	73.21	73.65	73.69	74.64	75.26	75.46	75.72	76.00	76.27
TiO$_2$	0.26	0.29	0.18	0.25	0.26	0.22	0.27	0.25	0.24	0.17	0.15	0.17	0.17	0.15	0.05	0.05	0.05	0.05	0.05
Al$_2$O$_3$	18.30	16.64	15.60	13.89	14.16	13.45	13.95	13.73	13.70	12.96	13.03	12.84	13.77	13.03	12.78	12.95	13.10	12.56	13.03
Fe$_2$O$_3$t	3.96	4.03	2.88	1.97	2.02	1.73	2.20	2.11	2.12	1.44	1.35	1.44	1.36	1.44	0.80	0.76	0.88	0.78	0.80
MnO	0.14	0.16	0.11	0.07	0.07	0.06	0.07	0.07	0.07	0.04	0.05	0.05	0.04	0.04	0.07	0.07	0.07	0.04	0.05
MgO	1.81	1.59	1.28	0.38	0.38	0.30	0.43	0.39	0.38	0.20	0.18	0.21	0.19	0.20	0.02	0.02	0.02	0.02	0.02
CaO	1.56	1.32	1.05	1.33	1.32	1.17	1.42	1.26	1.32	0.87	0.81	0.92	0.87	0.93	0.39	0.12	0.41	0.11	0.30
Na$_2$O	5.63	4.74	4.44	3.82	3.96	3.69	3.89	3.78	3.69	3.65	3.51	3.61	3.84	3.75	4.03	3.98	4.39	3.90	4.13
K$_2$O	4.91	4.82	5.37	4.64	4.90	4.51	4.48	4.76	4.61	4.68	4.94	4.59	4.92	4.91	4.31	3.99	4.43	4.29	4.53
P$_2$O$_5$	0.07	0.08	0.05	0.07	0.07	0.06	0.07	0.08	0.07	0.04	0.04	0.04	0.03	0.03	0.01	0.02	0.01	0.01	0.01
LOI	0.30	0.80	0.60	1.70	0.60	1.50	0.70	0.90	0.60	1.70	1.50	1.30	1.00	0.70	1.10	1.30	0.80	1.10	0.70
Total	99.82	99.88	99.80	99.04	99.79	98.96	99.81	99.84	99.76	98.72	101.77	98.82	107.88	99.82	105.82	104.72	110.88	98.86	101.89
Trace elements (ppm)																			
Ba	300.0	322.0	249.0	609.2	709.0	561.5	569.0	671.0	672.0	401.9	430.7	414.7	463.0	415.0	16.4	15.4	18.0	23.4	20.0
Rb	707.0	763.1	725.8	579.3	487.9	634.2	515.1	506.5	523.4	470.1	594.8	547.9	505.0	456.4	893.2	841.9	746.5	912.1	782.2
Sr	145.0	85.5	118.9	135.8	134.8	108.8	140.8	133.1	139.7	78.5	81.8	91.3	83.2	77.2	5.6	3.8	4.9	5.2	4.4
Zr	173.4	193.2	131.1	174.4	175.4	172.5	187.2	184.7	186.5	146.5	133.7	147.2	126.0	128.9	100.0	103.5	89.6	112.9	87.6
Nb	14.6	29.0	12.6	24.1	19.0	30.2	17.6	17.5	18.0	33.4	31.7	30.7	29.9	29.0	57.1	70.9	60.9	69.5	56.7
Y	18.3	29.3	17.3	42.3	35.5	48.4	27.8	30.4	28.4	72.0	66.4	51.3	90.0	47.5	104.4	29.2	99.7	26.3	52.7
Ga	18.7	22.0	14.4	21.4	17.9	23.5	18.6	17.7	18.6	22.9	23.4	23.1	20.8	19.0	29.1	29.2	24.7	30.5	25.2
Th	14.4	28.9	12.7	28.0	25.0	29.9	23.6	24.7	26.1	31.6	37.5	33.3	27.3	35.0	51.6	43.8	39.2	47.1	44.2
U	6.9	9.6	5.4	7.4	4.7	7.2	4.3	6.5	6.1	9.3	9.7	8.0	10.3	13.2	12.4	12.6	15.7	15.6	14.2
La	53.3	43.0	37.4	48.9	50.3	51.9	53.6	48.0	50.6	43.4	40.8	37.3	79.6	38.6	19.3	9.1	20.8	7.8	14.0
Ce	90.5	73.8	65.0	104.9	97.4	111.7	105.8	96.3	98.0	89.8	89.8	79.4	127.5	78.2	45.8	22.4	45.9	48.3	33.0
Pr	9.2	7.5	6.5	11.2	10.4	11.7	9.8	10.5	10.5	9.8	9.6	8.6	18.5	8.3	5.6	2.1	5.6	2.1	3.7
Nd	30.2	25.6	21.7	37.9	35.0	42.1	36.4	32.5	36.4	34.2	34.8	30.4	63.1	28.4	20.1	5.8	20.4	6.7	12.3
Sm	4.2	3.8	3.1	6.7	5.7	7.4	5.8	32.5	6.0	6.9	6.9	6.3	12.2	5.7	5.3	1.3	4.8	1.5	2.8
Eu	0.7	0.5	0.6	0.7	0.6	0.7	0.7	0.6	0.7	0.6	0.5	0.5	1.0	0.5	0.1	0.1	0.1	0.1	0.1
Gd	3.2	3.4	2.7	5.0	4.9	5.9	4.5	4.3	4.6	7.1	6.0	5.3	10.8	5.2	5.5	1.4	5.9	1.3	3.4
Tb	0.5	0.5	0.4	1.0	0.8	1.0	0.7	0.7	0.7	1.3	1.2	1.0	1.9	1.0	1.2	0.4	1.2	0.4	0.7
Dy	2.4	3.2	2.1	5.3	4.5	6.2	3.9	4.0	4.2	8.7	7.7	6.6	11.3	6.3	8.6	2.9	8.7	3.0	5.3
Ho	0.5	0.8	0.4	1.1	1.0	1.3	0.8	0.9	0.9	2.1	1.7	1.5	2.5	1.5	2.2	0.8	2.2	0.8	1.4
Er	1.5	2.7	1.3	3.8	3.3	4.6	2.6	2.8	2.7	7.1	6.0	5.0	7.9	4.9	8.8	3.2	8.4	3.4	5.5
Tm	0.3	0.5	0.3	0.6	0.6	0.7	0.4	0.5	0.5	1.2	1.0	0.9	1.4	0.9	1.7	0.7	1.6	0.7	1.1
Yb	2.0	3.6	1.9	4.2	3.7	5.0	2.9	3.3	3.3	7.9	7.1	6.4	10.2	6.2	12.9	5.2	13.2	5.2	8.3
Lu	0.4	0.6	0.3	0.7	0.6	0.8	0.5	0.5	0.5	1.3	1.2	1.0	1.6	1.1	2.2	1.0	2.3	0.9	1.5
FeOt/FeOt+MgO	0.66	0.70	0.67	0.82	0.83	0.84	0.82	0.83	0.83	0.87	0.87	0.86	0.87	0.87	0.97	0.97	0.98	0.97	0.97
Mg#	47.52	43.87	46.82	27.65	27.15	25.57	27.91	26.80	26.21	21.58	20.90	22.42	21.68	21.58	4.72	4.96	4.31	4.83	4.72
Na$_2$O+K$_2$O/CaO	6.76	7.24	9.34	6.36	6.71	7.01	5.89	6.78	6.29	9.57	10.43	8.91	10.07	9.31	21.38	66.42	21.51	74.45	28.87
ASI	1.06	1.09	1.04	1.02	1.00	1.03	1.01	1.01	1.02	1.03	1.04	1.02	1.04	0.99	1.07	1.17	1.03	1.12	1.07
Rb/Sr	4.9	8.9	6.1	4.3	3.6	5.8	3.7	3.8	3.7	6.0	7.3	6.0	6.1	5.9	159.5	221.6	152.3	175.4	177.8
ΣREE	198.7	169.5	143.6	231.9	218.7	251.0	229.9	236.6	219.6	221.3	214.2	190.1	349.5	186.7	139.4	56.2	141.2	82.2	93.0
(La/Yb)$_N$	17.7	8.0	13.5	7.9	9.1	7.0	12.5	9.9	10.4	3.7	3.9	4.0	5.3	4.2	1.0	1.2	1.1	1.0	1.1
Eu/Eu*	0.6	0.4	0.6	0.4	0.4	0.3	0.4	0.1	0.4	0.3	0.3	0.2	0.3	0.3	0.1	0.1	0.1	0.2	0.1

Fe$_2$O$_3$t = total iron recalculated as Fe$_2$O$_3$; Eu/Eu* = Eu$_N$/[(Sm$_N$ + Gd$_N$)/2]; La$_N$, Yb$_N$, Eu$_N$, Sm$_N$ and Gd$_N$ normalized to C1 chondrite (McDonough and Sun, 1995). Abbreviations: ASI - Alumina saturation index (Frost et al., 2001); LOI - loss on ignition, hBMzG - heterogranular biotite monzogranite; eBMzG - equigranular biotite monzogranite; ME - microgranular enclave; pME - porphyritic microgranular enclave.

The samples of the hBMzG facies present very similar REE patterns. These rocks can be distinguished from those of the Jamon suite by their lack of HREE fractionation and from those of the Velho Guilherme suite by their more discrete negative Eu anomalies and greater La/YbN ratios (Fig. 8b). However, the REE patterns of the hBMzG facies show greater affinity with those of the Serra dos Carajás suite, differing in terms of the greater enrichment in LREEs in the latter (Fig. 8a). On the other hand, the REE patterns of the eBMzG facies exhibit strong affinities with those of the Velho Guilherme suite, whose pronounced negative Eu anomalies distinguish them from the patterns presented by the other suites. Finally, the REE patterns of the pME (Fig. 8c) resemble those of the hBMzG facies of the Marajoara granite, and the patterns of the ME with slight HREE fractionation are similar to those of the Jamon suite rocks.

Figure 7 - Harker diagrams (in wt.%) for the Marajoara granite compared with the Paleoproterozoic suites in the Carajás province.
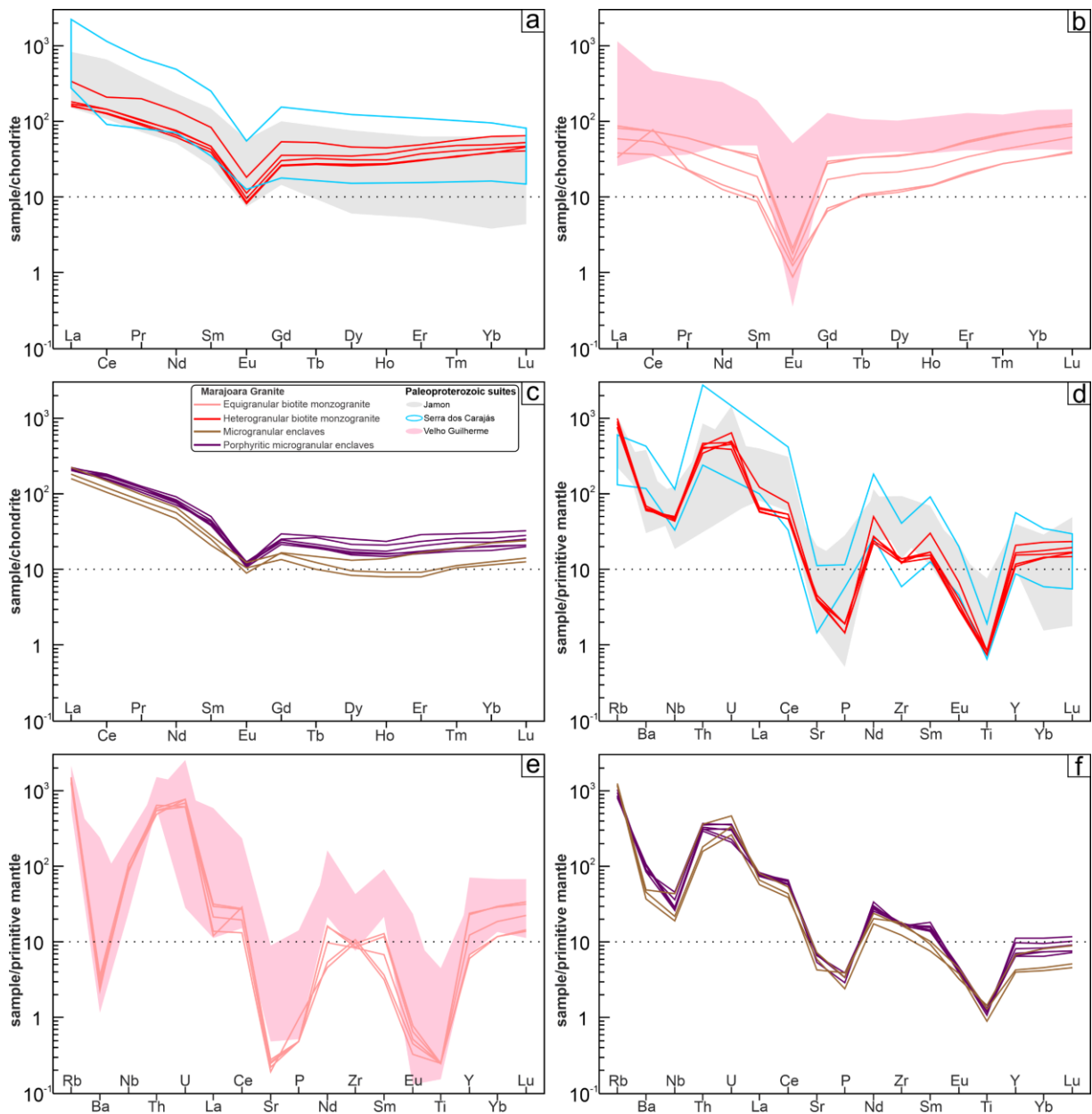
Figure 8 - (a, b and c) REE and (c, d and e) multielement patterns of the Marajoara granite. The values are normalized to those of C1 chondrites and the primitive mantle (McDonough and Sun, 1995).

The samples of the hBMzG facies present very similar REE patterns. These rocks can be distinguished from those of the Jamon suite by their lack of HREE fractionation and from those of the Velho Guilherme suite by their more discrete negative Eu anomalies and greater La/YbN ratios (Fig. 8b). However, the REE patterns of the hBMzG facies show greater affinity with those of the Serra dos Carajás suite, differing in terms of the greater enrichment in LREEs in the latter (Fig. 8a). On the other hand, the REE patterns of the eBMzG facies exhibit strong affinities with those of the Velho Guilherme suite, whose pronounced negative Eu anomalies distinguish them from the patterns presented by the other suites. Finally, the REE patterns of the pME (Fig. 8c) resemble those of the hBMzG facies of the Marajoara granite, and the patterns

of the ME with slight HREE fractionation are similar to those of the Jamon suite rocks.

In the multielement diagram, the Marajoara granite samples (Fig. 8d and e) exhibit negative anomalies in Ba, Nb, Sr, P, Eu, and Ti, whereas the enclave samples (Fig. 8f) exhibit anomalies in Nb, P, and Ti. The REE patterns clearly indicate that the eBMzG facies is closely related to the Velho Guilherme suite (Fig. 8e) since it presents strongly negative anomalies in Ba, Sr, and Ti. On the other hand, the hBMzG facies shows similarities with the Jamon suite, as it displays moderate negative anomalies in Nb, P, and Ti (Fig. 8d).

4.4 CLASSIFICATION, TYPOLOGY AND TECTONIC AFFINITY

The Marajoara pluton is characterized by high SiO_2 contents (>72 wt%); moderate HFSE contents, ΣREE values (56.24–349.54 ppm) and Na_2O+K_2O/CaO values (7.97–8.82); high FeOt/(FeOt+MgO) ratios (0.86–0.98); and low concentrations of CaO (0.11–0.93 wt%), Al_2O_3 (12.56–13.77 wt%) and Sr (3.80–91.30 ppm). In diagram A-B (Debon and Le Fort, 1983), the rocks of the Marajoara granite are essentially peraluminous (Fig. 9a), with ASI (alumina saturation index) values predominantly > 1 (Table 3) The eBMzG plots in the field where muscovite predominates, while the hBMzG plots in the biotite field. In the MALI (modified alkali–lime index) diagram, the rocks of the Marajoara granite plot in the field of alkalic–calcic granites (Fig. 9b). In the classification proposed by Frost et al. (2001), which utilizes the Fe* index (FeOt/FeOt+MgO) to differentiate ferroan granites from those with magnesian affinity, the rocks of the Marajoara granite are categorized as ferroan granites (Fe*>0.9 – Fig. 9c), unlike the enclaves, which resemble magnesian granites. Their geochemical features are compatible with those of A-type granites according to the major and trace element-based discrimination diagrams of Whalen et al. (1987) and Dall'Agnol and Oliveira (2007) (Fig. 9d and Fig. 9e, respectively). The eBMzG facies has an affinity with reduced A-type granites, the hBMzG facies has an affinity with oxidized A-type granites, and the microgranular enclaves have an affinity with calc-alkaline granitoids (Fig. 9e). In the Nb–Y diagram of Pearce et al. (1984), the Marajoara granite correlates with intraplate granites (Fig. 9f).

4.5 ZIRCON DATING

4.5.1 Marajoara granite

Sixteen zircon crystals were examined (Tab. 4), of which 11 yielded useable data for age determination. Cathodoluminescence images (Fig. 10) reveal the presence of fractures,

small irregular inclusions, frequent concentric oscillatory zoning, and the absence of inherited cores. These crystals exhibit euhedral to subhedral morphologies, with pyramidal terminations that are occasionally subrounded, and they exhibit varying dimensions ranging from approximately 90 to 300 microns in length and 60 to 170 microns in width.
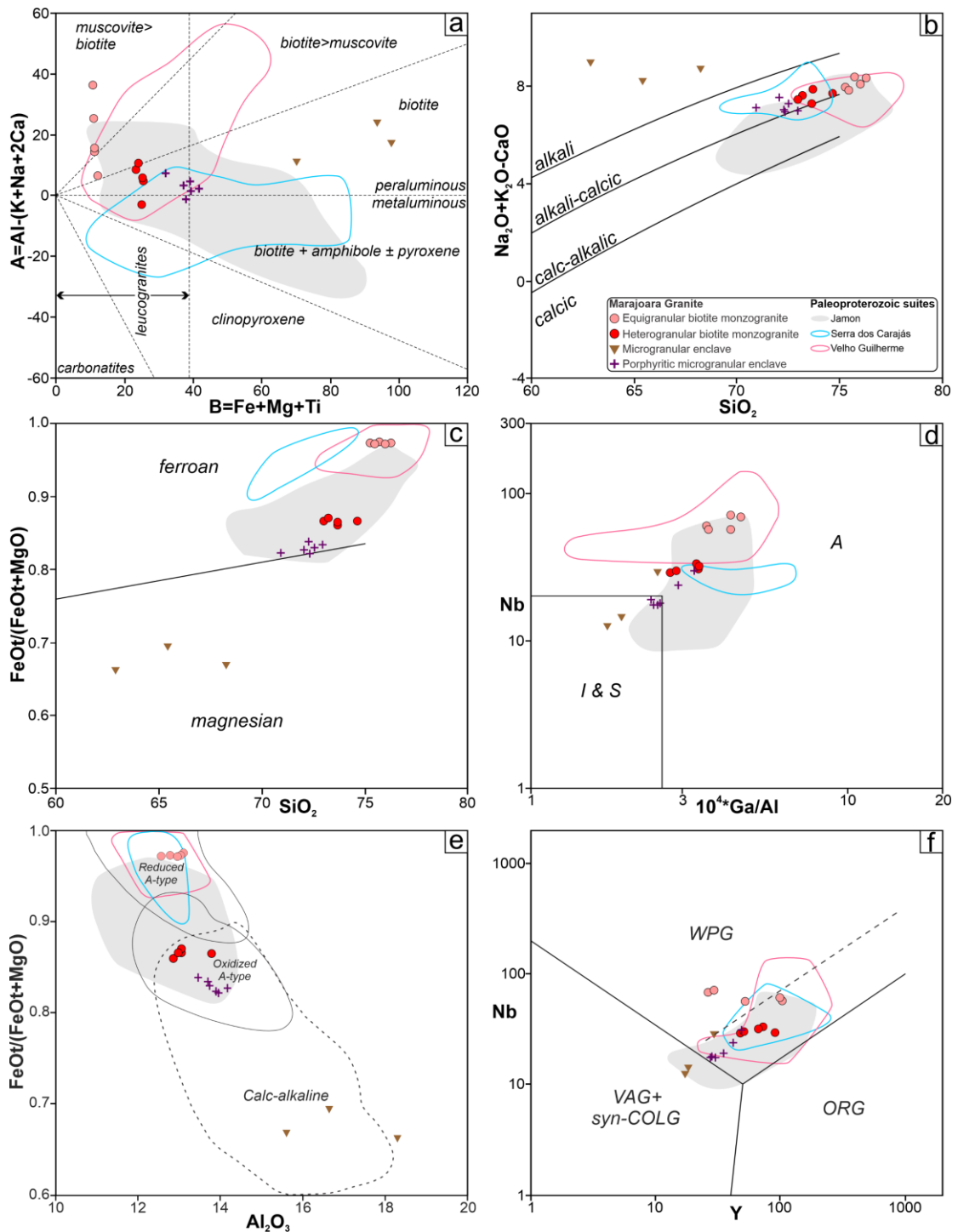
Figure 9 - Geochemical classification and typology of Marajoara granite: (a) A-B diagram from Debon and Le Fort (1983); (b) Na_2O+K_2O–CaO (MALI) vs. SiO_2 diagram (Frost et al., 2001); (c) $10^4*Ga/Al$ vs. Nb diagram (Whalen et al., 1987); (e) Al_2O_3 vs. FeOt/FeOt+MgO diagram (Dall'Agnol and Oliveira, 2007); and (f) Y vs. Nb diagram (Pearce et al., 1984).

Table 4 - Zircon U–Pb isotope data obtained with a SHRIMP for the Marajoara granite (GDR-9FB).

GDR-9FB					Isotopics Ratios [c]							Ages (Ma)						
Spot ID	f_{206} [a]	U	Th	Th/U [b]	$^{207}Pb/^{235}U$	1σ	$^{206}Pb/^{238}U$	1σ	Rho [d]	$^{207}Pb/^{206}Pb$ [e]	1σ	$^{206}Pb/^{238}U$	1σ	$^{207}Pb/^{235}U$	1σ	$^{207}Pb/^{206}Pb$	1σ	Conc [f]
	(%)	ppm	ppm			(%)		(%)			(%)		abs		abs		abs	(%)
2.4	0.21	124	104	0.87	4.4967	1.6	0.2804	1.2	0.75	0.1163	1.1	1593	17	1730	21	1900	20	92.1
2.5 *	0.00	101	123	1.25	5.5074	1.6	0.3436	1.2	0.80	0.1162	0.9	1904	20	1902	24	1899	18	100.1
3.2 *	0.19	244	268	1.13	5.3880	1.3	0.3401	1.1	0.83	0.1149	0.7	1887	18	1883	20	1878	13	100.2
3.5 *	0.14	346	219	0.65	5.3661	1.4	0.3399	1.0	0.72	0.1145	1.0	1886	17	1879	19	1872	18	100.4
4.2	0.00	95	72	0.78	5.6783	1.5	0.3574	1.3	0.86	0.1152	0.7	1970	21	1928	24	1884	14	102.2
4.3 *	-0.19	25	30	1.25	5.7312	2.3	0.3470	1.6	0.70	0.1198	1.6	1920	27	1936	32	1953	32	99.2
5.1 *	0.08	317	230	0.75	5.2663	1.2	0.3331	1.1	0.92	0.1147	0.5	1853	18	1863	21	1875	9	99.5
5.2 *	0.15	72	69	0.99	5.3329	1.8	0.3380	1.3	0.75	0.1144	1.1	1877	22	1874	25	1871	21	100.2
5.5 *	0.31	126	125	1.02	5.5209	1.6	0.3449	1.2	0.79	0.1161	1.0	1910	21	1904	24	1897	17	100.3
6.2 *	0.32	27	38	1.44	5.6287	2.4	0.3492	1.6	0.68	0.1169	1.7	1931	27	1921	32	1910	33	100.5
6.4 *	0.34	169	135	0.82	5.2474	1.5	0.3296	1.2	0.76	0.1155	1.0	1836	19	1860	22	1887	18	98.7
5.3	*0.01*	*888*	*610*	*0.71*	*1.9894*	*1.2*	*0.1531*	*1.1*	*0.91*	*0.0942*	*0.5*	*918*	*9*	*1112*	*12*	*1513*	*8*	*82.6*
6.1	*0.44*	*849*	*245*	*0.30*	*1.6589*	*1.4*	*0.1343*	*1.1*	*0.76*	*0.0896*	*0.9*	*813*	*8*	*993*	*11*	*1416*	*13*	*81.8*
6.3	*0.41*	*3305*	*3159*	*0.99*	*1.4560*	*1.3*	*0.1249*	*1.1*	*0.85*	*0.0845*	*0.6*	*759*	*8*	*912*	*10*	*1305*	*8*	*83.2*
7.3	*0.74*	*1300*	*680*	*0.54*	*1.0899*	*1.8*	*0.1028*	*1.1*	*0.61*	*0.0769*	*1.4*	*631*	*7*	*748*	*8*	*1118*	*15*	*84.3*
9.4	*0.60*	*8007*	*1740*	*0.22*	*0.4131*	*1.9*	*0.0516*	*1.4*	*0.72*	*0.0581*	*1.3*	*324*	*4*	*351*	*5*	*533*	*7*	*92.3*

* Concordant zircon. *Italics = zircon excluded from age calculation*.

[a] Fraction of the nonradiogenic ^{206}Pb in the analyzed zircon spot, where f_{206} = [$^{206}Pb/^{204}Pb$]c / [$^{206}Pb/^{204}Pb$]s (c=common; s=sample).

[b] Th/U ratios and amount of Pb, Th and U (in pmm) are calculated relative to Temora reference zircon.

[c] Corrected for background and within-run Pb/U fractionation and normalized to reference zircon Temora (ID-TIMS values/measured value).

[d] Rho is the error correlation defined as the quotient of the propagated errors of the $^{206}Pb/^{238}U$ and the $^{207}/^{235}U$ ratio.

[e] Corrected for mass-bias by normalising to Temora reference zircon and common Pb using the model Pb composition of Stacey and Kramers (1975).

[f] Degree of concordance = ($^{206}Pb/^{238}U$ age / $^{207}Pb/^{235}U$ age) * 100, according to Horstwood et al. (2016).
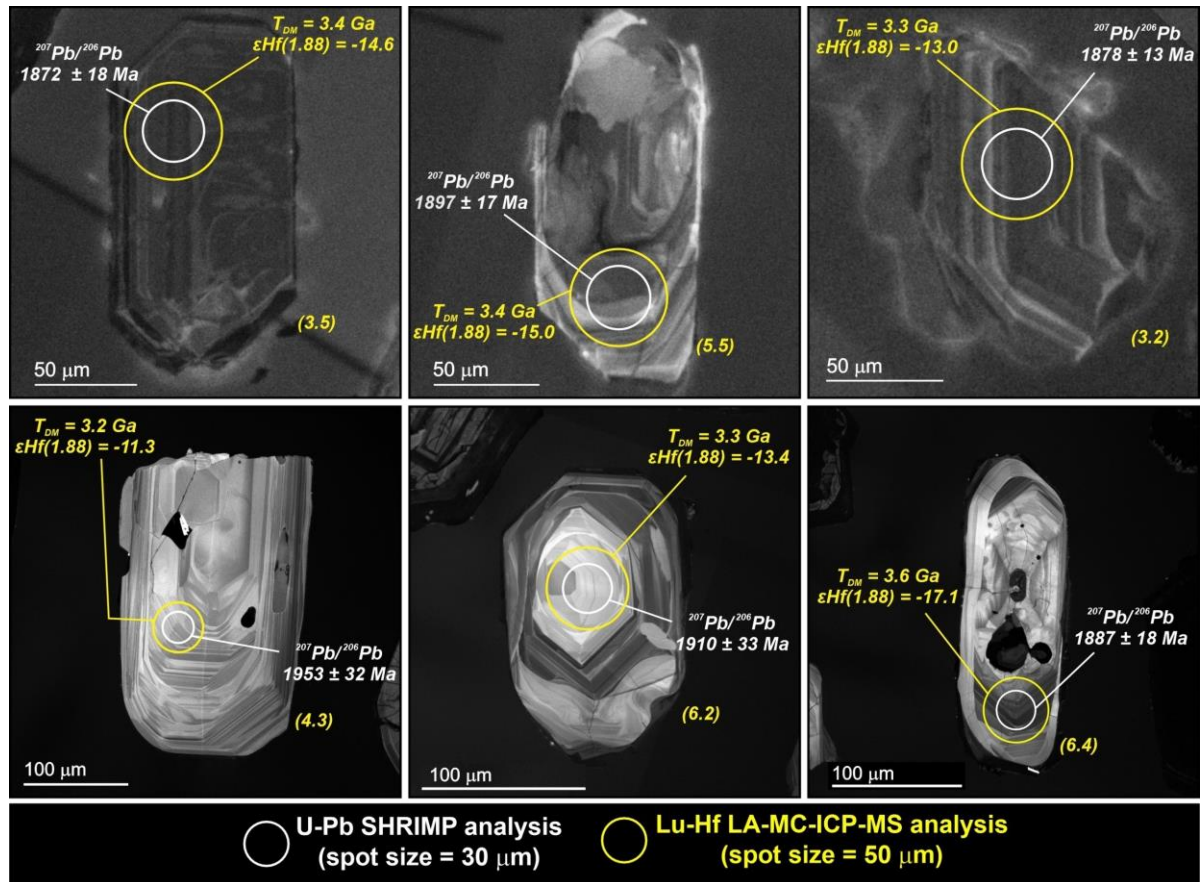
Figure 10 - Cathodoluminescence images representative of zircon grains from the Marajoara granite, with their respective in situ U–Pb (^{207}Pb/^{206}Pb ages; white values) and Lu–Hf (ε_{Hf} and Hf–T_{DM}^C; yellow values) data. The numbers in parentheses correspond to the analyzed spots.

All ages were calculated assuming a concordance level of $100 \pm 2\%$. The U–Pb diagram indicates an upper intercept age of 1884 ± 11 Ma (2σ, MSWD = 1.13, n = 11), with a ^{207}Pb/^{206}Pb weighted average age of 1884 ± 9.5 Ma (2σ, MSWD = 0.93, n = 11), and a concordia age of 1883 ± 8.8 Ma (2σ, MSWD = 0.001, n = 9). The resulting mean age is interpreted as the crystallization age of the Marajoara granite. This age coincides with the crystallization ages of Paleoproterozoic A-type granites found in the Carajás province (Fig. 11a).

4.5.2 Composite and porphyry granite dikes

The zircon grains range in color from colorless and transparent to dark brown or pink (Fig. 11b). They exhibit euhedral to subhedral shapes and vary in form from long to slightly elongated. Their lengths range from 120 to 350 μm, with length–width ratios between 2 and 3. Sample DR-2D from the composite dike yielded twenty-three zircon crystals. Only six crystals (DR2D/1, DR2D/4, DR2D/6, DR2D/7, DR2D/8 and DR2D/9 – Table 5) presented satisfactory Pb values for calculating an age, which was found to be 1885 ± 4 Ma on average.

Table 5 - Analytical results for Pb–Pb evaporation for the composite dike.

Zircon	Temperature	Ratios	$^{204}Pb/^{206}Pb$	2σ	$^{208}Pb/^{206}Pb$	2σ	$^{207}Pb/^{206}Pb$	2σ	$(^{207}Pb/^{206}Pb)c$	2σ	Age	2σ
DR2D/1	1450	0/34	0.000177	25	0.17786	101	0.1163	27	0.11393	64	1863	10
	1500	34/34	0.000091	13	0.19074	45	0.11603	26	0.11469	31	1875	5
	1550	38/38	0.000115	26	0.20006	58	0.11637	48	0.11491	41	1879	6
DR2D/3	#1500	0/8	0.001641	492	0.31524	251	0.13103	366	0.10874	782	1779	131
	#1500	0/8	0.003325	2312	0.32702	169	0.12194	367	0.07465	3505	1059	945
DR2D/4	*1450	0/32	0.000056	8	0.22067	471	0.11526	32	0.11448	40	1872	6
	1550	30/30	0.000015	4	0.21946	106	0.1158	38	0.11559	37	1889	6
DR2D/5	*1450	0/36	0.000123	6	0.20905	47	0.11485	18	0.11308	21	1850	3
	*1550	0/20	0.000073	13	0.24948	289	0.11529	41	0.11404	37	1865	6
DR2D/6	1450	28/28	0.000185	5	0.25013	67	0.11785	40	0.11539	38	1886	6
	1500	36/36	0.000097	3	0.21538	137	0.11704	15	0.11566	20	1891	3
DR2D/7	#1450	0/16	0.000494	107	0.2388	70	0.1219	58	0.11491	59	1879	9
	1500	36/36	0.000035	4	0.2537	94	0.116	15	0.11554	15	1889	2
DR2D/8	*1450	0/36	0.000082	11	0.19871	99	0.11328	19	0.11219	18	1835	3
	1500	38/38	0.000033	3	0.23674	584	0.11513	15	0.11467	16	1875	2
DR2D/9	*1450	0/16	0.00026	16	0.24495	118	0.11819	49	0.11471	40	1876	6
	1500	34/34	0.00004	7	0.24355	77	0.11604	15	0.11546	16	1887	2
	1550	40/40	0.000032	2	0.23961	115	0.11591	24	0.11549	24	1888	4
DR2D/10	*1550	0/34	0.000233	24	0.22231	146	0.11617	20	0.11317	45	1851	7
	Total	314/554								Average age 1885		4

(#) Evaporation stage eliminated for present $^{204}Pb/^{206}Pb$ ration higher than 0.0004; (*) Evaporation stage eliminated subjectively.
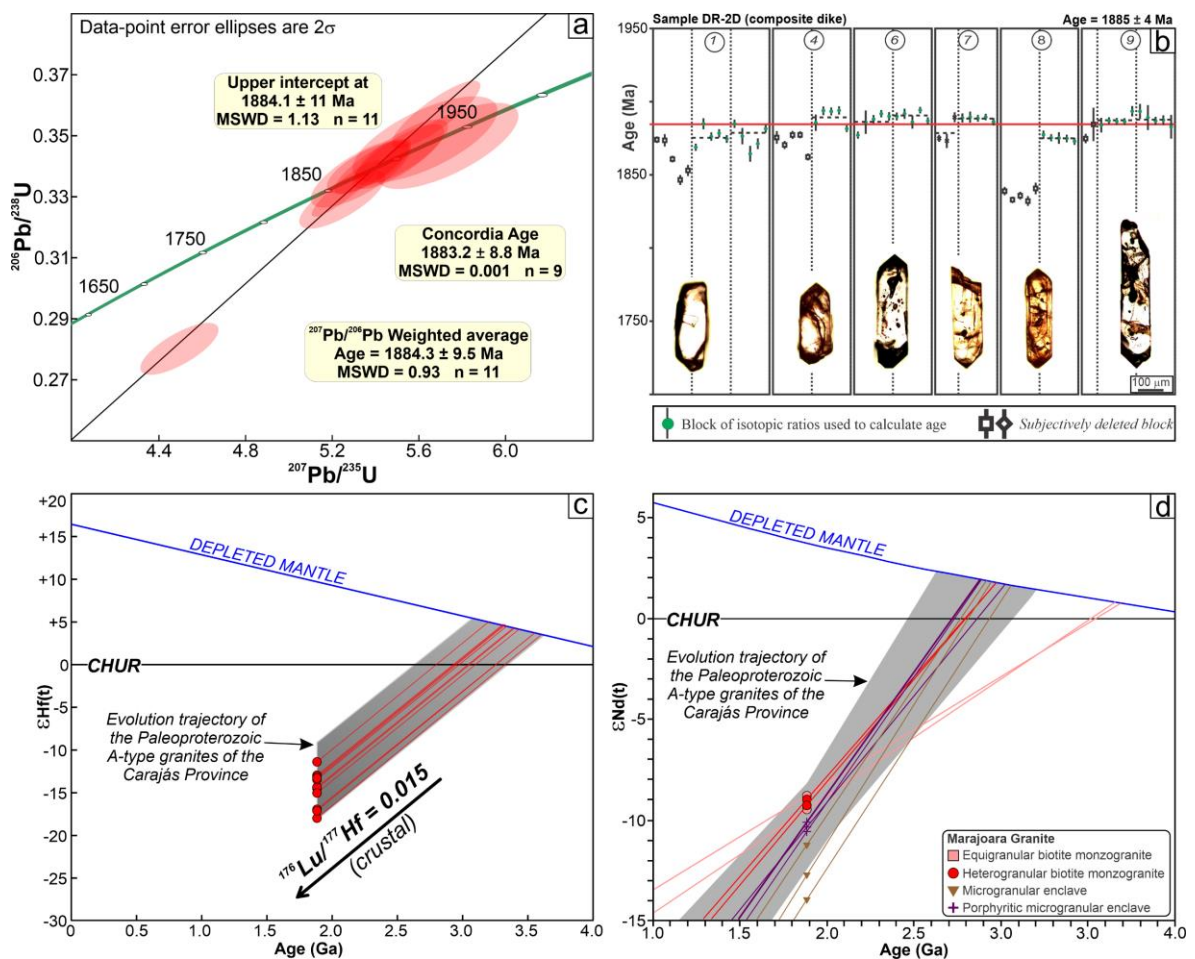
Figure 11 - Isotopic data for the Marajoara granite: (a) Concordia diagram showing U–Pb analyses for zircon crystals; (b) zircon crystals and Pb–Pb mean ages of the composite dike in the Rio Maria region; (c) and (d) $\varepsilon_{Hf}(t)$ and $\varepsilon_{Nd}(t)$ vs. age (Ga), respectively, showing the evolutionary trajectory of the Marajoara granite in comparison with the Paleoproterozoic A-type granites of the Carajás province (Rämö et al., 2002; Teixeira et al., 2019). In the Hf diagram, values for the CHUR (uniform chondritic reservoir) are based on Bouvier et al. (2008), whereas those for the DM (depleted mantle) are based on Andersen et al. (2009).

Twenty-seven zircon crystals from the porphyry granite sample DR-34 were analyzed. From these analyses, 6 crystals (DR34/1, DR34/2, DR34/3, DR34/7, DR34/9, DR34/11 - Table 6) contained sufficient Pb and were used for age calculation, providing a mean age of 1885 ± 2 Ma. Both determined ages are fully concordant with the crystallization ages of the Marajoara granite, as well as with other anorogenic plutons and various dikes, also of Paleoproterozoic age, from the Carajás province, in addition to other provinces of the Amazonian craton.

Table 6 - Analytical results for Pb–Pb evaporation for the porphyry granite.

Zircon	Temperature	Ratios	$^{204}Pb/^{206}Pb$	2σ	$^{208}Pb/^{206}Pb$	2σ	$^{207}Pb/^{206}Pb$	2σ	$(^{207}Pb/^{206}Pb)c$	2σ	Age	2σ
DR34/1	1450	32/32	0.000119	9	0.32639	87	0.11674	16	0.11514	22	1882	3
DR34/2	1450	28/32	0.000143	4	0.30611	77	0.11714	20	0.11519	21	1883	3
	1500	16/40	0.000399	10	0.3266	400	0.12103	27	0.11569	31	1891	5
DR34/3	1450	30/36	0.000121	3	0.37234	93	0.11683	18	0.11524	17	1884	3
DR34/4	#1450	0/4	0.00527	354	0.43372	697	0.18143	48	0.11193	506	1831	82
	*1500	0/40	0.000036	12	0.3659	109	0.11681	35	0.11607	27	1897	4
	*1550	0/38	0.000066	11	0.36696	148	0.117	36	0.11617	44	1898	7
DR34/7	1450	32/32	0.000087	3	0.34457	536	0.11627	16	0.11512	17	1882	3
	1500	14/14	0.000006	2	0.36444	127	0.11606	52	0.11598	54	1895	8
	1500	8/8	0.000029	4	0.36779	186	0.11578	28	0.11539	28	1886	4
DR34/8	#1450	0/40	0.001738	104	0.34707	194	0.13872	176	0.11471	66	1876	10
	#1500	0/32	0.004685	486	0.50424	1798	0.17114	801	0.11495	114	1879	18
DR34/9	1450	28/28	0.000154	9	0.2928	288	0.1176	45	0.11544	36	1887	6
DR34/10	*1450	0/8	0.000297	96	0.31036	286	0.11793	28	0.11393	133	1863	21
DR34/11	1500	38/38	0.000105	4	0.33232	76	0.11667	19	0.1153	17	1885	3
	1550	24/40	0.000341	5	0.35872	103	0.12017	33	0.11562	34	1890	5
	Total	250/462							**Average age**		**1885**	**2**

(#) Evaporation stage eliminated for present $^{204}Pb/^{206}Pb$ ration higher than 0.0004. (*) Evaporation stage eliminated subjectively.

4.6 Lu–Hf ZIRCON ISOTOPES

The concordant to subconcordant zircon crystals from the Marajoara granite (heterogranular biotite monzogranite, sample GDR-9FB), which yielded a concordant curve (Fig. 11a), were analyzed via LA–MC–ICP–MS, and the results are presented in Table 7. The Hf isotope analyses present $^{176}Hf/^{177}Hf$ initial ratio values varying between 0.281146 and 0.281287, all with very negative $\varepsilon_{Hf}(t)$ values (-11.33 to -17.93) and Hf-T_{DM}^C with Archean ages (3.21–3.62 Ga). Thus, a Paleoarchean crustal source contributed to magma genesis, and the Marajoara granite experienced an extended crustal residence period.

4.7 WHOLE-ROCK Sm–Nd ISOTOPES

The Sm–Nd isotope data obtained from 10 samples of the Marajoara granite and their enclaves are listed in Table 8 and are plotted in the Nd evolution diagram (Fig. 11d). The Sm contents vary between 3.36 and 13.06 ppm, and the Nd concentrations range from 14.43 to 67.35 ppm. There is a small variation in $^{147}Sm/^{144}Nd$ (0.0862–0.1172), and eBMzG presents the highest values (0.1502–0.1544). The T_{DM} model ages vary from 2.86 to 3.66 Ga, and the $\varepsilon_{Nd}(t)$

values at 1884 Ma are highly negative, varying from -8.66 to -13.94.

Table 7 - Lu–Hf isotopic data on zircon by LA–MC–ICP–MS. *Calculated from the ratio $^{176}Lu/^{177}Hf = 0.015$, mean value for the continental crust (Griffin et al., 2002).

Spot ID	$^{176}Hf/^{177}Hf$	2SE	$^{176}Lu/^{177}Hf$	2SE	$^{176}Yb/^{177}Hf$	2SE	$\varepsilon_{Hf}(0)$	$t_{(U-Pb)}$ (Ma)	$^{176}Hf/^{177}Hf_{(Zr,t)}$	$\varepsilon_{Hf}(t)$	$T_{DM}{}^{C}$ (Ga)*
2.4	0.281287	0.000082	0.002091	0.000080	0.128230	0.003103	-52.99	1884	0.281212	-13.13	3.32
2.5	0.281175	0.000065	0.002051	0.000078	0.142342	0.004294	-56.92	1884	0.281102	-17.03	3.56
3.2	0.281264	0.000050	0.001372	0.000023	0.112130	0.001568	-53.77	1884	0.281215	-13.01	3.32
3.5	0.281235	0.000072	0.001793	0.000078	0.142620	0.003692	-54.82	1884	0.281171	-14.59	3.42
4.2	0.281234	0.000095	0.000781	0.000040	0.047763	0.002156	-54.84	1884	0.281206	-13.32	3.34
4.3	0.281283	0.000107	0.000563	0.000020	0.032224	0.001133	-53.13	1884	0.281263	-11.33	3.21
5.1	0.281231	0.000075	0.001465	0.000055	0.114997	0.004993	-54.97	1884	0.281178	-14.33	3.40
5.2	0.281146	0.000104	0.001937	0.000191	0.117463	0.010491	-57.96	1884	0.281077	-17.93	3.62
5.5	0.281209	0.000058	0.001370	0.000046	0.096745	0.004607	-55.74	1884	0.281160	-14.98	3.44
6.2	0.281237	0.000051	0.000953	0.000103	0.060260	0.003848	-54.73	1884	0.281203	-13.44	3.34
6.4	0.281217	0.000084	0.003276	0.000595	0.201190	0.022719	-55.45	1884	0.281100	-17.11	3.57

Table 8 - Whole-rock Sm–Nd isotope data for Marajoara granite.

Samples	Sm (ppm)	Nd (ppm)	$^{147}Sm/^{144}Nd$	$^{143}Nd/^{144}Nd$	2σ	$f_{(Sm/Nd)}$	$\varepsilon_{Nd}(0)$	T_{U-Pb} (Ma)	$\varepsilon_{Nd}(t)$	Nd-T_{DM} (Ga)	Nd-$T_{DM}{}^{2}$ (Ga)
eBMzG											
RDF-2	3.72	15.09	0.1489	0.511568	0.000014	-0.24	-20.87	1884 *	-9.35	3.58	2.89
RDF-11	5.89	23.04	0.1544	0.511672	0.000010	-0.21	-18.84	1884 *	-8.66	3.66	2.84
hBMzG											
RDF-8	13.06	67.35	0.1172	0.511200	0.000001	-0.40	-28.05	1884	-8.87	2.95	-
RDF-9A	5.27	27.71	0.1149	0.511156	0.000004	-0.42	-28.91	1884	-9.17	2.95	-
pME											
RDF-9BL1	4.08	22.09	0.1117	0.511060	0.000005	-0.43	-30.78	1884	-10.27	3.00	-
RDF-9BL3	6.23	37.92	0.0992	0.510918	0.000004	-0.50	-33.55	1884	-10.03	2.86	-
RDF-14BL	6.61	38.38	0.1041	0.510978	0.000006	-0.47	-32.38	1884	-10.03	2.90	-
ME											
RDF-9B1	3.36	22.61	0.0899	0.510602	0.000021	-0.54	-39.72	1884	-13.94	3.04	-
RDF-9B2	4.56	32.01	0.0862	0.510620	0.000005	-0.56	-39.37	1884	-12.70	2.93	-
RDF-9BL2	4.17	26.79	0.0942	0.510797	0.000010	-0.52	-35.91	1884	-11.18	2.89	-

T_{DM} and $\varepsilon_{Nd}(t)$ were calculated relative to CHUR and depleted mantle (DM) with present-day values of $^{143}Nd/^{144}Nd = 0.512638$ and $^{147}Sm/^{144}Nd = 0.1967$, following the De Paolo and Wasserburg (1976) and De Paolo (1981) models, respectively, for Nd isotope evolution of depleted mantle. [2] Two-Stage Model Age; * Inferred Age; Abbreviations: hBMzG - heterogranular biotite monzogranite; eBMzG - equigranular biotite monzogranite; ME - microgranular enclave; pME - porphyritic microgranular enclave.

5 DISCUSSION

5.1 PETROLOGICAL AFFINITIES

The Marajoara granite shows strong geochemical, mineralogical and textural affinities with the other Paleoproterozoic granites of the Carajás province. All granitic samples have high SiO_2 (>72 wt%) contents; very high $FeOt/FeOt+MgO$ (0.86–0.98), ($K_2O + Na_2O$)/CaO (7.97–8.82) and Rb/Sr (5.91–221.55) ratios; and very low Mg# values (4.31–22.42). The Marajoara granite is composed of monzogranitic rocks with mafic mineral contents typically less than 5%. These rocks also feature significant fluorite and allanite contents, with an absence of amphibole and a scarcity of magmatic titanite. In these aspects, the studied pluton displays strong similarities with the granites of the Velho Guilherme suites (characterized by the absence of

magmatic titanite and an enrichment in fluorite and topaz) and Serra dos Carajás (where titanite is rare or absent, whereas fluorite and allanite are more common). Unlike the oxidized granites of the Jamon suite, the Marajoara granite differs primarily in having less evolved facies, which are characterized by the frequent presence of amphibole and a relatively high ferromagnesian mineral content ranging between 5% and 20%, with magmatic titanite representing a common phase. However, the notable occurrence of magnetite in rocks belonging to the hBMzG facies and its greater scarcity in the eBMzG variety of Marajoara granite, as well as in the rocks of the Velho Guilherme and Serra dos Carajás suites, aligns the hBMzG facies more closely with the granites that represent the final stages of construction of the Jamon suite, in which biotite is the main ferromagnesian mineral.

The affinities between these rock groups are further supported by the more evolved characteristics of the reduced granites (evidenced by low levels of Ba, Sr and Ti, compared with those with an oxidized character, as shown in Fig. 8e). Regarding the amplitude of negative Eu anomalies observed in the Paleoproterozoic suites of Carajás, moderate anomalies found in the Marajoara granite are exclusively associated with the hBMzG rocks and are consistent with those exhibited by the oxidized rocks of the Jamon suite. These characteristics differ notably from the pronounced anomalies observed in the eBMzG facies of the Marajoara granite, which are similar, in this regard, to those of the Velho Guilherme suite (see Fig. 8b). This correlation is also evident in the varying magnitudes of negative anomalies in Ba, Sr, P, and Ti within the Marajoara granite facies (see Fig. 8e).

Magnetic susceptibility (MS) data were collected from the granitic varieties comprising the Marajoara granite to enhance the petrological affinity analysis (see Supplementary Data Table A). This information is summarized in Fig. 12, as are data on the magnetic signatures of the Paleoproterozoic suites of the Carajás province. The MS values are attributed primarily to the modal content of magnetite, allowing for the differentiation of these suites on the basis of the oxidation state of their parent magmas (Dall'Agnol et al., 2005). A magnetic petrologic study conducted on the Marajoara granite rocks revealed variable MS values ranging between 1.23×10^{-5} and 6.46×10^{-3} SIv. However, notably, the different facies exhibit a consistent pattern of contrasting MS behavior (bimodal distribution). In the heterogranular granites, the MS values range between 2.46×10^{-4} and 6.46×10^{-3}, whereas in the equigranular rocks, the values are very low, ranging between 1.23×10^{-5} and 2.67×10^{-5}. Consequently, as shown in the frequency histogram (Fig. 12), although there is not a complete overlap in the MS value ranges, the ambiguous magnetic behavior of the Marajoara granite demonstrates that the hBMzG facies

resembles both the oxidized granites of the Jamon suite and the more magnetic varieties of the Serra dos Carajás suite, whereas the eBMzG variety exhibits affinity with the plutons formed under reduced conditions in the Velho Guilherme suite.

	Paleoproterozoic suites			Marajoara granite		
	Jamon	Serra dos Carajás	Velho Guilherme	eBMzG	hBMzG	
MS interval (x10³)	1.3−1.7	0.05−0.32	0.63−4	0.123−0.150	2.3−6.46	
Opaques (vol%)	2	0.1	0.7	0.1−0.6	0.1−2	
Primary magnetite	Abundant	Variable	Common in amphibole-bearing facies	Absent	Common	
Ilmenite	Common in monzogranites	Common to all facies	Common to all facies	Common	Variable	
Hematite/ Martite	Common	Common	Common	Absent	Resulting from the oxidation of magnetite	

Figure 12 - Comparative MS data obtained for the Marajoara granite and Paleoproterozoic suites from Carajás province. (Comparison data obtained from Santos et al., 2013). Abbreviations: hBMzG - heterogranular biotite monzogranite; eBMzG - equigranular biotite monzogranite.

In the Marajoara granite rocks, an increase in MS values is observed with higher concentrations of opaque minerals, which is particularly evident in the hBMzG variety, where concentrations exceed 0.8%. In these rocks, magnetite predominates, accompanied by subordinate ilmenite. Conversely, the eBMzG rocks present a lower opaque mineral content (≤ 0.5%) and are characterized by the absence of magnetite, with ilmenite being the single Fe–Ti oxide mineral present. These observations suggest that the Marajoara granite pluton formed through the injection of magmas with different compositions, including reduced granites of the ilmenite series and oxidized granites of the magnetite series.

Anderson and Morrison (2005) established that the FeOt/(MgO+FeOt) ratio in the Laurentia magnetite-series granites ranges between 0.80 and 0.88, whereas those related to the ilmenite series are higher (> 0.88). In the A-type granite discrimination diagrams that use the Fe* index as a parameter of classification, such as those proposed by Dall'Agnol and Oliveira (2007) (Fig. 9e), the eBMzG facies (Fe* ≥ 0.97) has affinity with the reduced ferroan granites with Fe* values as high as those of the ilmenite-series plutons in the Velho Guilherme and Serra dos Carajás suites (Fe* > 0.90). Conversely, the hBMzG rocks (Fe* ~0.86) resemble the oxidized ferroan granites related to the magnetite-series plutons in the Jamon suite (Fe* = 0.83–0.94).

The biotite in the Marajoara pluton is relatively enriched in Fe (Fig. 13a). This mineral in the enclaves and the hBMzG facies approaches the composition of eastonite, whereas the

biotite in the eBMzG variety is closer to the endmember annite. In addition, biotite has Fe/(Fe+Mg) ratios (hBMzG – 0.51 to 0.69; eBMzG – 0.89 to 0.96) and $Al^{IV} + Al^{VI}$ ratios (hBMzG – 2.61 to 3.50; eBMzG – 3.87 to 4.86) that differ from those of both magnetite- and ilmenite-series granites in the United States, as well as those of reduced granites in Fennoscandia and Laurentia (Fig. 13b). For more details on the biotite composition of the different varieties of Marajoara granite and enclaves, see Supplementary Data (Table B).
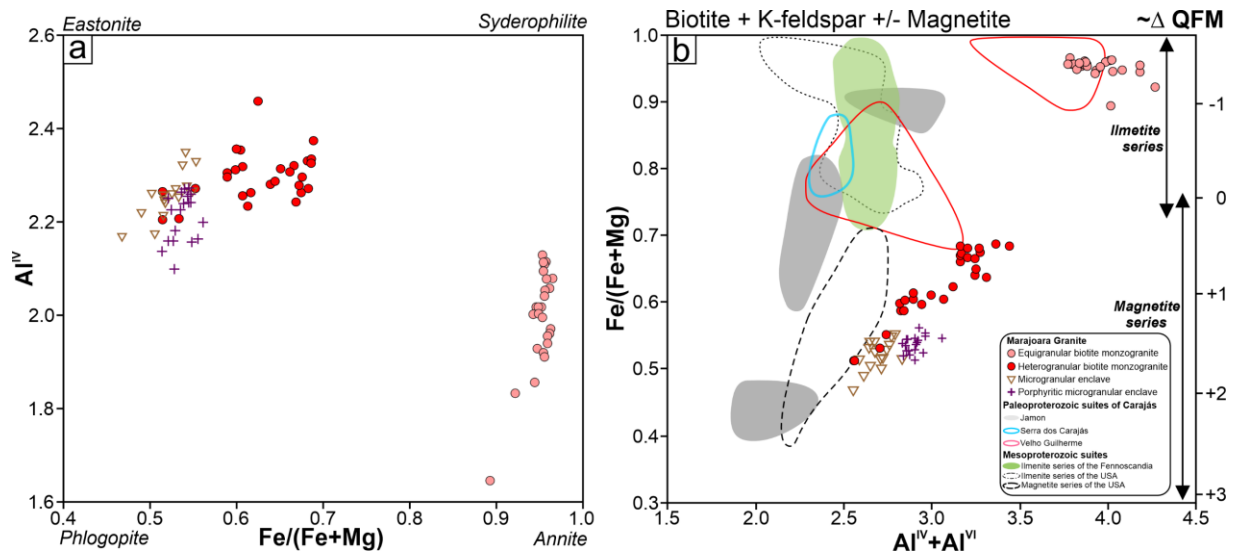
Figure 13 - Fe/(Fe + Mg) vs. Al^{IV} diagram (Rieder, 1998); (b) $Al^{IV} + Al^{VI}$ vs. Fe/(Fe + Mg) diagram (Anderson et al., 2008), showing the biotite composition of Marajoara granite and that of A-type granites of the Carajás suites (Dall'Agnol et al., 2005); A-type Mesoproterozoic granites from the United States according to Anderson and Bender (1989): dashed fields are the magnetite-series granites based on the Bowmans Wash, Davis Dam, Fort Huachuca, Gold Butte, Holy Moses, Newberry and Parker Dam plutons; dotted fields are the ilmenite-series granites based on the Pikes Peak (Barker et al., 1975) and Sherman (Frost et al., 1999) batholiths; the greenish field is the ilmenite series based on the Obbnäs and Bodom plutons from Fennoscandia (Kosunen, 2004).

5.2 ORIGIN OF THE MARAJOARA GRANITE-FORMING MAGMA

Numerous petrogenetic models have been proposed for the generation of A-type granites via crustal anatexis caused by mafic underplating (Rämö et al., 2002). Such models adopt various sources linked to processes that range from partial melting of tonalites and granodiorites (Creaser et al., 1991) and quartz-diorites (Dall'Agnol et al., 2005) to differentiation of tholeiitic basalts (Frost and Frost, 1997). The fractional crystallization of alkaline basalts (Eby, 1992) or other mantle-derived magmas (Bonin, 1986) and the melting of residual granulitic sources (Collins et al., 1982; Clemens et al., 1986) have also been proposed as the origins of A-type plutons. Although the residual source model can explain some characteristics of A-type granites, depleted rocks (granulites) do not have adequate compositions to generate A-type granitic magma (high contents of LILEs (Ba), HFSEs and Fe/Mg and K+Na/Ca ratios), for

which a mineral assemblage containing quartz, biotite, K-feldspar, and plagioclase in the source is expected (Creaser et al., 1991). Likewise, the model of mafic magma as a precursor does not seem to adequately explain the origin of A-type granites, since their source rocks should contain accessory minerals such as apatite, zircon and titanite (King et al., 2001). In this sense, tholeiitic basalts cannot explain the origin of oxidized A-type granites belonging to the magnetite series (Anderson and Bender, 1989; Anderson and Morrison, 2005; Dall'Agnol et al., 2005), since, from the fractional crystallization of tholeiitic melts, an Fe-rich source will produce reduced magmas, which would theoretically explain the low fO$_2$ and the higher Fe/Mg ratio of the rapakivi granites of the ilmenite series (Frost and Frost 1997; Frost et al., 1999).

An alternative model adopted for the origin of magmas with H$_2$O contents and geochemical characteristics compatible with those of A-type granites involves the partial melting of calc-alkaline granitoids at a rate of ~15 to 40% (Creaser et al., 1991). Dehydration melting experiments on magnesian tonalitic gneisses containing different proportions of biotite and amphibole indicate that ferrous granites can originate only at shallow crustal levels (4 kbar, 950 °C); however, under high pressures (8 kbar), the liquid produced is magnesian and strongly peraluminous (Patiño Dulce, 1997). Within this context and considering that Dall'Agnol et al. (2005) noted a probable quartz–feldspar source of intermediate composition for the Jamon suite, the magmas that formed the Marajoara pluton probably developed from the partial melting of Mesoarchean tonalitic rocks.

Mass-balance calculations have been conducted to determine the nature of the Marajoara granite source and the processes the magma experienced prior to its eventual crystallization (Tables 9 and 10). These calculations employed the software GENESIS 4.0 (Teixeira, 2005), which adjusts the relative proportions of residual minerals in the source to simulate the composition of the resultant melt. The reliability of the calculated data is confirmed if the sum of the squared residuals ($\sum$R^2) is ≤ 1.2, allowing to proceed with trace element modeling. This modeling uses Excel sheets developed by the authors on the basis of the equilibrium partial melting equation (Wilson, 1989, Eq. (1)):

$$\frac{CL}{C0} = \frac{1}{F + D - FD}$$

Where CL (liquid) and $C0$ (solid) are the trace element concentrations, F is the weight fraction of melt formed, and D is the bulk distribution coefficient for the residual solids at the moment when melt is removed from the system. The mineral/liquid partition coefficients (Kd)

utilized in the modeling were sourced from the online database at https://earthref.org/KDD/ and are detailed in the Supplementary Data (Table C).

The geochemical modeling approaches indicate that the Mesoarchean Arco Verde tonalite (AM-04) has a composition suitable for generating the Marajoara granite (RDF-8 - hBMzG) with a 16% partial melting rate (Fig. 14a). This degree of melting results in a residual mineral assemblage consisting of plagioclase (55.6%), quartz (27.4%), biotite (13.2%), magnetite (2.9%), and ilmenite (0.9%). Furthermore, considering that the eBMzG facies resembles the products of reduced magmas in the Velho Guilherme suite and displays strongly peraluminous characteristics, geochemical calculations were conducted to trace its source. The findings suggest that the reduced magmas originated from the partial melting of a source comprising the Mesoarchean Arco Verde tonalite (AM-04) and metasedimentary rocks from the Sapucaia Greenstone Belt (MCS-43B), leaving plagioclase (49.7%), quartz (30.7%), biotite (13.7%), amphibole (4.5%), magnetite (0.8%) and ilmenite (0.6%) as residual minerals (Fig. 14b).

Table 9 - Modeling major and trace element compositions and residual mineral assemblages for generation of the heterogranular biotite monzogranite of the Marajoara granite protolith by partial melting of the Arco Verde tonalite.

	AM-04 (C$_0$)[a]	Residue (Cs)	Composition of minerals					Calculated	RDF-8
	Tonalite	Bulk	Pl[b]	Qz	Bt[b]	Mag[c]	Ilm[c]	Magma (CL')	Heterogranular biotite monzogranite (CL)
			55.55%	27.43%	13.22%	2.91%	0.89%		
Major elements (weight %)									
SiO$_2$	67.73	66.51	60.60	100.00	41.00	0.00	0.00	73.58	74.65
TiO$_2$	0.51	0.66	0.00	0.00	1.63	0.00	50.00	0.10	0.17
Al$_2$O$_3$	15.45	15.93	24.72	0.00	16.58	0.00	0.00	13.79	13.95
FeOt	4.64	5.37	0.13	0.00	14.69	100.00	50.00	1.17	1.24
MnO	0.10	0.03	0.00	0.00	0.19	0.00	0.00	0.11	0.04
MgO	1.53	2.09	0.00	0.00	15.64	0.00	0.00	-0.06	0.19
CaO	3.99	3.81	6.86	0.00	0.00	0.00	0.00	1.52	0.88
Na$_2$O	3.68	4.16	7.49	0.00	0.00	0.00	0.00	3.46	3.89
K$_2$O	2.35	1.45	0.16	0.00	10.26	0.00	0.00	5.33	4.98
Trace elements (ppm)									
Ba	683.0							476.0	463.0
Rb	136.7							486.3	505.0
Sr	302.3							89.2	83.2
Y	60.3							95.2	90.0
Zr	167.2			$\Sigma R^2 = 0.263$				185.6	126.0
Nb	17.3			Melt fraction				23.3	29.9
La	34.2			F = 18%				81.8	79.6
Ce	52.1							128.9	127.5
Nd	29.5							61.6	63.1
Sm	5.9							13.3	12.2
Eu	1.1							0.9	1.0
Gd	6.5							10.3	10.8
Yb	4.9							10.3	10.2
Lu	0.7							1.7	1.6

ΣR^2 = sum of the squared residuals. All iron is reported as FeO. All oxide values recast to 100%. [a] Almeida (2010), [b] Leite (2001), [c] Martin (1987). Abbreviations: Bt – biotite, Ilm – ilmenite, Mag – magnetite, Pl – plagioclase, Qz – quartz.

The results obtained through geochemical modeling are consistent with those acquired from Lu–Hf isotope data, which show strongly negative $\varepsilon_{Hf}(t)$ values (-11 to -18) and Hf-T_{DM}^{C} from 3.2 to 3.6 Ga, suggesting that the parent magmas of the Marajoara granite were derived from Meso- to Paleoarchean TTG crust (Fig. 11c). Furthermore, the Marajoara granite has strongly nonradiogenic initial Nd isotopic compositions, indicating sources with a long crustal residence time (Table 8). The model ages (T_{DM}) for the pluton range from 2.91 to 3.62 Ga, suggesting that the source rocks have ages and Nd isotopes similar to those of the Mesoarchean basement rocks of the Carajás province. This isotopic behavior is generally compatible with that of other Paleoproterozoic suites from Carajás (T_{DM} model ages from 3.35 to 2.60 Ga; ε_{Nd} values from -9 to -8 at 1.88 Ga).

Table 10 - Modeling major and trace element compositions and residual mineral assemblages for generation of the equigranular biotite monzogranite of the Marajoara granite protolith by partial melting of Arco Verde tonalite and 20% metasedimentary rock from the Sapucaia greenstone belt.

	AM-04[a]	MCS-43B[b]	Modeled source	Residue (Cs)	Composition of minerals						Calculated	GDR-7
	Tonalite	Metasedimentary	80% tonalite + 20% metasedimentary[c]	Bulk	Pl[d]	Qz	Bt[d]	Amp[d]	Mag[e]	Ilm[e]	Magma (CL')	Equigranular biotite monzogranite (CL)[c]
					49.72%	30.70%	13.68%	4.50%	0.83%	0.57%		
Major elements (weight %)												
SiO₂	66.22	74.88	69.61	68.20	60.60	100.00	39.00	45.17	0.00	0.00	77.12	77.09
TiO₂	0.47	0.44	0.47	0.51	0.00	0.00	1.59	0.27	0.00	50.00	0.08	0.05
Al₂O₃	15.11	11.90	14.82	15.02	24.72	0.00	17.00	8.96	0.00	0.00	13.19	13.09
FeO*	4.45	3.38	4.34	4.97	0.13	0.00	20.20	22.76	100.00	50.00	0.77	0.74
MnO	0.07	0.07	0.07	0.07	0.00	0.00	0.26	0.67	0.00	0.00	0.08	0.07
MgO	1.50	0.13	1.51	1.95	0.00	0.00	11.48	8.05	0.00	0.00	-0.12	0.02
CaO	3.90	1.61	3.52	3.95	6.86	0.00	0.00	12.00	0.00	0.00	0.52	0.40
Na₂O	3.60	2.94	3.55	3.79	7.49	0.00	0.00	1.20	0.00	0.00	3.85	4.13
K₂O	2.26	1.23	2.10	1.55	0.16	0.00	10.40	0.94	0.00	0.00	4.52	4.41
Trace elements (ppm)												
K	18760.3	10210.2	17050.3								36738.7	35777.3
Rb	136.7	337.9	176.9								644.5	893.2
Y	60.3	3.5	48.9								102.2	104.4
Hf	4.7	2.7	4.3		ΣR² = 0.141						8.3	8.2
U	3.6	0.8	3.0		Melt fraction						13.1	12.4
La	34.2	26.1	32.6		F = 15%						16.4	19.3
Ce	52.1	30.4	47.8								46.3	45.8
Nd	29.5	11.7	25.9								21.0	20.1
Sm	5.9	2.0	5.1								5.4	5.3
Eu	1.1	0.6	1.0								0.2	0.1
Gd	6.5	1.6	5.5								6.4	5.5
Tb	1.2	0.2	1.0								1.2	1.2
Dy	7.5	1.3	6.2								9.2	8.6
Er	4.9	0.9	4.1								9.2	8.8
Yb	4.9	1.1	4.1								12.7	12.9
Lu	0.7	0.2	0.6								2.3	2.2

$\sum R^2$ = sum of the squared residuals. All iron is reported as FeO. All oxide values recast to 100%. [a] Almeida (2010), [b] Sousa (2020), [c] Original oxide values recast to 100% [d] Leite (2001), [e] Martin (1987). Abbreviations: Bt – biotite, Ilm – ilmenite, Mag – magnetite, Pl – plagioclase, Qz – quartz.
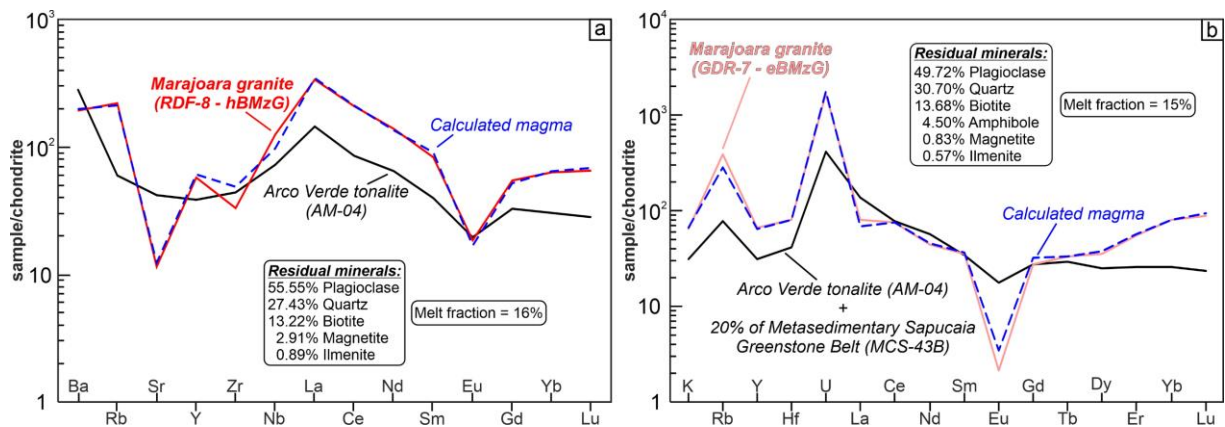
Figure 14 - Trace element models for the generation of the Marajoara granite: (a) partial melting of a tonalitic protolith and (b) partial melting of 80% Arco Verde tonalite and 20% metasedimentary greenstone rock. The chondrite (C1) normalization values are from McDonough and Sun (1995). Abbreviations: hBMzG - heterogranular biotite monzogranite; eBMzG - equigranular biotite monzogranite.

5.3 GENESIS OF THE MICROGRANULAR ENCLAVES AND THE MAGMA MIXING PROCESS

Microgranular magmatic enclaves are commonly found within granitic plutons and influence the role of mantle-derived melts in the genesis and evolution of their magmas. As a result, several models have been proposed for the origin of ME: i) mixing between melts derived from the mantle and crust, from the injection of basic magma into granitic magmatic chambers (Barbarin and Didier, 1992); ii) representatives of a nonhybridized portion of the granite source or the residue of a metamafic source (restite model) (White et al., 1999); iii) the product of accumulation of early crystallized minerals from a more mafic cogenetic melt (Dahlquist, 2002); and iv) disrupted chilled margins of the host granite (Donaire et al. 2005).

In the Marajoara pluton, ME occur in the hBMzG facies in the central portion of the pluton. Their textural features suggest that there was significant interaction between magma of calc-alkaline affinity and the liquid forming the hBMzG facies. In this case, feldspar phenocrysts found in the internal domains of the pME come from the host granite (hBMzG) through a transfer process (magma mingling), indicating the coexistence of two magmas with different compositions. The occurrence of enclaves devoid of such features (ME) also indicates that the action of magma mixing processes was not effective in some portions of the pluton. Therefore, we examined whether the mechanisms of fractional crystallization, mixing, or assimilation and fractional crystallization (AFC) were involved in the origin of the enclaves. In this context, three components were tested: (i) basic magma forming Paleoproterozoic mafic dikes from different areas of the Rio Maria domain; (Silva Jr. et al., 1999; Marangoanha and Oliveira 2014; Silva et al., 2016); (ii) Mesoarchean crust represented by the Arco Verde tonalite

(samples AM-04–Almeida, 2010); and (iii) felsic magma that formed the hBMzG in the Marajoara granite.

In the model, we evaluated the interaction between the starting composition (C0) represented by the initial mafic liquid and the assimilated crust composition (tonalite), with an assimilation rate of 20% (r = 0.2). The results (Fig. 15a-d) show that the enclaves plot on the magma mixing line between the host granite (Marajoara granite) and mafic magma, excluding the involvement of AFC or fractional crystallization processes in the generation of enclaves. Additionally, a model based on binary mixing was used to explain the origin of enclaves through normalized REE and multielement diagrams (Fig. 15e and f), where the compositions of the enclaves and the hBMzG variety are shown. Using the equation presented above, it was possible to determine the degree of mixing (f) capable of generating a liquid with the composition of the enclaves. The calculated liquid that shows the greatest affinity with the compositional patterns of pME has f = 0.55, which means that it originated from a mixture of 55% mafic magma and 45% hBMzG (Fig. 15e). On the other hand, the ME formed from a mixture of 75% mafic component and 25% felsic component (Fig. 15f), indicating a greater contribution of magnesian magma to the formation of these rocks.

The microgranular textures indicative of rapid cooling observed in the ME with excessive nucleation of biotite $\pm$ Fe–Ti oxides, the presence of chilled margins defining their contours and the occurrence of "megacrystals" with corroded borders of composition and dimensions analogous to those of the host granite (see Fig. 3b) are evidence of injections of more primitive liquid into the granitic chamber (Barbarin and Didier, 1992). These features suggest that these pulses of mafic magma, having higher *solidus* curve temperatures (~1200°C) than the granitic liquid (~700°C), quickly solidified (chilling) within the granitic mush and fragmented, forming discrete bodies (enclaves). In the case of ME, contrary to the process that formed the pME, the presence of regular and straight contacts and the absence of xenocrysts originating from the host granite magma imply that there were no liquid-state interactions between the enclave melt and the granitic magma in the later stage of crystallization (Fig. 3e). Given that the two types of enclaves found in the Marajoara pluton are associated with only the main facies (hBMzG), the ME represent an isolated fraction of the same magma that produced the porphyritic-type matrix.
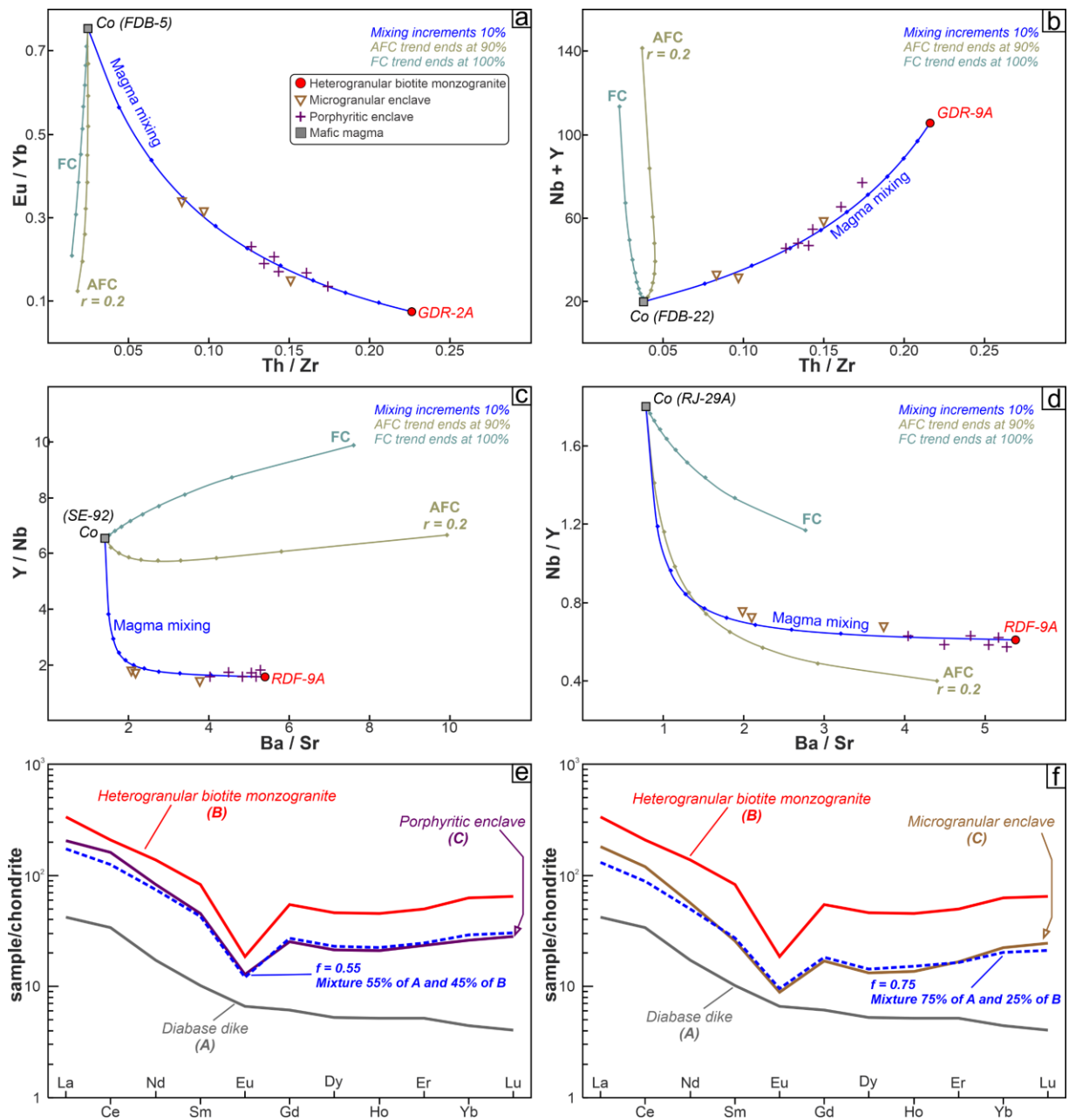
Figure 15 - Trace element and REE plots for the Marajoara granite, microgranular and porphyritic enclaves, and mafic dikes showing models of fractional crystallization (FC), crustal assimilation and fractional crystallization (AFC), and magma mixing: (a) and (b) Tucumã (Silva et al., 2016); (c) Nova Canadá (Marangoanha and Oliveira 2014); (d) Rio Maria (Silva Jr. et al., 1999); (e) and (f) REE patterns quantifying the mixing between mafic and felsic magmas. We used the PETROMODELER software from Ersoy (2013) based on equations from DePaolo (1981). The chondrite (C1) normalization values are from McDonough and Sun (1995).

This interpretation is further supported by whole-rock Sm–Nd isotope data from the enclaves. The samples yield negative $\varepsilon_{Nd(t)}$ values varying from -10.0 to -13.9 and T_{DM} values ranging from 2.86 Ga to 3.0 Ga, which are consistent with those of the host granite ($\varepsilon_{Nd(t)}$ = -8.6 to -9.3, T_{DM} = 2.9 to 3.5 Ga). The T_{DM} values indicate that Meso- to Paleoarchean crustal material was involved in the source region of these melts. Close similarities in Nd initial isotopic ratios among all samples support the idea that these magmas were part of the same system,

regardless of the whole-rock composition. These features also suggest that the ME were produced by magma mixing in the early stage of formation of the host granite and preceded the formation of the pME by mingling. Alternatively, the hypothesis that the ME represent disrupted fragments of rapidly cooled fine-grained borders (chilled margins) of the Marajoara pluton allows the similar isotopic characteristics of the ME and their host rocks to be easily interpretable. On the other hand, neither the observed geochemical contrast with the host granite nor the mingling and disequilibrium textures present in the pME can be explained by such a hypothesis.

5.4 DYNAMICS OF MAGMA CHAMBERS AND MARAJOARA PLUTON CONSTRUCTION

5.4.1 Microgranular enclaves and host magma crystallization

The evolution of the rheological contrast between magmas can be reconstructed from the study of magmatic enclaves. The diverse forms of ME are controlled by differences in the viscosities of the magmas, and the more complex the forms are, the greater the viscosity differences were (Perugini and Poli, 2012). A variety of structures can be produced by injecting mafic magma into a felsic magma at various stages of crystallization (*cf.* Fernandez and Barbarin, 1991). A transition from Newtonian to non-Newtonian behavior occurs in magmas, regardless of composition, when the host magma is between 30% and 50% crystallized (Petford, 2003). In the Marajoara pluton, there are ME with different shapes and sizes (Fig. 16). Some are globular, elongated shapes and have well-defined contacts (lobate and sinuous), whereas others resemble large angular fragments (with the absence of mingling and chilled margins). These features indicate that mafic magmas were injected during three different crystallization stages in the Marajoara granite magmatic chamber. The ME with globular shapes formed when mafic magma was injected into the felsic magmatic chamber when it was up to 30% crystallized, and the mafic magma was disaggregated by convective movements that induced the dispersion of smaller mafic magma droplets (Fig. 3c). This hypothesis is in keeping with the interpretations of other authors about the genesis of globular ME (e.g., Vernon et al., 1988, Castro et al., 1991; Liu et al., 2013; Shukla and Mohan, 2019). Since ME with such features are densely distributed throughout the Marajoara pluton, we believe that the input of mafic magma in this stage was high in the central portion of the pluton. The Marajoara pluton ME with lobate and sinuous contacts likely formed when the felsic magmatic chamber had a degree of crystallization greater than 30% (viscoplastic behavior), as a greater difference in viscosity is necessary to generate

these more complex forms (e.g., Perugini and Poli, 2012).
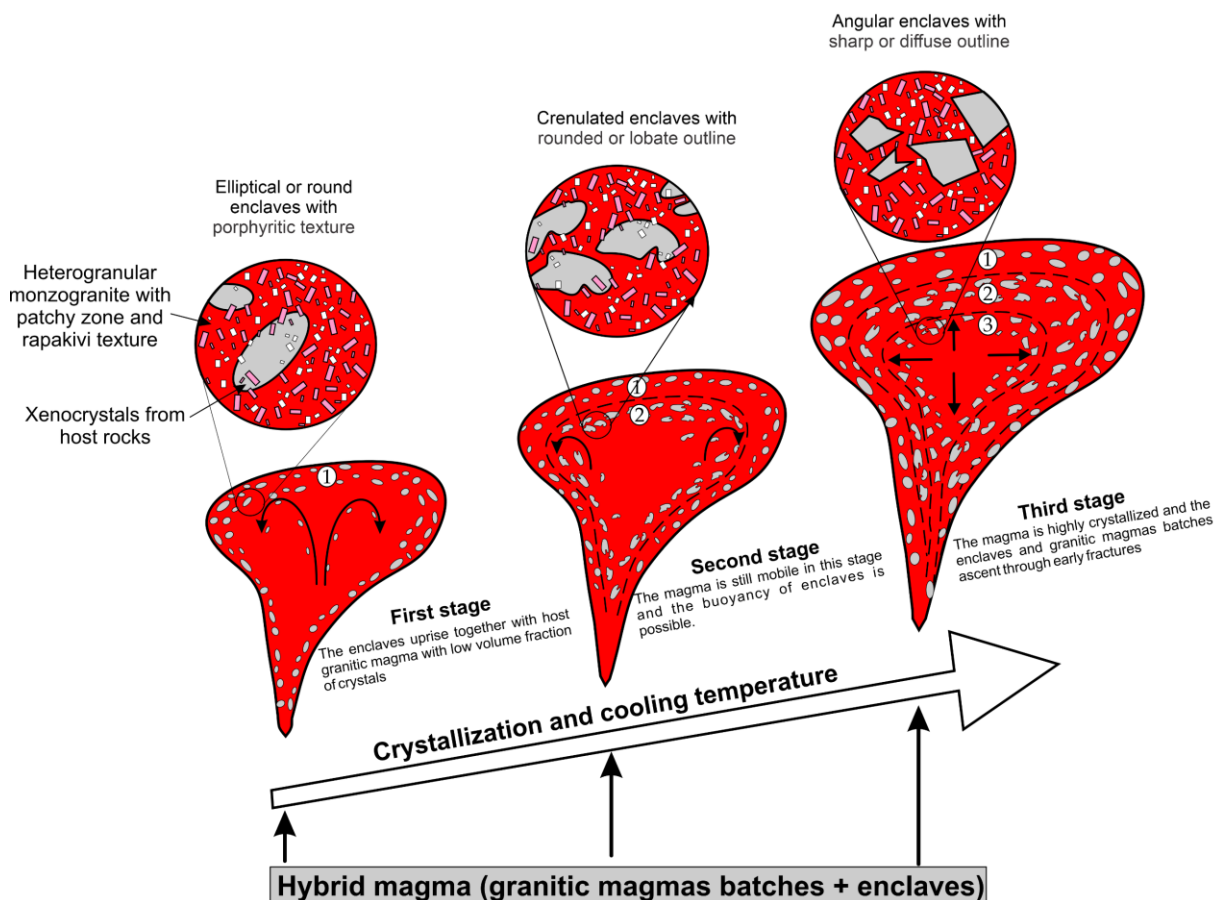
Figure 16 - Sketch showing the various types of enclaves resulting from the injection of hybrid magmas into a granitic magma at different stages of crystallization (from Barbarin and Didier, 1992). See the text for descriptions of the complete scenario.

Finally, the large ME with angular shapes indicate the occurrence of already-hybridized mafic magma pulses when 70–90% of the felsic magmatic chamber had crystallized. In the late stages of crystallization, early fractures formed and allowed the injection of mafic magma, which resulted in the composite and synplutonic (disrupted) dikes (*cf*. Fernandez and Barbarin, 1991). The input of mafic magma was probably more restricted at this stage, as enclaves with these types of contacts are limited in the Marajoara pluton.

5.4.2 Tectonic model for magma transport and granite emplacement

The shallow depth (mid- to upper-crustal levels) at which the Marajoara granite-forming magmas were emplaced is inferred from the differences in formation age between the basement rocks (2.87–2.97 Ga) and the pluton (1.88 Ga). This interpretation is further supported by the fact that the E–W regional foliation pattern is abruptly truncated by the epizonal pluton, revealing that the surrounding rocks behaved rigidly when it was emplaced. Angular xenoliths

related to the 2.97 Ga Arco Verde tonalite indicate a high viscosity contrast between the tonalite and the granitic magma and indicate that the pluton was forcefully emplaced in the upper part of the middle crust. In addition, the lack of orientation of both the set of ME and the granitic varieties reflects the absence of regional deformation during magma emplacement. Despite the roughly circular shape of the Marajoara granite, the contacts, occasionally in extensive rectilinear segments, with some angular indentations, suggest that its emplacement was controlled by fractures prior to intrusion.

The model proposed to illustrate the emplacement history of the Marajoara pluton shows that the granitic magma chamber formed at depth, because the additional mafic magma in the lower crust was initially undercooled in a steady state (closed system), enabling the formation of K-feldspar crystals. Then, small pulses of hot, dense mafic magma were repeatedly injected into the base of the granite reservoir, causing large-scale convection (driving magma mixing) and forming a stratified chamber. The pronounced temperature elevation of the granitic magma caused the resorption of preexisting K-feldspar phenocrysts during felsic–mafic magma interactions, as well as the crystallization of plagioclase mantles around these phenocrysts as the temperature decreased (Fig. 6e). The pME formed due to magma mingling in localities where contrasting temperatures between the felsic and mafic magmas existed, indicating that the mafic magma was introduced shortly after the start of crystallization of the granite. The magma resulting from this process produced oxidized granite (magnetite series) with a medium-to-coarse heterogranular texture (hBMzG) and a set of coexisting ME. On the other hand, the more evolved aspects of the reduced magma (ilmenite series), which resulted in the variety with an even-grained texture (eBMzG), and the absence of ME in this variety indicate that its formation was related to injections of basaltic magma that, during its rise, became trapped at higher crustal levels (out of the magma-mixing zone), causing partial melting of more evolved portions of the Mesoarchean crust (Fig. 17). The hBMzG might have formed earlier than the eBMzG when the magma was less evolved. The intensity and profusion of the patchy zoning in plagioclases confirm this interpretation, as patchy zoning is common in the former, suggesting its origination at deeper levels followed by considerable decompression (*cf.* Singer, 1993; Fig. 6g).
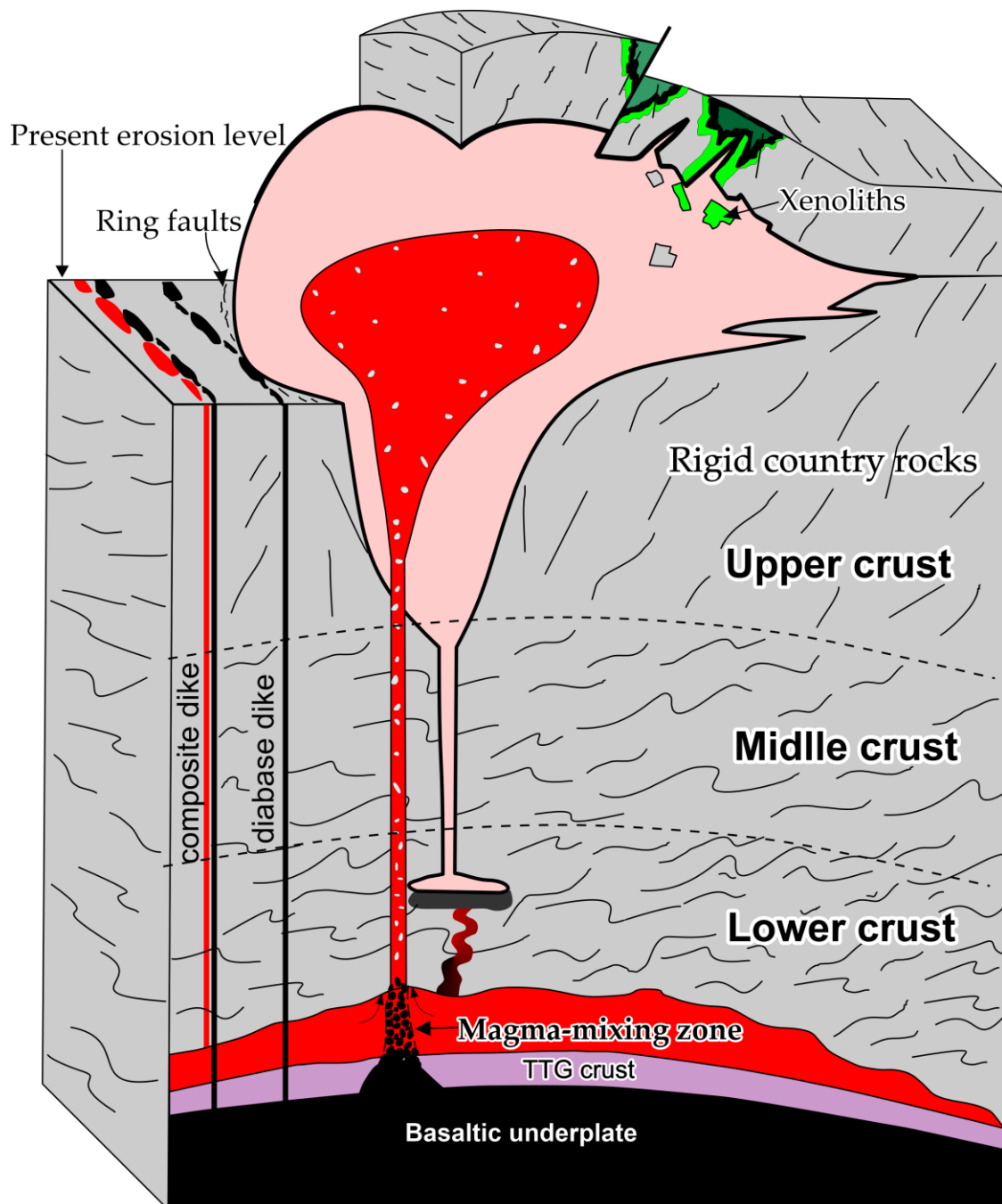
Figure 17 - Schematic diagram showing the evolution of the Marajoara pluton and coexisting diabase and granite porphyry dikes, involving magma generation, hybridization in the deep crustal hot zone, magma ascent and shallow-level crystallization. See the text for a detailed explanation.

Composite dikes appear to be associated with a contemporaneous mafic magma chamber. In the Rio Maria area, a porphyry granite–diabase composite dike illustrates the bimodality typical of A-type granite complexes (see Fig. 4). The compositionally unique basic–evolved pair in the dike is consistent with the sampling of a compositionally stratified magma chamber at different levels or at different stages of its evolution. In this arrangement, the primitive basaltic margins of the composite dike may represent batches of new magma

(replacement events) that rapidly ascended to settle at shallower crustal levels, whereas other batches mixed with magma in the deeper chamber to recharge the system and contribute to the heat balance for TTG basement melting (Fig. 17). Dikes of this type with a silicic interior and mafic margins (with mingling in the marginal parts) can develop when the central component (porphyry granite) intersects chambers filled with relatively dense mafic magma that remains unchanged. The granitic magma was produced by the partial melting of Mesoarchean crust shortly before or during the emplacement of the dike.

The arrangement of the Paleoproterozoic A-type plutons in the Carajás province along a belt that follows the overall NW–SE trend defined by swarms of coexisting diabase and granite porphyry dikes indicates that they were emplaced in an extensional tectonic environment with extension in the NE–SW direction. Considering the tabular geometry (lacoliths) inferred from the batholiths of the Jamon suite (Oliveira et al. 2008, 2010), the rheological behavior of the surrounding rocks and the reduced or null influence of regional forces during the emplacement of the Marajoara granite, it is assumed that magma transport took place through dikes. In this case, deep faults served as channels allowing magma to rise, and tectonic discontinuities represented zones of weakness that favored emplacement at shallow crustal levels. The extensional tectonics associated with the emplacement of the Marajoara pluton driven by magma comingling and mixing support the conclusion that the genesis of the Paleoproterozoic A-type granites in the Carajás province was related to the same tectonic-magmatic event that produced the rapakivi granites in the southwestern United States and southern Finland. Their origins were related to fragmentation of a Paleoproterozoic supercontinent at ~2.0 Ga, which involved regional thermal anomalies in the upper mantle and mafic underplating (Rämö and Haapala, 1995; Rämö et al., 2002; Dall'Agnol et al., 2005).

6 CONCLUSIONS

The Marajoara granite is a stock intruded into Mesoarchean rocks of the Rio Maria domain and has a zircon U–Pb crystallization age of 1884 ± 11 Ma. The pluton is composed of rocks with no observed traces of deformation in the solid state and contains angular xenoliths of the host rocks. The pluton is zoned and features equi- to heterogranular biotite monzogranite varieties. The numerous porphyritic and microgranular enclaves are restricted to the heterogranular facies. They are peraluminous granites similar to ferroan granites, with high $Na_2O + K_2O/CaO$ and $FeOt/(FeOt+MgO)$ ratios. They are also enriched in HFSEs and show geochemical affinities with both oxidized (magnetite series) and reduced (ilmenite series) A-

type intraplate granites. The microgranular enclaves show affinities with magnesian granites and those of the calc-alkaline series.

The existence of compositional differences between the Marajoara pluton varieties indicates that the evolution of the pluton did not occur through fractional crystallization from a single magma but rather through more complex processes involving significant variations in the compositions of the source rocks and/or formation conditions. The data presented in this paper, therefore, confirm the role of Mesoarchean crust in the origin of these granites. Geochemical modeling suggests that the hBMzG facies was generated from partial melting of the 2.97 Ga Arco Verde tonalite in the Rio Maria domain, whereas the eBMzG facies was generated by partial melting of tonalite rocks, with assimilation of a supracrustal (metasedimentary) component. This interpretation is consistent with the Lu–Hf and Sm–Nd isotope data, with $\varepsilon_{Hf}(t)$ values between -11 and -18 and Hf-T_{DM}^{C} of 3.2 to 3.6 Ga. Nd isotope analysis also yielded similar results (Nd-T_{DM} from 3.35 to 2.60 Ga; ε_{Nd} values from -12 to -8). The microgranular and porphyritic enclaves formed from different degrees of mixing (55–75%) between mafic liquids and the oxidized granitic magma.

Zircon Pb–Pb evaporation analyses of the composite dike and porphyry granite revealed crystallization ages of 1885 ± 4 and 1885 ± 2 Ma, respectively. Both ages are entirely concordant with the crystallization ages of the Marajoara pluton. The porphyry granite–diabase composite dike illustrates the bimodality typical of A-type granite complexes and is consistent with a compositionally stratified magma chamber at different levels. The arrangement of the Paleoproterozoic A-type plutons in the Carajás province, which coexist with diabase and granite porphyry dikes, indicates that they were emplaced in an extensional tectonic setting. Considering the tabular geometry inferred from the batholiths of the Jamon suite and the rheological behavior of the surrounding rocks, it is assumed that magma transport took place through dikes during the emplacement of the Marajoara pluton. The extensional tectonics associated with the emplacement of the A-type granites of the Carajás province were related to fragmentation of a Paleoproterozoic supercontinent at ~2.0 Ga and underplating of mantle magmas.

ACKNOWLEDGMENTS

REFERENCES

Ali, K.M., Kroner, A., Hegner, E., Wong, J., Li, S.Q., Gahlan, H.A., Abu El Ela, F.F. 2015. U–Pb zircon geochronology and Hf–Nd isotopic systematics of Wadi Beitan granitoid gneisses, South Eastern Desert, Egypt. Gondwana Research, 27: 811-824.

Almeida, F.F.M., Hasui, Y., Brito Neves, B.B., Fuck, R.A., 1981. Brazilian structural provinces: an introduction. Earth Sci. Rev. 17, 1–29.

Almeida, J.A.C., Dall'Agnol, R., Oliveira, D.C. 2006. Geologia, Petrografia e Geoquímica do Granito Anorogênico Bannach, Terreno Granito-Greenstone de Rio Maria, Pará. Revista Brasileira de Geociências, 36(2), 282-295.

Almeida, J.A.C., 2010. Geologia, geoquímica, geocronologia e petrogênese das suítes TTG e dos leucogranitos arqueanos do Terreno Granito-Greenstone de Rio Maria, Sudeste do Cráton Amazônico. In: Programa de Pós-graduação em Geologia e Geoquímica, Instituto de Geociências, Universidade Federal do Para, Belém, 208p. Dr. Thesis (in Portuguese).

Almeida, J.A.C., Dall'Agnol, R., Oliveira, M.A., Macambira, M.J.B., Pimentel, M.M., Rämö, O.T., Guimarães, F.V., Leite, A.A.S., 2011. Zircon geochronology, geochemistry and origin of the TTG suites of the Rio Maria granite-greenstone terrane: implications for the growth of the Archean crust of the Carajás Province, Brazil. Precambrian Res. 187, 201–221.

Almeida, J.A.C., Dall'Agnol, R., Leite, A.A.S., 2013. Geochemistry and zircon geochronology of the Archean granite suites of the Rio Maria granite greenstone terrane, Carajás Province, Brazil. J.S. Am. Earth Sci. 42, 103–126.

Althoff, F.J., Barbey, P., Boullier, A.M., 2000. 2.8-3.0 Ga plutonism and deformation in the SE Amazonian craton: the Archean granitoids of Marajoara (Carajás mineral province, Brazil). Precambrian Res. 104, 187–206.

Anderson, J.L., 1983. Proterozoic anorogenic granite plutonism of North America. Geol. Soc. Am. Mem. 161, 133-154.

Anderson, J.L., Bender, E.E., 1989. Nature and origin of Proterozoic A-type granitic magmatism in the southwestern United States of America. Lithos, 23(1-2), 19–52.

Andersen, T., Andersson, U.B., Graham, S., Aberg, G., Simonsen, S.L., 2009. Granitic magmatism by melting of juvenile continental crust: new constraints on the source of Paleoproterozoic granitoids in Fennoscandia from Hf isotopes in zircon. J. Geol. Soc. Lond. 166, 233–247.

Anderson, J.L., Barth, A.P., Mazdab, J.L.W.F., 2008. Thermometers and thermobarometers in granitic systems. Rev. Mineral. Geochem. 69, 121–142.

Anderson, J.L., Morrison, J., 2005. Ilmenite, magnetite, and peraluminous Mesoproterozoic anorogenic granites of Laurentia and Baltica. Lithos 80, 45–60.

Antonio, P.Y.J., D'Agrella-Filho, M.S., Nedelec, A., Poujol, M., Sanchez, C., Dantas, E.L., Dall'Agnol, R., Teixeira M.F.B., Proietti, A., Martínez Dopico, C.I., Oliveira D.C., Silva, F.F., Marangoanha, B., Trindade, R.I.F., Trindade, R.I.F.D., 2021. New constraints for paleogeographic reconstructions at ca. 1.88 Ga from geochronology and paleomagnetism of the Carajás dyke swarm (eastern Amazonia). Precambrian Research, 353, 106039.

Barbarin, B., Didier, J., 1992. Genesis and evolution of mafic microgranular enclaves through various types of interaction between coexisting felsic and mafic magmas. Transactions of the Royal Society of Edinburgh Earth Sciences, 83(1-2), 145–153.

Barbarin, B., 2005. Mafic magmatic enclaves and mafic rocks associated with some granitoids of the central Sierra Ne vada batholith, California: nature, origin, and relations with the hosts. Lithos, 80(1-4), 155–177.

Barker, F., Wones, D.R., Sharp, W.N., Desborough, G.A., 1975. The Pikes Peak batholith, Colorado Front Range, and a model for the origin of the gabbro–anorthosite–syenite–potassic granite suite. Precambrian Res. 2, 97–160.

Bettencourt, J.S., Juliani, Xavier, R.P., Monteiro, L.V.s., Neto, A.C.B., Klein, E.L., Assis, R.R., Leite Jr., W.P., Moreto, C.P.N., Fernandes, C.M.D., Pereira, V.P., 2016. Metallogenetic systems associated with granitoid magmatism in the Amazonian Craton: an overview of the present level of understanding and exploration significance. J. S. Am. Earth Sci. 68, 22-49.

Black, L.P., Kamo, S.L., Allen, C.M., Aleinikoff, J.N., Davis, D.W., Korsch, R.J., Foudoulis, C., 2003. TEMORA 1: a new zircon standard for Phanerozoic U–Pb geochronology. Chemical Geology, 200(1-2), 155–170.

Bonin, B. 1986. Ring complex granites and anorogenic magmatism. BRGM, Orleans, 189 pp.

Bonin, B., 2007. A-type granites and related rocks: evolution of a concept, problems and prospects. Lithos 97 (1–2), 1–2.

Bouvier, A., Vervoort, J.D., Patchett, P.J., 2008. The Lu–Hf and Sm–Nd isotopic composition of CHUR: constraints from unequilibrated chondrites and implications for the bulk composition of terrestrial planets. Earth Planet. Sci. Lett. 273 (1–2), 48–57.

Castro A., Moreno-Ventas I., De La Rosa J.D., 1991. H-type (hybrid) granitoids: a proposed revision of the granite-type classification and nomenclature. Earth-Science Reviews, 31(3-4):237-253.

Chappell, B.W., White, A.J.R., 1974. Two contrasting granite types. Pac. Geol. 8, 173–174.

Cheng, Y., Spandler, C., Mao, J., Rusk, B.G., 2012. Granite, gabbro and mafic microgranular enclaves in the Gejiu area, Yunnan Province, China: A case of two-stage mixing of crust- and mantle-derived magmas. Contributions to Mineralogy and Petrology, 164(4), 659–676.

Chu, N.C., Taylor, R.N., Chavagnac, V., Nesbitt, R.W., Boella, R.M., Milton, J.A., German, C.R., Bayon, G., Burton, K., 2002. Hf isotope ratio analysis using multicollector inductively coupled plasma mass spectrometry: an evaluation of isobaric interference corrections. J. Anal. Atomic Spectrom. 17, 1567-1574.

Clemens, J.D., Holloway, J.R., White, A.J.R., 1986. Origin of an A-type granite: experimental constraints. American Mineralogist, 71, 317–324.

Clemens, J.D., Watkins, J.M., 2001. The fluid regime of high-temperature metamorphism during granitoid magma genesis. Contributions to Mineralogy and Petrology 140, 600–606.

Collins, W.J., Beams, S.D., White, A.J., Chappell, B.W., 1982. Nature and origin of A-type granites with particular reference to Southeastern Australia. Contributions to Mineralogy and Petrology, 80(2), 189–200.

Creaser, R.A., Price, R.C., Wormald, R.J., 1991. A-type granites revisited: assessment of a residual-source model. Geology, 19(2), 163–166.

Cunha, I.R.V., Dall'Agnol, R., Feio, G.R.L., 2016. Mineral chemistry and magnetic petrology of the Archean Planalto suite, Carajás province, Amazonian craton: implications for the evolution of ferroan Archean granites. J. S. Am. Earth Sci. 67, 100–121.

Dahlquist, J.A., 2002. Mafic microgranular enclaves: early segregation from metaluminous magma (Sierra de Chepes), Pampean Ranges, NW Argentina. Journal of South American Earth Sciences, 15(6), 643-655.

Dall'Agnol, R., Costi, H.T., Leite, A.A., Magalhães, M.S., Teixeira, N.P., 1999a. Rapakivi granites from Brazil and adjacent areas. Precambrian Research, 95(1-2), 9-39.

Dall'Agnol, R., Ramö, O.T., Magalhães, M.S., Macambira, M.J.B., 1999b. Petrology of the anorogenic oxidized Jamon and Musa granites, Amazonian Craton: implications for the genesis of Proterozoic, A-type Granites. Lithos, 46(3), 431-462.

Dall'Agnol, R., Teixeira, N.P., Rämö, O.T., Moura, C.A.V., Macambira, M.J.B., Oliveira, D.C., 2005. Petrogenesis of the Paleoproterozoic, rapakivi, A-type granties of the Archean Carajás Metallogenic Province, Brazil. Lithos, 80(1-4), 102-129.

Dall'Agnol, R., Oliveira, M.A., Almeida, J.A.C., Althoff, F.J., Leite, A.A.S., Oliveira, D.C., Barros, C.E.M., 2006. Archean and Paleoproterozoic granitoids of the Carajás metallogenetic province, eastern amazonian craton. In: Dall'Agnol, R., Rosa-Costa, L.T., Klein, E.L. (Eds.), Symposium on Magmatism, Crustal Evolution, and Metallogenesis of the Amazonian Craton. Abstracts Volume and Field Trips Guide. PRONEX-UFPA/SBG-NO, Belem, pp. 99-150.

Dall'Agnol R., Oliveira, D.C., 2007. Oxidized, magnetite-series, rapakivi-type granites of Carajás, Brazil: Implications for classification and petrogenesis of A-type granites. Lithos, 93(3-4), 215–233.

Dall'Agnol, R., Frost, C.D., Rämö, O.T., 2012. IGCP Project 510 "A-type granites and related rocks through time": project vita, results, and contribution to granite research. Lithos 151, 1–16.

Dall'Agnol, R., Oliveira, D.C., Guimarães, F.V., Gabriel, E.O., Feio, G.R.L., Lamarão, C.N., Althoff, F.J., Santos, P.A., Teixeira, M.F.B., Silva, A.C., Rodrigues, D.S., Santos, M.J. P., Silva, C.R.P., Santos, R.D., Santos, P.J.L., 2013. Geologia do Subdomínio de Transição do Domínio Carajás – Implicações para a evolução arqueana da Província Carajás - Pará. In: SBG, Simpósio de Geologia da Amazônia, vol. 13 (CD-ROM, Anais, Belém. (in Portuguese).

Dall'Agnol, R., Cunha, I.R.V., Guimarães, F.V., Oliveira, D.C., Teixeira, F.B.T., Feio, G.R., Lamarão, C.N., 2017. Mineralogy, geochemistry, and petrology of Neoarchean ferroan to magnesian granites of Carajás Province, Amazonian Craton: The origin of hydrated granites associated with charnockites. Lithos, 277: 3 - 32.

Debon, F., Le Fort, P., 1983. A chemical–mineralogical classification of common plutonic rocks and associations. Trans. R. Soc. Edinb. Earth Sci. 73 (3), 135–149.

De Paolo, D.J., 1981. Trace element and isotopic effects of combined wall-rock assimilation and fractional crystallization. Earth and Planetary Science Letters, 53(2), 189-202.

Didier, J., 1973. Granites and their enclaves. Amsterdam: Elsevier.

Donaire, T., Pascual, E., Pin, C., Duthou, J.L., 2005. Microgranular enclaves as evidence of rapid cooling in granitoid rocks: the case of the Los Pedroches granodiorite, Iberian Massif, Spain. Contributions to Mineralogy and Petrology, 149, 247-265.

Dowty, E., 1980. Synneusis reconsidered. Contributions to Mineralogy and Petrology, 74(1), 75-84.

Eby, G.N., 1992. Chemical subdivision of the A-type granitoids: petrogenetic and tectonic implications. Geology, 20(7), 641-644.

Ersoy, E.Y., 2013. PETROMODELER (Petrological Modeler): a Microsof Excel spreadsheet program for modelling melting, mixing, crystallization and assimilation processes in magmatic systems. Turk. J. Earth Sci. 22, 115–125.

Feio, G.R.L., Dall'Agnol, R., Dantas, E.L., Macambira, M.J.B., Santos, J.O.S., Althoff, F.J., Soares, J.E.B., 2013. Archean granitoid magmatism in the Canaã dos Carajás area: implications for crustal evolution of the Carajás province, Amazonian craton, Brazil. Precambrian Res. 227, 157–185.

Fernandez, A.N., Barbarin, B., 1991. Relative rheology of coexisting mafic and felsic magmas: Nature of resulting interaction processes. Shape and mineral fabricsof mafic microgranular enclaves. In: Didier, J., Barbarin, B. (Eds.), Enclaves and Granite Petrology, Developments in Petrology. Vol. 13. Elsevier, Amsterdam, pp. 263–275.

Ferreira, A.T.R., 2009. Petrografia, geoquímica e geocronologia dos diques da área de Bannach, Terreno Granito-Greenstone de Rio Maria, SE do Pará. In: Trabalho de Conclusão de Curso – Federal University of Pará, Belém, pp. 55 (in Portuguese).

Frost, B.R., Barnes, C., Collins, W., Arculus, R., Ellis, D., Frost, C., 2001. A Chemical classification for granitic rocks. J. Petrol. 42(11), 2033–2048.

Frost, C.D., Frost, B.R., 1997. Reduced rapakivi type granites: the tholeiitic connection. Geology, 25(7), 647–650.

Frost, C.D., Frost, B.R., Chamberlain, K.R., Edwards, B., 1999. Petrogenesis of the 1.43 Ga Sherman batholith, SE Wyoming, USA: a reduced, rapakivi-type anorogenic granite. J. Petrol. 40, 1771–1802.

Frost, C.D., Frost, B.R., 2011. On ferroan (A-type) granitoids: their compositional variability and modes of origin. Journal of petrology, 52(1), 39-53.

Gastal, M.C.P., 1987. Mapeamento e petrologia do maciço granítico Musa. Rio Maria, Sudeste do Pará. Unpublished M.Sc. Thesis. Universidade Federal do Pará, Belem.

Gioia, S.M.C.L., Pimentel, M.M., 2000. The Sm-Nd Isotopic Method in the Geochronology Laboratory 820 of the University of Brasília. Anais da Academia Brasileira de Ciências. 72: 219-246.

Goodge, J.W., Vervoort, J.D., 2006. Origin of Mesoproterozoic A-type granites in Laurentia: Hf isotope evidence. Earth and Planetary Science Letters, 243:711-731.

Griffin, W.L., Wang, X., Jackson, S.E., Pearson, N.J., O'Reilly, S.Y., 2002. Zircon geochemistry and magma mixing, SE China: in-situ analysis of Hf isotopes, Tonglu and Pingtan igneous complexes. Lithos 61, 237–269.

Heinonen, A., Andersen, T., Rämö, O.T., 2010. Re-evaluation of rapakivi petrogenesis: Source constraints from the Hf isotope composition of zircon in the rapakivi granites and associated mafic rocks of southern Finland. Journal of Petrology, 51: 1687–1709.

Hibbard, M.J., 1991. Textural anatomy of twelve magma-mixed granitoid systems. In: Didier J., Barbarin B. (Eds.). Enclaves and granite petrology (developments in petrology). Amsterdam: Elsevier, 431-444.

Hoffman, P.F., 1988. United Plates of America, the birth of a craton-Early Proterozoic assembly and growth of Laurentia. Annual Review of Earth and Planetary Sciences, 16: 543–603.

Horstwood, M.S.A., Kosler, J., Gehrels, G., Jackson, S.E., McLean, N.M., Paton, C., Pearson, N.J., Sircombe, K., Sylvester, P., Vermeesch, P., Bowring, J.F., Condon, D.J., Schoene, B., 2016. Community-Derived Standards for LA-ICP-MS U-Th-Pb Geochronology – Uncertainty Propagation, Age Interpretation and Data Reporting. Geostand. Geoanal. Res. 40 (3), 311–332.

Ishihara, S., 1977. The magnetite-series and ilmenite-series granitic rocks. Min. Geol. 27 (145), 293–305.

Janoušek, V., Farrow, C.M., Erban, V., 2006. Interpretation of whole-rock geochemical data in igneous geochemistry: introducing Geochemical Data Toolkit (GCDkit). J. Petrol. 47 (6), 1255–1259.

Javier Rios, F., Villas, R.N., Dall'Agnol, R., 1995. O Granito Serra dos Carajás: fácies petrográficas e avaliação do potencial metalogenético para estanho no setor norte. Revista Brasileira de Geociencias 25, 20–31 (in Portuguese).

Johannes, W., Holtz, F., 1996. Petrogenesis and Experimental Petrology of Granitic Rocks. Springer, Berlin Heidelberg (335 pp.).

King, P.L., Chappell, B.W., Allen, C.M., White, A.J.R., 2001. Are A-type granites the high-temperature felsic granites? Evidence from fractionated granites of the Wangrah Suite. Australian Journal of Earth Sciences, 48(4), 501–514.

Kober, B., 1987. Single-zircon evaporation combined with Pb$^+$ emitter bedding for ^{207}Pb/^{206}Pb-age investigations using thermal ion mass spectrometry, and implications to zirconology. Contribution Mineralogy and Petrology 96, 63–71.

Kosunen, P.J., 2004. Petrogenesis of Mid-Proterozoic A-Type Granite: Case Studies from Fennoscandia (Finland) and Laurentia (New Mexico). Department of Geology, University of Helsinki, Finland. Dr. Thesis.

Kumar, S., Bora, S., Sharma, U.K., Yi K., Kim, N., 2017. Early Cretaceous subvolcanic calc-alkaline granitoid magmatism in the Nubra-Shyok valley of the Shyok Suture Zone, Ladakh Himalaya, India: Evidence from geochemistry and U–Pb SHRIMP zircon geochronology. Lithos, 277:33- 50.

Lamarão, C.N., Pinho, S.C.C., Paiva Júnior, A.L., Galarza-Toro, M.A., 2012. Mineralogy and geochemistry of the Paleoproterozoic, tin mineralized Bom Jardim Granite of the Velho Guilherme Suite, eastern Amazonian Craton. Journal of South American Earth Sciences 38, 159–173.

Leite, A.A.S., 2001. Geoquímica, petrogênese e evolução estrutural dos granitoides arqueanos da região de Xinguara, SE do Cráton Amazônico. In: Belém, Universidade Federal do Pará, Centro de Geociências, Brazil. Dr. Thesis. (in Portuguese).

Le Maitre, R.W., Streckeisen, A., Zanettin, B., Le Bas, M.J., Bonin, B., Bateman, P., Bellieni, G., Dudek, A., Efremova, J., Keller, J., Lameyre, J., Sabine, P.A., Schmidt, R., Sørensen, H., Woolley, A.R., 2002. Igneous rocks. A classification and glossary of terms. In: Recommendations of the International Union of Geological Sciences Subcommission on the Systematics of Igneous Rocks. Cambridge University Press, Cambridge, p. 252.

Lima, P.H.A., 2011. Geologia, petrografia e geocronologia do Granito São Joao, Província Carajás, SSE do Pará. In: Trabalho de Conclusão de Curso – Federal University of Pará, Belém, pp. 1–47 (in Portuguese).

Liu L., Qiu J.S., Li Z., 2013. Origin of mafic microgranular enclaves (MMEs) and their host quartz monzonites from the Muchen pluton in Zhejiang Province, Southeast China: Implications for magma mixing and crust– mantle interaction. Lithos, 160-161:145-163.

Loiselle, M.C., Wones, D.R., 1979. Characteristics and origin of anorogenic granites. Abstracts with programs. Geol. Soc. Am. 11, 468.

Ludwig, K.R., 2003. User's Manual for Isoplot/ex Version 3.00 e A Geochronology Toolkit for Microsoft Excel, vol. 4. Special Publication, Berkeley Geochronological Center, p. 70.

Macambira, M.J.B., Moura, C.A.V., Lafon, J.M., Scheller, T., 1994. O método Pb-Pb por Evaporação em Zircão: avaliação dos Dados Obtidos no Laboratório de Geologia Isotópica da UFPA. In: Congresso brasileiro de geologia, 38. Camboriú, pp. 404–406, 1994. Anais SBG.

Macambira M.J.B., Lancelot J.R., 1996. Time Constraints for the Formation of the Archean Rio Maria Crust, Southeastern Amazonian Craton, Brazil. International Geology Review 38(12): 1134-1142.

Machado, N., Lindenmayer, Z., Krogh, T.H., Lindenmayer, D., 1991. U-Pb geochronology of Archaean magmatism and basement reactivation in the Carajás area, Amazon shield, Brazil. Precambrian Research, 49(3-4), 329-354.

Marangoanha, B., Oliveira, D.C., 2014. Diabásios e anfibolitos da área de Nova Canadá: natureza e implicações tectônicas para a Província Carajás. Boletim do Museu Paraense Emílio Goeldi-Ciências Naturais, 9(3), 565-596.

Marangoanha, B., Oliveira, D.C., Dall'Agnol, R., 2019. The Archean granulite-enderbite complex of the northern Carajás province, Amazonian craton (Brazil): Origin and implications for crustal growth and cratonization. Lithos 350–351, 105275.

Martin, H., 1987. Petrogenesis of Archaean trondhjemites, tonalites and granodiorites from eastern Finland: major and trace element geochemistry. J. Petrol. 28, 921–953.

Milhomem Neto, J.M.., Lafon, J.M., Galarza, M.A., 2017. Lu-Hf em zircão por LA-MC-ICP-MS no laboratório Pará-Iso (UFPA): metodologia e primeiro exemplo de aplicação na porção sudeste do Escudo das Guianas, estado do Amapá. In: Lima A.M & Gorayeb P. (eds.) Contribuições à geologia da Amazônia, 10, p. 195-208. (in Portuguese).

McDonough, W.F., Sun, S.S., 1995. The composition of the Earth. Chem. Geol. 120 (3–4), 223–253.

Oliveira, D.C., 2006. Modelos de Evolução e Colocação dos Granitos Paleoproterozoicos da Suíte Jamon, SE do Cráton Amazônico. Federal University of Pará. Dr. Thesis. Institute of Geosciences, pp. 186 In Portuguese.

Oliveira, D.C., Dall'Agnol, R., Barros, C.E.M., Oliveira, M.A., 2009. Geology, geochemistry and magmatic evolution of the Paleoproterozoic, anorogenic oxidized A-type Redenção granite of the Jamon Suite, eastern Amazon Craton, Brazil. Canadian Mineralogist, 47(6), 1441–1468.

Oliveira, D.C., Silva, L.R., Nascimento, A.C., Marangoanha, B., Gabriel, E.O., Leite-Santos, P.J., Machado, J.R.M., Felix, W.Q., Silva-Silva, L.C., Santos, R.F.S., 2023. Revisão litoestratigráfica com implicações para compartimentação tectônica da Província Mineral de Carajás, sudeste do Cráton Amazônico. In: Anais do 17° Simpósio de Geologia da Amazônia (pp. 434-441), Santarém: SBG-Núcleo Norte.

Oliveira, M.A., Dall'Agnol, R., Almeida, J.A.C., 2011. Petrology of the Mesoarchean Rio Maria and the discrimination of sanukitoid series. Lithos 137, 193–209.

Paiva Jr., A.L., 2009. Geologia, petrografia, geocronologia e geoquímica do Granito anorogênico Seringa, Província Mineral de Carajás, SSE do Pará. Federal University of Pará. Dissertation. Graduated Program on Geology and Geochemistry. Institute of Geosciences, p. 158 (in Portuguese).

Patchett, P.J., Tatsumoto, M., 1980. A routine high-precision method for Lu-Hf isotope geochemistry and chronology. Contrib. Mineral. Petrol. 75, 263–267.

Patiño Douce, A.E., 1997. Generation of metaluminous A-type granites by low-pressure melting of calc-alkaline granitoids. Geology 25 (8), 743–746.

Pearce, J.A., Harris, N.B.W., Tindle, A.G., 1984. Trace element discrimination diagrams for the tectonic interpretation of granitic rocks. J. Petrol. 25 (4), 956–983.

Perugini, D., Poli, G., 2012. The mixing of magmas in plutonic and volcanic environments: Analogies and differences. Lithos, 153, 261–277.

Petford N. 2003. Rheology of granitic magmas during ascent and emplacement. Annual Review of Earth and Planetary Sciences, 31:399-427.

Pidgeon, R.T., Macambira, M.J.B., Lafon, J.M., 2000. Th-U-Pb isotopic systems and internal structures of complex zircons from an enderbite from the Pium complex, Carajás Province, Brazil: evidence for the ages of granulites facies metamorphism and the protolith of the enderbite. Chem. Geol. 166, 159–171.

Rämö, O.T., 1991. Petrogenesis of the Proterozoic rapakivi granites and related basic rocks of the southeastern Fennoscandia: Nd and Pb isotopic and general geochemical constraints. Geological Survey of Finland Bulletin, 355.

Rämö, O.T., Haapala, I., 1995. One hundred years of rapakivi granite. Mineralogy and Petrology, 52(3-4), 129–185.

Rämö, O.T., Dall'Agnol, R., Macambira, M.J.B., Leite, A.A.S., Oliveira, D.C., 2002. 1.88 Ga oxidized A-type granites of the Rio Maria region, eastern Amazonian craton, Brazil: Positively anorogenic!. Journal of Geology, 110(5):603-610.

Rieder, M., 1998. Nomenclature of the micas. Clay Clay Miner. 63, 267–279.

Rivalenti, G., Mazzuchelli, M., Girardi, V.A.V., Cavazzini, G., Finatti, C., Barbieri, M.A., Teixeira, W., 1998. Petrogenesis of the Paleoproterozoic basaltic- andesite-rhyolite dyke association in the Carajás region, Amazonian craton. Lithos, 43(4), 235-265.

Reubi, O., Blundy, J., 2009. A dearth of intermediate melts at subduction zone volcanoes and the petrogenesis of arc andesites. Nature, 461:1269-1273.

Rodrigues, E.S., Lafon, J.M., Scheller, T., 1992. Geocronologia Pb-Pb da Província Mineral de Carajás: primeiros resultados. In: 37º Congresso Brasileiro de Geologia, v. 2, p. 183-184. Boletim de Resumos Expandidos. São Paulo.

Ruprecht, P., Bergantz, G.W., Cooper, K.M., Hildreth, W., 2012. The crustal magma storage system of Volcán Quizapu, Chile, and the effects of magma mixing on magma diversity. Journal of Petrology, 53(4):801-840.

Russell, W.A., Papanastassiou, D.A., Tombrello, T.A., 1978. Ca isotope fractionation on the earth and other solar system materials. Geochim. Cosmochim. Acta 42, 1075–1090.

Santos, J.O.S., 2003. Geotectônica do Escudo das Guianas e Brasil-Central. In: Bizzi, L. A. et al. (Ed.). Geologia, tectônica e recursos minerais do Brasil: texto, mapas e SIG. Brasília DF. CPRM- Serviço Geológico do Brasil, 169-226, il.

Santos, P.A., Feio, G.R.L., Dall'Agnol, R., Costi, H.T., Lamarão, C.N., Galarza, M.T., 2013. Petrography, magnetic susceptibility and geochemistry of the Rio Branco granite, Carajás province, southeast of Pará, Brazil. Braz. J. Genet. 43, 2–15.

Santos, R.F.S., Oliveira, D.C., Silva, F.F., 2018. Geocronologia U-Pb, classificação e aspectos evolutivos do Granito Marajoara, Província Carajás. Geologia USP. Série Científica 18 (4), 89–124 (in Portuguese).

Santos, R.F.S., Oliveira, D.C., Marangoanha, B., Galarza, M.A., Santos, M.R., 2023. Geochemistry, zircon U-Pb geochronology and Lu-Hf isotopes of the Manda Saia granite: Petrological affinity and magma source of evolved A-type granites from the Carajás province, southeastern Amazonian craton, Brazil. Lithos, 462, 107412.

Sato, K., Tassinari, C.C.G.T., Basei, M.A.S., Siga Júnior, O., Onoe, A.T., Souza, M.D., 2014. Sensitive high resolution, ion microprobe (SHRIMP IIe/MC) of the Institute of Geoscience of University of Sao Paulo, Brazil: analytical method and first results. Geol. Usp. Serie Científica 14 (3), 3-18.

Silva, F.S., Oliveira, D.C., Antonio, P.Y., D'Agrella-Filho, M., Lamarão, C.N., 2016. Bimodal magmatism of the Tucumã area, Carajás Province: U-Pb geochronology, classification and processes. J. S. Am. Earth Sci. 72, 95–114.

Silva Jr., R.O, Dall'Agnol, R., Oliveira, E.P., 1999. Geologia, petrografia e geoquímica dos diques proterozoicos da região de Rio Maria, sudeste do Pará. Geoch. Brasiliensis, 13(2), 163-181.

Silva, L.R., Oliveira, D.C., Dantas, E.L., 2023. Isótopos de Nd dos granitoides mesoarqueanos de Ourilândia do Norte, Terreno Canaã dos Carajás: Implicações para extração e retrabalhamento crustal na Província Carajás. In: Anais do 17° Simpósio de Geologia da Amazônia (p. 434-441), Santarém: SBG-Núcleo Norte.

Singer, B.S., Pearce, T.H., 1993. Plagioclase zonatton in a basaltto rhyodacite eruptive suite, Seguam island, Alaska: observations bv nomarski contrast interference. Canadian Mineralogist, 31, 459-466.

Siuda, J.D., Bagiński, B., 2019. Magma mingling textures in granitic rocks of the eastern part of the Strzegom-Sobótka Massif (Polish Sudetes). Acta Geologica Polonica, 69(1):143-160.

Skjerlie, K.P., Johnston, A.D., 1993. Fluid-absent melting behavior of F-rich tonalitic gneiss at mid-crustal pressures: implications for the generation of anorogenic granites. Journal of Petrology, 34(4), 785–815.

Shukla S., Mohan M.R., 2019. Magma mixing in Neoarchean granite from Nalgonda region, Eastern Dharwar Craton, India: Morphological, mineralogical and geochemical evidences. Journal of Earth System Science, 128(3):71.

Smith, J.V., 1974. Feldspar Minerals. Volume 2. Chemical and Textures properties. Springer-Verlag, Berlim, Heidelberg and New York. Prince DM 130.50.

Sousa, S.D., 2020. O Greenstone Belt Sapucaia: implicações para a evolução crustal mesoarqueana da Província Carajás, Instituto de Geociências. University of São Paulo, São Paulo. Dr. Thesis (in Portuguese).

Souza, Z.S., Potrel, H., Lafon, J.M., Althoff, F.J., Pimentel, M.M., Dall'Agnol, R., Oliveira, C.G., 2001. Nd, Pb and Sr isotopes of the identidade belt, an Archaean greenstone belt of the Rio Maria region (Carajás province, Brazil): implications for the Archaean geodynamic evolution of the Amazonian craton. Precambrian Res. 109, 293–315.

Spencer, C.J., Kirkland, C.L., Taylor, R.J.M., 2016. Strategies towards statistically robust interpretations of in situ U-Pb zircon geochronology. Geoscience Frontiers 7, 581-589.

Stacey, J.S., Kramers, J.D., 1975. Approximation of terrestrial lead isotope evolution by two-stage model. Earth and Planetary Science Letters 26 (2), 207–221.

Stern, R.A., 1998. High resolution SIMS determination of radiogenic trace isotope ratios in minerals. In: Cabri, L. J., Vaughan, D. J (Eds). Modern approaches to ore and environmental mineralogy. Mineralogical Association of Canada. Short Course Series, 27, 241-268.

Stevens, G., Clemens, J.D., 1993. Fluid–absent melting and the roles of fluids in the lithosphere: a slanted summary? Chemical Geology 108, 1–17.

Tassinari, C.C.G., Macambira, M., 2004. A evolução tectônica do Craton Amazônico. In: Mantesso – Neto, V., Bartorelli, A., Carneiro, C. D. R., Brito Neves, B. B. (Eds.), Geologia do Continente Sul Americano: Evolução da obra de Fernando Flávio Marques Almeida. São Paulo, p. 471-486.

Tavares, F.M., Trouw, R.A.J., Silva, C.M.G., Justo, A.P., Oliveira, J.K.M., 2018. The multistage tectonic evolution of the northeastern Carajás Province, Amazonian Craton, Brazil: revealing complex structural patterns. J. S. Am. Earth Sci. 88, 238–252.

Teixeira, L.R., 2005. GENESIS 4.0—Software de Modelamento Geoquímico.

Teixeira, M.F.B., Dall'Agnol, R., Santos, J.O.S., Sousa, L.A.M., Lafon, J.-M., 2017. Geochemistry, geochronology and Nd isotopes of the Gogó da Onça Granite: a new Paleoproterozoic A-type granite of Carajás Province, Brazil. J. S. Am. Earth Sci. 80, 47–65.

Teixeira, M.F.B., Dall'Agnol, R., Santos, J.O.S., Oliveira, D.C., Lamarão, C.N., McNaughton, N.J., 2018. Crystallization ages of Paleoproterozoic A-type Granite Suites and Related Granites of Carajás Province, Amazon Craton: constraints from U-Pb geochronology of zircon and titanite. J. S. Am. Earth Sci. 88, 312–331.

Teixeira, M.F.B., Dall'Agnol, R., Santos, J.O.S., Kemp, A., Evans, N., 2019. Petrogenesis of the Paleoproterozoic (Orosirian) A-type granites of Carajás province, Amazon craton, Brazil: combined in situ Hf–O isotopes of zircon. Lithos 323–333, 1–22.

Teixeira, N.P., 1999. Contribuição ao estudo das rochas granitoides e mineralizações associadas da Suíte Intrusiva Velho Guilherme, Província Estanífera do Sul do Pará. São Paulo University. Institute of Geosciences, p. 508 Dr. Thesis. (in Portuguese).

Teixeira, N.P., Bettencourt, J.S., Moura, C.A.V., Dall'Agnol, R., Macambira, E.M.B., 2002. Archean crustal sources for Paleoproterozoic tin-mineralized granites in the Carajás Province, SSE Pará, Brazil: Pb–Pb geochronology and Nd isotope geochemistry. Precambrian Research 119, 257–275.

Teixeira, W., Hamilton, M.A., Girardi, V.A., Faleiros, F.M., Ernst, R.E., 2019. U-Pb baddeleyite ages of key dyke swarms in the Amazonian Craton (Carajás/Rio Maria and Rio Apa areas): Tectonic implications for events at 1880, 1110 Ma, 535 Ma and 200 Ma. Precambrian Research, 329, 138-155.

Thirlwall, M.F., Anczkiewicz, R., 2004. Multidynamic isotope ratio analysis using MC–ICP–MS and the causes of secular drift in Hf, Nd and Pb isotope ratios. Int. J. Mass Spectrom. 235, 59–81.

Vance, J.A., 1965. Zoning in igneous plagioclase: patchy zoning. The Journal of Geology, 73(4), 636-651.

Vasquez, M.L., Macambira, M.J.B., Armstrong, R.A., 2008. Zircon geochronology of granitoids from the western Bacajá domain, southeastern Amazonian craton, Brazil: Neoarchean to Orosirian evolution. Precambrian Res. 161, 279–302.

Vasquez, M.L., Rosa-Costa, L.T., 2008. Geologia e Recursos Minerais do Estado do Pará: Sistema de Informações Geográficas – SIG: texto explicativo dos mapas Geológico e Tectônico e de Recursos Minerais do Estado do Pará. Escala 1:1.000.000. CPRM, Belém, pp. 329.

Vernon, R.H., Etheridge, M.A., Wall, V.J., 1988. Shape and microstructure of microgranitoid enclaves: indicators of magma mingling and flow. Lithos 22, 1–11.

White, A.J.R., Chappell, B.W., Wyborn, D., 1999. Application of the restite model to the Deddick granodiorite and its enclaves. A reinterpretation of the observations and data of Maas et al. (1997). Journal of Petrology 40, 413–421.

Whalen, J.B., Currie, K.L., Chappell, B.W., 1987. A-types granites: geochemical characteristics, discrimination and petrogenesis. Contributions of Mineralogy and Petrology, 95(4), 407–419.

Wilson, M., 1989. Igneous Petrogenesis e A Global Tectonic Approach. Springer, Dordrecht.

Yu, K., Liu, Y., Hu, Q., Ducea, M. N., Hu, Z., Zong, K., 2018. Magma recharge and reactive bulk assimilation in enclave-bearing granitoids, Tonglu, South China. Journal of Petrology, 59(5), 795–824.

CAPÍTULO 4 CONSIDERAÇÕES FINAIS

- Os granitos Marajoara e Manda Saia representam intrusões (*stocks*) encaixadas em rochas mesoarqueanas do Domínio Rio Maria. São formados por rochas sobre as quais não foram observados vestígios de deformação no estado sólido (aspecto isotrópico) e frequentemente apresentam enclaves angulosos de suas rochas encaixantes (granitoides tipo TTG e sequência *greenstone belt*). Esses plútons teriam sido colocados em níveis crustais rasos (epizona) em um ambiente de tectônica extensional sob a influência reduzida dos esforços regionais.

- O GMJ é formado por biotita monzogranitos de texturas equi- e heterogranular, além de inúmeros enclaves porfiríticos e microgranulares de ocorrência restrita à fácies heterogranular. Por sua vez, o GMS é formado por sieno- e monzogranitos.

- São granitos peraluminosos afins dos granitos *ferroan* de Frost *et al*. (2001), com altas razões K_2O/Na_2O e $FeOt/(FeOt+MgO)$. São enriquecidos em HFSE e mostram afinidades geoquímicas tanto com os granitos intraplaca tipo-A oxidados de Dall'Agnol & Oliveira (2007) e da série magnetita (fácies heterogranular e enclaves porfiríticos) quanto com os granitos tipo-A reduzidos e da série ilmenita (fácies equigranular). Já o GMS mostra um caráter moderadamente reduzido. Por fim, os enclaves microgranulares mostram afinidade com os granitos magnesianos e da série cálcio-alcalina**.**

- A existência de intervalos ou *gaps* composicionais que separam as fácies identificadas no GMJ, indica que a evolução do plúton não se deu por cristalização fracionada a partir de um único magma, e sim, por processos mais complexos em que sua origem estaria relacionada a variações significativas nas composições de seus protólitos e/ou condições de formação.

- As análises U-Pb em zircão (SHRIMP) forneceram idades de cristalização de 1884 ± 11 Ma para o GMJ e de 1866 ± 10 Ma para o GMS. Os dados isotópicos de Lu-Hf indicam $\varepsilon_{Hf}(t)$ entre -11 e -18 e $Hf-T_{DM}^{C}$ de 3,2 a 3,6 Ga para o GMJ; e $\varepsilon_{Hf}(t)$ entre -13 e -19 e $Hf-T_{DM}^{C}$ de 3,3 a 3,6 Ga para o GMS. Esses dados são compatíveis com a hipótese de que estes granitos foram gerados a partir da fusão de uma crosta félsica mesoarqueana e que a colocação desses plútons se deu em um intervalo de ~20 Ma.

- O modelamento geoquímico sugere que a fácies heterogranular do GMJ e as rochas do GMS foram gerados a partir de fusão parcial de rochas tonalíticas de composição análoga ao do Tonalito Arco Verde ou Tonalito Caracol do Domínio Rio Maria, com uma taxa de fusão que varia de 16 a 18% e uma assembleia residual composta por plagioclásio, quartzo, biotita, magnetita e ilmenita. Já as rochas da fácies equigranular do plúton Marajoara e amostra

PMD-15 do plúton Manda Saia mostram que elas foram geradas por fusão parcial também de rochas tonalíticas, porém, com eventual assimilação de componente supracrustal (metassedimentar).

- O modelamento geoquímico também indicou que os diversos enclaves (microgranulares e porfiríticos) encontrados na fácies heterogranular do plúton Marajoara, foram formados a partir de diferentes graus de mistura (55-75 %) entre líquidos máficos (basaltos) e o magma félsico que deu origem às rochas heterogranulares.

- O evento magmático de 1,88 Ga que originou esses granitos também ocorreu em outras províncias do Cráton Amazônico, podendo estar associado à formação da LIP (*Large Igneous Province*) Uatumã. Esse evento foi amplamente extensivo e está registrado em diversos crátons ao redor do mundo, evidenciando sua importância na evolução tectônica da crosta continental no Proterozóico. Os dados apresentados nesta Tese, ratificam a importância da crosta arqueana na origem destes granitos, e, em particular no caso do GMJ destaca-se ainda a contribuição de processos de mistura de magma na dinâmica da câmara magmática durante o *underplating* máfico.

REFERÊNCIAS

Abrantes Júnior F.R. & Lamarão C.N. 2011. Petrografia e variação composicional de zircão do Granito Gradaús, Província Carajás, Centro-Sul do Pará. *In:* 13º Congresso Brasileiro de Geoquímica & 3º Simpósio de Geoquímica dos Países do Mercosul, Gramado. *Anais*[...]. p. 713-716.

Almeida J.A.C, Dall'Agnol R., Leite A.A.S. 2013. Geochemistry and zircon geochronology of the Archean granite suites of the Rio Maria granite-greenstone terrane, Carajás Province, Brazil. *Journal of South American Earth Sciences*, **42**:103-126.

Almeida J.A.C., Dall'Agnol R., Oliveira D.C. 2006. Geologia, Petrografia e Geoquímica do Granito Anorogênico Bannach, Terreno Granito-Greenstone de Rio Maria, Pará. *Revista Brasileira de Geociências*, **36**(2):282-295.

Almeida J.A.C., Guimarães F.V., Dall'Agnol R. 2007. Petrologia magnética do granito anorogênico Bannach, Terreno Granito-Greenstone de Rio Maria, Pará. *Revista Brasileira de Geociências*. **37**:17-36.

Almeida J.A.C., Dall'Agnol R., Dias S.B., Althoff F.J. 2010. Origin of the Archean leucogranodiorito-granite suites: evidence from the Rio Maria terrane and implications for granite magmatism in the Archean. *Lithos,* **120**: 235-257.

Almeida J.A.C., Dall'Agnol R., Oliveira M.A., Macambira M.J.B., Pimentel M.M., Rämö O.T., Guimarães F.V., Leite A.A.S. 2011. Zircon geochronology and geochemistry of the TTG suites of the Rio Maria granite-greenstone terrane: implications for the growth of the Archean crust of Carajás Province, Brazil. *Precambrian Research*, **187**:201-221.

Althoff F.J., Barbey P., Boullier A.M. 2000. 2.8-3.0 Ga plutonism and deformation in the SE Amazonian craton: The Archean granitoids of Marajoara (Carajás Mineral Province, Brazil). *Precambrian Research,* **104**(3-4):187-206.

Anderson J.L. 1983. Proterozoic anorogenic granite plutonism of North America. *In*: Medaris L.G., Mickelson D.M., Byers C.W., Shanks W.C. (eds.). *Proterozoic geology:* selected papers from an International Proterozoic Symposium. Boulder, Colorado The Geological Society of America, Inc. **161**:133–154.

Anderson J.L. & Smith D.R. 1995. The Effects of temperature and fO_2 on the Al-in-hornblende barometer. *American Mineralogist*, **80**:549-559.

Azevedo R.C. 2013. *Suscetibilidade magnética e minerais óxidos de Fe e Ti do Granito Marajoara, Domínio Rio Maria - Província Carajás*. Trabalho de Conclusão de Curso, Instituto de Geociências, Universidade Federal do Pará, Belém, 66 p.

Barbarin B. 2005. Mafic magmatic enclaves and mafic rocks associated with some granitoids of the central Sierra Ne vada batholith, California: nature, origin, and relations with the hosts. *Lithos*, **80**(1-4):155–177.

Barbosa O., Ramos J. R.de Andrade, Gomes F.A., Helmbold R. (eds). 1966. Geologia estratigráfica, estrutural e econômica da área do Projeto Araguaia. *Divisão de Geologia e Mineralogia*, Rio de Janeiro, **19**:1-94.

Barros C.E.M., Dall'Agnol R., Vieira E.A.P., Magalhães M.S. 1995. Granito Central da Serra dos Carajás: avaliação do potencial metalogenético para estanho com base em estudos da borda oeste do corpo. *Boletim do Museu Paraense Emílio Goeldi.* Série Ciências da Terra **7**:93–123.

Black L.P., Kamo S.L., Williams I.S., Mundil R., Davis D.W., Korsch R.J., Foudoulis C. 2003. The application of SHRIMP to Phanerozoic geochronology: a critical application of four zircon standards. *Chem. Geol.* **200**: 171–188.

Carvalho T.A. 2017. *Petrografia, geoquímica e suscetibilidade magnética do granito Gradaús, Província Carajás, SE do Pará.* MS Dissertation, Instituto de Geociências, Pós-graduação em Geologia e Geoquímica, Universidade Federal do Pará, 63 p.

Chappell B.W. & White A.J.R. 1974. Two contrasting granite types. *Pacific Geology*, **8**:173-174.

Chemale Júnior F., Kawashita K., Dussin I.V., Ávila J.N., Justino D., Bertotti A. 2012. U-Pb zircon in situ dating with LA-MC-ICP-MS using a mixed detector configuration. *Anais da Academia Brasileira de Ciências*, **84**(2):275-295.

Cheng Y., Spandler C., Mao J., Rusk B.G. 2012. Granite, gabbro and mafic microgranular enclaves in the Gejiu area, Yunnan Province, China: A case of two-stage mixing of crust- and mantle-derived magmas. *Contributions to Mineralogy and Petrology*, **164**(4): 659–676.

Chu N.C., Taylor R.N., Chavagnac V., Nesbitt R.W., Boella R.M., Milton J.A., German C.R., Bayon G., Burton K. 2002. Hf isotope ratio analysis using multi-collector inductively coupled plasma mass spectrometry: an evaluation of isobaric interference corrections. *Journal of Analytical Atomic Spectrometry*, **17**:1567-1574.

Clemens J.D. & Watkins J.M. 2001. The fluid regime of high-temperature metamorphism during granitoid magma genesis. *Contributions to Mineralogy and Petrology* **140**: 600–606.

Collins W.J., Beams S.D., White A.J., Chappell B.W. 1982. Nature and origin of A-type granites with particular reference to Southeastern Australia. *Contributions to Mineralogy and Petrology*, **80**(2):189–200.

Costa F.G., Santos P.A., Serafim I.C.C.O., Costa I.S.L., Roopnarain S. 2020. From Mesoarchean drips to modern–style tectonics in the Carajás Province, Amazonian Craton. *Journal of South American Earth Sciences* **104**:102817.

Creaser R.A., Price R.C., Wormald R.J. 1991. A-type granites revisited: assessment of a residual-source model. *Geology*, **19**(2): 163–166.

Dall'Agnol R. & Oliveira D.C. 2007. Oxidized, magnetite-series, rapakivi-type granites of Carajás, Brazil: Implications for classification and petrogenesis of A-type granites. *Lithos*, **93**(3-4):215–233.

Dall'Agnol R., Scaillet B., Pichavant M. 1999b. An experimental study of the Lower Proterozoic Jamon Granite, eastern Amazonian craton, Brazil. *Journal of Petrology*, **40**(11):1673-1698.

Dall'Agnol R., Oliveira M.A., Almeida J.A.C., Althoff F.J., Leite A.A.S.L., Oliveira D.C., Barros C.E.M. 2006. Archean and Paleoproterozoic granitoids of the Carajás Metallogenic Province, eastern Amazonian Craton. *In:* Symposium on Magmatism, Crustal Evolution, and Metallogenesis of the Amazonian Craton. *Abstracts volume and field trips guide*. Belém, PRONEX-UFPA/SBG-NO, p 97-150.

Dall'Agnol R., Ramö O.T., Magalhães M.S., Macambira M.J.B. 1999a. Petrology of the anorogenic oxidised Jamon and Musa granites, Amazonian Craton: implications for the genesis of Proterozoic, A-type Granites. *Lithos*, **46**(3):431-462.

Dall'Agnol R., Teixeira N.P., Rämö O.T., Moura C.A.V., Macambira M.J.B., Oliveira D.C. 2005. Petrogenesis of the Paleoproterozoic, rapakivi, A-type granites of the Archean Carajás Metallogenic Province, Brazil. *Lithos*, **80**(1-4):102-129.

Dall'Agnol R., Oliveira D.C., Guimarães F.V., Gabriel E.O., Feio G.R.L., Lamarão C.N., Althoff F.J., Santos P.A., Teixeira M.F.B., Silva A.C., Rodrigues D.S., Santos M.J.P., Silva C.R.P., Santos R.D., Santos P.J.L. 2013. Geologia do Subdomínio de Transição do Domínio Carajás e Implicações para a evolução arqueana da Província Carajás e Pará. *In:* SGB, 13° Simpósio de Geologia da Amazônia, Belém. *Recursos Minerais e Sustentabilidade Territorial na Amazônia*: anais, p.1082-1085.

De Paolo D.J. 1981. Trace element and isotopic effects of combined wall-rock assimilation and fractional crystallization. *Earth and Planetary Science Letters*, **53**(2):189-202.

Dupuis C. & Beaudoin G. 2011. Discriminant diagrams for iron oxide trace element fingerprinting of mineral deposit types. *Mineral. Deposita*, **46**(4):319–335.

Ersoy E.Y. 2013. Petromodeler (Petrological Modeler): a Microsoft® Excel© spreadsheet program for modelling melting, mixing, crystallization and assimilation processes in magmatic systems. *Turkish Journal of Earth Sciences*, **22**(1):115-125.

Favacho I.N.S. 2013. *Petrografia, susceptibilidade magnética e microscopia eletrônica de varredura, do Granito Manda Saia, Terreno Granito-Greenstone de Rio Maria, sudeste do estado do Pará*. Trabalho de Conclusão de Curso, Instituto de Geociências, Universidade Federal do Pará, Belém, 83 p.

Ferreira A.T.R. 2009. *Petrografia, geoquímica e geocronologia dos diques da área de Bannach, Terreno Granito-Greenstone de Rio Maria, SE do Pará*. Trabalho de Conclusão de Curso, Instituto de Geociências, Universidade Federal do Pará, Belém, 55 p.

Frei D. & Gerdes A. 2009. Accurate and precise in-situ zircon U-Pb age dating with high spatial resolution and high sample throughput by automated LA-SF-ICP-MS. *Chemical Geology*, **261**(3–4): 261–270.

Frost B.R., Barnes C., Collins W., Arculus R., Ellis D., Frost C. 2001. A chemical classification for granitic rocks. *Journal of Petrology*, **42**(11):2033–2048.

Frost C.D. & Frost B.R. 2011. On ferroan (A-type) granitoids: their compositional variability and modes of origin. *Journal of Petrology*, **52**(1): 39-53.

Gabriel E.O. & Oliveira D.C. 2014. Geologia, petrografia e geoquímica dos granitoides arqueanos de alto magnésio da região de Água Azul do Norte, porção ao sul do Domínio Carajás, Pará. *Boletim do Museu do Pará. Emílio Goeldi.* Ciências Nat. **9**:533-564.

Gastal M.C.P. 1987. *Petrologia do maciço granítico Musa, Sudeste do Pará.* MS Dissertation, Instituto de Geociências, Universidade Federal do Pará, Belém, 316p.

Gioia S.M.C.L. & Pimentel M.M. 2000. The Sm-Nd Isotopic Method in the Geochronology Laboratory of the University of Brasília. *Anais da Academia Brasileira de Ciências*. **72**:219-246.

Guimarães F.V.G., Dall'Agnol R., Almeida J.A.C., Oliveira M.A. 2010. Caracterização geológica, petrográfica e geoquímica do Trondhjemito Mogno e Tonalito Mariazinha, Terreno Granito-Greenstone de Rio Maria, SE do Pará. *Revista Brasileira de Geociências*, **40**(2):196–211.

Hibbard M.J. 1991. Textural anatomy of twelve magma-mixed granitoid systems. *In*: Didier J. & Barbarin B. (eds.). *Enclaves and granite petrology* (developments in petrology). Amsterdam, Elsevier, p. 431-444.

Horstwood M.S.A., Košler J., Gehrels G., Jackson S.E., McLean N.M., Paton C., Pearson N.J., Sircombe K., Sylvester P., Vermeesch P., Bowring J.F., Condon D.J., Schoene B. 2016. Community-Derived Standards for LA-ICP-MS U-Th-Pb Geochronology – Uncertainty Propagation, Age Interpretation and Data Reporting. *Geostandards and Geoanalytical Research*, **40**(3): 311-332.

Ishihara S. 1977. The magnetite-series and ilmenite-series granitic rocks. *Mining Geology*, **27**(145):293–305.

Javier Rios F., Villas R.N., Dall'Agnol R. 1995. O Granito Serra dos Carajás: Fácies petrográficas e evolução petrológica do setor norte. *Revista Brasileira de Geociências* **25**(1):20-31.

Jackson S.E., Pearson N.J., Griffin W.L., Belousova E.A. 2004. The application of laser ablation-inductively coupled plasma-mass spectrometry to in situ U-Pb zircon geochronology. *Chemical Geology*, **211**: 47–69.

Johannes W. & Holtz F. 1996. *Petrogenesis and experimental petrology of granitic rocks*. Berlin Heidelberg, Springer, 335 p.

Kober B. 1987. Single-zircon evaporation combined with Pb$^+$ emitter bedding for ^{207}Pb/^{206}Pb-age investigations using thermal ion mass spectrometry, and implications to zirconology. *Contributions to Mineralogy and Petrology,* **96**:63-71.

Kumar S., Bora S., Sharma U.K., Yi K., Kim N. 2017. Early Cretaceous subvolcanic calc-alkaline granitoid magmatism in the Nubra-Shyok valley of the Shyok Suture Zone, Ladakh Himalaya, India: Evidence from geochemistry and U–Pb SHRIMP zircon geochronology. *Lithos*, **277**:33-50.

Lafon J.M., Macambira M.J.B., Pidgeon R.T. 2000. Zircon U–Pb SHRIMP dating of Neoarchean magmatism in the southwestern part of the Carajás Province (eastern Amazonian Craton, Brazil). *In*: 30th International Geological Congress, *Abstract Volume*, 1CDROM.

Lamarão C.N., Pinho S.C.C., Paiva Junior A.L., Galarza Toro M.A. 2012. Mineralogy and geochemistry of the Paleoproterozoic, tin-mineralized Bom Jardim Granite of the Velho Guilherme Suite, eastern Amazonian Craton. *Journal of South American Earth Science,* **38**:159-173.

Leite A.A.S., Dall'Agnol R., Macambira M.J.B, Althoff F.J. 2004. Geologia e geocronologia dos granitoides arqueanos da região de Xinguara (PA) e suas implicações na evolução do terreno granito-greenstone de Rio Maria. *Revista Brasileira de Geociências,* **34**:447-458.

Le Maitre R.W. 2002. *A classification of igneous rocks and glossary of terms*. 2nd. London, 193 p.

Lima P.H.A., Lamarão C.N., Santo M.J.P. 2014. Petrografia, geoquímica e suscetibilidade magnética do Granito Paleoproterozoico São João, sudeste do Cráton Amazônico, Província Carajás. *Boletim do Museu Paraense Emilio Goeldi*. **9**:47-72.

Loiselle M.C. & Wones D.R. 1979. *Characteristics and origin of anorogenic granites*. [*S.l.*, *s.n.*], 468. (Geological Society of America 11).

Ludwig K.R. 2003. *User's manual for isoplot/Ex Version 3.00 e a geochronology Toolkit for Microsoft Excel, v. 4*. Berkeley Geochronological Center, Special Publication, 70 p.

Ludwig K.R. 2009. *Isoplot v.4 for Excel 2007*, Berkeley Geochronology Center, Berkeley, California, 71 p.

Macambira M.J.B. & Lancelot J. 1991. Em busca do embasamento arqueano da região de Rio Maria, sudeste do Estado do Pará. *In:* SBG, 3º Simpósio de Geologia da Amazônia, Belém, *Resumos Expandidos*, p.49-58.

Machado N., Lindenmayer Z., Krogh T.E., Lindenmayer D. 1991. U-Pb geochronology of Archean magmatism and basement reactivation in the Carajás Área, Amazon shield, Brazil. *Precambrian Research*, **49**:329-354.

Macambira M.J.B., Moura C.A.V., Lafon J.M., Scheller T. 1994. O método Pb-Pb por Evaporação em Zircão: avaliação dos Dados Obtidos no Laboratório de Geologia Isotópica da UFPA. *In*: SBG, 38º Congresso Brasileiro de Geologia, Camboriú, *Anais*[...], p.404–406.

Mesquita C.J.S., Dall'Agnol R., Almeida J.A.C. 2018. Mineral chemistry and crystallization parameters of the A-type Paleoproterozoic Bannach granite, Carajás province, Pará, Brazil. *Brazilian Journal of Geology*, **48**:575-601.

Milhomem Neto J.M., Lafon J.M. Galarza M.A. 2017. Lu-Hf em zircão por LA-MC-ICP-MS no laboratório Pará-Iso (UFPA): metodologia e primeiro exemplo de aplicação na porção sudeste do Escudo das Guianas, estado do Amapá. *In*: Lima A.M & Gorayeb P. (eds.) *Contribuições à geologia da Amazônia*, **10**:195-208.

Nadoll P., Angerer T., Mauk J.L., French D., Walshe J. 2014. The chemistry of hydrothermal magnetite: A review. *Ore Geology Reviews*, **61**:1–32.

Nery P.H.S. 2019. *Química mineral e condições de cristalização do granito Gradaús, Sul do Pará, Província Carajás.* MS Dissertation, Programa de Pós-Graduação em Geologia e Geoquímica, Instituto de Geociências, Universidade Federal do Pará, Belém. 99 p.

Nery P.H.S., Lamarão C.N., Nascimento A.C., Marangoanha B., Silva L.R., Oliveira D.C., Carvalho T.A. 2023. Mineral chemistry and crystallization conditions of the anorogenic Gradaús batholith from the Carajás Province, Amazonian craton (Brazil). *Journal of South American Earth Sciences*, **131**: e104593.

Oliveira D.C., Dall'Agnol R., Barros C.E.M, Figueiredo M.A.B.M. 2002. Petrologia magnética do Granito Paleoproterozoico Redenção, SE do Cráton Amazônico. *In*: Klein E.L, Vasquez M.L., Rosa-Costa L.T. (eds.) *Contribuições à geologia da Amazônia*. Belém, SBG Núcleo Norte, v.3, p.115-132.

Oliveira D.C., Dall'Agnol R., Barros C.E.M., Oliveira M.A. 2009. Geology, geochemistry and magmatic evolution of the Paleoproterozoic, anorogenic oxidized A-type Redenção granite of the Jamon Suite, eastern Amazon Craton, Brazil. *Canadian Mineralogist*, **47**(6):1441–1468.

Oliveira D.C., Sérgio P.N., Ricardo I.F.T., Roberto D.A., Gorki M., Paulo B.C. 2010. Magnetic anisotropy of the Redenção granite, eastern Amazonian craton (Brazil): implications for the emplacement of A-type. *Tectonophysics*, **493**(1-2):27-41.

Oliveira D.C., Silva L.R., Nascimento A.C., Marangoanha B., Gabriel E.O., Leite-Santos P.J., Machado J.R.M., Felix W.Q., Silva-Silva L.C., Santos R.F.S., 2023. Revisão litoestratigráfica com implicações para compartimentação tectônica da Província Mineral de Carajás, sudeste do Cráton Amazônico. *In*: SBG-Núcleo Norte, 17º Simpósio de Geologia da Amazônia, Santarém, *Anais*[...], p. 434-441.

Oliveira M.A., Dall'Agnol R., Althoff F.J., Leite A.A.S. 2009. Mesoarchean sanukitoid rocks of the Rio Maria Granite-Greenstone Terrane, Amazonian craton, Brazil. *Journal of South American Earth Sciences*, **27**:146-160.

Paiva Júnior A.L., Lamarão C.N., Lima P.H.A. 2011. Geologia, petrografia e geoquímica do Batólito Seringa, Província Carajás, SSE do Para. *Revista Brasileira de Geociências* **41**:185-202.

Patchett P.J. & Tatsumoto M. 1980. A routine high-precision method for Lu-Hf isotope geochemistry and chronology. *Contributions to Mineralogy and Petrology*, **75**:263-267.

Pimentel M.M. & Machado N. 1994. Geocronologia U-Pb do Terrenos Granito-*Greenstone* de Rio Maria, Pará. *In*: 38º Congresso Brasileiro de Geologia, Camboriú, *Resumos Expandidos*, p.390–391.

Ragland P.C. 1989. *Basic analytical petrology*. 2 ed. New York, Oxford University Press.

Rämö O.T., Dall'Agnol R., Macambira M.J.B., Leite A.A.S., Oliveira D.C. 2002. 1.88 Ga oxidized A-type granites of the Rio Maria region, eastern Amazonian craton, Brazil: positively anorogenic! *Journal of Geology*, **110**: 603-610.

Reubi O. & Blundy J. 2009. A dearth of intermediate melts at subduction zone volcanoes and the petrogenesis of arc andesites. *Nature*, **461**:1269-1273.

Rivalenti G., Mazzuchelli M., Girardi V.A.V., Cavazzini G., Finatti C., Barbieri M.A., Teixeira W. 1998. Petrogenesis of the Paleoproterozoic basaltic-andesite-rhyolite dyke association in the Carajás region, Amazonian craton. *Lithos*, **43**(4):235-265.

Rocha Júnior G.L.D. 2004. *Caracterização petrográfica do Granito Paleoproterozóico Marajoara, Terreno Granito-Greenstone de Rio Maria, SE do estado do Pará.* Trabalho de Conclusão de Curso, Instituto de Geociências, Universidade Federal do Pará, Belém, 45 p.

Rolando A.P. & Macambira M.J.B. 2003. Archean crust formation in Inajá range area, SSE of Amazonian Craton, Brazil, basead on zircon ages and Nd isotopes. *In:* 4° South American Symposium on Isotope Geology, Salvador. *Expanded Abstracts*, 1CD-ROM.

Rollinson H.R. & Pease V. 2021. *Using geochemical data:* to understand geological processes. Cambridge, Cambridge University Press, 358 p.

Ruprecht P., Bergantz G.W., Cooper K.M., Hildreth W. 2012. The crustal magma storage system of Volcán Quizapu, Chile, and the effects of magma mixing on magma diversity. *Journal of Petrology*, **53**(4):801-840.

Russell W.A., Papanastassiou D.A., Tombrello T.A. 1978. Ca isotope fractionation on the earth and other solar system materials. *Geochimica et cosmochimica acta*, **42**(8):1075-1090.

Santos A. & Pena Filho J.I.C. 2000. *Xinguara*: folha SB.22-Z-C. Estado do Pará, escala 1:250.000. Brasília, DF, CPRM, 1 CDROM. (Programa Levantamentos Geológicos Básicos do Brasil - PLGB).

Santos J.O.S. 2003. Geotectônica do Escudo das Guianas e Brasil-Central. *In:* Bizzi L.A. *et al*. (eds.). *Geologia, tectônica e recursos minerais do Brasil*: texto, mapas e SIG. Brasília, DF, CPRM- Serviço Geológico do Brasil, p.169-226.

Santos M.M., Lana C., Scholz R., Buick I., Schmitz M.D., Kamo S.L., Gerdes A., Corfu F., Tapster S., Lancaster P., Storey C.D., Basei M.A.S., Tohver E., Alkmim A., Nalini H., Krambrock K., Fantini C., Wiedenbeck M. 2017. A new appraisal of Sri Lankan BB zircon as a reference material for LA-ICP-MS U-Pb geochronology and Lu-Hf isotope tracing. *Geostandards & Geoanalytical Research*, **41**(3): 335-358.

Santos M.R. 2020. *Petrografia e geoquímica do Granito Manda Saia, Província Carajás*. MS Dissertation. Programa de Pós-graduação em Geologia e Geoquímica, Instituto de geociências, Universidade Federal do Pará, Belém, 42 p.

Santos, P.A., Feio, G.R.L., Dall'Agnol, R., Costi, H.T., Lamarão, C.N., Galarza, M.T., 2013. Petrography, magnetic susceptibility and geochemistry of the Rio Branco granite, Carajás province, southeast of Pará, Brazil. *Brazilian Journal of Geology*. **43**(1):2–15.

Santos R.F.S., Oliveira D.C., Silva F.F. 2018. Geocronologia U-Pb, classificação e aspectos evolutivos do Granito Marajoara, Província Carajás. *Geologia USP. Série Científica*, **18**(4):89-124.

Santos-Silva R.C., Sabóia A.M., Oliveira H.J. 2021. *Projeto integração geológica-geofísica-metalogenética das sequências de Greenstone Belts do Domínio Rio Maria – Novas Fronteiras Rio Maria*. Escalas: 1.250.000–1:100.000. CPRM, Belém, 274 p.

Sato K., Tassinari C.C.G., Basei M.A.S., Siga Júnior O., Onoe A.T., Souza M.D. 2014. Sensitive High Resolution Ion Microprobe (SHRIMP IIe/MC) of the Institute of Geosciences of the University of São Paulo, Brazil: analytical method and first results. *Geologia USP*-Série Científica*, **14**(3):3-18.

Silva F.F., Oliveira D.C., Antonio P.Y.J., D'Agrella M.S.F., Lamarão C.N. 2016. Bimodal magmatism of the Tucumã area, Carajás province: U-Pb geochronology, classification and processes, *Journal of South American Earth Sciences*,**72**:95-114.

Silva L.R. 2022. *Petrogênese e história tectônica dos granitoides mesoarqueanos de Ourilândia do Norte (PA) – Província Carajás*. PhD Thesis, Instituto de Geociências, Programa de Pós-Graduação em Geologia e Geoquímica, Belém, 317 p.

Silva-Silva L.C., Oliveira D.C., Souza D.B. 2020. Geology and geochemical constraints on the origin of the Mesoarchean granitoids from Carajás province, Amazonian craton. *Journal of South American Earth Sciences*, **100**:102–568.

Silva Júnior R.O., Dall'Agnol R., Oliveira E.P. 1999. Geologia, petrografia e geoquímica dos diques proterozoicos da região de Rio Maria, Sudeste do Pará. *Geochimica Brasiliensis*, **13**(2):163-181.

Siuda J.D. & Bagiński B. 2019. Magma mingling textures in granitic rocks of the eastern part of the Strzegom-Sobótka Massif (Polish Sudetes). *Acta Geologica Polonica*, **69**(1):143-160.

Spencer C.J., Kirkland C.L., Taylor R.J.M. 2016. Strategies towards statistically robust interpretations of in situ U-Pb zircon geochronology. *Geoscience Frontiers*, **7**(4):581-589.

Souza S.Z., Dall'Agnol R., Althoff F.J., Leite A.A.S., Barros C.E.M. 1996. Carajás mineral province: geological, geochronological and tectonic constrasts on the Archean evolution of the Rio Maria Granite-Greenstone Terrain and the Carajás block. *In:* Symposium on Archean Terranes of South America Platform. Brasília, DF, *Extended Abstract*, p. 31-32.

Souza Z. S., PotreL A., Lafon J. M., Althoff F. J., Pimentel M. M., Dall'Agnol R., Oliveira C. G. 2001. Nd, Pb and Sr Isotopes in the Identidade Belt, an Archaean Greenstone Belt of the Rio Maria region (Carajás Province, Brazil): Implications for the Archaean Geodynamic Evolution of the Amazonian Craton. *Precambrian Research*, **109**: 293-315.

Stacey J.S. & Kramers J.D. 1975. Approximation of terrestrial lead isotope evolution by a two-stage model. *Earth and Planetary Science Letters*, **26**:207-221.

Stern R.A. 1998. High resolution SIMS determination of radiogenic trace isotope ratios in minerals. *In:* Cabri L.J., Vaughan D.J. (eds.). *Modern approaches to ore and environmental mineralogy*. Ottawa, [*s.n.*], p. 241-268. (Mineralogical Association of Canada, 27).

Stevens G. & Clemens J.D. 1993. Fluid–absent melting and the roles of fluids in the lithosphere: a slanted summary? *Chemical Geology* **108**: 1–17.

Tassinari C.C.G. & Macambira M.J.B. 2004. A evolução tectônica do Craton Amazônico. *In:* Mantesso – Neto V., Bartorelli A., Carneiro C.D.R., Brito Neves B.B. (eds.). *Geologia do Continente Sul Americano*: evolução da obra de Fernando Flávio Marques Almeida. São Paulo, p. 471-486.

Teixeira L.R. 2005. *Genesis versão 4.0. Aplicativo de modelamento geoquímico*. Universidade Federal da Bahia.

Teixeira M.F.B., Dall'Agnol R., Santos J.O.S., Kemp A., Evans N. 2019. Petrogenesis of the Paleoproterozoic (Orosirian) A-type granites of Carajás Province, Amazon Craton, Brazil: Combined in situ Hf–O isotopes of zircon. *Lithos*, **332-333**: 1–22.

Teixeira M.F.B. Dall'Agnol R., Santos J.O.S., Oliveira D.C., Lamarão C.L., McNaughton N.J. 2018. Crystallization ages of Paleoproterozoic A-type granites of Carajás province, Amazon Craton: Constraints from U-Pb geochronology of zircon and titanite. *Journal of South American Earth Sciences,* **88**:312-331.

Teixeira M.F.B., DallAgnol R., Santos J.S.O., Souza L.A.M., Lafon J.M. 2017. Geochemistry, geochronology and Nd isotopes of the Gogó da Onça Granite: A new Paleoproterozoic A-type granite of Carajás Province, Brazil. *Journal of South American Earth Sciences*, **80**:47-65.

Teixeira N.P., Bettencourt J.S., Moura C.A.V., Dall'Agnol R., Macambira E.M.B. 2002. Archean crustal sources for Paleoproterozoic tin-mineralized granites in the Carajás Province, SSE Pará, Brazil: Pb–Pb geochronology and Nd isotope geochemistry. *Precambrian Research,* **119**: 257–275.

Thirlwall M.F. & Anczkiewicz R. 2004. Multidynamic isotope ratio analysis using MC–ICP–MS and the causes of secular drift in Hf, Nd and Pb isotope ratios. *International Journal of Mass Spectrometry*, **235**:59-81.

Vasquez M.L. & Rosa-Costa L.T. 2008. *Geologia e recursos minerais do Estado do Pará:* Sistema de Informações Geográficas – SIG: texto explicativo dos mapas Geológico e Tectônico e de Recursos Minerais do Estado do Pará. Escala 1:1.000.000. CPRM, Belém, 329p.

Whalen J.B., Currie K.L., Chappell B.W. 1987. A-types granites: geochemical characteristics, discrimination and petrogenesis, *Contributions of Mineralogy and Petrology*, **95**:407–419.

Yu K., Liu Y., Hu Q., Ducea M.N., Hu Z., Zong K. 2018. Magma recharge and reactive bulk assimilation in enclave-bearing granitoids, Tonglu, South China. *Journal of Petrology*, **59**(5): 795–824.

ANEXOS

Tabela Suplementar A
Medições de suscetibilidade magnética realizadas em amostras representativas do Granito Marajoara.

	Sample	Mean (x10⁻³)	K (Siv)	Log (K)	%Opaque	Facies	M	Biotite	Qz+Kfs
	GDR-5A	0,0123	1,23333E-05	-4,9089195	0,1	eBMzG	5,0	4,6	64,8
	GDR-8B	0,0130	0,000013	-4,8860566	Tr	eBMzG	3,3	3,1	71,6
A	GDR-7	0,0140	0,000014	-4,8538720	0,2	eBMzG	5,7	4.7	64,6
	GDR-6	0,0150	0,000015	-4,823908741	0,1	eBMzG	5	4,7	67,1
	GDR-8A	0,0267	2,66667E-05	-4,574031268	0,6	eBMzG	4,1	3,2	65,7
B	GDR-9G	0,2460	0,000246	-3,609064893	0,2	hBMzG	4,3	2,7	70,4
	GDR-4A	0,2893	0,000289333	-3,53860153	0,3	hBMzG	2,9	1,7	65,7
	GDR-1A	0,9037	0,000903667	-3,043991737	0,5	hBMzG	6,7	5,2	65,8
	GDR-4B	0,9470	0,000947	-3,0236500	1,2	pME	4	2	60,2
C	GDR-2B (b)	0,9837	0,000983667	-3,0071520	2,0	hBMzG			
	GDR-2D (b)	1,2300	0,00123	-2,910094889	0,5	pME			
	GDR-2B (a)	1,7657	0,001765667	-2,753091282	2,0	hBMzG	5,2	2,3	68,7
	GDR-2A (a)	2,3000	0,0023	-2,638272164	0,3	hBMzG	3	2,1	67,3
	GDR-2A (b)	2,4367	0,002436667	-2,613203878	0,3	hBMzG			
	GDR-2D (a)	2,4400	0,00244	-2,612610174	0,5	pME	3,3	1,5	61,3
	GDR-3	2,6900	0,00269	-2,57024772	0,8	hBMzG	2,9	1,4	74,3
	GDR-9D (a)	3,2467	0,003246667	-2,488562298	1,5	hBMzG	5,3	2,8	61,5
D	GDR-3A	3,2567	0,003256667	-2,487226691	1,0	pME	4,1	2,7	59,3
	GDR-2E	3,4033	0,003403333	-2,468095513	1,8	pME	5,6	2,9	63,3
	GDR-1B	4,2567	0,004256667	-2,370930357	0,5	hBMzG	4,6	2	63,4
	GDR-9F (b)	4,4200	0,00442	-2,354577731	0,1	hBMzG	1,7	1,3	72,8
	GDR-1C	4,6533	0,004653333	-2,332235836	1,3	hBMzG	4,8	2,6	65,1
	GDR-9F (a)	4,9570	0,004957	-2,304781081	0,5	pME	6,8	5,4	64,2
	GDR-9C	6,2867	0,006286667	-2,201579566	1,0	hBMzG	4,5	2,7	62,7
E	GDR-9A	6,4633	0,006463333	-2,189543446	0,2	hBMzG	2,1	1,7	70,5
	GDR-9B	6,6933	0,006693333	-2,174357546	0,5	pME	2,5	1	59,2
	GDR-9D (b)	7,6600	0,00766	-2,11577123	1,0	pME	7,2	5,5	62,2

Statistical Parameters	K (x10-3 Siv)				
	Population A	Population B	Population C	Population D	Population E
Mean	0,0162	0,2677	1,1660	3,4600	6,7758
Median	0,0140	0,2677	0,9837	3,2567	6,5783
Geometric Mean	0,0155	0,2668	1,1282	3,3386	6,7560
Variance	0,0000	0,0009	0,1284	0,9338	0,3752
Standard Deviation	0,0059	0,0306	0,3584	0,9663	0,6125
Minimum Value	0,0123	0,2460	0,9037	2,3000	6,2867
Maximum Value	0,0267	0,2893	1,7657	4,9570	7,6600

Statistical Parameters Number of Samples = 27	K (x10-3 Siv)		A	B	C
Mean	2,6522	eBMzG	100,0		
Median	2,4367	hBMzG		100,0	
Geometric Mean	0,9297	pME	40,0	60,0	
Variance	5,5128				
Standard Deviation	2,3479				
Minimum Value	0,0123				
Maximum Value	7,6600				
Total samples:27	%				
Pop A: 5	18,5				
Pop B: 2	7,4				
Pop C: 20	74,1				

Abreviações: hBMzG - heterogranular biotite monzogranite; eBMzG - equigranular biotite monzogranite; pME - porphyritic microgranular enclave; M - Mafic; Kfs - K-feldspar; Qz - Quartz.

Tabela Suplementar B
Análises de microssonda eletrônica de biotita (% em peso) em amostras do Granito Marajoara e enclaves.

Samples	GDR-1A					GDR-2B									GDR-9A					
	C1					C1					C3				C2					
Spot	Bt 1	Bt 2	Bt 3	Bt 4	Bt 5	Bt 1	Bt 2	Bt 5	Bt 7	Bt 8	Bt 1	Bt 2	Bt 4	Bt 5	Bt 1	Bt 2	Bt 3	Bt 4	Bt 5	Bt 6
SiO_2 (wt%)	37,37	37,74	36,92	37,78	37,42	36,94	37,45	37,42	37,60	37,25	37,00	37,24	37,24	37,61	38,33	38,07	36,71	38,12	38,58	36,82
TiO_2	1,74	2,49	2,48	2,14	1,80	2,15	2,16	2,58	2,39	2,40	2,80	3,29	2,40	2,10	1,64	2,69	2,43	2,97	2,37	2,96
Al_2O_3	18,21	19,42	18,72	17,81	18,14	17,30	18,14	17,50	18,09	18,30	18,08	17,61	17,52	17,82	15,17	15,43	15,53	14,41	14,42	15,73
FeO	19,93	18,93	20,07	19,35	20,50	20,01	19,48	19,41	18,77	17,85	19,58	20,04	19,98	20,13	18,66	18,83	20,84	18,50	18,48	20,56
MgO	5,38	4,87	5,11	5,39	5,77	5,50	5,88	5,26	5,91	5,67	5,12	5,18	5,75	5,26	9,21	8,59	7,84	9,83	9,82	7,58
MnO	1,10	0,79	1,04	0,99	0,97	1,05	0,99	1,01	0,75	0,92	1,10	1,07	1,03	0,85	1,23	0,98	1,08	0,80	0,77	1,02
CaO	0,00	0,00	0,07	0,02	0,01	0,05	0,00	0,02	0,03	0,02	0,00	0,01	0,09	0,00	0,00	0,02	0,06	0,03	0,03	0,06
Na_2O	0,09	0,06	0,02	0,01	0,08	0,07	0,04	0,14	0,05	0,03	0,12	0,08	0,12	0,06	0,12	0,06	0,15	0,09	0,18	0,16
K_2O	10,11	10,29	9,71	10,00	9,87	9,80	9,87	9,86	9,68	9,98	9,69	9,55	9,69	10,23	9,80	10,07	9,92	9,76	9,70	9,07
F	1,84	1,04	1,05	1,19	1,42	1,24	1,26	1,42	1,36	1,34	1,77	1,74	2,09	1,60	3,67	3,44	3,11	3,56	4,27	3,00
Cl	0,09	0,01	0,03	0,07	0,05	0,06	0,04	0,18	0,04	0,01	0,05	0,08	0,03	0,09	0,04	0,04	0,08	0,04	0,08	0,05
H_2O	4,62	4,59	4,98	5,51	4,47	6,24	5,01	5,49	5,68	6,76	5,15	4,69	4,77	4,73	3,47	2,95	3,26	3,07	2,88	3,81
Subtotal	100,48	100,22	100,20	100,27	100,49	100,41	100,33	100,28	100,34	100,53	100,48	100,57	100,69	100,47	101,33	101,16	101,00	101,18	101,56	100,81
(O=F-Cl)	0,80	0,44	0,45	0,52	0,61	0,53	0,54	0,64	0,58	0,56	0,76	0,75	0,89	0,69	1,56	1,46	1,33	1,51	1,82	1,27
Total	99,68	99,78	99,75	99,75	99,88	99,88	99,79	99,64	99,76	99,97	99,72	99,82	99,80	99,78	99,77	99,70	99,67	99,67	99,74	99,54
Structural formula on the bases of twenty two oxygen atoms, considering all iron as Fe^{+2}																				
Si	5,80	5,77	5,71	5,86	5,77	5,81	5,78	5,84	5,82	5,81	5,76	5,76	5,79	5,83	5,91	5,84	5,72	5,85	5,92	5,73
^{IV}Al	2,20	2,23	2,29	2,14	2,23	2,19	2,22	2,16	2,18	2,19	2,24	2,24	2,21	2,17	2,09	2,16	2,28	2,15	2,08	2,27
[T] site																				
^{VI}Al	1,13	1,27	1,12	1,12	1,07	1,01	1,09	1,05	1,12	1,17	1,07	0,98	0,99	1,09	0,67	0,63	0,58	0,46	0,53	0,62
Ti	0,20	0,29	0,29	0,25	0,21	0,25	0,25	0,30	0,28	0,28	0,33	0,38	0,28	0,25	0,19	0,31	0,29	0,34	0,27	0,35
Fet	2,59	2,42	2,60	2,51	2,65	2,63	2,52	2,53	2,43	2,33	2,55	2,59	2,60	2,61	2,41	2,42	2,72	2,37	2,37	2,68
Mg	1,24	1,11	1,18	1,25	1,33	1,29	1,35	1,22	1,36	1,32	1,19	1,20	1,33	1,22	2,12	1,97	1,82	2,25	2,25	1,76
Mn	0,15	0,10	0,14	0,13	0,13	0,14	0,13	0,13	0,10	0,12	0,15	0,14	0,14	0,11	0,16	0,13	0,14	0,10	0,10	0,13
[M] site																				
Ca	0,00	0,00	0,01	0,00	0,00	0,01	0,00	0,00	0,00	0,00	0,00	0,00	0,02	0,00	0,00	0,00	0,01	0,00	0,00	0,01
Na	0,03	0,02	0,01	0,00	0,02	0,02	0,01	0,04	0,01	0,01	0,04	0,02	0,04	0,02	0,03	0,02	0,04	0,03	0,05	0,05
K	2,00	2,01	1,92	1,98	1,94	1,97	1,94	1,96	1,91	1,99	1,92	1,89	1,92	2,02	1,93	1,97	1,97	1,91	1,90	1,80
[I] site																				
F	0,91	0,50	0,51	0,59	0,69	0,62	0,62	0,70	0,67	0,66	0,87	0,85	1,03	0,79	1,79	1,67	1,53	1,73	2,07	1,48
Cl	0,02	0,00	0,01	0,02	0,01	0,02	0,01	0,05	0,01	0,00	0,01	0,02	0,01	0,02	0,01	0,01	0,02	0,01	0,02	0,01
OH	3,96	4,23	4,67	5,17	3,98	5,99	4,61	5,05	5,27	6,45	4,55	4,07	4,02	4,18	1,97	1,52	2,00	1,60	1,09	2,64
Fe/(Fe + Mg)	0,68	0,69	0,69	0,67	0,67	0,67	0,65	0,67	0,64	0,64	0,68	0,68	0,66	0,68	0,53	0,55	0,60	0,51	0,51	0,60
Mg/Mg + Fe	0,32	0,31	0,31	0,33	0,33	0,33	0,35	0,33	0,36	0,36	0,32	0,32	0,34	0,32	0,47	0,45	0,40	0,49	0,49	0,40
Al total	3,33	3,50	3,41	3,26	3,30	3,21	3,30	3,22	3,30	3,36	3,32	3,21	3,21	3,26	2,76	2,79	2,85	2,61	2,61	2,89

Samples	GDR-9D-A								GDR-6								
Spot	C2				C3				C2			C3		C5			
	Bt 1	Bt 2	Bt 3	Bt 4	Bt 1	Bt 2	Bt 3	Bt 4	Bt 1	Bt 2	Bt 3	Bt 1	Bt 2	Bt 1	Bt 2	Bt 3	Bt 4
SiO_2 (wt%)	35,95	38,01	38,18	38,46	37,24	37,81	37,66	37,13	41,90	40,15	42,48	39,64	44,20	42,18	43,51	41,64	41,68
TiO_2	1,63	2,25	2,03	2,26	2,09	2,73	2,74	2,42	1,02	1,10	1,07	1,29	0,49	0,93	0,77	0,88	0,55
Al_2O_3	17,17	16,26	17,29	16,94	16,32	15,86	15,94	16,04	22,65	22,17	24,22	21,51	25,53	23,86	25,37	23,30	23,46
FeO	22,58	20,53	19,01	19,53	19,97	19,76	19,71	20,39	14,70	17,21	12,69	17,83	11,30	14,64	12,14	14,90	14,91
MgO	7,64	7,20	6,94	6,94	7,55	7,77	7,75	7,44	0,39	0,39	0,40	0,37	0,38	0,32	0,33	0,36	0,34
MnO	0,93	0,77	1,00	0,60	0,91	0,95	0,93	0,76	2,06	2,44	1,96	2,64	1,62	2,12	1,66	1,89	1,98
CaO	0,06	0,01	0,01	0,00	0,01	0,00	0,05	0,02	0,05	0,00	0,06	0,14	0,01	0,07	0,03	0,03	0,07
Na_2O	0,06	0,11	0,07	0,08	0,13	0,08	0,15	0,05	0,16	0,24	0,26	0,22	0,28	0,18	0,14	0,18	0,25
K_2O	8,17	9,73	9,79	9,77	10,04	10,10	9,87	9,93	9,70	9,83	9,50	9,88	9,44	9,48	9,64	9,61	9,86
F	1,00	1,88	1,23	1,53	2,70	2,56	2,73	2,65	5,37	4,61	3,86	4,34	3,69	4,18	4,29	4,73	4,80
Cl	0,05	0,14	0,07	0,07	0,06	0,07	0,06	0,07	0,00	0,02	0,00	0,05	0,01	0,02	0,00	0,00	0,06
H_2O	4,80	3,83	4,67	4,34	3,82	3,20	3,45	3,63	3,30	2,87	4,17	3,08	3,60	2,80	2,80	3,56	3,10
Subtotal	100,02	100,72	100,28	100,52	100,84	100,88	101,04	100,50	101,29	101,02	100,65	100,99	100,52	100,78	100,69	101,08	101,06
(O=F-Cl)	0,43	0,82	0,53	0,66	1,15	1,09	1,16	1,13	2,26	1,95	1,63	1,84	1,55	1,77	1,81	1,99	2,04
Total	99,59	99,90	99,75	99,86	99,69	99,79	99,88	99,37	99,03	99,07	99,02	99,15	98,97	99,01	98,88	99,09	99,02
Structural formula on the bases of twenty two oxygen atoms, considering all iron as Fe^{+2}																	
Si	5,61	5,85	5,86	5,89	5,78	5,81	5,80	5,78	6,30	6,11	6,29	6,07	6,40	6,24	6,32	6,24	6,24
^{IV}Al	2,39	2,15	2,14	2,11	2,22	2,19	2,20	2,22	1,70	1,89	1,71	1,93	1,60	1,76	1,68	1,76	1,76
[T] site																	
^{VI}Al	0,76	0,79	0,98	0,94	0,77	0,68	0,69	0,72	2,31	2,08	2,51	1,96	2,76	2,40	2,67	2,36	2,38
Ti	0,19	0,26	0,23	0,26	0,24	0,32	0,32	0,28	0,12	0,13	0,12	0,15	0,05	0,10	0,08	0,10	0,06
Fet	2,94	2,64	2,44	2,50	2,59	2,54	2,54	2,65	1,85	2,19	1,57	2,28	1,37	1,81	1,48	1,87	1,87
Mg	1,78	1,65	1,59	1,58	1,75	1,78	1,78	1,72	0,09	0,09	0,09	0,08	0,08	0,07	0,07	0,08	0,08
Mn	0,12	0,10	0,13	0,08	0,12	0,12	0,12	0,10	0,26	0,31	0,25	0,34	0,20	0,26	0,20	0,24	0,25
[M] site																	
Ca	0,01	0,00	0,00	0,00	0,00	0,00	0,01	0,00	0,01	0,00	0,01	0,02	0,00	0,01	0,01	0,00	0,01
Na	0,02	0,03	0,02	0,02	0,04	0,02	0,04	0,02	0,05	0,07	0,07	0,06	0,08	0,05	0,04	0,05	0,07
K	1,63	1,91	1,92	1,91	1,99	1,98	1,94	1,97	1,86	1,91	1,79	1,93	1,74	1,79	1,79	1,84	1,88
[I] site																	
F	0,49	0,92	0,60	0,74	1,33	1,24	1,33	1,30	2,55	2,22	1,81	2,10	1,69	1,96	1,97	2,24	2,27
Cl	0,01	0,04	0,02	0,02	0,02	0,02	0,02	0,02	0,00	0,01	0,00	0,01	0,00	0,01	0,00	0,00	0,02
OH	4,54	3,09	4,23	3,76	2,77	2,16	2,36	2,59	1,04	0,93	2,51	1,27	1,98	1,02	0,96	1,57	1,06
Fe/(Fe + Mg)	0,62	0,62	0,61	0,61	0,60	0,59	0,59	0,61	0,96	0,96	0,95	0,96	0,94	0,96	0,95	0,96	0,96
Mg/Mg + Fe	0,38	0,38	0,39	0,39	0,40	0,41	0,41	0,39	0,04	0,04	0,05	0,04	0,06	0,04	0,05	0,04	0,04
Al total	3,16	2,95	3,13	3,06	2,99	2,87	2,89	2,94	4,01	3,97	4,23	3,88	4,36	4,16	4,35	4,12	4,14

Samples	RDF-11																
Spot	C1				C2					C3				C4			
	Bt 1	Bt 2	Bt 3	Bt 4	Bt 1	Bt 2	Bt 3	Bt 4	Bt 6	Bt 1	Bt 2	Bt 3	Bt 4	Bt 1	Bt 2	Bt 3	Bt 4
SiO_2 (wt%)	45,37	41,74	39,98	47,58	41,95	40,89	39,90	41,13	41,74	40,41	39,95	39,53	41,23	40,32	40,26	40,18	40,60
TiO_2	0,54	1,06	1,48	0,19	0,97	1,41	1,44	0,75	0,76	1,50	1,71	1,06	1,25	1,83	2,01	1,18	1,01
Al_2O_3	26,64	23,18	22,13	25,50	23,96	22,17	21,67	23,08	22,63	21,95	22,41	22,05	22,94	22,17	22,17	21,70	22,08
FeO	9,85	15,51	17,73	9,37	14,97	16,59	18,70	16,15	16,06	17,23	17,62	18,12	15,62	17,22	17,13	17,72	16,50
MgO	0,47	0,54	0,45	0,63	0,48	0,51	0,49	0,46	0,39	0,45	0,49	0,49	0,49	0,43	0,47	0,46	0,46
MnO	1,08	2,36	2,77	1,05	1,99	1,93	2,34	1,88	1,75	2,18	1,99	2,27	1,88	1,82	2,03	2,11	1,98
CaO	0,01	0,03	0,00	0,01	0,00	0,00	0,01	0,00	0,01	0,00	0,06	0,02	0,01	0,00	0,00	0,02	0,00
Na_2O	0,31	0,25	0,25	0,14	0,29	0,22	0,19	0,33	0,27	0,33	0,22	0,26	0,30	0,26	0,24	0,30	0,28
K_2O	9,38	9,50	9,69	9,59	9,89	9,95	9,94	9,97	9,73	9,76	9,84	9,96	9,50	9,76	9,61	9,60	9,91
F	3,16	4,54	4,36	2,88	3,75	4,45	4,06	3,93	4,20	4,09	4,16	4,25	4,31	3,99	4,38	4,15	4,03
Cl	0,01	0,00	0,02	0,00	0,00	0,00	0,04	0,02	0,00	0,01	0,02	0,03	0,01	0,00	0,02	0,01	0,03
H_2O	4,38	3,11	2,90	4,17	3,08	3,61	2,86	3,72	4,11	3,70	3,14	3,52	4,28	3,67	3,28	4,07	4,80
Subtotal	101,19	101,82	101,75	101,11	101,32	101,73	101,63	101,40	101,64	101,62	101,61	101,55	101,82	101,48	101,60	101,49	101,66
(O=F-Cl)	1,33	1,91	1,84	1,21	1,58	1,88	1,72	1,66	1,77	1,73	1,75	1,80	1,82	1,68	1,85	1,75	1,70
Total	99,86	99,91	99,91	99,90	99,74	99,85	99,91	99,74	99,87	99,89	99,86	99,75	100,00	99,80	99,75	99,74	99,96
Structural formula on the bases of twenty two oxygen atoms, considering all iron as Fe^{+2}																	
Si	6,45	6,20	6,04	6,69	6,18	6,16	6,05	6,17	6,26	6,12	6,03	6,04	6,19	6,09	6,07	6,13	6,18
^{IV}Al	1,55	1,80	1,96	1,31	1,82	1,84	1,95	1,83	1,74	1,88	1,97	1,96	1,81	1,91	1,93	1,87	1,82
[T] site																	
^{VI}Al	2,91	2,25	1,98	2,92	2,35	2,10	1,92	2,25	2,27	2,03	2,01	2,01	2,24	2,04	2,01	2,03	2,14
Ti	0,06	0,12	0,17	0,02	0,11	0,16	0,16	0,08	0,09	0,17	0,19	0,12	0,14	0,21	0,23	0,13	0,12
Fet	1,17	1,93	2,24	1,10	1,85	2,09	2,37	2,03	2,02	2,18	2,22	2,31	1,96	2,17	2,16	2,26	2,10
Mg	0,10	0,12	0,10	0,13	0,11	0,11	0,11	0,10	0,09	0,10	0,11	0,11	0,11	0,10	0,10	0,10	0,10
Mn	0,13	0,30	0,35	0,12	0,25	0,25	0,30	0,24	0,22	0,28	0,25	0,29	0,24	0,23	0,26	0,27	0,25
[M] site																	
Ca	0,00	0,01	0,00	0,00	0,00	0,00	0,00	0,00	0,00	0,00	0,01	0,00	0,00	0,00	0,00	0,00	0,00
Na	0,08	0,07	0,07	0,04	0,08	0,06	0,06	0,09	0,08	0,10	0,06	0,08	0,09	0,07	0,07	0,09	0,08
K	1,70	1,80	1,87	1,72	1,86	1,91	1,92	1,91	1,86	1,88	1,89	1,94	1,82	1,88	1,85	1,87	1,92
[I] site																	
F	1,42	2,13	2,08	1,28	1,75	2,12	1,94	1,87	1,99	1,96	1,98	2,05	2,05	1,91	2,09	2,00	1,94
Cl	0,00	0,00	0,01	0,00	0,00	0,00	0,01	0,00	0,00	0,00	0,00	0,01	0,00	0,00	0,01	0,00	0,01
OH	2,90	1,19	1,06	2,77	1,47	1,74	1,16	2,06	2,34	1,99	1,40	1,75	2,46	2,01	1,43	2,36	3,15
Fe/(Fe + Mg)	0,92	0,94	0,96	0,89	0,95	0,95	0,96	0,95	0,96	0,96	0,95	0,95	0,95	0,96	0,95	0,96	0,95
Mg/Mg + Fe	0,08	0,06	0,04	0,11	0,05	0,05	0,04	0,05	0,04	0,04	0,05	0,05	0,05	0,04	0,05	0,04	0,05
Al total	4,46	4,06	3,94	4,23	4,16	3,94	3,87	4,08	4,00	3,91	3,99	3,97	4,06	3,95	3,94	3,90	3,96

Continua

Samples	RDF-09B															
	C1										C2					
Spot	Bt 1	Bt 2	Bt 3	Bt 4	Bt 5	Bt 6	Bt 7	Bt 8	Bt 9	Bt 10	Bt 1	Bt 2	Bt 3	Bt 4	Bt 5	Bt 6
SiO_2 (wt%)	38,57	38,66	38,87	38,55	38,35	38,23	38,23	38,47	38,05	38,53	38,82	38,58	38,10	38,25	38,64	38,16
TiO_2	1,86	2,04	2,14	2,26	2,08	2,34	2,22	2,21	2,14	2,14	2,42	2,39	2,20	2,28	2,61	2,46
Al_2O_3	16,09	16,52	16,28	16,63	16,49	16,49	16,11	17,37	16,10	16,34	16,04	15,73	15,99	16,14	15,22	15,72
FeO	18,55	18,24	18,01	17,90	18,02	17,96	18,20	17,25	18,52	17,29	18,35	18,22	19,27	18,89	18,40	18,98
MgO	8,92	8,49	8,79	8,46	8,75	8,60	8,53	8,03	8,69	8,91	8,66	8,79	8,52	8,43	8,86	8,55
MnO	0,89	0,87	0,82	0,87	0,95	0,91	0,94	0,79	0,93	1,32	0,74	0,74	0,71	0,68	0,89	0,83
CaO	0,02	0,00	0,00	0,00	0,01	0,00	-0,02	-0,01	0,00	0,02	0,02	0,02	0,01	0,03	0,03	0,02
Na_2O	0,06	0,07	0,07	0,07	0,09	0,08	0,06	0,07	0,08	0,09	0,09	0,08	0,07	0,05	0,06	0,05
K_2O	9,77	9,76	9,77	9,77	9,61	9,59	9,64	9,71	9,88	9,67	9,71	9,77	9,65	9,81	9,74	9,79
F	1,61	1,39	1,57	1,40	1,54	1,50	1,43	1,58	1,69	1,71	1,39	1,39	1,32	1,25	1,50	1,37
Cl	0,06	0,05	0,12	0,05	0,05	0,05	0,10	0,04	0,06	0,15	0,05	0,06	0,16	0,05	0,06	0,07
H_2O	4,28	4,58	4,36	4,78	4,69	4,71	5,37	5,08	4,60	4,28	4,04	4,37	4,32	4,61	4,52	4,61
Subtotal	100,67	100,67	100,81	100,73	100,61	100,45	100,79	100,60	100,73	100,45	100,32	100,14	100,30	100,45	100,51	100,60
(O=F-Cl)	0,69	0,60	0,69	0,60	0,66	0,64	0,62	0,67	0,72	0,75	0,59	0,60	0,59	0,54	0,65	0,59
Total	99,98	100,07	100,12	100,13	99,95	99,81	100,17	99,93	100,01	99,70	99,73	99,54	99,71	99,91	99,86	100,01

Structural formula on the bases of twenty two oxygen atoms, considering all iron as Fe^{+2}

	Bt 1	Bt 2	Bt 3	Bt 4	Bt 5	Bt 6	Bt 7	Bt 8	Bt 9	Bt 10	Bt 1	Bt 2	Bt 3	Bt 4	Bt 5	Bt 6
Si	5,88	5,88	5,90	5,87	5,85	5,84	5,87	5,86	5,84	5,87	5,90	5,90	5,84	5,85	5,91	5,85
^{IV}Al	2,12	2,12	2,10	2,13	2,15	2,16	2,13	2,14	2,16	2,13	2,10	2,10	2,16	2,15	2,09	2,15
[T] site																
^{VI}Al	0,77	0,85	0,81	0,85	0,82	0,81	0,79	0,99	0,75	0,81	0,77	0,74	0,74	0,77	0,66	0,69
Ti	0,21	0,23	0,24	0,26	0,24	0,27	0,26	0,25	0,25	0,25	0,28	0,28	0,25	0,26	0,30	0,28
Fet	2,37	2,32	2,29	2,28	2,30	2,30	2,34	2,20	2,38	2,20	2,33	2,33	2,47	2,42	2,35	2,43
Mg	2,03	1,93	1,99	1,92	1,99	1,96	1,95	1,83	1,99	2,03	1,96	2,00	1,95	1,92	2,02	1,95
Mn	0,11	0,11	0,11	0,11	0,12	0,12	0,12	0,10	0,12	0,17	0,09	0,10	0,09	0,09	0,11	0,11
[M] site																
Ca	0,00	0,00	0,00	0,00	0,00	0,00	0,00	0,00	0,00	0,00	0,00	0,00	0,00	0,01	0,00	0,00
Na	0,02	0,02	0,02	0,02	0,03	0,02	0,02	0,02	0,02	0,03	0,03	0,02	0,02	0,01	0,02	0,02
K	1,90	1,90	1,89	1,90	1,87	1,87	1,89	1,89	1,93	1,88	1,88	1,91	1,89	1,92	1,90	1,91
[I] site																
F	0,78	0,67	0,75	0,67	0,74	0,73	0,69	0,76	0,82	0,82	0,67	0,67	0,64	0,60	0,73	0,66
Cl	0,01	0,01	0,03	0,01	0,01	0,01	0,02	0,01	0,01	0,04	0,01	0,02	0,04	0,01	0,01	0,02
OH	3,65	4,04	3,72	4,25	4,10	4,15	4,87	4,49	3,97	3,59	3,50	3,85	3,81	4,15	3,95	4,11
Fe/(Fe + Mg)	0,54	0,55	0,53	0,54	0,54	0,54	0,54	0,55	0,54	0,52	0,54	0,54	0,56	0,56	0,54	0,55
Mg/Mg + Fe	0,46	0,45	0,47	0,46	0,46	0,46	0,46	0,45	0,46	0,48	0,46	0,46	0,44	0,44	0,46	0,45
Al total	2,89	2,96	2,91	2,98	2,97	2,97	2,92	3,12	2,91	2,94	2,87	2,84	2,89	2,91	2,74	2,84

Continua

Samples	RDF-09B							RDF-14B											
Spot				C2										C1					
	Bt 7	Bt 8	Bt 9	Bt 10	Bt 11	Bt 12	Bt 13	Bt 1	Bt 2	Bt 3	Bt 4	Bt 5	Bt 6	Bt 7	Bt 8	Bt 9	Bt 10	Bt 11	Bt 12
SiO_2 (wt%)	38,65	38,25	38,61	37,74	39,07	38,40	38,60	38,43	38,93	38,59	38,13	38,57	38,35	38,07	38,52	38,09	38,49	38,52	37,35
TiO_2	2,63	2,38	2,53	2,38	2,00	2,29	2,28	2,32	1,81	2,40	2,36	2,21	2,05	2,30	2,14	2,27	2,65	2,23	2,86
Al_2O_3	15,88	15,82	15,62	15,69	16,07	16,51	16,26	16,52	16,06	16,63	16,13	16,20	15,91	16,50	15,89	16,29	15,43	15,78	16,55
FeO	17,90	18,98	18,90	19,79	18,18	18,76	18,73	18,30	18,26	18,57	18,25	17,56	18,44	18,43	18,50	19,36	19,80	18,85	20,06
MgO	8,52	8,48	8,44	8,55	8,60	8,26	8,27	8,45	9,19	8,37	9,10	9,32	9,30	9,37	9,57	8,50	8,50	8,33	7,69
MnO	0,89	0,95	0,89	0,62	0,92	0,80	0,64	0,97	0,90	0,92	0,85	0,82	0,88	0,64	0,85	0,94	1,05	0,95	1,03
CaO	-0,02	0,03	0,01	0,03	0,01	0,02	0,00	0,02	0,01	-0,01	0,00	-0,01	0,02	0,01	0,02	0,02	0,02	-0,01	0,03
Na_2O	0,08	0,07	0,09	0,05	0,05	0,07	0,07	0,09	0,13	0,10	0,07	0,10	0,11	0,09	0,10	0,09	0,08	0,08	0,06
K_2O	9,76	9,80	9,64	9,59	9,89	9,69	9,73	9,76	9,78	9,96	9,63	9,68	9,81	9,74	9,65	9,68	9,68	9,69	9,58
F	1,48	1,30	1,32	1,19	1,37	1,32	1,30	2,20	2,39	2,41	2,38	2,60	2,52	2,30	2,44	2,07	1,26	1,47	1,19
Cl	0,05	0,05	0,20	0,06	0,05	0,04	0,04	0,04	0,08	0,05	0,04	0,04	0,16	0,04	0,04	0,04	0,10	0,06	0,03
H_2O	4,65	4,18	4,31	4,72	4,58	4,50	4,54	3,55	3,37	2,94	3,95	3,71	3,52	3,46	3,50	3,44	3,29	4,51	3,13
Subtotal	100,46	100,28	100,53	100,40	100,78	100,64	100,47	100,65	100,91	100,92	100,88	100,81	101,08	100,98	101,22	100,79	100,36	100,46	99,56
(O=F-Cl)	0,63	0,56	0,60	0,52	0,59	0,56	0,56	0,94	1,03	1,03	1,01	1,10	1,09	0,98	1,04	0,88	0,55	0,63	0,51
Total	99,83	99,72	99,93	99,88	100,19	100,08	99,91	99,71	99,88	99,89	99,87	99,71	99,99	100,00	100,18	99,91	99,81	99,83	99,05
Structural formula on the bases of twenty two oxygen atoms, considering all iron as Fe^{+2}																			
Si	5,90	5,86	5,90	5,81	5,94	5,85	5,89	5,85	5,90	5,84	5,82	5,87	5,85	5,78	5,84	5,81	5,85	5,90	5,72
^{IV}Al	2,10	2,14	2,10	2,19	2,06	2,15	2,11	2,15	2,10	2,16	2,18	2,13	2,15	2,22	2,16	2,19	2,15	2,10	2,28
[T] site																			
^{VI}Al	0,76	0,71	0,71	0,66	0,82	0,82	0,81	0,81	0,77	0,80	0,73	0,77	0,70	0,73	0,68	0,73	0,62	0,76	0,71
Ti	0,30	0,27	0,29	0,28	0,23	0,26	0,26	0,27	0,21	0,27	0,27	0,25	0,23	0,26	0,24	0,26	0,30	0,26	0,33
Fet	2,29	2,43	2,41	2,55	2,31	2,39	2,39	2,33	2,32	2,35	2,33	2,23	2,35	2,34	2,35	2,47	2,52	2,42	2,57
Mg	1,94	1,94	1,92	1,96	1,95	1,88	1,88	1,92	2,08	1,89	2,07	2,11	2,11	2,12	2,16	1,93	1,93	1,90	1,76
Mn	0,11	0,12	0,11	0,08	0,12	0,10	0,08	0,13	0,12	0,12	0,11	0,11	0,11	0,08	0,11	0,12	0,14	0,12	0,13
[M] site																			
Ca	0,00	0,01	0,00	0,01	0,00	0,00	0,00	0,00	0,00	0,00	0,00	0,00	0,00	0,00	0,00	0,00	0,00	0,00	0,00
Na	0,02	0,02	0,03	0,01	0,01	0,02	0,02	0,03	0,04	0,03	0,02	0,03	0,03	0,03	0,03	0,03	0,02	0,02	0,02
K	1,90	1,91	1,88	1,88	1,92	1,88	1,89	1,89	1,89	1,92	1,88	1,88	1,91	1,89	1,87	1,88	1,88	1,89	1,87
[I] site																			
F	0,72	0,63	0,64	0,58	0,66	0,64	0,63	1,06	1,15	1,15	1,15	1,25	1,21	1,10	1,17	1,00	0,61	0,71	0,58
Cl	0,01	0,01	0,05	0,02	0,01	0,01	0,01	0,01	0,02	0,01	0,01	0,01	0,04	0,01	0,01	0,01	0,03	0,02	0,01
OH	4,10	3,70	3,78	4,32	4,05	4,01	4,05	2,65	2,37	1,93	2,99	2,65	2,47	2,51	2,49	2,60	2,78	3,97	2,68
Fe/(Fe + Mg)	0,54	0,56	0,56	0,56	0,54	0,56	0,56	0,55	0,53	0,55	0,53	0,51	0,53	0,52	0,52	0,56	0,57	0,56	0,59
Mg/Mg + Fe	0,46	0,44	0,44	0,44	0,46	0,44	0,44	0,45	0,47	0,45	0,47	0,49	0,47	0,48	0,48	0,44	0,43	0,44	0,41
Al total	2,86	2,85	2,81	2,85	2,88	2,96	2,92	2,96	2,87	2,96	2,90	2,90	2,86	2,95	2,84	2,93	2,77	2,85	2,99

Samples	RDF-9B															
Spot	C1				C2				C3			C4				
	Bt 1	Bt 2	Bt 3	Bt 4	Bt 10	Bt 11	Bt 12	Bt 13	Bt 5	Bt 6	Bt 7	Bt 1	Bt 2	Bt 3	Bt 6	Bt 7
SiO_2 (wt%)	37,91	38,98	36,82	38,26	37,22	37,88	38,37	37,60	38,50	38,88	38,50	38,11	37,69	37,92	38,29	38,18
TiO_2	0,55	0,36	0,53	0,83	1,78	1,43	1,16	1,30	1,01	0,96	1,30	1,36	1,10	0,95	0,88	1,23
Al_2O_3	15,21	14,49	15,36	14,67	14,80	15,01	14,69	15,50	15,98	15,01	15,42	15,49	15,46	14,81	15,29	15,10
FeO	19,14	18,20	21,20	18,73	20,83	20,27	19,85	20,23	18,20	18,52	18,76	19,34	20,11	20,24	19,41	19,74
MgO	10,67	11,63	9,63	10,93	9,90	9,62	10,51	9,78	9,62	10,19	9,85	9,66	9,26	9,95	10,22	9,99
MnO	0,71	0,72	0,87	0,87	0,79	0,74	0,97	1,01	0,69	0,83	1,03	0,93	0,78	0,97	0,92	0,82
CaO	0,02	0,00	0,01	0,00	0,04	0,02	0,03	0,04	0,03	0,02	0,01	0,00	0,04	0,04	0,00	0,01
Na_2O	0,12	0,12	0,09	0,09	0,11	0,10	0,15	0,09	0,03	0,07	0,09	0,04	0,05	0,06	0,12	0,13
K_2O	10,15	9,95	9,75	9,79	9,84	10,08	9,90	9,59	9,98	9,98	10,17	10,06	9,91	9,87	9,79	9,86
F	4,33	4,75	3,89	4,53	3,49	3,83	3,82	3,78	4,41	4,47	4,16	4,22	3,80	3,85	4,08	4,17
Cl	0,10	0,05	0,08	0,06	0,02	0,04	0,04	0,04	0,04	0,03	0,04	0,04	0,06	0,06	0,08	0,04
H_2O	2,01	1,89	2,51	2,20	1,55	1,70	1,22	1,79	2,47	2,07	1,45	1,47	2,34	1,87	1,66	1,48
Subtotal	100,91	101,14	100,73	100,95	100,35	100,71	100,71	100,74	100,97	101,02	100,78	100,73	100,59	100,59	100,73	100,74
(O=F-Cl)	1,85	2,01	1,66	1,92	1,47	1,62	1,62	1,60	1,87	1,89	1,76	1,79	1,61	1,63	1,73	1,77
Total	99,06	99,13	99,07	99,03	98,88	99,09	99,09	99,14	99,10	99,13	99,02	98,94	98,98	98,96	99,00	98,97
Structural formula on the bases of twenty two oxygen atoms, considering all iron as Fe^{+2}																
Si	5,85	5,97	5,76	5,90	5,74	5,83	5,86	5,78	5,91	5,96	5,88	5,84	5,84	5,86	5,87	5,86
^{IV}Al	2,15	2,03	2,24	2,10	2,26	2,17	2,14	2,22	2,09	2,04	2,12	2,16	2,16	2,14	2,13	2,14
[T] site																
^{VI}Al	0,61	0,58	0,59	0,56	0,44	0,56	0,51	0,59	0,80	0,67	0,66	0,64	0,66	0,55	0,63	0,59
Ti	0,06	0,04	0,06	0,10	0,21	0,17	0,13	0,15	0,12	0,11	0,15	0,16	0,13	0,11	0,10	0,14
Fet	2,47	2,33	2,77	2,41	2,69	2,61	2,54	2,60	2,34	2,37	2,40	2,48	2,60	2,61	2,49	2,53
Mg	2,45	2,65	2,24	2,51	2,28	2,21	2,39	2,24	2,20	2,33	2,24	2,21	2,14	2,29	2,33	2,29
Mn	0,09	0,09	0,11	0,11	0,10	0,10	0,13	0,13	0,09	0,11	0,13	0,12	0,10	0,13	0,12	0,11
[M] site																
Ca	0,00	0,00	0,00	0,00	0,01	0,00	0,01	0,01	0,00	0,00	0,00	0,00	0,01	0,01	0,00	0,00
Na	0,04	0,04	0,03	0,03	0,03	0,03	0,04	0,03	0,01	0,02	0,03	0,01	0,01	0,02	0,03	0,04
K	2,00	1,94	1,95	1,92	1,94	1,98	1,93	1,88	1,95	1,95	1,98	1,97	1,96	1,94	1,91	1,93
[I] site																
F	2,11	2,30	1,92	2,21	1,70	1,86	1,84	1,84	2,14	2,16	2,01	2,05	1,86	1,88	1,98	2,02
Cl	0,03	0,01	0,02	0,01	0,01	0,01	0,01	0,01	0,01	0,01	0,01	0,01	0,01	0,02	0,02	0,01
OH	0,16	-0,12	0,88	0,29	0,08	0,08	-0,41	0,19	0,62	0,18	-0,31	-0,33	0,76	0,25	-0,08	-0,30
Fe/(Fe + Mg)	0,50	0,47	0,55	0,49	0,54	0,54	0,51	0,54	0,51	0,50	0,52	0,53	0,55	0,53	0,52	0,53
Mg/Mg + Fe	0,50	0,53	0,45	0,51	0,46	0,46	0,49	0,46	0,49	0,50	0,48	0,47	0,45	0,47	0,48	0,47
Al total	2,76	2,61	2,83	2,67	2,69	2,72	2,64	2,81	2,89	2,71	2,78	2,80	2,82	2,70	2,76	2,73

Tabela Suplementar C
Coeficientes de partição mineral/líquido (Kd) utilizados no modelamento geoquímico para a geração do Granito Marajoara.

Modelling of the heterogranular biotite monzogranite of the Marajoara granite protolith by partial melting of the Arco Verde tonalite.

Mineral	Ba	Rb	Sr	Y	Zr	Nb	La	Ce	Nd	Sm	Eu	Gd	Yb	Lu
Plagioclase	1,05	0,016	6,8	0,51	0,55	0,06	0,45	0,347	0,29	0,013	2	0,9	0,13	0,13
Quartz	0,022	0,041					0,015	0,014	0,016	0,014	0,056		0,017	0,014
Biotite	7	0,936	0,447	1,4	1,8	4	0,272	0,037	0,339	1,55	0,145	0,442	1,473	1,617
Magnetite	0,1	0,01	0,01	3,21	8,45	2,5	0,22	2,7	3,5	1,9	0,91		2,2	0,1
Ilmenite			0,66	0,2	10,4	6,58	1	1,19	7,6	6,9	2,5		4,1	0,74

Modelling of the equigranular biotite monzogranite of the Marajoara granite protolith by partial melting of the 80% Arco Verde tonalite and 20% of metasedimentary rock.

Mineral	K	Rb	Y	Hf	U	La	Ce	Nd	Sm	Eu	Gd	Tb	Dy	Er	Yb	Lu
Plagioclase	0,040	0,011	0,02	0,170	0,05	0,07	0,4	0,29	0,05	7,9	0,90	0,19	0,180	0,03	0,30	0,130
Quartz	0,013	0,041		0,03	0,025	0,015	0,014	0,016	0,014	0,056			0,015		0,017	0,014
Biotite	2,50	0,936	0,0	2,10	0,46	15,100	3,49	5,7	1,8	4,7	0,442	3,90	0,200	0,171	0,32	0,330
Magnetite		0,01	0,12	0,95	0,21	1	26	18,6	12,5	7,2		7,50	1,6		0,09	0,1
Ilmenite			0,21	3,1	0,063	7,1	7,8	7,6	6,9	2,5		6,50	4,90		0,55	0,74
Amphibole	0,081	0,008	8,3	0,52		0,26	2,130	3,28	11,3	5,9	7	2,400	10,200	7	0,022	0,022

ATA-PARECER

Sobre a Defesa Pública da Tese de Doutorado de
RODRIGO FABIANO SILVA SANTOS

A banca examinadora da Tese de Doutorado de **RODRIGO FABIANO SILVA SANTOS** orientando do Prof. Dr. Davis de Carvalho Oliveira (UFPA), composta pelos professores doutores Gilmara Regina Lima Feio (Membro-UNIFESSPA), Luciano Ribeiro da Silva (Membro-UFOPA), Valdecir de Assis Janasi (Membro-USP) e João Marinho Milhomem Neto (Membro-UFPA), após apresentação da sua tese intitulada "**PETROGÊNESE DOS GRANITOS MANDA SAIA E MARAJOARA: CONTRIBUIÇÕES PARA A DEFINIÇÃO DA NATUREZA DO MAGMATISMO PALEOPROTEROZOICO DA PROVÍNCIA CARAJÁS**", emite o seguinte parecer:

O candidato realizou sua apresentação de forma clara, organizada e segura no tempo estipulado. Na arguição mostrou domínio da temática abordada e respondeu a maioria das perguntas formuladas pela banca. O trabalho escrito foi apresentado na forma de inclusão de artigos, sendo um já publicado no periódico *Lithos* e outro submetido na *Precambrian Research*, ambos de impacto internacional. Dessa forma, todos os artigos atendem às exigências básicas para uma tese de doutorado.

Recomenda-se que as contribuições expostas pela banca examinadora durante a arguição sejam avaliadas e incorporadas no corpo da Tese. Incluindo as tabelas de dados, anexos e material suplementar. Finalmente, a banca examinadora decidiu por unanimidade aprovar a tese de doutorado.

Belém, 13 de dezembro de 2024

Prof. Dr. Davis de Carvalho Oliveira (Orientador – UFPA)

Prof.ª Dr.ª Gilmara Regina Lima Feio (Membro-UNIFESSPA)

Prof. Dr. Luciano Ribeiro da Silva (Membro-UFOPA)

Prof. Dr. Valdecir de Assis Janasi (Membro-USP)

Prof. Dr. João Marinho Milhomem Neto (Membro-UFPA)